NYC TOWN+GOWN CLIMATE VULNERABILITY, IMPACT, AND ADAPTATION (VIA) ANALYSIS

2024

FINAL REPORT

April 2024

Mayor's Office of Climate & Environmental Justice

THE NEW SCHOOL

NYC DCAS Citywide Administrative Services

ARCADIS

Columbia University

CUNY The City University of New York

Drexel

NRDC

Population Council Ideas. Evidence. Impact.

Sarah Lawrence College

Stevens Institute of Technology

Cornell University

Forest Service U.S. Department of Agriculture

New York City Town+Gown Climate Vulnerability, Impact, and Adaptation Analysis

Final Report

April 2024

Table of Contents

How to cite this report:

McPhearson, T., Towers, J., Balk, D., Horton, R., Madajewicz, M., Montalto, F., Neidell, M., Orton, P., Rosenzweig, B., Bader, D., Chen, Z., DeGaetano, A., Evans, C., Golkhandan, M. R., Gurian, P., Kaatz, J., Herreros-Cantis, P., Lo, R., Ortiz, L., Braneon, C., Branco, B., Campbell, L., Dubay, F., Graziano, K., Jiang, L., Johnson, M., Kennedy, C., Kioumourtzoglou, M.-A., Kleyman, J., Kleyman, J., Knowlton, K., Limaye, V., Matte, T., Munoz Perez, S., Reed, D., Shakya, M., Svendsen, E., Tipaldo, J., Zoraghein, H. (2024). *New York City Town+Gown Climate Vulnerability, Impact, and Adaptation Analysis Final Report.* New York City Mayor's Office of Climate and Environmental Justice.

Executive Summary

New York City faces significant threats from climate change, with current climate models highlighting the likelihood of increasing temperatures, rising sea levels, and more frequent extreme weather events. These current and emerging hazards pose substantial challenges to the city's infrastructure and communities, with projections aligned with those used at the State level, emphasizing the importance of regional consistency in risk assessment. In this report, members of the NYC VIA team present key findings and recommendations from an 18-month study to understand future climate change in New York City.

Below, we summarize many of the key findings, which are described in more detail in the full report:

- Sea level rise estimates project a high-end increase of approximately four to five feet by the end of the century, with projections available for multiple decades. Flood risk studies traditionally treat rain and storm surge as independent processes. However, historical data analysis reveals low, non-zero correlations between rain and surge, particularly in hurricanes. This poses a direct threat to coastal communities and infrastructure, with increased risk of storm surge flooding during hurricanes and other high-tide events. The potential co-occurrence of rain and storm surge, while not always additive in terms of flooding depth, adds a layer of complexity to risk assessment and necessitates further investigation through advanced flood modeling.
- While less frequent than other storm types, tropical cyclones (TC) pose a greater threat due to their intensity and destructive nature. Their potential impact warrants separate analysis in all hazard assessments, utilizing both historical data and modeled events. Comprehensive future assessments focusing on hurricane risks and employing multiple methods, models, and researchers, are crucial for robust planning and resilience strategies. Future projects are encouraged to assess climate-sensitive hurricane risks comprehensively.
- Understanding the characteristics and trends of extreme rainfall is critical for managing urban pluvial flooding, triggered by intense, localized downpours that overwhelm drainage network systems. Future projections based on updated climate models (CMIP6 model[1]) indicate greater changes in daily extreme rainfall compared to earlier models. These changes include higher projected rainfall amounts for the 100-year storm event. There is only limited evidence to suggest the rate of increase for hourly precipitation extremes is faster than that for daily totals. Limited subdaily rainfall data

[1] CMIP6 stands for Coupled Model Intercomparison Project Phase 6. It is a collaborative international effort among climate modeling groups to systematically compare and evaluate climate models.

hinders efforts to fully characterize pluvial flood risks, highlighting the need for a network of high-resolution rain gauges across the City and its watersheds. Analysis of historical trends reveals significant increases in the frequency and duration of events with extreme peak and average precipitation intensities, suggesting a future with more frequent and potentially more impactful pluvial floods.

- Task 4 focuses on a systematic evaluation of health-related economic costs attributed to climate-sensitive events in New York City. Divided into three parts, the task involves assessing costs from past events, understanding future population changes in New York City, and examining the implications of these changes on health economic damages. The section details health-related economic costs due to past events from 2000 to 2019, utilizing a multi-step approach that includes a literature review, calculation of mortality and morbidity cases, and monetization of these cases. Noteworthy findings include an annual average of 361 additional deaths, 1,833 hospital visits, and 1,404 emergency department visits due to climate-sensitive events, resulting in annual health-related economic costs of $4.17 billion and a total of $83.45 billion over two decades. The study also acknowledges potential underestimation of morbidity costs due to limitations in available studies and monetization techniques.
- The six Flood Vulnerability Indices (FVIs) for New York City, which the study team developed, enable users to view vulnerability of the City's population to six flood hazard scenarios, providing guidance for policies and operations to enhance flood resilience. Each index consists of two components. One component is exposure to one of the hazard scenarios, including current and two future storm surge scenarios and current and two future tidal flooding scenarios. The second component, which remains the same across all six indices, assesses susceptibility to harm from flooding and capacity to recover in the population. The FVIs are innovative in their demonstration of exposure, in representing susceptibility to harm and capacity to recover with indicators that have been validated for the case of storm surge flooding, and in the method used to aggregate the indicators into an index.

Recommendations based on this research include the need for improved high resolution temporal and spatial precipitation data quality, standardized procedures for sub hourly rainfall data collection, and the establishment of a network of maintained precipitation gauges. Ongoing assessment of TC climatology changes, consideration of compound rain-surge flooding, and validation of flood vulnerability indicators through further flood impact analysis are also essential for robust climate risk assessment and planning, as are greater understanding of climate related morbidity costs.

In conclusion, New York City faces significant challenges from climate change, but proactive measures grounded in robust data analysis, advanced hydrologic & hydraulic modeling, and

targeted vulnerability assessments can enable it to build resilience and navigate the changing climate with greater preparedness, confidence, and advanced flood warning systems. Investing in climate-resilient infrastructure, improving drainage systems, supporting residents' efforts to reduce impacts, and implementing early warning systems are crucial steps to mitigate the worst impacts of extreme weather events. By understanding the specific vulnerabilities of its diverse communities and prioritizing targeted adaptation strategies, New York City can rise to the challenges posed by climate change and emerge as a model for urban resilience in the face of a changing world.

Introduction

The Town+Gown New York City Climate Change Vulnerability, Impacts, and Adaptation Study (VIA) brings together an interdisciplinary team of researchers, climate scientists, and professionals co-led by The New School's Timon McPhearson and Joel Towers to work closely with the NYC Mayor's Office of Climate & Environmental Justice (MOCEJ), Interagency Collaborators, and the New York City Panel on Climate Change Working Groups (NPCC WGs) to develop a comprehensive analysis of, and deliver data on, future climate conditions and associated socio-economic impacts in New York City.

The VIA team includes colleagues from Arcadis, Columbia University, Cornell University, City University of New York, Drexel University, Lamont Doherty Earth Observatory, NASA/GISS, Natural Resources Defense Council (NRDC), Population Council, Sarah Lawrence College, Science and Resilience Institute at Jamaica Bay (SRIJB), Stevens Institute of Technology, and USDA Forest Service.

The findings from the VIA study reflect the immense value of co-production leveraging expertise from across the City's diverse academic institutions and private sector with New York City Interagency collaborators to address the pressing issue of climate change across the region. This collaboration has yielded detailed insights into critical areas such as future projections of sea level rise, the increasing frequency and severity of extreme weather events, the substantial health-related economic impacts of climate change, and the development of the first Flood Vulnerability Index for New York City. Significantly, the co-production approach has ensured these strategies are grounded in scientific rigor and strategic recommendations that have strong potential to inform future responses to the multiple impacts of climate change in the near term and future. Throughout the 18 month duration of the study, research deliverables have evolved in consultation and collaboration with NYC Interagency Collaborators highlighting the commitment of the overall VIA team to this dynamic, complementary, and coproduced undertaking. The VIA final report underscores the necessity

for ongoing research and collaboration, calling upon stakeholders to utilize the study's findings to secure a resilient and sustainable future for New York City.

The report is organized around primary tasks identified by MOCEJ and agreed on in the project scope:

- Task 2: Climate Projections and Climate-Sensitive Hazards for NYC Region
- Task 3: Current and Future Extreme Heavy Rainfall in New York City
- Task 4: Systematic Assessment of Health-Related Economic Costs from Climate-Sensitive Events in New York City
- Task 5: Flooding Vulnerability Index and Impact Assessment for New York City

Task 2: Climate Projections and Climate-Sensitive Hazards for New York City Region

Task 2: Climate Projections and Climate-Sensitive Hazards for New York City Region

Core Team Members:

- Philip Orton, Co-Lead (Stevens Institute of Technology)
- Radley Horton, Co-Lead (Columbia University)
- Dan Bader (Columbia University)
- Franco Montalto (Drexel University)
- Luis Ortiz (George Mason University)
- Timon McPhearson (The New School)
- Christian Braneon (CUNY)

New York City Interagency Collaborators:

- Lauren Smalls-Mantey (Department of Health)
- Jarrod Sims (Office of Management and Budget)
- Alan Cohn (NYC Department of Environmental Protection)
- Jennifer Garigliano (NYC Department of Environmental Protection)
- Erika Jozwiak (MOCEJ)

2.1 Key Messages

- Updated climate projections, developed using the latest models and data, continue to predict a future of higher temperatures, rising sea levels, and more frequent extreme events. The projections for New York City and the City's risk assessment are aligned with those being prepared for New York State's Climate Impact Assessment.
- For sea level rise, the VIA projections (developed for this study) show a high estimate of between approximately four to five feet by the end of the century. Projections are now available for all decades from the 2030s through the 2090s, 2100, and now, 2150.
- Flood risk studies, insurance products and flood maps typically assume rain and storm surge are independent processes. Our analyses of New York City historical data show rain and storm surge generally have low, but non-zero correlations. However, for Tropical Cyclones (TCs), our results also show there is a moderate probability of one variable being high when the other is extreme.
- Co-occurrence of rain and surge does not guarantee additive behavior where flooding is increased in depth or spatial extent. Therefore, a recommended next research step is understanding New York City compound rain-surge flooding will be in order to simulate a set of extreme event scenarios in flood models.

- TCs generally cause more extreme hazards compared with other storm types and are responsible for a majority of the most extreme events, even though they occur far less frequently. As a result, we recommend considering separate analysis of TCs in all hazard assessments, including rain, coastal flooding and compound rain-surge, using observed historical data where available, but also modeled events if helpful to reduce uncertainties.
- We recommend future projects and NPCC assessments embark on a comprehensive assessment with multiple TC climatology change assessment methods and additional researchers, to better understand future climate-sensitive hurricane risks. This could help New York City achieve its goal of properly quantifying and planning for high-end risk, more in-line with its request for NPCC to use the 90th percentile sea level rise projections in future flood maps.

2.2 Objectives and Research Activities

The objectives of Task 2 were to (1) synchronize and apply outputs from the New York State Climate Impacts Assessment (NYSCIA) to the heterogeneous environment and diversity of stakeholders within New York City; and (2) develop new hazard assessments, and climate impact projections with associated sensitivity analyses based on the needs and gaps identified by the Client team, and related stakeholder workshops in which the NYSCIA projections were presented. Below we introduce these assessments, analyses and projections.

A key component of Task 2 was facilitating the review and adaptation of NYSCIA projections to the New York City context, inclusive of New York City stakeholder feedback (**Section 2.3** below). These projections are a key component of the NPCC4 climate science special report (Braneon et al., in press). A confluence of factors aligned to make this a timely moment for updated New York City climate projections. The Intergovernmental Panel on Climate Change Sixth Assessment Report (IPCC AR6) report emphasized the primacy of climate science aspects the NPCC and MOCEJ have long highlighted, such as the focus on extreme events, stakeholder-driven climate metrics, low probability high-consequence outcomes, and compound events/cascading impacts. The IPCC's application of the latest climate models and most recent data to this adapted lens thus provided fertile avenues for the Task 2 Team.

In addition, the NYSCIA projections, which are based on the latest IPCC report and associated global climate models (GCMs), provided the opportunity to explore the applicability for New York City stakeholders of key NYSCIA updates relative to prior New York City and New York State assessments, such as higher spatial resolution (**Section 2.6, 2.7**) and bias-correction

based on quantile mapping. The high-resolution dynamically downscaled heat impact projections are a potential product for a future NPCC5 report.

Lastly, Task 2 developed new hazard assessments and projections (**Sections 2.4-2.5**) and sensitivity analyses (**Sections 2.8-2.9**), based in most cases on needs and gaps identified by the Client team and stakeholder feedback. This includes calls for research on compound and cascading hazards (City of New York, 2021) and feedback at the NYSCIA workshop in collaboration with the Client Team and NPCC Climate Science Working Group. A summary of the assessment of the potential for compound rain-surge flooding is included in the NPCC4 Flooding chapter (Rosenzweig et al., in review). The sensitivity study of the importance of TC climatology change (**Section 2.8**) influenced the final text for the climate science special report (Braneon et al., in press).

2.3. Climate projections for NPCC4

The Task 2 team was responsible for preparing updated climate change projections, specifically for sea level rise in New York City. In addition to these projections, the Task 2 team was also tasked with integrating updated climate projections developed for the New York State Assessment (Lamie et al., 2024) for additional climate variables (such as temperature, precipitation, and extreme events), to the work of the VIA project and NPCC. A description of methodologies for theNew York State Assessment Climate Impacts Assessment (NYSCIA) (Bader and Horton, 2023) can be found online here. The New York City region in NYSCIA are the projections used in this project and by the NPCC. The data is now available online atNYC Open Data.

In June 2022, a workshop was held to coordinate efforts between the NYSCIA and VIA project. The workshop was attended by VIA project team members, members of the NPCC, and representatives from New York State and New York City (Towers, McPhearson et al., 2023). Task 2 scientists helped co-organize the workshop and led multiple presentations over the course of the event. One of the primary objectives of the meeting was to ensure the climate risk information used by both the City and State is coordinated and consistent. A secondary objective of the meeting was to have subject matter experts present on the state-of-the-science for a variety of climate hazards impacting New York State, including New York City. Presentations covered topics such as the updated climate science projections using Coordinated Model Intercomparison Project (CMIP6) model data, sea level rise projections and methodologies and climate extremes and storms, and compound extreme events.

Over the duration of the VIA project, interactions between VIA, NYSCIA, and NPCC continued, ensuring continuity in the projections used across the projects and maintaining the use of the best available, local climate risk information. Methodologies (and the projections) for sea level rise are consistent in this project, the NPCC Climate Science Special Report, and the NYSCIA report. Since the interim report, collaborations between the projects have further led to 1) preparation of additional metrics of temperature extremes specific to New York City stakeholders and 2) discussion of the selection of the SSP5-8.5 scenario[2].

In some ways, the VIA project served as a "bridge" that strengthened the relationship between the NYSCIA and NPCC. As VIA was tasked with providing updated projections for New York City support for NPCC, Task 2 researchers were effectively able to facilitate and translate the information across the different projections, while also tailoring it to specific applications and needs of New York City stakeholders here.

a. Methods

Since the 2015 NPCC, there have been advances in sea level rise understanding and projection methodologies, including new approaches to capture the possibility of rapid ice melt from land-based ice sheets (Bamber et al., 2019; Gornitz et al., 2019; Fox-Kemper et al., 2021). Several recent studies confirm the plausibility of high-end sea level rise scenarios (e.g., Slangen et al., 2017) and offer techniques to adapt projections to the regional/local scale (Carson et al., 2016; Fox-Kemper et al., 2021). There is growing evidence that supports the plausibility of higher-end sea level rise projections, primarily based on observations of land-based ice loss and advances in climate modeling.

Our analysis includes updated sea level rise projections for New York City based on those developed for the IPCC 6th Assessment report (see Table for the updated projections and stand-alone document for description of methods). These projections are based on the CMIP6 models and SSP framework (Eryring et al., 2016; O'Neill et al., 2016; Riahi et al., 2017), and incorporate advances in process understanding, improved and lengthened observational records, and improved ice-sheet modeling. The sea level rise projections were developed in coordination with the NYSCIA and the NPCC to ensure the methodologies are consistent in New York City.

Projections for extreme events (such as the additional temperature metrics prepared for the City) for this project align with those from the NYSCIA, using a method known as quantile

[2] The SSP5-8.5 scenario is a future pathway outlined in the Shared Socioeconomic Pathways (SSPs) framework, which is used in climate change research to explore different societal, economic, and environmental trajectories. SSP5-8.5 represents a pathway where global development is characterized by high levels of socioeconomic inequality, rapid economic growth, high energy demand, and limited environmental regulations or climate change mitigation efforts.

mapping. The projections are based on two SSPS, SSP2-4.5 and SSP58.5 (Riahi et al., 2017), the same scenarios used for sea level rise, and use 16 global climate change models (Bader and Horton, 2023; Lamie et al., 2024).

The additional metrics are:

1. Days with maximum temperature at or above 82F
2. Days with minimum temperature at or above 80F

Full data tables with the updated results will be in the NPCC4 report. Additional extreme heat metrics include days at or above 90F and the frequency and duration of heat waves.

b. Results

The table here presents the updated sea level rise projections for New York City (in inches).

	10th	25th	50th	75th	90th	ARIM
2030s	6	7	9	11	13	
2040s	9	11	12	15	17	
2050s	12	14	16	19	23	
2060s	15	18	21	24	29	
2070s	18	21	25	31	36	
2080s	21	25	30	39	45	81
2090s	24	28	34	47	58	114
2100	25	30	36	50	65	
2150	38	47	59	89	177	

Table 2.1. Updated sea level rise projections for New York City

Using the middle range (25th to 75th percentiles) across all three scenarios, sea level is projected to rise along the New York City coastline by seven to 11 inches by the 2030s, 14 to 19 inches by the 2050s, and 25 to 39 inches by the 2080s. The high-end estimate (90th percentile) for sea level rise by the 2080s is 45 inches. By 2100, sea levels are projected to rise by as much as 65 inches.

Based on the ARIM scenario from the 2019 New York City Panel on Climate Change report, accelerated loss of land-based ice could lead to sea level rise of up to 81 inches by the 2080s and 114 inches by 2100 under a plausible “worst-case” scenario. While unlikely, these projections are included here because they cannot entirely be ruled out and would have very high consequences, should they occur. Such low-probability, high-consequence scenarios may be of interest for some risk-management decisions.

c. Discussion

In the review of the NYSCIA report and the NPCC Climate Science Special report, a couple of the reviewers commented on the selection of SSP scenarios used in the updated projections (SSP2-4.5 and SSP5-8.5). These comments focused on the use and plausibility of SSP5-8.5. The sea level rise projections for the VIA project use both the low and medium confidence scenarios from SSP5-8.5, and the projections for NPCC/NYSCIA also use SSP5-8.5. The Task 2 team prepared multiple sets of projections for internal review to look at the different pairings of sea level rise scenarios and agreed upon the approach outlined here.

Our rationale for selecting the scenarios used for VIA includes:

1. These scenarios have the same end-of-century radiative forcing as the two representative concentration pathways (RCPs) used in previous New York City projections, providing continuity with that work. Stakeholder feedback also illustrated a preference for the use of these two scenarios (NYSERDA, 2020).
2. Relative to many other scenarios, there were also a large number of climate models available for these two SSPs.
3. They span a broad range of what we consider plausible climate outcomes, including the high-consequence outcomes that are critical for risk management.

4) While most would argue the balance of evidence suggests lower greenhouse gas (GHG) forcing/concentrations are more likely than those associated with SSP5-8.5, the balance of evidence also now suggests the changes in extreme-event statistics, and climate impacts, are unrealistically low. (See NPCC 2022) Inclusion of SSP5-8.5 offers partial protection against the severe limitations of climate and impact models to assess tail risks, including but not limited to those associated with extreme events.

For the interpretation of results from the 2014 New York State Climate Projections Update (Horton et al., 2014) and New York City Panel on Climate 2015 (Horton et al., 2015), these updated projections for sea level rise are lower at the high-end 90th percentile, but broadly consistent at the 50th percentile. Despite these differences, these changes fall within the uncertainty we would expect with such projections, given the deep uncertainty about the amount of long-term sea level rise.

d. Research Gaps

Moving forward, there is a need for further research in several areas related to climate projections in urban contexts.

First and most fundamentally, more and improved observational data, including new weather stations, and modeling are essential. Higher resolution global models will also yield new insights over time.

Next, the last decade revealed the importance of compound and sequential extreme events. Most assessments to date have not considered these rigorously, and their impacts have not been extensively evaluated yet with GCMs. Below, in Sections 2.4 and 2.5, we assess rain and storm surge compound hazard and rain and humid-heat sequential hazards. However, other hazard combinations are possible and should be comprehensively assessed.

Finally, further work is also needed on identifying climate metrics of particular use to decision-makers and those with climate impact expertise.

2.4. Compound rain-surge hazard

Coastal-urban areas are vulnerable to intense rainfall and extreme storm surge and their potential compound flooding effects. While recent studies have provided evidence of widespread, and in some cases rising, joint occurrence of extreme rainfall and storm surge, few studies have investigated these phenomena locally in detail.

Tropical cyclones (TCs, including post-tropical cyclones) and extratropical cyclones (ETCs) both can cause coastal hazard extremes and compound flooding. However, these storm types have different energy and moisture sources and as a result, cause different hazard intensity in terms of maximum wind speed, storm surge (See **Section 2.8** below) and rainfall rates. Probabilistic assessments for areas susceptible to rare, extreme TCs, should evaluate TCs as a separate population of data to avoid mistaking these events as outliers in comparison to other much more frequent storms.

In this subtask, we present the most detailed statistical assessment to date for New York City co-occurring rain and storm surge, including combined and separated assessments of different storm types. A manuscript with detailed descriptions of the research is submitted for peer-reviewed publication (Chen et al., submitted) and included here as **Appendix 2**.

a. Methods

Our research is more detailed than prior studies because we utilized hourly rainfall data with a specific focus on simultaneous and near-simultaneous occurrence of rain and surge events. One prior research study of NYC exemplifies the typical approach of other studies, utilizing daily rainfall totals with hourly storm surge data, considering them as occurring jointly if they were within plus or minus one day (Wahl et al., 2015). NYC encompasses many small urbanized watersheds with rapid drainage, where rain and surge must happen nearly simultaneously to cause compounding, so our approach will provide more useful results.

We utilize storm track data for TCs (HURDAT) and Extratropical Cyclones (ETCs) to assess data separately to determine whether resulting correlations and probabilities are higher than a merged assessment of all storm types (see **Appendix 2** for further details; Landsea and Franklin, 2013). Historical data for both rain and surge show the most extreme historical events were tropical (or post-tropical) cyclones (TCs). Historically, severe coastal floods (e.g., Hurricane Sandy in 2012, a Nor'easter in December 1992), pluvial floods (e.g., Hurricane Ida in 2012) and compound floods (Hurricane Irene in 2012; Orton et al., 2012) have struck New York City, and can be associated with TCs, ETCs and convective thunderstorms. Four of New York City's top five storm surges from 1788-present were TC (or post-tropical cyclones), three of the top five hourly rain events from 1948-present were TC (KNYC: Central Park), and four of the top five daily rain events from 1869-present were TC (KNYC: Central Park).

We quantitatively evaluate characteristics of compound flood drivers (rain and surge, quantified as the non-tidal residual NTR) including their dependency, magnitude, lag time and joint return periods. We follow a common approach for statistical analysis of compound extremes, with "two-sided sampling" (e.g., Jane et al., 2022; Wahl et al., 2015; Ward et al., 2018) where one case looks at surge during high rain events and the other rain during high surge events. Our statistical analyses are conditioned on the **primary flood driver** being top-ranked, while the **secondary flood driver** can be any value. We refer to the top-ranked rain events as **Pluvial-Coastal (P-C)** events (with durations from 1-48 hours), and top-ranked surge events as **Coastal-Pluvial (C-P)** events. The primary flood drivers are sampled by peaks-over-threshold (POT) approach based on a per-year average (PYA) frequency of five events.

Compound flood drivers and their co-variation can vary across different locations within New York City. For example, a TC event hitting New Jersey may cause large surge but little rainfall at NYC (e.g. Sandy). Or, a TC crossing over Long Island to the east of New York City may cause storm surge at Kings Point (near La Guardia Airport - see map in **Appendix 2**) and intense rain "to the left of" the storm (e.g. the 1938 Long Island Express Hurricane). This study conducted evaluations at both The Battery and Kings Point to represent the flood hazards pertinent to South Bronx and Northern Queens, respectively.

b. Results and Discussion

Here, we summarize some primary findings of likely interest to New York City stakeholders. Again, more detail is given in **Appendix 2**. New York City rain and surge generally have low-to-moderate correlations, but one exception is for top-ranked rain events that come from TCs. While the correlation for all top-ranked rain event data combined is near zero, correlations for TC events alone are high (0.52) (**Figure 2.1**).

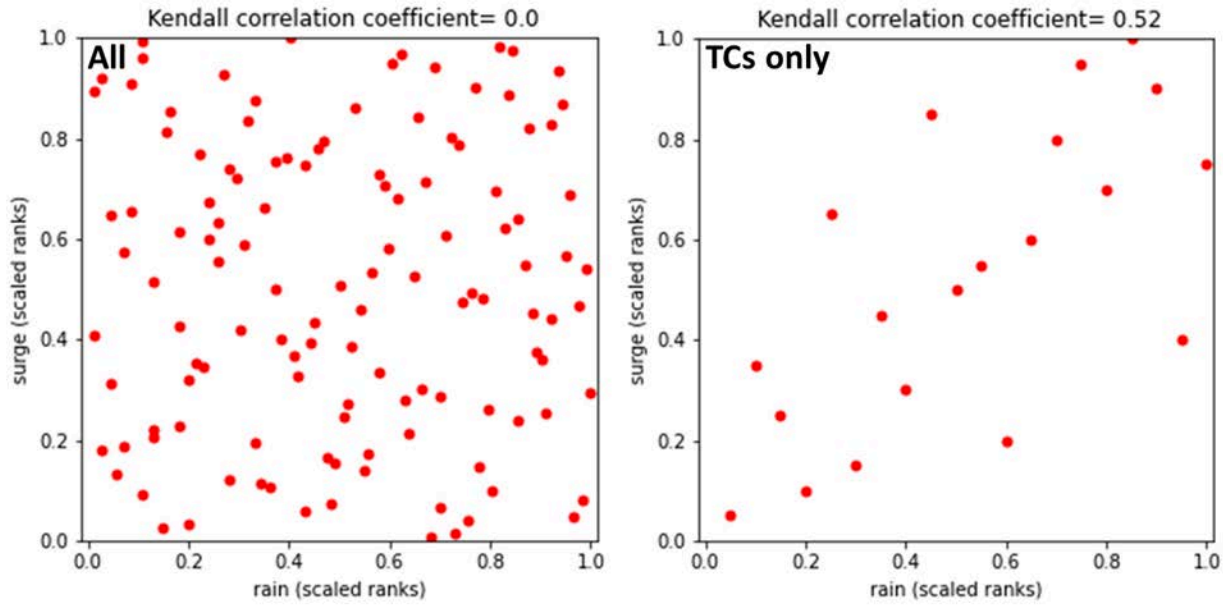

Figure 2.1: Plots of non-tidal residual ("surge") and rain for the top-ranked rain events from 1948-2021, all events (left) and TC (and post-TC) events only (right). Data are plotted as scaled ranks from 0 to 1, used in computing the Kendall rank correlations of 0.0 and 0.52, respectively.

The hourly data reveal subtle but important spatial differences in lag times between the joint flood drivers (**Figure 2.2**). The lags for TCs tend to be smaller than those for ETCs, and those for Neither are very spread out across a large range of lag times. This indicates that during extreme rain or surge events, the secondary driver's peak is more likely to co-occur with the extreme driver, thus more likely compound its effects. For the South Bronx, where surge typically lags rain by two to six hours, this leads to a lower probability of simultaneous pluvial-coastal compound flooding but a higher probability of fluvial-coastal compound flooding on the Bronx River. To see this, compare red to black bars and median lag times in **Figure 2.2**.

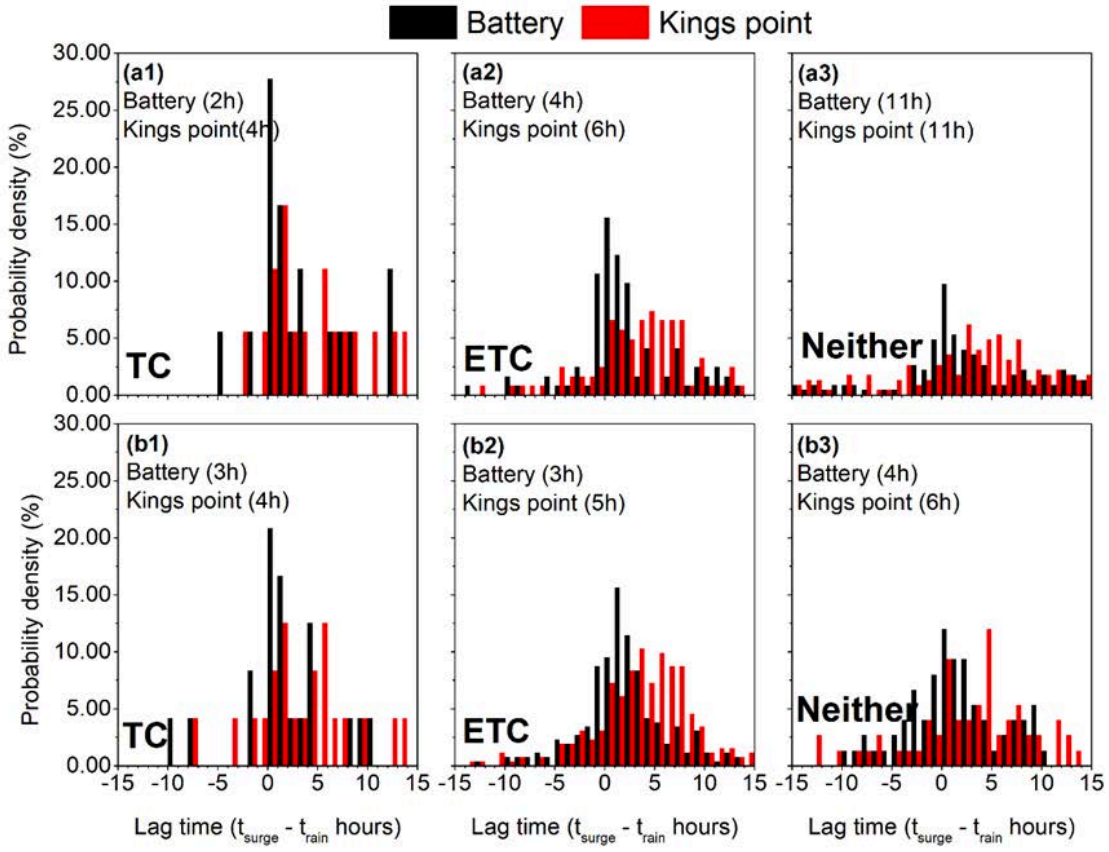

Figure 2.2: Histograms of lag time for the P-C compound floods (a) and the C-P compound floods (b). The left, middle and right panels are associated with TC (1), ETC (2) and Neither (3). The red and black colors represent histograms for The Battery and Kings Point separately. The numbers in each plot are the median of the absolute lag time for The Battery and Kings Point. Positive lag time values indicate peak storm surge occurs after peak of rainfall.

TCs have markedly different compound rain-surge hazard characteristics from other storm types and dominate the joint probabilities of the most extreme events, even though they occur much less frequently (**Figure 2.3**). As a result, jointly occurring rain and storm surge for 50-year to 200-year return periods are equal or higher when only assessing TC events versus assessing "ALL" events together. A similar result has been observed for New York City storm tide events (Orton et al., 2016) and the general topic of separating TCs from other storm types in hazard assessment is covered elsewhere within this report (**Section 2.8**).

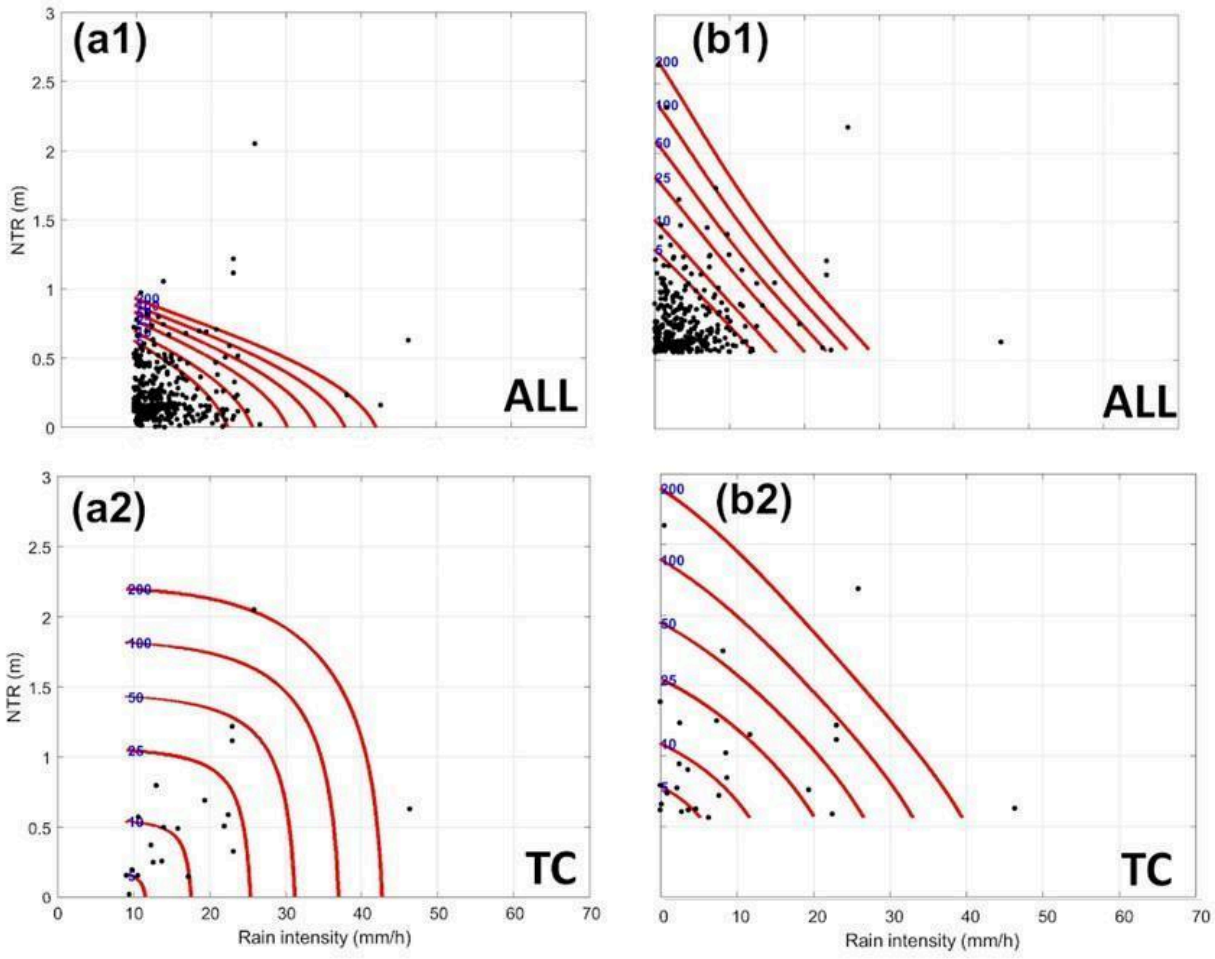

Figure 2.3: The joint return period curves (red lines, blue text labels) for simultaneous rain and surge (NTR) for P-C compound events (left; a1-a2) and C-P compound events (right; b1-b2) for ALL data (top row) and for TC data only (bottom row). The black dot points are the observed events.

Previous studies have assessed the joint probability of rainfall and storm surge (or coastal water level) hazards for the New York City area (e.g. Wahl et al., 2015; also, the Community Stormwater Resiliency Study). The research typically uses the daily rainfall data and ±1 day window to capture the compound flood drivers and evaluate the joint return periods using "All" events (e.g., Lai et al., 2021; Wahl et al., 2015). However, these studies did not assess the simultaneous compound flood drivers, which is a more direct impact-oriented metric for pluvial and compound flooding for this urban environment. More importantly, using compound samples from "All" events could underestimate the joint probability of extreme compound hazards, in contrast with a storm separation approach. Recent studies (e.g., Gori et al., 2022) have begun using synthetic TC storms to evaluate the joint probability of compound rain and coastal flood hazards, which can be particularly useful for assessing future climate change. The

observation-based approach we have used, and this new model-based approach, can be complementary. While the observation-based approach is grounded in real-world data, the model-based approach can improve sample sizes for extreme events and enable extending the science to climate projections.

c. Research Gaps

Statistical and probabilistic assessments of rain and storm surge such as this one can demonstrate that flood drivers can co-occur during extreme storm events. Co-occurrence does not guarantee additive behavior where flooding is actually compounded, which could be a vertical effect (deepened flood depths) or a spatial effect (greater flood area). Therefore, we recommend as a next step that modelers simulate the flooding from these extreme event scenarios. Given the availability of one or more flood city-wide flood models owned by New York City (e.g. Ghanbari et al. 2024), it is recommended an assessment of actual compound flood risk is initiated.

This research does not evaluate historical or future climate change but focuses instead on establishing a baseline assessment of rain-surge compound hazard. We use past data to look at the present compound flood risk, requiring an assumption that the past processes and probabilities reflect those of the present. We remove sea level rise from the storm surge data in order to eliminate the most well-established climate change effect. Future work should assess future changes to compound flood drivers and risk due to climate change.

2.5 Sequential hazard

There is growing awareness that sequential hazards can pose outsized, non-linear impacts on cities and communities (Raymond et al., 2020). Furthermore, recent research has revealed how the frequency and intensity of sequential extremes can change dramatically under even small amounts of global warming (Zcheishchler et al., 2020). It is thus perhaps surprising that historical risk assessments have generally not considered sequential hazards, in any detail. We focus on sequential relationships between high precipitation and high humid heat, since both types of events are projected to increase with climate change, and because associated infrastructure disruptions and challenges to emergency management can be expected to make the second event in the sequence more impactful than it would otherwise be.

a. Methods

Gridded temperature, humidity and precipitation fields from the fifth major global reanalysis produced by the European Centre for Medium-Range Weather Forecasts (ERA5) high-resolution product (Hersbach et al., 2020) (1979-2019) were analyzed on a 1° x 1° grid for June - August (JJA). Daily maximum wet bulb temperatures (WBT) are calculated as in

Rogers et al., 2021, using code adapted from Kopp et al., 2020, that executes an algorithm from Buzan et al., 2015 for the Davies-Jones method (2008).

Daily summer climatologies are calculated at each gridpoint for precipitation and WBT smoothed with a 30-day running mean. Use of a 30-day running mean smoothes the day-to-day climatology by removing the random timing of stochastic weather events. Daily anomalies are computed by subtracting these smoothed climatologies from the raw daily data. Extreme WBT values are computed using the 90th percentile threshold of the daily anomalies. In contrast, the 90th percentile precipitation threshold is calculated using only the subset of days that include at least one mm of rainfall. Anomalies are used to remove the predominating influence of the seasonal cycle on humidity, temperature, and precipitation, which would obscure the influence of synoptic variability. Furthermore, anomalies better capture relatively extreme events outside the warmest or the wettest weeks in the seasonal composites.

The difference in daily average extreme WBT anomalies conditioned on extreme precipitation anomaly days, relative to all days of the summer months, are composited to generate maps in the days prior to and following an extreme precipitation anomaly day. We compute these composite maps for a) the single day of the local extreme precipitation event, and the average across three days b) before and c) after the local extreme precipitation event. These composites are also generated in the reverse direction, plotting precipitation anomalies conditioned on local extreme WBT events. The methods used for these two sets of composites are repeated using dry bulb temperature (DBT) in place of WBT for comparison. Lastly, a two-sample Kolmogorov-Smirnov test for goodness of fit with a p-value of less than 0.05 is conducted and plotted on top of each global difference map to show areas of significance.

In addition to the gridpoint-level analysis described above, a smaller, New York City region is defined as 40-41N and 71-72W. In this region, we show the evolution of WBT, DBT, specific humidity, and precipitation over the eleven days surrounding a 90th percentile precipitation event. Summer daily total precipitation, maximum WBT, mean DBT and mean specific humidity data from ERA5 were averaged across each grid point for the regions, after the location were selected from the raw daily data. The daily anomalies for these region averages are then calculated as above. Composites showing the temporal evolution of these variables five days before and after extreme precipitation events are then plotted for the New York City region as described above.

b. Results

Figure 2.4 shows results for days with enough precipitation to classify as a 90th percentile rain event. The left panel shows WBT anomalies on the three days before the rain event, with both

the rain event and the WBT anomaly being defined for each separate box in the mapped region. The map shows WBT tends to be slightly above normal in the days leading up to the heavy rain event, although the opposite is observed over coastal Long Island. The next four panels of Figure 2.4 show spatially averaged values, over the smaller boxed New York City region domain, of four variables conditioned on a heavy rain day. This shows WBT rises slightly in the lead up to the rain event, with a slight peak on the day of the rain, followed by a slight drop in the days thereafter. When WBT is decomposed into its two constituent parts (specific humidity and dry bulb temperature), a similar pattern is observed, with both variables above normal before the event, and then dropping from a peak after the event. However, the pattern is much more pronounced for specific humidity, with a strong spike beginning in the day or two before the rain, peaking strongly on the day of the rain, and then dropping sharply to normal over the next two days. In contrast, air temperature drops more gradually, from a tiny positive anomaly before the rains to a more noteworthy drop on the day of the rain, and especially the day after the rain.

Figure 2.5 shows the same-day relationship between humid heat and extreme precipitation, averaged over the New York City region. The left panel shows, only for the days with 90th percentile or greater precipitation, what percentile bins for wet bulb temperature are most common. While encouraging to see the 90th percentile humid heat bin is not the most common, it's discouraging to see humid heat values in the 60th-100th percentiles are far more common than humid heat values in the 0-40th percentile bins. Results are similar when conditioned on extreme humid heat days, defined as 90th percentile or greater. On those days, it is far more common to have precipitation in the 60th-100th percentile than it is to have precipitation in the 0-40th percentile bin.

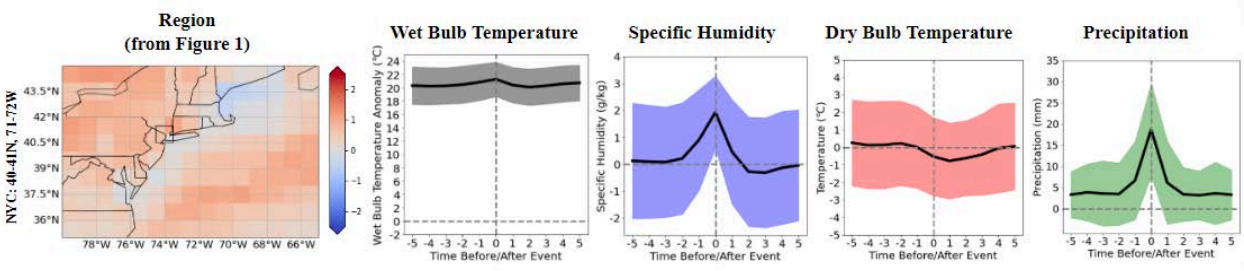

Figure 2.4: Results for days with enough precipitation to classify as a 90th percentile rain event. The left panel shows WBT anomalies on the three days before the rain event, with both the rain event and the WBT anomaly being defined for each separate box in the mapped region.

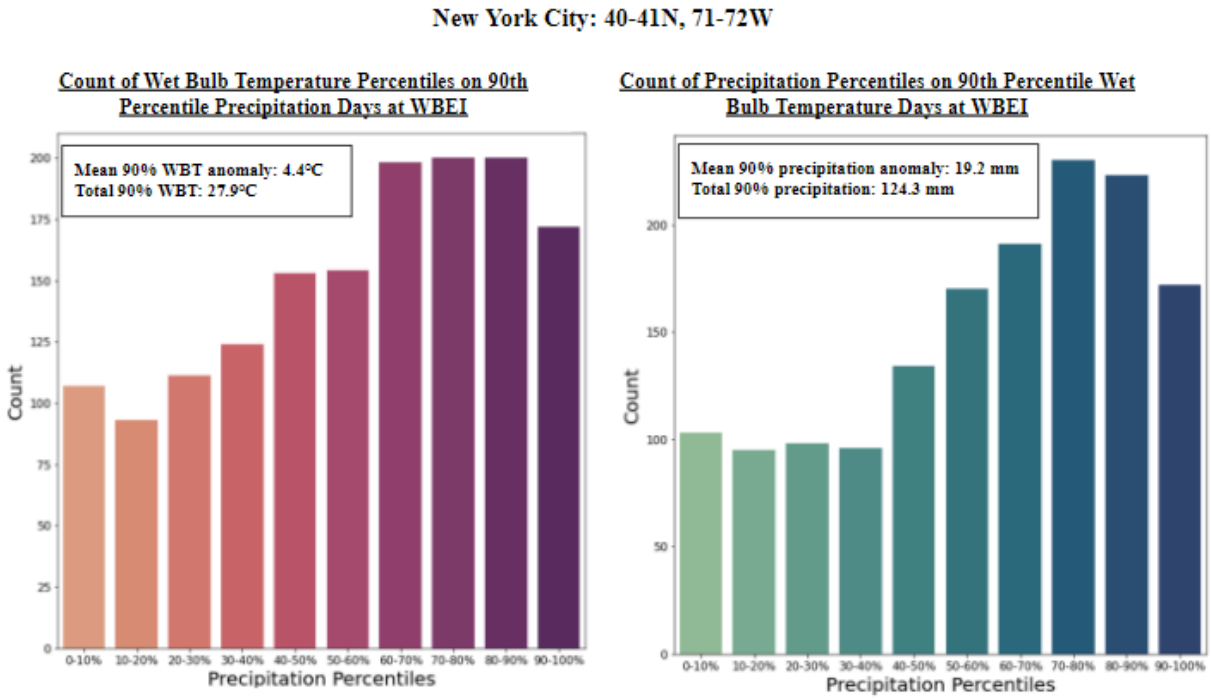

Figure 2.5: Same-day relationship between humid heat and extreme precipitation, averaged over the New York City-region. WBEI refers to Water Benefit-Based Ecological Index.

c. Discussion

In general, we found relationships between humid heat and extreme precipitation, but they were not particularly strong. We found evidence that humid heat builds in the lead up to a heavy rain event, and then drops in the day afterwards. Dry bulb temperature follows a generally similar pattern although dry bulb temperature drops on the day of the heavy rain, whereas humid heat drops the day after. Perhaps the key point though is the magnitude of these changes is relatively small. When same-day occurrences of high humid heat and high precipitation are considered, a positive correlation is apparent, pointing to heightened risks, although it is somewhat less extreme, given that that the 90th percentile is not the most common bin for each variable when the other variable is experiencing a 90th percentile value.

d. Research Gaps

Future work should focus on the most extreme humid heat and precipitation events (e.g. 99th percentile rather than 90th percentile events). However, due to small sample sizes for 99th percentile events, a larger spatial domain would be needed, and the observational data used here might need to be supplemented by model outputs. More generally, projections would be a

logical next step for sequential humid-heat and extreme precipitation analyses, model limitations notwithstanding. Additionally, future sequential work should explore additional physical hazards, like cold air outbreaks and winter precipitation. Finally, the compound hazard framework could be extended beyond sequential/simultaneous hazards in New York City to consider simultaneous hazards between New York City and other regions, such as other cities in the Northeast.

2.6. Land Surface Temperature Projections

a. Methods

Projections of Land Surface Temperature for the end of century (2070-2099) across four Shared Socioeconomic Pathways (SSPs) as well as Representative Concentration Pathways (RCPs) scenarios were taken into consideration. These are a low (SSP1-2.6), middle (SSP2-4.5), and two high emissions (SSP3-7.0 and SSP5-8.5) scenarios and use global climate model data from the 6th Coupled Model Intercomparison Project (CMIP6). CMIP6 is a multi-model ensemble of simulations of historical and future climate which include, among others, simulations of the global earth system using a shared set of initial and boundary conditions. To preserve information about the spread between the various models, we computed projections along the 25th, 50th (median), and 75th percentiles of the CMIP6 model ensemble for each scenario. These global modal data have a typical horizontal resolution ranging between 1.5-1 degrees.

Land surface temperature data are computed for the New York City boundary based on a multi-image mean of summer dates (May-Sept.) from 2013-2022. A multi-year period was selected to ensure it represents the typical climatic surface temperatures during summer instead of any individual day. Imagery was screened for cloud cover and quality control flags, with a resulting subset of 34 images. To represent sub-grid scale information on land surface temperature projections, we compute the mean change in the CMIP6 model data and use it as a delta added to satellite imagery from the Landsat Analysis ready Product. The spatial distribution of the data is scaled to preserve the standard deviation of the historical surface temperature imagery.

b. Results

Our analysis shows while there is significant spread in the projections in the CMIP6 inter-model ensemble, there is a general increase in surface temperatures by end of century. Absent any adaptive action, there is no change in the location of temperature hotspots. The analysis also shows the value of global mitigation on surface temperatures. In SSP1-2.6, the expected temperature change is between 0-4°C across the entire CMIP6 ensemble. Meanwhile,

temperatures in the hottest models of the high emission scenarios may expect increases between 10-14°C across the City (**Figure 2.6**, below).

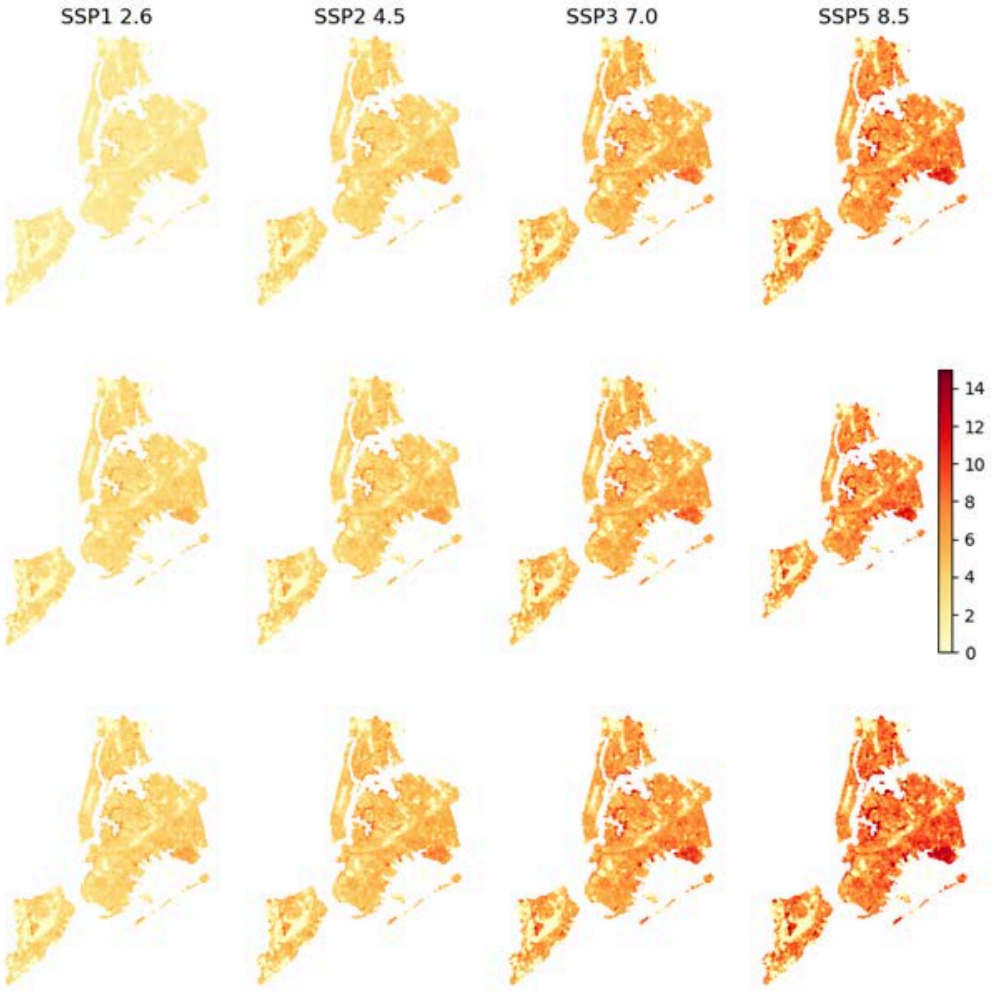

Figure 2.6: Projected Increase in NYC Temperatures by 2100. Change in land surface temperature (°C) in New York City for SSP1-2.6, SSP2-4.5, SSP3-7.0, and SSP5-8.5. Rows represent the 25th (top), 50th (center), and 75th (bottom) percentile of the CMIP6 model ensemble.

c. Research Gaps

The projections developed as part of this study focus on the impact of the climate change signal on land surface temperatures. However, one key limitation of this work is the assumption that increases in surface temperature across all land surface types will respond equally to this climate change signal. There is evidence this may not be the case. For example, heat storage in buildings and other high heat capacity materials may increase temperatures over time. Indeed, this heat storage is a key process that often leads to air temperature urban heat islands (Oke et al., 1981). Another key limitation in this work is the assumption of a static land surface in New York City. These projections do not account for long-term changes to the built environment, which would have an impact on the surface temperature characteristics. A dense network of surface termperature monitoring stations could provide observational data to inform this research gap.

These gaps may also require the use of sub-kilometer dynamic modeling of the city's climate, either by use of an urban canopy model or a micro-meteorological model. Dynamical modeling would represent many of the feedback processes related to land-atmosphere interactions at the urban scale, as well as the impacts that change in this land cover may induce. Examples of this type of model include the UMEP model that models the SEUWS urban energy balance to compute thermal comfort metrics (Lindberg et al., 2016) and PALM4U (Salim et al., 2019), among others.

2.7 Spatially explicit Cooling and Heating Degree Days Projections

Demand for indoor cooling and heating are a function of not only building infrastructure, but also a location's climate. As NYC's climate warms due to rising temperatures, there are potential consequences to energy consumption due to increased demand for indoor cooling during the warm months and decreased demand for heating in winter.

Moreover, temperatures in NYC exhibit spatial variability due to a variety of land use and meteorological factors. The spatial extent, geometry, and materials properties of built-up surfaces play a crucial role in the surface energy balance of cities, mediating the portion of the incoming solar energy that may result in warmer air (Oke, 1982). Sea and land breezes, elevation, and other prevailing weather conditions also play a significant role in determining temperatures through NYC and its broader metropolitan region (Bauer, 2020; Bornstein, 1968; González et al., 2019; L. E. Ortiz et al., 2018).

Given the spatial variability of temperatures due to urban and geographical features of NYC and the expected warming of the city throughout the 21st century, we conducted a simulation of

typical historical and future climate in the city in order to estimate the impact of climate change on cooling and heating loads. While changes to these heating and cooling load indicators can be computed from readily available point records, there is still a gap on their spatial variability in future climates. We address this gap with a combination of high resolution physics-based modeling and computation of cooling and heating degree-days, a common indicator of these loads.

a. Methods

Simulations of local climate in NYC were conducted using the Weather and Research Forecasting Model (WRF) version 4.4 (Skamarock et al., 2019). WRF is a numerical weather prediction model that solves the equations of motion of the atmosphere and its interactions with the land and ocean surface. We configured the model using a 1 km spatial resolution to approximate the neighborhood-scale centered around the city. We configured the model using three nested domains of increasing resolution (Figure 2.7), with a domain of analysis (D03) with 1 km grid spacing.

Figure 2.7. Map of WRF simulation domain showing the 9 km resolution parent domain (map extent), intermediate 3 km resolution domain (D02) and the 1 km analysis domain (D01).

Model input for the simulations include meteorological and geographical data. For meteorological data we used Bias-corrected model CMIP6 outputs (Xu et al., 2021). Xu et al (2021) provide data at 1.25° x 1.25° horizontal resolution and 14 vertical levels. The data is corrected using a Multimodel Ensemble (MME) method with 18 ensemble members from CMIP6 and corrected using ERA5 reanalysis. The dataset contains three scenarios from the

CMIP6 ensemble: (1) Historical, (2) SSP2-4.5, and (3) SSP5-8.5. Our approach to model future climate here consisted of selecting a typical year based on monthly average temperatures for two 30-year time slices from the CMIP6 data. To accomplish this, we took the median value of monthly mean temperatures for 1981-2010 for the Historical scenario and 2070-2099 for the two SSPs, then found the year closest to each median value for each dataset, as shown in Figure 2.8. WRF simulations were then conducted for each of these selected years. The simulations were based on a physics suite used in previous NYC studies that showed good agreement with observations (González et al., 2019). For each simulation, a 2 month model spinup (i.e., a period of time to allow the model to develop independent solutions from initial conditions) was used, consisting of the November and December of the preceding year.

Cooling degree-days were computed as follows:

$$CDD = T_{mean} - T_{base} \; if \; T_{mean} > T_{base}$$
$$CDD = 0 \; if \; T_{mean} \leq T_{base}$$

Where *CDD* is cooling degree-day, T_{mean} is the daily mean temperature, and T_{base}, the baseline temperature where cooling is needed, is 65°F. Similarly, heating degree-days are computed as:

$$HDD = T_{base} - T_{mean} \; if \; T_{base} > T_{mean}$$
$$HDD = 0 \; if \; T_{base} \leq T_{mean}$$

Where *HDD* is heating degree-days.

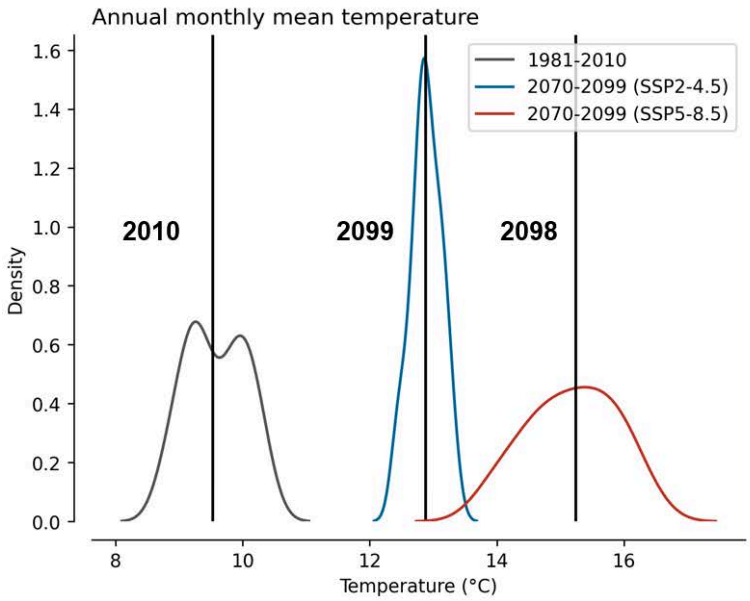

Figure 2.8. Kernel density estimates of the bias corrected historical, SSP2-4.5, and SSP5-8.5 monthly mean temperatures. The vertical lines represent the distribution median and the corresponding closest year.

b. Results

WRF raw simulation results consist of 3-hourly data of all state variables in the model. HDD and CDDs are computed from 2-meter air temperature, a diagnostic variable meant to describe near-surface conditions. Daily mean temperatures for model outputs are warmer by the end of the typical year, with daily mean temperatures of 13.4°C (56.1°F), 15.2°C (59.4°F), and 17.5°C (65.5°F), with overall distributions shown in Figure 2.9. The spatial distribution across all three scenarios is similar, with warmer temperatures over the NYC metropolitan area (Figure 2.10). Temperatures also decrease closer to the southern coastline of Queens and Brooklyn, likely due to the cooling effect of afternoon sea-breezes. In all three scenarios, the highest temperatures occur west of the Hudson River in New Jersey. These results are consistent with observation and modeling studies conducted in the region (Gedzelman et al., 2003; L. E. Ortiz et al., 2018).

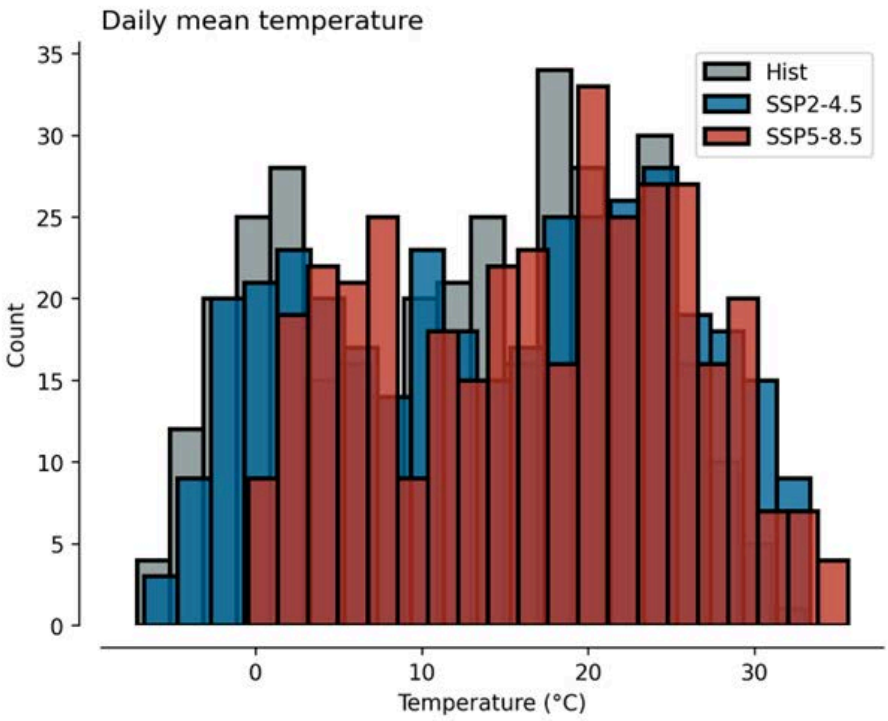

Figure 2.9. Histogram of daily mean temperatures for the typical years from the historical simulation (2010), SSP2-4.5 (2099), and SSP5-8.5 (2098).

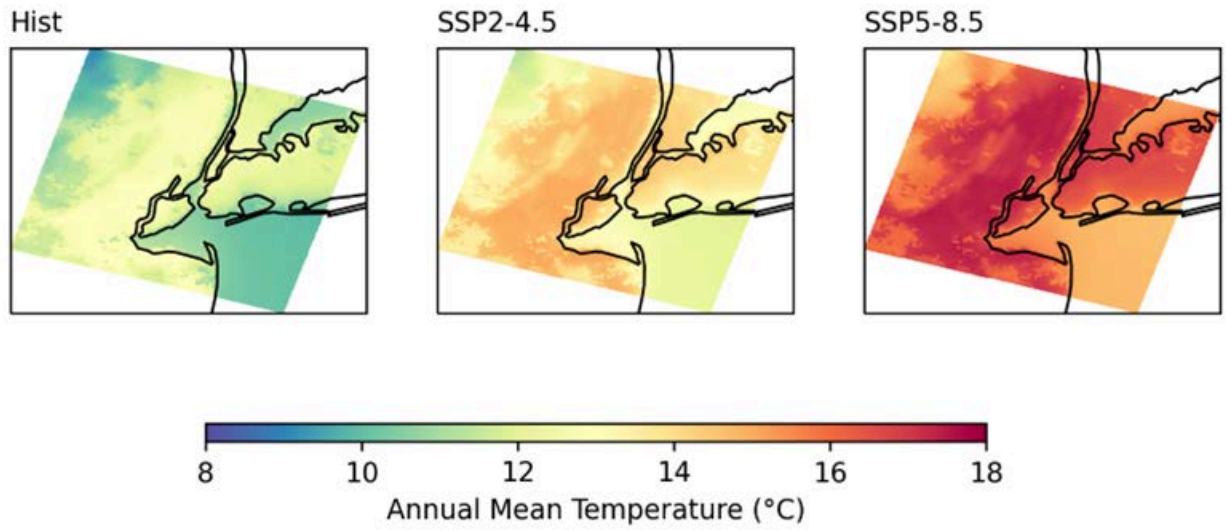

Figure 2.10. Spatial distribution of mean daily temperatures for the three scenarios.

CDD and HDD results show a similar spatial distribution to daily mean temperatures, although with opposing spatial gradients. CDDs are highest within NYC and east of the Hudson River in New Jersey (Figure 2.11, top row). The temperature gradient linked to a southerly sea breeze

is also more pronounced in CDDs due to these circulations being more prevalent during the warm months when CDDs are computed.

CDDs increase across both end of century scenarios, with the highest changes occurring in SSP5-8.5, the higher emissions pathway. Changes in CDD increase by 200-300 degree-days in SSP2-4.5, and nearly double in SSP5-8.5. CDDs are highest in the urbanized NYC Metropolitan Area due to the urban heat island effect. HDDs follow an inverse trend, decreasing as winters grow warmer as a result of climate change. HDDs decrease by ~350 degree-days in SSP2-4.5 compared to Historical baseline, and plunge to less than 2000 degree-days in SSP5-8.5 (Figure 2.11, bottom row).

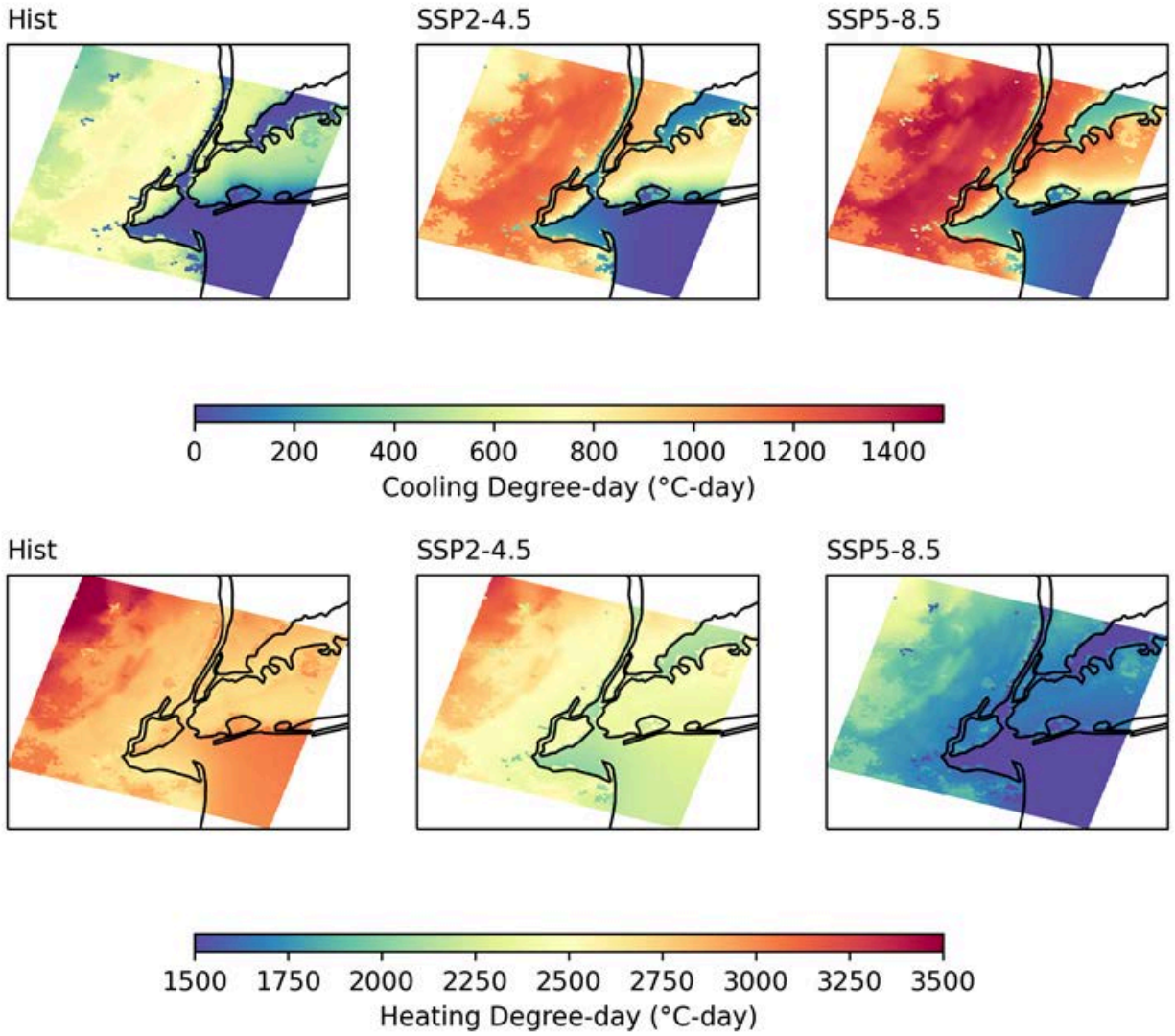

Figure 2.11. Spatial distribution of cooling degree-days (top row) and heating degree-days (bottom row) for each scenario.

c. Research Gaps

Although the work here leverages state-of-the-art high resolution climate models that bridge the gap between coarse global models (~1° resolution) to the neighborhood scale, there are several gaps that were not addressed in this work. One such gap is the simulation time limited to a single typical year. True climatological time scales typically use 30-year time slices to provide a range of the typical climate of a region. While the approach followed here displays a typical year in terms of annual mean temperatures, future research could expand this to form a multi-year ensemble.

Another limitation lies in the use of CDDs and HDDs themselves, which are common yet incomplete measure of cooling and heating loads. These indicators only consider mean daily temperatures and fail to account for sub-daily variability. This variability can be quite large, particularly in transition months. Another limitation of degree-day indicators is that they do not account for either population or infrastructure change and their impacts on energy consumption. More recent advances have tried to address some of these gaps by using population data to estimate population-weighted degree-day indicators (Kennard et al., 2022), while others use advanced modeling to directly estimate electric loads based on combined building energy and climate models (Ortiz et al., 2022). Nevertheless, this work showcases the impact of year-round climate change on NYC's demand for energy to maintain thermal

2.8. Sensitivity study of tropical cyclone (TC) climate change: Literature review

a. Summary

Hurricane Sandy caused New York City's worst coastal flood and second largest storm surge in at least 300 years (Orton et al., 2016) and occurred during our current period of rapid climate change. This raises obvious concerns that tropical cyclone (TC) climatology change could be causing worsened New York City storm surges. Research has shown atmospheric warming will likely intensify TCs in the future (Emanuel 2005; Knutsen et al., 2020; Emanuel 2021). For the United States Gulf Coast, two different approaches for simulating future TC storm surges have revealed substantial future increases, which will increase future flood risk (e.g. Marsooli et al., 2019; Yin et al., 2020). However, an assumption applied in creating NPCC coastal flood maps is and continues to be that future coastal flooding in New York City will only change due to sea

level rise. Here, we summarize findings from a review of recent literature on the impact of TC changes on coastal flooding for the region.

An emerging consensus is TC climatology change will cause a small increase in New York City storm surges (perhaps 10%) relative to the increase in extreme water levels due to sea level rise. However, mixed results from different methods and climate models suggest continued caution in using results of individual studies or methods. Methods applied to study the topic have recently grown more diverse, which will help reduce these uncertainties. Until recently, most studies neglected possible future changes in TC frequency, yet epistemic uncertainties in the response of cyclogenesis to warming remain a fundamental challenge for projecting future changes to storm surges (Lee et al., 2020; Sobel et al., 2021). As a result, there remains insufficient evidence and consistency between studies to incorporate TC change into current assessments of future New York City flood risk.

We recommend future projects and NPCC assessments embark on a comprehensive assessment with multiple TC climatology change assessment methods and additional researchers, to better understand future New York City coastal flood risk. This could help New York City achieve its goal of properly quantifying and planning for high-end risk, more in-line with its request for NPCC to use the 90th percentile sea level rise projections in future flood maps.

b. Changes in storm surge: Past to present

Historical trends in storm surges were reviewed by NPCC3 and found (Orton et al., 2019):

> *No significant evidence in this region for larger storm tides due to the effect of climate change on storms (e.g. Marcos and Woodworth, 2017; Wahl and Chambers, 2016). Moreover, no quantitative evidence has been presented demonstrating that Hurricane Sandy was intensified or its storm tide was increased or made more likely by climate change (Lackmann, 2015; Mattingly et al., 2015). Sandy had hybrid cyclone characteristics as it approached the region and therefore represents a relatively complex case study (Galarneau et al., 2013; Zambon et al., 2014).*

One recent study attributed a portion of Sandy's damages and affected property and population to anthropogenic climate change-driven sea level rise (Strauss et al., 2021), but did not assess storm or storm surge changes.

c. Influence of future TC climatology change on coastal flooding

1. Review of methods

Global climate models have major weaknesses in representing tropical cyclones (TCs) due to coarse resolution and inadequate representation of physical processes (e.g. convection). As a result, downscaling approaches are typically used to improve this understanding, including statistical/ deterministic downscaling (e.g. Lin et al., 2012; Mayo and Lin 2022) and deterministic dynamical downscaling (Camelo et al., 2020). Here, we review three approaches that have been utilized to study how TC changes may affect storm surge.

A statistical/deterministic downscaling approach utilizes climate model data with simplified hurricane models and hydrodynamic models to simulate storm surges, and then uses extreme value analysis to determine probabilities of various coastal flood levels.

A deterministic dynamical downscaling approach embeds high-resolution regional weather and flood models inside global climate model outputs, either directly or through implementation of representative boundary conditions (Gutmann et al., 2018).

Lastly, pioneering efforts have begun to use the global climate models themselves in long-term atmospheric-ocean simulation studies of TC and storm surge climate changes, though the storms are very coarsely resolved (e.g. a one-degree global model grid) and storm surges relatively muted (Yin et al., 2020).

d. Review of results

Resulting assessments of future changes to storm surge using the statistical/deterministic approach have shown mixed results but landing between a finding of no change or a modest increase in storm surge. However, differences with different climate models and different IPCC assessment cycles (e.g. AR4, AR5) indicate moderate uncertainty in these results. Initial results of the statistical/deterministic approach for New York City found projections using two of four climate models show substantial increases in storm surge similar in magnitude to future sea level rise (Lin et al., 2012).

Subsequent statistical/deterministic studies using similar methods found changes in storm tracks may offset the intensity increase, resulting in relatively small changes in storm surges at New York City (e.g. Garner et al., 2017). The most recent results with the statistical/deterministic approach have converged toward relatively small increases in storm surge that are about 5-10% as large as the increase due to sea level rise (Marsooli et al., 2019).

Using the deterministic dynamical downscaling approach to study storm surge changes, Carmelo et al., (2020) found climate change driven storm changes cause the inundation area and extent of most historical storms to increase.

Recent research studies have demonstrated that tropical cyclone frequency may decrease due to climate warming (Chand et al., 2022) and uncertainties in future storm frequencies remain too high to make confident predictions of the changes in effects in New York City (Lee et al., 2021). Both the statistical/deterministic and dynamical downscaling approaches revised above do not capture the effect of these changes (Sobel et al., 2021), and therefore may overestimate the impact of climate warming and stronger TCs on future storm surges in New York City.

A way to study the complete effect of climate change on both storm frequency and intensity is to apply the highest-resolution climate models to study the problem. Applying a climate model for a 150-year simulation with a 1% per year increase in CO2, Yin et al., (2020) found the main driver of increased coastal flooding along the East Coast would be sea level rise, with minimal changes to storm surge climate.

e. Synthesis: Effects on future extreme floods and assessment uncertainty

Overall, two summary conclusions on future changes to New York storm surge can be drawn from the studies reviewed above. An emerging consensus among several techniques has been that TC climatology change will cause an increase in New York City storm surges, yet this would be small relative to the increase in extreme water levels due to sea level rise (~10%). Also, mixed results from different models and methods suggest continued caution in using results of individual studies or methods, which are gradually becoming more diverse.

More broadly, other neglected factors should also be studied with regard to future flood risk, including pluvial contributions that are likely to increase (e.g. Gori et al., 2022). Modeling of the effect of rainfall on coastal flood zones is an additional useful future endeavor.

2.9. Sensitivity study of TC separation in extreme value analysis

a. Summary

A fundamental challenge with coastal storm hazard assessment for many mid-latitude areas is tropical cyclones (TCs) are responsible for the largest events but occur infrequently relative to extratropical cyclones (ETCs). Therefore, TC hazard data are non-ergodic, meaning that distributions are typically under-sampled. As a result, in spite of large differences in TC and ETC maximum intensities, observation-based assessments of surge, wind and rain hazards typically merge data from TCs with far more numerous data from ETCs. Here, we explore the utility and challenges of separating storm types for extreme value analysis (EVA) of coastal hazards, which can include extreme rain, wind and storm surge. We use Monte Carlo simulations of a large number of stochastic synthetic storm tide datasets to assess common EVA approaches using both separated and merged TC and ETC data. Steps included: (1)

developing *a priori* assumed probability distributions for TC and ETC that represent the U.S. New York Bight and Southern New England; (2) sampling from these distributions to create synthetic 50, 120 and 300-year datasets of TC and ETC storm tides; and (3) assess the 100-year storm tide with two methods: (a) a NOAA standard EVA practice with merged data and (b) an approach that separates TC and ETC data before EVA. Results show the NOAA approach underestimates the 100-year event by ~15% for any duration of historical data, whereas the separated approach has lower bias and can provide unbiased estimates if using longer datasets (e.g. 120 years). The separated approach suffers from greater random error, however, and the longest possible datasets should be used to minimize uncertainty. This can be accomplished using regionalized EVA (multiple locations) or supplementing tide gauge data with other forms of data (e.g. reports in newspapers).

b. Introduction and Motivation

Tropical cyclones (TCs, including post-tropical cyclones) and extratropical cyclones (ETCs) both can cause extreme winds, storm surge and rainfall, as well as compound flooding. However, these storm types have different energy and moisture sources and as a result cause different hazard intensity in terms of maximum wind speed, storm surge (Orton et al., 2016) and rainfall rates. ETCs normally have a larger spatial extent and have wind speeds far below the maxima exhibited by TCs (e.g. Dolan & Davis, 1992; Landsea & Franklin, 2013) and TCs can have more abundant moisture. Each storm type has often been shown to exhibit different univariate extreme value probability distributions (e.g. Orton et al., 2016).

For hazard assessment, the process of extreme value analysis (EVA) has the goal of estimating the exceedance probability or return period for a given variable of concern. It requires assembling data values representing each case of an extreme event, then fitting an extreme value probability model to the data. Where TCs are relatively less common than ETCs, for practicality a common assumption is often applied in EVA, that TC and ETC data can be merged prior to fitting the distribution. This is a practical solution for using the limited available historical data. This increases the number of data points and can often have the appearance of reducing uncertainty, or at least its quantified estimates. However, the approach could be problematic because of the maximum intensity differences between TCs and ETCs and our specific interest in the extremes of their distributions. Thinking more broadly, many coastal areas can also have rare extreme tsunamis, but for most purposes one would not mix in these events into a flood hazard EVA, due to their far different physical behaviors and thus probability distributions.

A long-time and widely used source of information on coastal flood hazards is the NOAA's Tides and currents "Extreme Water Levels" webpage. The resulting plots of return period versus storm tide, which is total water level with the sea level rise trend taken out, often show

good model/data fit except at the extremes (Figure 2.12). After Hurricane Sandy occurred and its data included (the outlier in the top panel), the probability of Sandy's storm tide was estimated to be 1570 years (Sweet et al., 2013), in contrast to studies where TCs and ETCs were analyzed as separate data populations (e.g. 100 years in FEMA, 2014; 260 years in Orton et al., 2016).

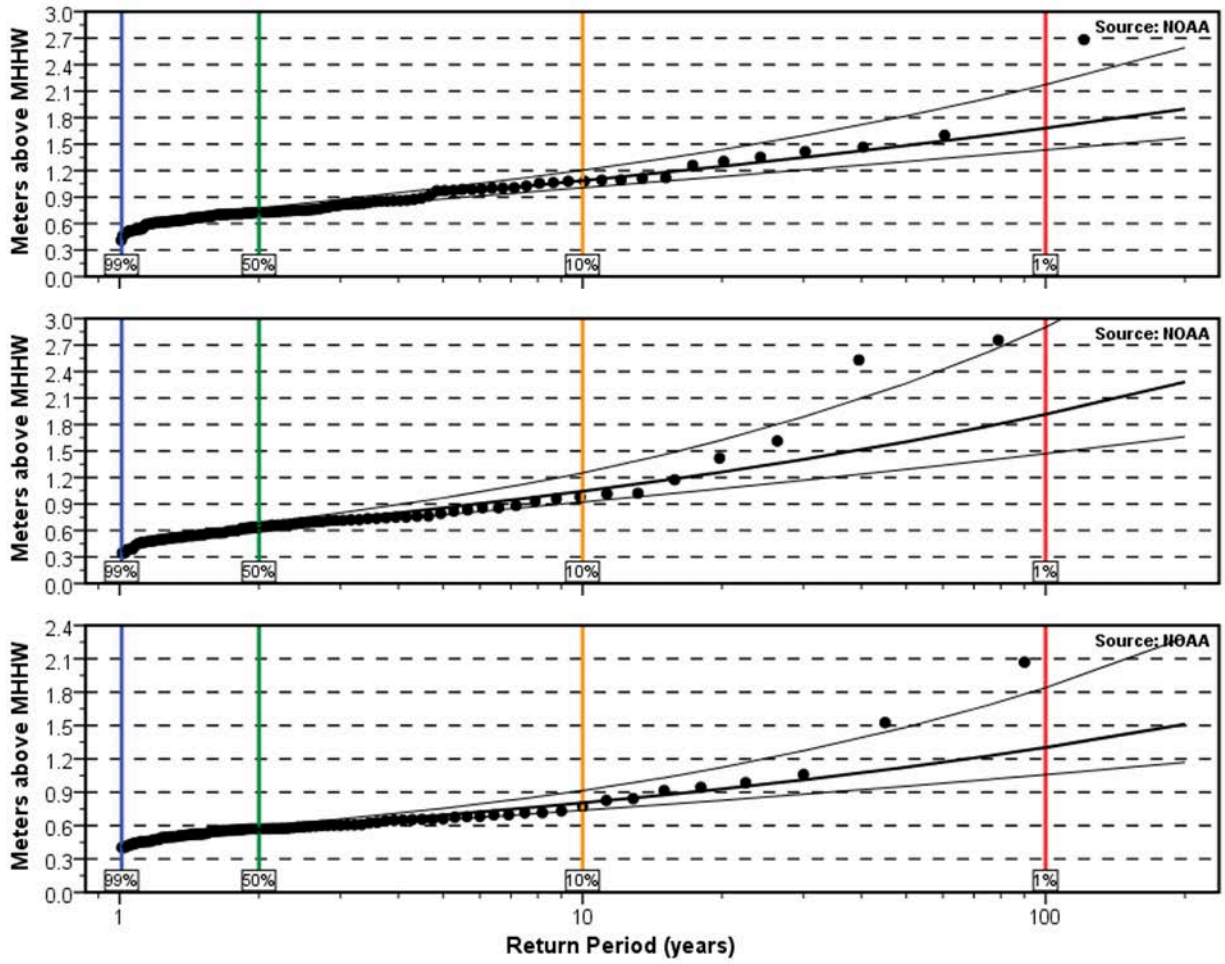

Figure 2.12: Examples of cases where the most extreme storm tide events appear to be outliers, outside the 95% confidence limits of estimated probability distributions: (top) New York City at The Battery, (middle) Woods Hole Massachusetts, and (bottom) Charleston, South Carolina (NOAA, 2024). The method used was Generalized Extreme Value distributions fitted to annual maxima of combined population of TC, ETC events (Zervas, 2013).

The question addressed in the following pages, is "Could the approach of merging TC and ETC data into one analysis lead to chronic underestimation across multiple coastal storm-driven hazards?" The methodological approach of this research is to use a series of Monte Carlo

analyses using synthetic storm event data representing a range of idealized U.S. East Coast TC and ETC coastal flood hazard climates to assess different approaches to EVA. Assumed storm tide distributions are randomly sampled to create different duration datasets of temporal maximum (peak) TC and ETC storm tides that are then analyzed with different EVA techniques, and results for 100-year return period events are compared with the known values. A key goal is to assess whether we can improve the results with longer datasets or using different EVA methods.

c. Methods

1. *Idealized hazard curves*

A set of idealized storm tide exceedance curves is created that loosely represents United States New York Bight and southern New England TC and ETC coastal storm tides. These mimic physical model-based curves for synthetic TC and historical ETC storm tides (FEMA, 2014 and Orton et al., 2016, for New York and New Jersey).

The TC peak storm tide (h_{tc}) exceedance curves follow the Gumbel distribution, equivalent to Generalized Pareto or Generalized Extreme Value Distribution with a shape parameter of zero. A range of scale parameter (σ_{TC}) is used, from 0.2 to 1.0 with steps of 0.1, forming a set of nine exceedance curves. A location parameter x of 1 m is used, reflecting a minimal TC storm surge in a region with typical highest astronomical tides of ~1 m above mean sea level. Thus, the probability of a TC peak storm tide of 1 m $P(h_{tc}>z)$ is similar to the annual frequency of storms passing within 200 km, P_{tc} = ~0.3 (e.g. Lin et al. 2012; Orton et al. 2016). Resulting cases are shown in Figure 2.13 with a strong similarity to h_{tc} return period curves for Atlantic City and New York City (FEMA, 2014; Orton et al. 2016) and Woods Hole, Massachusetts.

A single ETC peak storm tide exceedance probability curve is utilized based on the Generalized Extreme Value (GEV) distribution that represents water level extremes for NY Bight and southern New England (e.g. Orton et al., 2016; Dullart et al., 2021). In this case, the location parameter is again 1.0 m, the shape parameter is -0.1 and scale parameter is 0.2, reflecting a lower slope to ETC storm tides in the return period plot (Figure 2.13). A frequency of ~20 ETC events per year with peak storm tides exceeding 1 m is typical of the region, as with many mid-latitude coastal regions of the world.

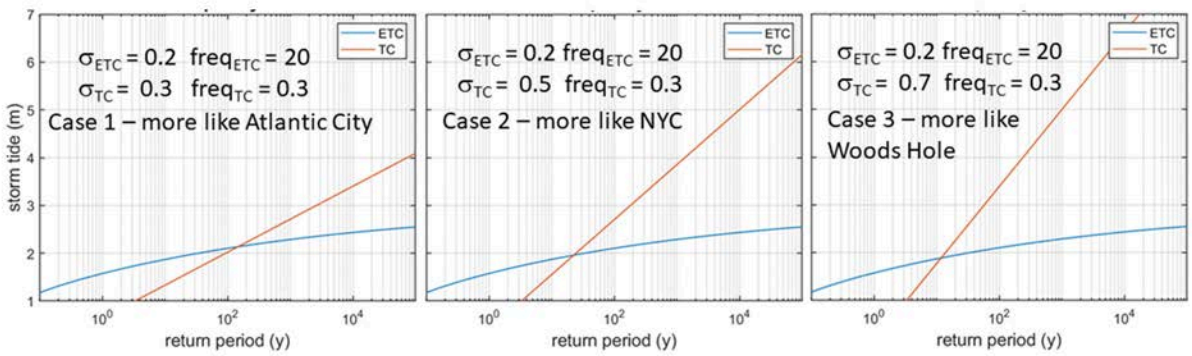

Figure 2.13: Assumed storm tide return period curves for TCs and ETCs, along with analogs along the U.S. East Coast. (a) TC curves are similar to those expected for Atlantic City, (b) for NYC, and (c) for Woods Hole, while for simplicity the ETC curves were chosen to be the same for all cases.

2. *Monte Carlo simulated events*

Stochastic event sets for h_{tc} and h_{etc} are created from these distributions in Monte Carlo simulations of historical periods of differing lengths (50, 120 and 300 years). Separately for TCs and ETCs, each year has a Poisson-distributed integer number of events (Stedinger, 1993). Each event's peak storm tide is sampled from its respective CDF by choosing a random number in the uniform distribution from 0 to 1, with one million divisions.

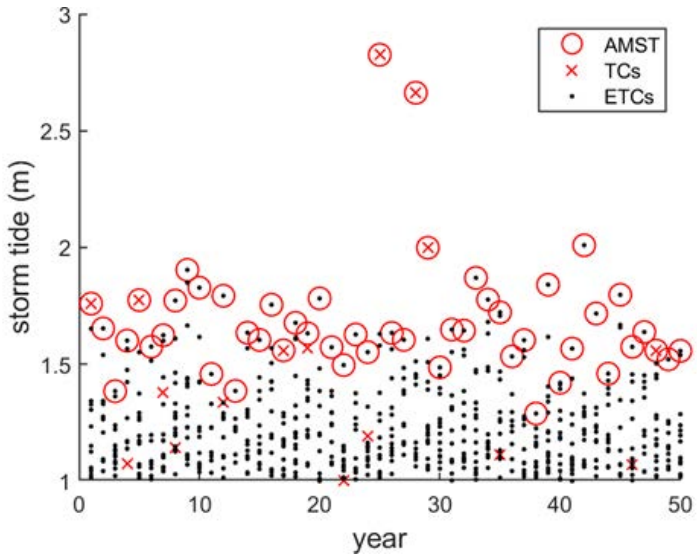

Figure 2.14: Example of a synthetic time series of storm tides (each point a temporal maximum during a storm event), including tropical cyclones (TCs), extratropical cyclones (ETCs) and annual maximum storm tide values (red circles).

3. Separated and combined data EVA

For the EVA where TC and ETC data are combined, datasets of the annual maximum storm tide (AMST) are created and GEV distributions fitted, mimicking the method used by NOAA (Figure 2.12; NOAA, 2024). To evaluate whether a Generalized Pareto Distribution (GPD) can improve these results, subsets of peaks over a threshold are created, and GPD distributions are fitted (e.g. Arns et al., 2013). The threshold (location parameter) is assigned based on the 95th and 99th percentile of all the event data, to enable comparison of the two different sets of results.

For the EVAs where TC and ETC data are kept separate, the ETC data are fitted with GEV and TC data are fitted with GPD distributions, the latter using a location parameter of 1 m (no events exist with lower values). The resulting annual exceedance probabilities for h_{tc} and h_{etc} are merged to give the probability of exceedance from either TC or ETC. The 100-year storm tide estimates are interpolated as the 0.01 exceedance probability in the results and compared across different methods and dataset lengths, alongside the *a priori* known 100-year storm tide values from the chosen distributions that were shown in (Figure 2.13).

d. Results

Figure 2.14 shows results of the analysis, demonstrating the two potential shortcomings of a short-duration EVA for estimating extreme events, bias and uncertainty. A substantial negative bias is reflected by the median estimate being far below the 1:1 diagonal. Also, the individual estimates show how a case of underestimation or overestimation of the 100-year event can also arise due to error.

For 50-year datasets, which are often the extent of tide gauge data worldwide, a low-bias exists for both approaches, though the bias for combined data is worse. However, the separated-storms analysis shows a far greater range of results, and thus error is a problem. This is due to the challenge of fitting a distribution to rare TCs for a short-duration historical period.

For 120-year datasets, which are less commonly available but available for perhaps one-two dozen sites in the United States, the combined-storm EVA continues to lead to bias, and the range of results narrows to the point that the 95th percentile is close to the 1:1 line, meaning about 90% of the estimates are too low. The separated-storm EVA shows very little bias, but continues to show the potential for error.

For the longest data duration of 300 years, the results show how the combined EVA continues to have the same bias but now very rarely avoids a low bias. One GEV distribution cannot fit two different physical processes, and thus the tail is poorly fitted. With 300 years of data, the separated EVA is unbiased and the error reduced.

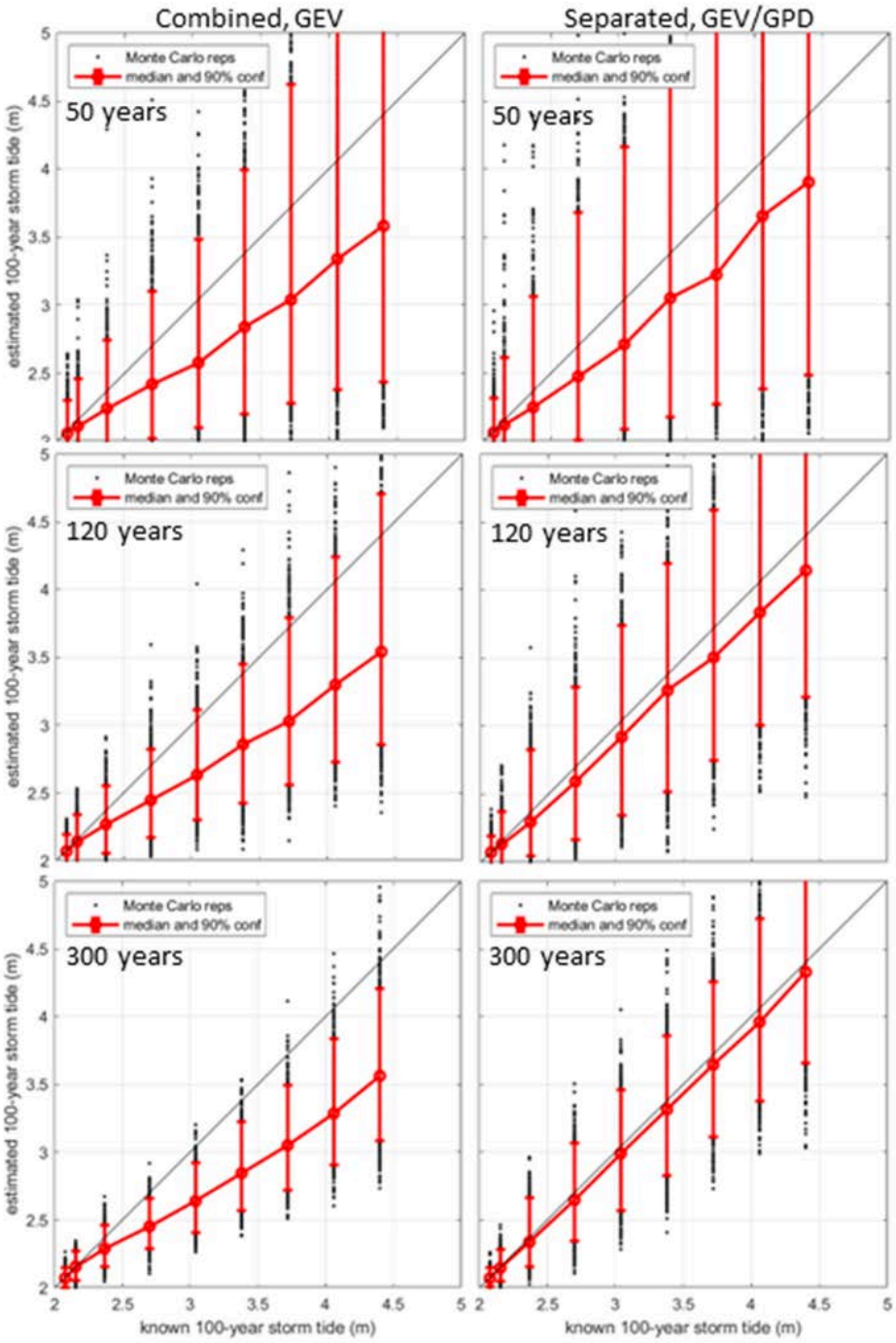

Figure 2.15: Monte Carlo simulation results across a wide range of storm tide climates based on EVA of combined data (left panels) and the separated approach (right panels), for data durations of 50 (top row), 120 (middle) and 300 years (bottom). Black points represent individual Monte Carlo simulations, red dots median results, and errorbars 95% variation ranges. Diagonal black lines show 1:1 correspondence (no bias), for comparison.

e. Discussion

It is well-known that reducing uncertainty in a given return period can require many times that period of data, and thus estimates of 100-year floods generally have high error. But there has been little attention paid to the potential low bias presented in this report. The result that a commonly applied method can chronically underestimate extreme events for storm tides raises attention to the danger of underestimating coastal storm hazards of any type. Prior to Hurricane Sandy's surprisingly large storm tide of 3.4 m, the estimated 100-year storm tide using the GEV approach with mixed storm data was only 2.22 m (Zervas et al., 2013), 1.2 m lower than Sandy, whereas by some measures (e.g. FEMA, 2014), Sandy was more similar to the 100-year storm tide. Post-tropical cyclone Ida surprised many in New York City with record-setting rainfall, but could this have been anticipated using separated storm types? Rain IDF curves are based on merged datasets, including those from Atlas 14 and those in the present Climate VIA study. Similarly, is there a hurricane wind disaster on the horizon for NYC in the coming decades? A focus of Climate VIA and NPCC is on climate-change driven impacts, but these results suggest more effort should be applied in assessing baseline hazards and their uncertainties.

1. Common approaches to improved EVA for merged datasets

Increasingly, researchers and FEMA are utilizing EVA assessment methods that may alleviate this bias. One example is the use of a POT approach with the GPD for fitting combined storm data, which can focus the fit on the tail of the distribution. In Figure 2.11, we show results where GPD was used with POT at the 95th and 99th percentiles of the storm event data. While using a higher and higher cutoff percentile, the bias is reduced, but the scatter grows, and much like the separated-storm approach, requires more years of data to have neither error nor bias. Also, more focus on tail squanders the value of using a fuller ETC distribution and can worsen the fit of the (single) distribution for 5-10-year events.

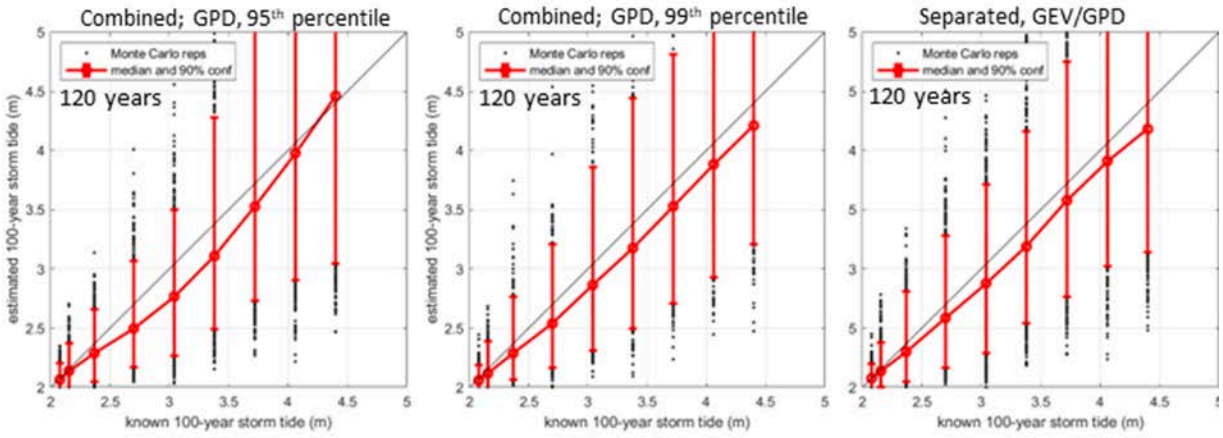

Figure 2.16: Monte Carlo simulation results using 120 years of combined data using the GPD with its threshold set as 95th percentile (left) and set as 99th percentile (center) and for separated data (right).

Another approach, called "regionalization", essentially adds more years of data by using neighboring tide gauges across a region (Sweet et al., 2022). However, if using GEV, more years of data do not help reduce bias, as shown herein. If using GPD, regionalization can be a good solution (e.g. Sweet et al., 2022).

2. *The TC/ETC separation approach*

The simulation results illustrate several challenges and benefits of storm-type separation in EVA of coastal storm hazards. While separation can reduce bias, it simultaneously increases error because it requires longer datasets to have enough TC data to fit the TC distribution. In the event that 300-year datasets are available, which is extremely rare globally, the results show how bias can be eliminated and error can be minimal, with 95% error range of about +/- 14% (Figure 2.15 bottom right panel). While U.S. tide gauge sites do not include 200 or more years of data, studies are increasingly supplementing these detailed observations with qualitative historical data from news (e.g. Orton et al., 2016; MacPherson et al., 2023) or paleoclimate data (e.g. Lin et al., 2014).

While the smaller uncertainty is often seen as a justification for using merged storm data, this smaller uncertainty is a fallacy and the bias can be large. The uncertainty is aleatoric and based purely on the population being studied, yet the probability distribution model (GEV alone) is incorrect and the epistemic uncertainty is not quantified.

Separation of TC and ETC storm data is increasingly possible with publicly available storm track databases. Storm track databases are available to identify when a storm surge comes from a nearby TC (the HURDAT2 datasets) and even go back to the 1600s (Boose et al., 2001) and

ETC track datasets are increasingly becoming available (e.g. Booth et al., 2016). Separation can be accomplished by identifying TC and ETC events from storm tracks, or by identifying TC events and treating all other storm surge events as non-TC.

Lastly, an approach that is particularly amenable to separate analysis of TCs and ETCs is the use of synthetic storm models, as is increasingly done by catastrophe modelers, FEMA, and USACE. A benefit of storm separation in EVA and also synthetic storms modeling is that climate changes for different storm types are different and warrant separate treatment of TCs and ETCs

f. Conclusions

This research studies hazard assessment methods using a Monte Carlo approach where assumed hazard probability distributions are randomly sampled to study error and biases from different extreme value analysis approaches. The research focuses on coastal areas where TCs are far less frequent but more extreme than ETCs, as is the case for New York Bight and southern New England. Similar results might be found for the Mid-Atlantic and South Atlantic Bight, though ETCs are less frequent and TCs more frequent as you move southward along the U.S. East Coast.

For a data period of 50 years, both combined and separated EVA for storm climates where TCs are far less frequent than ETCs leads to low-bias in estimates of extremes (the 100-year storm tide). Adding more years of data (e.g. 120 or 300 years) does not improve combined/GEV results, but improves the separated EVA results. Fitting GPD in a combined data approach can reduce bias but increases uncertainty unless more years of data are applied (e.g. using archival data, regional EVA). Separation of TCs and ETCs raises error higher, so also requires more years of data or regionalization.

Recommendations from this research include: (1) Consider using separate analysis of TCs in all hazard assessments, including rain, coastal flooding and compound rain-surge, using observed historical data where available, but also modeled events if helpful to reduce uncertainties; (2) Standardized assessments of hazards that use merged data (e.g. rainfall IDF curves) should test out the separated storm EVA approach. While rainfall records are shorter than those for coastal floods, and uncertainties may be a problem, such an analysis can at least serve as a tool to understand epistemic uncertainty. Acknowledging all uncertainties and not shying away from a complete assessment of the potential high-end of hazards can help avoid weather and climate surprises.

2.10 Climate projection data

A primary deliverable for Task 2 is all data and assets for climate projections (Deliverable 6), including data layers and metadata, as described more fully below.

The full set of climate data and climate projections produced for Task 2, which are identical to the New York City Region files in the NYSCIA report, have been sent to the City. They are preparing to upload the data into the Open Data portal. The Task 2 team has reviewed the corresponding metadata and the revised files (to meet format requirements).

Land surface temperature data is available for download as a set of GeoTIFF raster files: https://gmuedu-my.sharepoint.com/:u:/g/personal/lortizur_gmu_edu/ERR597juSWJDkxshVPI_rIUBzKMA5mZvWfTqZnpCF9LCHg?e=9nLeVq

The files hold land surface temperature change data compared to a historical baseline (2013-2022). Pixel size is 30-meter resolution. We note that thermal imagery native resolution from Landsat is 60-meter, and is interpolated to the 30-meter grid resolution to match other instruments on the satellite. Each file contains a single image, clipped to NYC boundaries. Each image represents the increase over the baseline for a combination of scenario and ensemble percentile.

File naming convention is as follows:

`lst_aaaa-bbbb_cccc_dddd.tif`

aaaa: Start of 30-year period
bbbb: End of 30-year period
cccc: Scenario (SSP and RCP combination
dddd: Intermodel percentile

References

Arns, A., T. Wahl, I. Haigh, J. Jensen, and C. Pattiaratchi (2013), Estimating extreme water level probabilities: a comparison of the direct methods and recommendations for best practise, Coast. Eng., 81, 51-66.

Bader, D., & Horton, R. (2023, December 21). New York State's Changing Climate. New York State Climate Impacts Assessment. https://nysclimateimpacts.org/explore-the-assessment/new-york-states-changing-climate/

Bauer, T. J. (2020). Interaction of Urban Heat Island Effects and Land–Sea Breezes during a New York City Heat Event. Journal of Applied Meteorology and Climatology, 59(3), 477–495. https://doi.org/10.1175/JAMC-D-19-0061.1

Booth, J. F., H. Rieder, and Y. Kushnir (2016), Comparing hurricane and extratropical storm surge for the Mid-Atlantic and Northeast Coast of the United States for 1979–2013, Environmental Research Letters, 11(9), 094004.

Boose, E. R., K. E. Chamberlin, and D. R. Foster (2001), Landscape and regional impacts of hurricanes in New England, Ecological Monographs, 71(1), 27-48.

Bornstein, R. D. (1968). Observations of the urban heat island effect in New York City. Journal of Applied Meteorology, 7(4), 575–582. https://doi.org/10.1175/1520-0450(1968)007<0575:OOTUHI>2.0.CO;2

Braneon, C., L. Ortiz, D. Bader, N. Devinen, P. Orton, B. Rosenzweig, T. McPhearson, L. Smalls-Mantey, V. Gornitz, T. Mayo, S. Kadam, H. Sheeraz, E. Glenn, L. Yoon, A. Derras-Chouk, J. Towers, R. Leichenko, D. Balk, P. Marcotullio, and R. Horton, in press: NYC Climate Risk Information 2022: Observations and Projections. Ann. N. Y. Acad. Sci.

Buzan, J. R., Oleson, K., & Huber, M. (2015). Implementation and comparison of a suite of heat stress metrics within the Community Land Model version 4.5. Geoscientific Model Development, 8(2), 151–170. https://doi.org/10.5194/gmd-8-151-2015

Camelo, J., Mayo, T. L., and Gutmann, E. D.: Projected climate change impacts on hurricane storm surge inundation in the coastal United States, Front. Built Environ., 6, 588049, https://doi.org/10.3389/fbuil.2020.588049, 2020.

Chand, S.S., Walsh, K.J., Camargo, S.J., Kossin, J.P., Tory, K.J., Wehner, M.F., Chan, J.C., Klotzbach, P.J., Dowdy, A.J., Bell, S.S. and Ramsay, H.A., 2022. Declining tropical cyclone frequency under global warming. Nature Climate Change, 12(7), pp.655-661.

Chen, Z., Orton, P. M., Booth, J. F., Wahl, T., DeGaetano, A., Kaatz, J., and Horton, R.M. (submitted), Influence of Storm Type on Compound Flood Hazard of a Coastal-Urban Environment, Weather and Climate Extremes.

City of New York, 2021: State of Climate Knowledge 2021.

Davies-Jones, R. An efficient and accurate method for computing the wet-bulb temperature along pseudoadiabats. Monthly Weather Review, 136(7), 2764–2785. https://doi.org/10.1175/2007MWR2224.1 (2008)

Dolan, R., and R. E. Davis (1992), An intensity scale for Atlantic coast northeast storms, J. Coast. Res., 8(4), 840-853.

Dullaart, J. C., S. Muis, N. Bloemendaal, M. V. Chertova, A. Couasnon, and J. C. Aerts (2021), Accounting for tropical cyclones more than doubles the global population exposed to low-probability coastal flooding, Communications Earth & Environment, 2(1), 135.

Emanuel, K., 2005. Increasing destructiveness of tropical cyclones over the past 30 years. Nature, 436(7051): 686-688.

Emanuel, K., 2021. Response of global tropical cyclone activity to increasing CO 2: Results from downscaling CMIP6 models. Journal of Climate, 34(1), pp.57-70.

Eyring, V., Bony, S., Meehl, G. A., Senior, C. A., Stevens, B., Stouffer, R. J., & Taylor, K. E. (2016). Overview of the Coupled Model Intercomparison Project Phase 6 (CMIP6) experimental design and organization. Geoscientific Model Development, 9(5), 1937–1958. https://doi.org/10.5194/gmd-9-1937-2016

FEMA (2014), Region II Coastal Storm Surge Study: Overview, prepared by Risk Assessment, Mapping, and Planning Partners (RAMPP), p. 15, Federal Emergency Management Agency, Washington, DC.

Galarneau, T.J., Davis, C.A. and Shapiro, M.A., 2013. Intensification of hurricane sandy (2012) through extratropical warm core seclusion. Mon. Weather. Rev., 141(12): 4296-4321.

Garner, A.J. et al., 2017. Impact of climate change on new york city's coastal flood hazard: Increasing flood heights from the preindustrial to 2300 ce. Proceedings of the National Academy of Sciences, 114(45): 11861-11866.

Gedzelman, S. D., Austin, S., Cermak, R., Stefano, N., Partridge, S., Quesenberry, S., & Robinson, D. A. (2003). Mesoscale aspects of the urban heat island around New York City. Theoretical and Applied Climatology, 75(1–2), 29–42. https://doi.org/10.1007/s00704-002-0724-2

Ghanbari, M., T. Dell, F. Saleh, Z. Chen, J. Cherrier, B. Colle, J. Hacker, L. Madaus, P. Orton, and M. Arabi, 2024: Compounding effects of changing sea level and rainfall regimes on pluvial flooding in New York City. Natural Hazards, 1-24.

Gori, A., Lin, N., Xi, D. and Emanuel, K., 2022. Tropical cyclone climatology change greatly exacerbates us extreme rainfall–surge hazard. Nature Climate Change, 12(2): 171-178.

González, J. E., Ortiz, L., Smith, B. K., Devineni, N., Colle, B., Booth, J. F., Ravindranath, A., Rivera, L., Horton, R., Towey, K., Kushnir, Y., Manley, D., Bader, D., & Rosenzweig, C. (2019). New York City Panel on Climate Change 2019 Report Chapter 2: New Methods for Assessing Extreme Temperatures, Heavy Downpours, and Drought. Annals of the New York Academy of Sciences, 1439(1), 30–70. https://doi.org/10.1111/nyas.14007

Gutmann, E.D., Rasmussen, R.M., Liu, C., Ikeda, K., Bruyere, C.L., Done, J.M., Garrè, L., Friis-Hansen, P. and Veldore, V., 2018. Changes in hurricanes from a 13-yr.

convection-permitting pseudo–global warming simulation. Journal of Climate, 31(9), pp.3643-3657.

Hersbach, H., Bell, B., Berrisford, P., Hirahara, S., Horányi, A., Muñoz-Sabater, J., Nicolas, J., Peubey, C., Radu, R., Schepers, D., Simmons, A., Soci, C., Abdalla, S., Abellan, X., Balsamo, G., Bechtold, P., Biavati, G., Bidlot, J., Bonavita, M., ... Thépaut, J.-N. (2020). The ERA5 global reanalysis. Quarterly Journal of the Royal Meteorological Society, 146(730), 1999–2049. https://doi.org/10.1002/qj.3803

Horton, R., D. Bader, C. Rosenzweig, A. DeGaetano, and W.Solecki. 2014. Climate Change in New York State: Updating the 2011 ClimAID Climate Risk Information. New York State Energy Research and Development Authority (NYSERDA), Albany, New York.

Horton, R., Little, C., Gornitz, V., Bader, D., & Oppenheimer, M. (2015). New York City Panel on Climate Change 2015 Report. Chapter 2: Sea level rise and coastal storms. Annals of the New York Academy of Sciences, 1336, 36–44. https://doi.org/10.1111/nyas.12593

Jane, R., Wahl, T., Santos, V. M., Misra, S. K., & White, K. D. (2022). Assessing the potential for compound storm surge and extreme river discharge events at the catchment scale with statistical models: sensitivity analysis and recommendations for best practice. Journal of Hydrologic Engineering, 27(3), 04022001.

Kennard, H., Oreszczyn, T., Mistry, M., & Hamilton, I. (2022). Population-weighted degree-days: The global shift between heating and cooling. Energy and Buildings, 271, 112315. https://doi.org/10.1016/j.enbuild.2022.112315

Knutson, T. et al., 2020. Tropical cyclones and climate change assessment: Part ii: Projected response to anthropogenic warming. Bull. Amer. Meteorol. Soc., 101(3): E303-E322.

Kopp, B. WetBulb.m. (2020). https://github.com/bobkopp/WetBulb.m

Lackmann, G.M., 2015. Hurricane Sandy before 1900 and after 2100. Bull. Amer. Meteorol. Soc., 96(4): 547-560.

Lamie, C., Bader, D., Graziano, K., Horton, R. John, K., O'Hern, N., & Spungin, S. (2024). Chapter 2: New York State's changing climate. In New York State Climate Impacts Assessment [Interim version for public release].

Landsea, C. W., and J. L. Franklin (2013), Atlantic hurricane database uncertainty and presentation of a new database format, Mon. Weather. Rev., 141(10), 3576-3592.

Lee, S. J. Camargo, A. H. Sobel, M. K. Tippett, Statistical-dynamical downscaling projections of tropical cyclone activity in a warming climate: Two diverging genesis scenarios. J. Climate 33, 4815–4834 (2020)

Lin, N., Emanuel, K., Oppenheimer, M. and Vanmarcke, E., 2012. Physically based assessment of hurricane surge threat under climate change. Nature Climate Change, 2(6): 462-467.

Lin, N., P. Lane, K. A. Emanuel, R. M. Sullivan, and J. P. Donnelly (2014), Heightened hurricane surge risk in northwest Florida revealed from climatological-hydrodynamic modeling and paleorecord reconstruction, Journal of Geophysical Research: Atmospheres, 119(14), 8606-8623.

Lindberg, F., Grimmond, C. S. B., Gabey, A., Huang, B., Kent, C. W., Sun, T., Theeuwes, N. E., Järvi, L., Ward, H. C., Capel-Timms, I., Chang, Y., Jonsson, P., Krave, N., Liu, D., Meyer, D., Olofson, K. F. G., Tan, J., Wästberg, D., Xue, L., & Zhang, Z. (2018). Urban Multi-scale Environmental Predictor (UMEP): An integrated tool for city-based climate services. *Environmental Modelling & Software*, *99*, 70–87. https://doi.org/10.1016/j.envsoft.2017.09.020

Marcos, M. and Woodworth, P.L., 2017. Spatiotemporal changes in extreme sea levels along the coasts of the north atlantic and the gulf of mexico. J. Geophys. Res., 122(9): 7031-7048.

Marsooli, R., Lin, N., Emanuel, K. and Feng, K., 2019. Climate change exacerbates hurricane flood hazards along us atlantic and gulf coasts in spatially varying patterns. Nature Communications, 10(1): 1-9.

Mattingly, K.S., McLeod, J.T., Knox, J.A., Shepherd, J.M. and Mote, T.L., 2015. A climatological assessment of greenland blocking conditions associated with the track of hurricane sandy and historical north atlantic hurricanes. Int. J. Climatol., 35(5): 746-760.

MacPherson, L. R., A. Arns, S. Fischer, F. J. Méndez, and J. Jensen (2023), Bayesian extreme value analysis of extreme sea levels along the German Baltic coast using historical information, Nat. Hazards Earth Syst. Sci., 23(12), 3685-3701, doi:10.5194/nhess-23-3685-2023.

Mayo, T. L. & Lin, N. Climate change impacts to the coastal flood hazard in the northeastern United States. Weather Clim. Extremes. 100453 (2022).

National Oceanic and Atmospheric Administration (NOAA). (2024). Extreme Water Levels—NOAA Tides & Currents. Retrieved January 30, 2024, from https://tidesandcurrents.noaa.gov/est/

New York State Energy Research and Development Authority (NYSERDA). 2020. “Climate Needs Assessment for New York State,” NYSERDA Report Number 20-31. Prepared by A. LoPresti, R. Horton, and D. Bader, Columbia University, New York, NY. nyserda.ny.gov/publications

O’Neill, B. C., Tebaldi, C., van Vuuren, D. P., Eyring, V., Friedlingstein, P., Hurtt, G., Knutti, R., Kriegler, E., Lamarque, J.-F., Lowe, J., Meehl, G. A., Moss, R., Riahi, K., & Sanderson, B. M. (2016). The Scenario Model Intercomparison Project (ScenarioMIP) for CMIP6.

Geoscientific Model Development, 9(9), 3461–3482. https://doi.org/10.5194/gmd-9-3461-2016

Oke, T. R., Kalanda, B. D., & Steyn, D. G. (1981). Parameterization of heat storage in urban areas. *Urban Ecology*, *5*(1), 45–54. https://doi.org/10.1016/0304-4009(81)90020-6

Oke, T. R. (1982). The energetic basis of the urban heat island. Quarterly Journal of the Royal Meteorological Society, 108(455), 1–24. https://doi.org/10.1002/qj.49710845502

Ortiz, L. E., Gonzalez, J. E., Wu, W., Schoonen, M., Tongue, J., & Bornstein, R. (2018). New York City Impacts on a Regional Heat Wave. Journal of Applied Meteorology and Climatology, 57(4), 837–851. https://doi.org/10.1175/JAMC-D-17-0125.1

Ortiz, L., Gamarro, H., Gonzalez, J. E., & McPhearson, T. (2022). Energy burden and air conditioning adoption in New York City under a warming climate. Sustainable Cities and Society, 76, 103465. https://doi.org/10.1016/j.scs.2021.103465

Orton, P., Georgas, N., Blumberg, A., & Pullen, J. (2012). Detailed modeling of recent severe storm tides in estuaries of the New York City region. Journal of Geophysical Research, 117, C09030.

Orton, P.M. et al., 2019. New York city panel on climate change 2019 report chapter 4: Coastal flooding. Ann. N. Y. Acad. Sci., 1439: 95-114.

Orton, P. M., T. M. Hall, S. Talke, A. F. Blumberg, N. Georgas, and S. Vinogradov (2016), A Validated Tropical-Extratropical Flood Hazard Assessment for New York Harbor, J. Geophys. Res., 121, doi:10.1002/ 2016JC011679.

Raymond, C., Horton, R., Zscheischler, J., Martius, O., AghaKouchak, A., Balch, J., Bowen, S. G., Camargo, S. J., Hess, J., Kornhuber, K., Oppenheimer, M., Ruane, A. C., Wahl, T., & White, K. (2020). Understanding and managing connected extreme events. Nature Climate Change, 10(7), 611–621. https://doi.org/10.1038/s41558-020-0790-4

Riahi, K., van Vuuren, D. P., Kriegler, E., Edmonds, J., O'Neill, B. C., Fujimori, S., Bauer, N., Calvin, K., Dellink, R., Fricko, O., Lutz, W., Popp, A., Cuaresma, J. C., Kc, S., Leimbach, M., Jiang, L., Kram, T., Rao, S., Emmerling, J., ... Tavoni, M. (2017). The Shared Socioeconomic Pathways and their energy, land use, and greenhouse gas emissions implications: An overview. Global Environmental Change, 42, 153–168. https://doi.org/10.1016/j.gloenvcha.2016.05.009

Rogers, C. D. W., Ting, M., Li, C., Kornhuber, K., Coffel, E. D., Horton, R. M., Raymond, C., & Singh, D. (2021). Recent Increases in Exposure to Extreme Humid-Heat Events Disproportionately Affect Populated Regions. Geophysical Research Letters, 48(19). https://doi.org/10.1029/2021GL094183

Salim, M. H., Schubert, S., Maronga, B., Schneider, C., & Cidek, M. F. (2020). Introducing the Urban Climate Model PALM System 6.0. *International Journal of Applied Energy Systems*, *2*(1), 15–18. https://doi.org/10.21608/ijaes.2020.169937

Skamarock, W. C., Klemp, J. B., Dudhia, J., Gill, D. O., Liu, Z., Berner, J., Wang, W., Powers, J. G., Duda, M. G., Barker, D. M., & Huang, X.-Y. (2019). A Description of the Advanced Research WRF Model Version 4. UCAR/NCAR. https://doi.org/10.5065/1dfh-6p97

Sobel, A. et al. Tropical cyclone frequency. Earth's Future 9, e2021EF002275 (2021).

Sweet, W. V., B. D. Hamlington, R. E. Kopp, C. P. Weaver, P. L. Barnard, D. Bekaert, W. Brooks, M. Craghan, G. Dusek, and T. Frederikse (2022), Global and regional sea level rise scenarios for the United States: Updated mean projections and extreme water level probabilities along US coastlines, National Oceanic and Atmospheric Administration.

Sweet, W., C. Zervas, S. Gill, and J. Park (2013), Hurricane Sandy Inundation Probabilities Today and Tomorrow [in "Explaining Extreme Events of 2012 from a Climate Perspective"], Bull. Amer. Meteorol. Soc., 94(9), S17-S20.

Strauss, B. et al., 2021. Economic damages from hurricane sandy attributable to sea level rise caused by anthropogenic climate change. Nature Communications, 12(2720).

Towers, J., McPhearson, T., et al. (2023). NYC Town+Gown Climate Vulnerability, Impact, and Adaptation Analysis: Interim Report. April 30, 2023.

Wahl, Jain, S., Bender, J., Meyers, S. D., & Luther, M. E. (2015). Increasing risk of compound flooding from storm surge and rainfall for major US cities. Nature Climate Change, 5(12), 1093-1097.

Wahl, T. and Chambers, D.P., 2016. Climate controls multidecadal variability in us extreme sea level records. J. Geophys. Res.

Ward, P. J., Couasnon, A., Eilander, D., Haigh, I. D., Hendry, A., Muis, S., et al. (2018). Dependence between high sea-level and high river discharge increases flood hazard in global deltas and estuaries. Environmental Research Letters, 13(8), 084012.

Xu, Z., Han, Y., Tam, C.-Y., Yang, Z.-L., & Fu, C. (2021). Bias-corrected CMIP6 global dataset for dynamical downscaling of the historical and future climate (1979–2100). Scientific Data, 8(1), 293. https://doi.org/10.1038/s41597-021-01079-3

Yin, J., Griffies, S.M., Winton, M., Zhao, M. and Zanna, L., 2020. Response of storm-related extreme sea level along the us atlantic coast to combined weather and climate forcing. J. Clim., 33(9): 3745-3769.

Zambon, J.B., He, R. and Warner, J.C., 2014. Tropical to extratropical: Marine environmental changes associated with superstorm sandy prior to its landfall. Geophys. Res. Lett., 41(24): 8935-8943.

Zervas, C. (2013), Extreme Water Levels of the United States 1893-2010, NOAA Technical Report NOS CO-OPS 067, NOAA National Ocean Service Center for Operational Oceanographic Products and ServicesRep., 200 pp, Silver Spring, Maryland.

Zscheischler, J., Martius, O., Westra, S., Bevacqua, E., Raymond, C., Horton, R. M., van den Hurk, B., AghaKouchak, A., Jézéquel, A., Mahecha, M. D., Maraun, D., Ramos, A. M., Ridder, N. N., Thiery, W., & Vignotto, E. (2020). A typology of compound weather and climate events. Nature Reviews Earth & Environment, 1(7), Article 7. https://doi.org/10.1038/s43017-020-0060-z

Task 3: Current and Future Extreme Heavy Rainfall in New York City

Task 3: Current and Future Extreme Heavy Rainfall in New York City

Core Team Members:

- Franco Montalto (Drexel University)
- Bernice Rosenzweig (Sarah Lawrence College)
- Arthur DeGaetano (Cornell University)
- Philip Orton (Stevens Institute of Technology)
- Jerry Kleyman (Arcadis)
- Joel Kaatz (Arcadis)
- Mobin Rahimi Golkhandan (Drexel University)
- Rachel Lo (Sarah Lawrence College)
- Colin Evans (Cornell University)
- Ziyu Chen (Stevens Institute of Technology)
- Patrick Gurian (Drexel University)
- Dan Bader (Columbia University)
- Matina Shakya (Drexel University)
- Fiona Dubay (Sarah Lawrence College)

NYC Interagency Collaborators:

- Alan Cohn (NYC DEP)
- Greg Mayes (NYC DEP)
- Erika Jozwiak (MOCEJ)
- Hayley Elszasz (MOCEJ)

3.1 Key Messages

- Based on nonparametric statistical tests, between 1955 and 2022, total annual precipitation has increased significantly at all NYC area gauges and the frequency of events with >95th percentile peak and average intensities have increased significantly at all of the NYC gauges. But while event frequency has increased, nonparametric trend analyses do not suggest that extreme precipitation events (>95th and >99th percentile) are getting larger, more intense, or are changing significantly in duration at NYC area gauges. When considering all events (not just the extreme events), the nonparametric analyses show statistically significant increases in peak and average intensities throughout the NYC area.

- Parametric analyses suggest that computed extreme precipitation characteristics have changed over time, and are heavily influenced by the occurrence of extreme events at each gauging station location. Parametric analyses reveal increases in the 2-, 5-, 10-,

25-, 50-, and 100-yr extreme rainfall events for durations of 1-hr through 24-hours at all stations, when the analyzed record includes data after 1990.

- Future changes in daily extreme rainfall are greater in the newer CMIP6 generation of climate models than in the previous CMIP5 models using LOCA method downscaling. The 2-yr 1-day rainfall amount associated with the 2020-2070 future period is 15% higher than the value reported by NOAA Atlas 14 under both higher SSP5-8.5 and lower SSP2-4.5 emissions scenarios. The 100-yr 1-day rainfall amount associated with the 2020-2070 future period is 30% higher than the value reported by NOAA Atlas 14 under the higher SSP5-8.5 emissions scenario and about 20% than the Atlas 14 value for lower SSP2-4.5 emissions.

- Differences in hyetograph shape (temporal distribution of precipitation intensity) can yield significant differences in flooding simulated using hydrologic and hydraulic (H&H) models. These differences are of the same order-of-magnitude as those associated with the simulated impacts of forecasted climate change. H&H modeling suggests that increases in flooding due to climate change are more pronounced for lower return period (more frequent) storms than for higher return period (less frequent) storms, because the less frequent storms already exceed the historical design level of service, even without intensification of precipitation due to climate change

3.2 Objectives and Research Activities

Urban stormwater and other critical infrastructure systems are designed to withstand a defined intensity and duration of rainfall, known as the 'design storm'. For any given rain event, the intensity of rainfall (defined as rainfall depth over a given duration) is associated with an annual probability of occurrence, usually described by its reciprocal return period. Accurate representation of the probability of rainfall intensity is thus critical for stormwater management and for flood resilience planning and design. This information is most commonly presented as site-specific Intensity-Duration-Frequency (IDF) curves, developed based on frequency analysis of historic rainfall at specific locations and under the assumption of stationarity - the idea that natural systems fluctuate within an envelope of variability that is unchanging with time (Milly et al., 2008). With projections of amplified precipitation intensity through the 21st century due to global climate change (Allan and Soden, 2008; Fowler et al., 2021b; Phahl et al.,, 2017), the appropriateness of this approach to urban drainage design has recently been called into question .

This issue is one of particular urgency for New York City, which is particularly vulnerable to pluvial flooding, triggered when the local intensity of precipitation and associated runoff exceeds the infiltration capacity of the land surface, and/or the conveyance capacity of natural

or engineered drainage systems (Rosenzweig et al., 2018). When the intensity of precipitation exceeds the design intensity used to compute peak flow rates to size drainage infrastructure, stormwater can back up and inundate topographically vulnerable areas. Flooding can also occur whenever the instantaneous rate of runoff presented to an inlet exceeds its interception capacity, a situation that triggers inlet bypass and eventual runoff concentration at lower elevation portions of the catchment. Due to the short (e.g. < 10 minute) time of concentration of most urban catchments, downstream flooding due to inlet bypass can thus be triggered by pulses of intense short duration rain events, commonly called cloudbursts. Cloudbursts may occur alone as convective storms or be embedded within longer precipitation events with lower average intensities.

Trends in historical precipitation amounts, intensities, and durations are highly variable due to differences in the data used to evaluate them, and different approaches to precipitation sampling and statistical analysis. The development of IDF curves that represent climate change-induced nonstationarities in precipitation is also challenging due to persistent uncertainties in how climate change will modify the frequency, intensity, and amounts of precipitation in specific places, especially at the fine (subdaily) time scales at which pluvial flooding typically occurs. Recent research suggests that the greatest increases in extreme rainfall intensity may be for short-duration storms (National Weather Service 2021), that changes in subhourly precipitation intensity may emerge sooner than changes in daily intensities (Kendon et al., 2018), and that more work is needed to evaluate the impact of global warming on short duration precipitation extremes in different locations (Barbero et al., 2019).

There is also emerging research suggesting that climate change may alter precipitation patterns in ways that are not represented by IDF curves. IDF curves provide probabilistic estimates of block (e.g. uniform) precipitation intensity for storms of specific intensities but do not represent how precipitation is distributed temporally within the event. Also, if climate change modifies the annual and seasonal pattern of precipitation, altering antecedent moisture conditions, the occurrence of flooding in response to specific events could also change relative to historical baselines. Thus, the occurrence of a given event must also be considered in its temporal context.

Task 3 used a literature review, expert elicitation methods, analyses of historical and future climatological data, and historical databases and media reports to explore why, how, and with what impacts precipitation has, is, and will continue to change in New York City. We developed future IDF curves for the city and used hydrologic and hydraulic modeling to explore the implications of these changes and other rainfall characteristics on pluvial flooding.

Task 3 included the following subtasks:

1. Subtask 1: Literature review regarding impacts of climate change on extreme precipitation
2. Subtask 2: Expert elicitation process designed to better understand the routine types of precipitation used in New York City policy and planning
3. Subtask 3: Historic heavy rainfall observations and event ranking
4. Subtask 4: Clausius-Clapeyron scaling analyses of observed rainfall
5. Subtask 5: Analysis of historical precipitation trends using non-parametric and parametric approaches
6. Subtask 6: Development of future IDF curves for NYC
7. Subtask 7: Hydrologic and Hydraulic (H&H) Modeling to evaluate the implications of design hyetograph assumptions and future IDF Curves on pluvial flooding in New York City

Methods and results for each of these subtasks are described individually below.

3.3 Literature Review

A comprehensive literature review was conducted to provide context for Task 3 precipitation analyses. Sources of information used for this review included peer-reviewed academic studies published in scientific journals and technical reports utilized in stormwater management practice. The full literature review is provided as a technical supplement for this report. Key outcomes from this work are summarized here.

a. Literature Review: Previously published reports of historical precipitation trends

The comprehensive literature review described research on observed increases in annual (Horton et al. 2015) and daily (Armstrong et al., 2014; Collins, 2009; DeGaetano, 2009; Easterling et al., 2017; Frei et al., 2015; Georgakakos, 2014; Huang et al., 2017, Peterson et al., 2013) precipitation in New York City and across the northeastern United States. However, fewer studies have been conducted of trends in subdaily precipitation in this region. Over the last decade, the City has commissioned several studies to investigate whether changes in the five-year storm intensity are evident in gauge records. In an analysis of 15-minute resolution precipitation data collected at LaGuardia, John F. Kennedy, Newark, and Central Park Automated Surface Observing Systems (ASOS) weather stations between 1969-2010, NYC DEP (2013) found no significant change in the relationship between the intensity and duration of five-year storms of up to 100 minutes in duration, when compared both with data provided in TP25, an IDF curve published by the U.S. Weather Bureau in 1955 (U.S. Weather Bureau, 1955). In 2015, NOAA released Atlas 14, Volume 10, an updated precipitation analysis that included IDF curves for rain gauge sites in and around New York City (Perica et al., 2019) and

NYCDEP repeated its analysis, again finding no change in the 5-year subdaily storm intensities, compared to TP25.

The lack of a discernible trend in short duration events in prior studies is perhaps unsurprising, given the sparse nature of rain gauges throughout the city and region. For example, in a remote sensing (ground-based radar) study conducted in Germany, only 17.3% of severe hourly precipitation events between 2001-2018 were captured in rain gauge observations, despite their relatively dense gauge network (Lengfeld et al., 2020). Wright et al. (2013) also suggest that sparse rain gauge networks are unlikely to represent historical trends in high intensity, short duration (e.g. < 1 hour) summertime thunderstorms and other convective events.

b. Literature Review: Spatial Variability in Rainfall Across NYC

Through an analysis of daily, hourly, and subhourly precipitation data from 10 stations in and around NYC, NYC DEP (2013) reports strong spatial variability in rainfall, with more rainfall generally occurring in the southwest portion of the city, and no one gauge station representative of the entire city. Analyzing high-resolution radar-based quantitative precipitation estimates, Smith and Rodriguez (2017) found the highest daily and hourly rainfall events peaked over the city center and an extended region downwind of the City, and contrasted these findings to previous work. Notably, from a flooding perspective, they found that flooding - as observed through 311 service requests - was correlated with localized subdaily rainfall, which may not be detected at standard gauge sites.

c. Literature Review: Precipitation non-stationarity

Precipitation nonstationarity can result from a variety of factors including interannual to multidecadal internal climate oscillations (Agilan and Umamahesh, 2017) and increased urbanization (Shepherd and Burian, 2003). Along with these regional processes, it is likely (>66% probability) that anthropogenic global warming has contributed to the intensification of heavy precipitation that has been observed across North America (Seneviratne et al., 2021). But while it is very likely (>90% probability; IPCC AR5) that extreme precipitation events will be more frequent and more intense over most mid-latitude regions with climate change (Seneviratne et al., 2021), the local quantitative projections of precipitation changes - particularly at the subdaily durations needed for design and planning - still remain uncertain.

Global warming can impact precipitation patterns through mechanisms that vary in importance by region, type of storm, and precipitation duration of interest. This review focuses on changes to short-duration (subdaily) precipitation rates, which are most salient to stormwater management in New York City. The most direct mechanism of precipitation intensification results from the thermodynamic relationship between atmospheric temperature and the saturation vapor pressure of water, which is known as the Clausius-Clapeyron (CC) Relation

('warmer air holds more moisture'). Under the temperature conditions relevant to weather, the amount of water vapor in the atmosphere at saturation will increase 6-7% per °C warming. From this thermodynamic relationship alone, it would be expected that precipitation would occur less frequently when the supply of atmospheric moisture is limited, since more moisture would be required for the atmosphere to reach saturation, condense and precipitate. However, under conditions where atmospheric moisture is not limited, there would be more precipitable water with warmer temperatures and, in turn, higher rainfall rates once saturation is reached (Trenberth et al., 2003).

Along with this direct thermodynamic effect, climate change can also influence short-duration precipitation extremes through several key atmospheric processes that take place at micro- to global spatial scales. At global scales, a fundamental effect of global warming will be the thermal expansion of the warming troposphere and stratospheric cooling, resulting in an increase in the height of the tropopause. Increased tropospheric heights will allow for deeper convection and increased precipitation rates when local conditions are favorable (Lenderink et al., 2017a; Loriaux et al., 2017; Santer et al., 2003).

Global warming can also influence precipitation patterns through changes in the continental-scale atmospheric circulation patterns that determine the transport of moisture across the globe. In the eastern United States, the climatology of large-scale moisture transport can be described by 16 spatially distinct atmospheric transport patterns, each with a distinct frequency and seasonality (Teale and Robinson, 2020). Anthropogenic climate change could potentially alter the frequency or seasonality of these patterns, with implications for local moisture availability and the probability of extreme precipitation in the future.

Large scale patterns associated with tropical cyclones (including tropical depressions, and hurricanes) also play an important role in the climatology of extreme precipitation in the northeast. This includes events associated with direct rainfall from tropical cyclones passing over, or very close to New York City. It also includes extreme rainfall that results from the remnants of tropical storms, such as the cloudburst associated with the remnants of Hurricane Ida in 2021, or changes to atmospheric dynamics such as lifting, instability, or moisture availability induced by tropical cyclones hundreds of kilometers away (Barlow, 2011). In an observational analysis study of the continental United States, Barlow (2011) found that over most of the Northeast, more than two-thirds of all extreme daily rainfall events between 1975 and 1999 were linked to tropical cyclone-related activity. In terms of the dynamics underlying the forcing of extreme precipitation, Barlow's study found the relationship between tropical cyclones or their remnants on large-scale lift was much greater than the relationship with moisture availability and buoyancy. It recommended further study of the interactions of tropical cyclones with large-scale circulation patterns that induce lift, such as the jet stream.

In a more recent study, Kunkel et al. (2020) found the tropical storms were directly responsible for only 11% of extreme daily precipitation in the Northeast. This study did not consider the indirect effects of tropical cyclones and their remnants, which suggest these dynamics may be more important contributors to extreme precipitation than direct rainfall from tropical cyclones passing through New York City. Studies on the contribution of tropical cyclones to subdaily rainfall in the New York City Metropolitan region are not yet available in the academic literature. In a modeling study, (Stansfield et al., 2020) found that intensity of tropical cyclone precipitation increases under scenarios of both moderate (RCP 4.5) and extreme (RCP8.5) climate change, but the total precipitation delivered by tropical cyclones decreased due to concomitant reductions in the total number of tropical cyclones in the Atlantic Basin. These results are consistent with those of other studies (Bacmeister et al., 2018; Chand et al., 2022; Guttman et al., 2018; Knutson et al., 2020), which suggest competing impacts from increased tropical cyclone precipitation rates and coinciding decreases in the total number of tropical cyclones in a warmer climate.

The influence of climate change on mesoscale storm processes also has the potential to result in more intense short-duration precipitation. Convective precipitation can occur in isolated thunderstorm cells or as part of organized clusters described as Mesoscale (10s to 100s of kilometers) Convective Systems (MCSs), which are often embedded into larger scale circulation such as squall lines or Nor'easters. Organized convection is associated with increased precipitation efficiency - the ratio of moisture that falls to the surface as precipitation to total condensed moisture within a storm - and more intense precipitation (Fowler et al., 2021). Moseley et al. (2016) found increased surface temperatures resulted in enhanced convective organization and more extreme precipitation and that, more broadly, the interactions amongst convective cells could be strongly influenced by large-scale changes in climate.

Historically, flash flooding in the Northeast has been more commonly associated with disorganized, localized convective cells rather than organized MCSs, especially when compared to other regions of the United States (Jessup and Colucci, 2012). The significance of potential changes in convective organization in more extreme precipitation with climate change remains uncertain and is still in early stages of investigation (Pendergrass, 2020), however, some initial studies indicate the storm areas may be larger and more organized under climate warming (Lenderink et al., 2017; Lochbiler et al., 2019. In a climate modeling study simulating an unmitigated global warming scenario (RCP 8.5), Prein et al. (2017) found the total volume of summertime precipitation increased with global warming due to both increased precipitation rates and increases in the area over which precipitation occurs in organized MCSs.

Within individual thunderstorms, the increased moisture from warmer temperatures will increase the release of latent heat, creating more instability and stronger updrafts within thunderstorms and increasing precipitation rates beyond what would be expected from the

increase in moisture availability alone. Assuming latent heat within a thunderstorm is proportional to precipitation intensity and kinetic energy of rising air within a thunderstorm increases proportionally with latent heating, precipitation intensity would be expected to increase at a rate twice that predicted by the CC relationship alone (2CC-scaling; Lenderink et al., 2017).

Changes in microphysical dynamics within thunderstorm clouds can also influence precipitation efficiency and convective precipitation rates. Precipitation efficiency is determined by the size distribution of hydrometeors (water and ice droplets) within thunderstorm clouds and the extent to which these hydrometeors re-evaporate or are re-entrained in updrafts before falling as precipitation to the ground. Singh and O'Gormam (2015) found climatic warming resulted in an increase in the fall speed of water and ice droplets within clouds. Higher fall speeds reduce the probability that a water droplet will evaporate or be reëntrained[3] in updrafts within the thunderstorm, resulting in higher precipitation efficiency within any given storm. However, the fall speed of water droplets within clouds can also influence updraft velocities, and in-turn precipitation rates (Bao and Sherwood, 2019; Parodi and Emanuel, 2009). Understanding the changes in these microphysical processes are most significant for subhourly precipitation rates (Singh and O'Gorman, 2015).

GCMs are numerical simulations that represent the coupled dynamics of the atmosphere, ocean, and land using mathematical equations (Figure 3.1). Climate models represent the earth as a three-dimensional grid of cells that exchange matter and energy over discrete intervals of time (time steps). Different GCMs may use different approaches to mathematically represent earth system processes and are run at different spatial and temporal resolutions. As a result, each GCM has strengths and weaknesses in their ability to represent different earth system processes and regions of the planet. Since no single GCM is able to perfectly represent earth's climate system, the results from multiple models are synthesized and evaluated in ensemble experiments.

[3] If a raindrop is reentrained into an updraft, it is prevented from immediately reaching the ground, thus reducing rainfall rates.

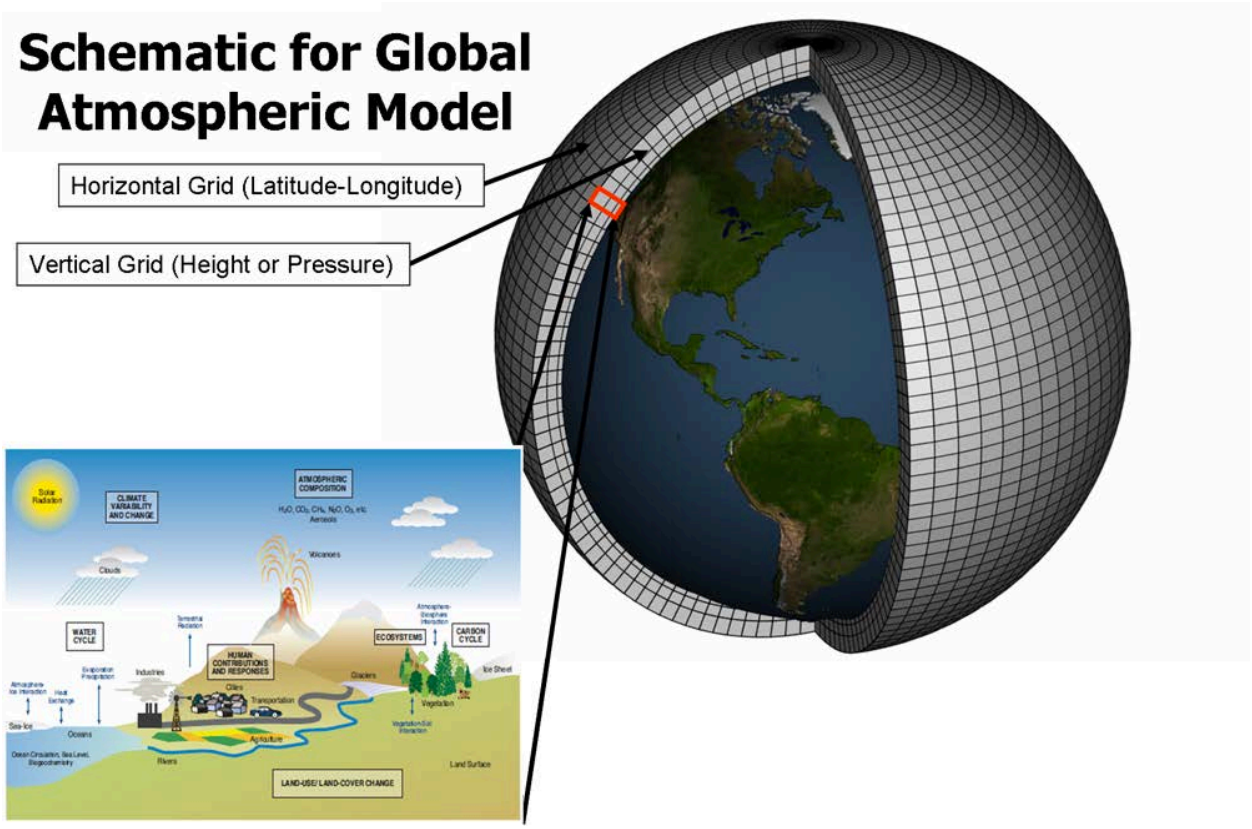

Figure 3.1: Generalized conceptual schematic for global climate models (Source: NOAA, Public Domain).

GCMs are able to represent the dynamics of large-scale atmospheric processes and their interactions across the globe. However, they are unable to represent atmospheric dynamics that take place at finer-spatial scales or generate outputs at the spatial scales needed for urban hydrological modeling and climate adaptation studies (Table 3.1; Maimone et al., 2019; Yu et al., 2018). Their use in understanding how climate change will impact future short-duration precipitation is dependent on additional downscaling methods (Lopez-Cantu et al., 2020).

As a result, a wide variety of techniques have been developed to downscale GCM projections from their native coarse spatial resolution to the resolution needed for adaptation researchers. These downscaling techniques fall into two categories: statistical and dynamic.

Statistical downscaling uses observational datasets to identify statistical relationships between the spatial distribution of precipitation parameters at fine-scale and what can be represented at the coarse-resolution of a GCM. These relationships are then applied to GCM-outputs to approximate fine-scale climate features in the future. The Localized Constructed Analogs (LOCA) method (Pierce et al., 2021; Pierce et al., 2014) is an example of

statistical downscaling. With this approach, a high-resolution, gridded observational time series dataset is coarsened to match the spatial resolution of GCM outputs. For each GCM time step, an historical analog that best matches the GCM output at selected grid cells that time step is identified in the coarsened observational dataset. That fine-scale spatial distribution of the parameter of interest associated with that analog is then reconstructed to create the downscaled field.

Dynamic downscaling methods generate high-resolution projections directly by running a high-resolution Regional Climate Model (RCM) with initial and lateral boundary conditions provided from the outputs of GCM runs (Laprise et al., 2008). RCMs dynamically simulate local climate and its future changes, and thus are not limited by assumptions of unchanging weather patterns through the future. The highest resolution RCMs are 'Convection Permitting' (CPRCMs) - these models are able to explicitly simulate the dynamics of convective precipitation that occur within rainstorms - and their potential changes with global warming. While ensemble experiments using CPRCMs may provide important insight on how climate change will impact short-duration extreme precipitation, their utilization currently remains limited by their computational expense and no ensemble studies are available for the U.S. Northeast.

3.4 Expert Elicitation

Subtask 3.2 explored how different types of precipitation data, specifically time series and intensity-duration-frequency (IDF) curves, are currently used by various NYC programs and agencies, particularly in stormwater and flooding planning and management. By identifying how precipitation information is used along with how it may change, we can begin to identify potential downstream impacts on stormwater management decision-making processes. We were specifically interested in flows of information, key decision points, and relevant spatial and temporal scales of precipitation data used in these processes, with a goal of understanding how future precipitation projections can be incorporated into city planning and decision-making.

Similar to the work of Jackson et al. (2012) and Eggers et al. (2011), we formulated a stakeholder map, expert model, and information flow diagram to conceptually model how IDF curves and precipitation information are used in the City. These conceptualizations were initially developed from extensive literature reviews, mainly of key City and New York State documents. We continued to iteratively refine these conceptual models through expert feedback from interviews with City professionals and from quarterly Stormwater Subcommittee (SSC) meetings, which convened stormwater management experts across the United States. It was important for us to engage directly with users of precipitation information

to ensure that the conceptualizations we developed addressed existing processes and priorities of stakeholders.

a. Methods: Expert Elicitation

We conducted an extensive review and coded gray literature and City documents, many of which were identified through key term searches or later referred to us by interviewees. We searched documents for mentions of IDF curves and other precipitation information(frequency, intensity, event, depths) used in City stormwater management.

Through referrals from our Interagency Collaborators, we interviewed New York City stormwater and flooding management experts, including employees from the NYC Department of Environmental Protection, Mayor's Office of Climate & Environmental Justice, New York City Emergency Management (NYCEM), Metropolitan Transit Authority, and Bureau of Water Supply, in addition to private sector practitioners engaged in stormwater planning and design in the City. Experts were interviewed about the use of IDF curves and other precipitation information in their work. Interview questions were developed in collaboration with Interagency Collaborators members.

Four quarterly Stormwater Sub-Committee meetings were convened via Zoom. These meetings included experts in stormwater management who were identified through recommendations from Interagency Collaborators partners, and the professional networks of the Task 3 project team. During meetings, we elicited feedback on the information flows diagram model of how IDF curves are used in various city agencies.

From the combination of literature reviews and expert elicitation, we developed the stakeholder map, expert model and information flow diagram. The development of these models was an iterative process beginning soon after initial interviews. These drafts were then vetted in subsequent interviews and SCC meetings. We formulated a stakeholder map to identify relevant direct and indirect users of precipitation data, and we used this map to inform future interviews and surveys. We next developed an expert model, which is a formal representation of stormwater infrastructure decision making to broadly identify design standards and planning processes that may be affected by changes in precipitation information. Lastly, we developed a detailed information flow diagram that represents how IDF curves and other types of precipitation information are used in various City programs related to stormwater and flooding management and planning. The information flow diagram identifies the specific IDF curves, design storms, historical time series, and other types of precipitation information used, their users, and relevant documents where their uses are codified.

b. Results: Expert Elicitation

Figure 3.2-3.3 shows the resulting stakeholder map of users of precipitation information in New York City. We identified major government agencies within New York City and State that act as decision makers in regards to stormwater and flooding management: Department of Environmental Conservation, Department of Environmental Protection (including Bureau of Water and Sewer Operations and Bureau of Water Supply), New York City Emergency Management, Department of Parks and Recreation, Department of Buildings, and Mayor's Office of Climate & Environmental Justice. The transactors include other government entities not directly charged with stormwater decision making, consultants, and others who do work that is influenced and/or determined by the stormwater decision-makers. The transactors are typically working in service of a variety of active interests (e.g. developers, private companies) and the broader public. The concentric circles in Figure 3.2 show the cascading impacts of stormwater decisions across different sectors and interest groups.

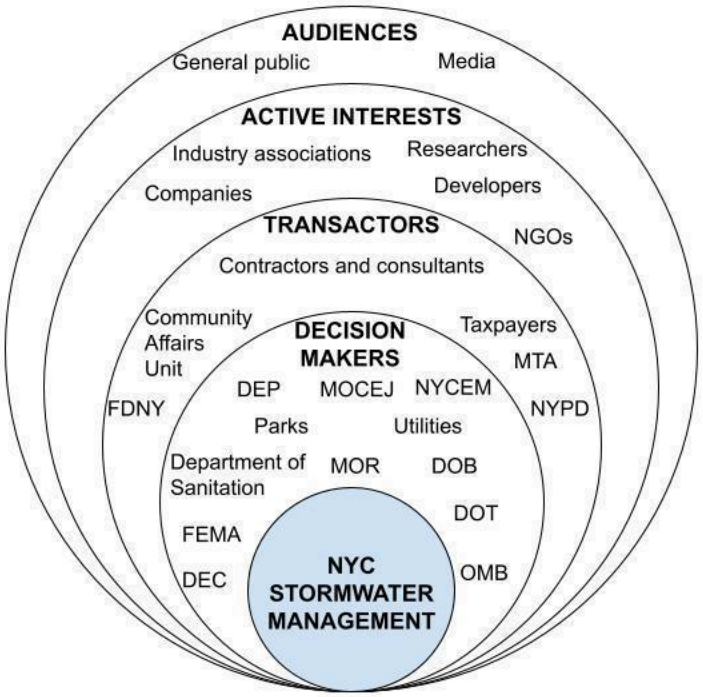

Figure 3.2: A stakeholder map for stormwater management in New York City.

Figure 3.3 presents a simple expert model of how stormwater infrastructure may be affected by potential changes in precipitation. In this diagram, ovals are used to denote variables and uncertain events; arrows indicate associations (causal or otherwise); decisions are represented by rectangles; and diamonds indicate outcomes. This formalism highlights different aspects of IDF decision-making, the conditions that trigger them, and how both are mapped to design standards and other outcomes. The expert model also highlights parallel roles for resilience and preparedness measures, other than hard infrastructure, that may directly and indirectly depend on changes in precipitation information.

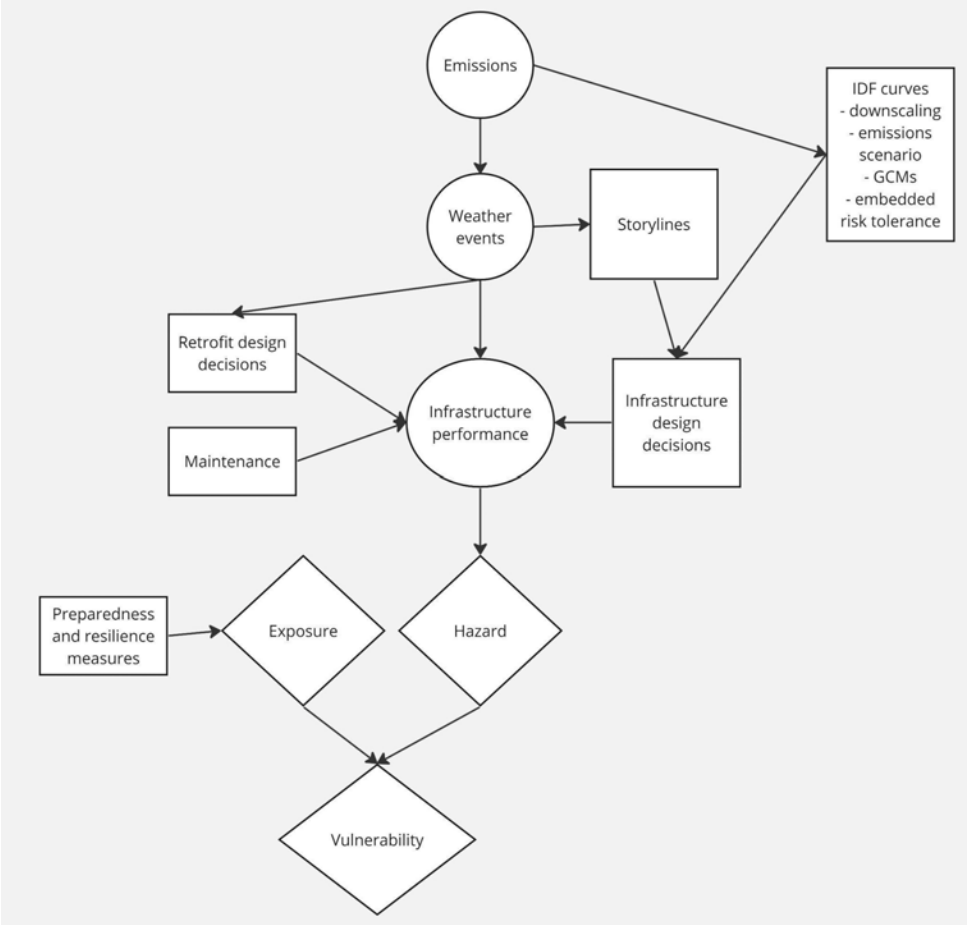

Figure 3.3: An expert model of stormwater management in New York City.

Figure 3.4 is an information flow diagram that summarizes how precipitation information, including specific precipitation events and precipitation time series, are used in New York City stormwater management. This diagram identifies 1) the specific precipitation event used (e.g. the return period of a storm and an associated duration), 2) which specific City programs and stormwater management processes uses them, and 3) where the uses are codified in documentation (if applicable). Additionally, Table 1 lists the key documents where the uses of precipitation information are codified.

We found there are two major types of precipitation information used in the NYC stormwater and flood management: specific precipitation time series and specific precipitation events. The most common specific precipitation time series used is the 2008 JFK rainfall year, which is used in development of Long-term Control Plans (LTCPs) for combined sewer overflow management, green infrastructure performance analysis, and in the City Environmental Quality Review. The 2008 JFK rainfall year is used for initial assessments but is understood not to represent the full range of possible conditions. It was supplemented with an additional 10 years of rainfall data from other NYC rain gauges in the NYC Wastewater Resiliency Plan; the

expanded time series is used in LTCP modeling. Lastly, long duration precipitation data (i.e., daily time steps) from GCM outputs is used by the Bureau of Water Supply to support reservoir operations under climate change.

For specific precipitation events, five- and 10-year storms are the most common specific precipitation events used in New York City stormwater management. As most NYC sewers are designed for the five-year storm (some areas of NYC are designed for a three-year storm) with a peak intensity of 5.95 in/hr., this also affects the design of other stormwater infrastructure. For instance, the Staten Island Bluebelts, naturally engineered drainage systems, are typically designed for a five-year 24-hour storm (some Bluebelts are designed for a 10-year 24-hour storm). Both five- and 10-year storms are used in the design of private on-site stormwater disposal systems and in the design of detention facilities, which in turn affects the sewer operations volume criteria for Stormwater Construction Permit requirements. Other specific precipitation events used in New York City stormwater management include the 90th percentile storm of all 24-hour storms in a given year, which amounts to 1.5 inches in New York City, as well as the 100-year storm. The 90th percentile storm is used for water quality volume calculations according to State DEC, which in turn affects water quality and runoff reduction criteria in Stormwater Construction Permit requirements. The 100-year one-hour storm is specified in certain parts of the Plumbing Code, and the 100-year 24-hour storm is also used to check that the FEMA base flood elevations are not exceeded in Bluebelt detention sites.

We found many key documents often did not reference the source of the precipitation information used. For instance, a 100-year storm is referenced in Chapter 11 Storm Drainage of the Department of Buildings Plumbing Code, but it is not specified if this 100-year storm comes from TP25, NOAA Atlas 14, or another source. They also did not reference the duration of the event, nor its temporal distribution. Furthermore, none of the key documents we reviewed specified procedures of how new or updated precipitation information could be incorporated into existing procedures. For instance, NOAA is expected to update its Precipitation Frequency Data Server with Atlas-15, which will also include future IDF estimates that take climate change into account, but it’s not clear how the new Atlas will be incorporated in any NYC stormwater management programs we identified.

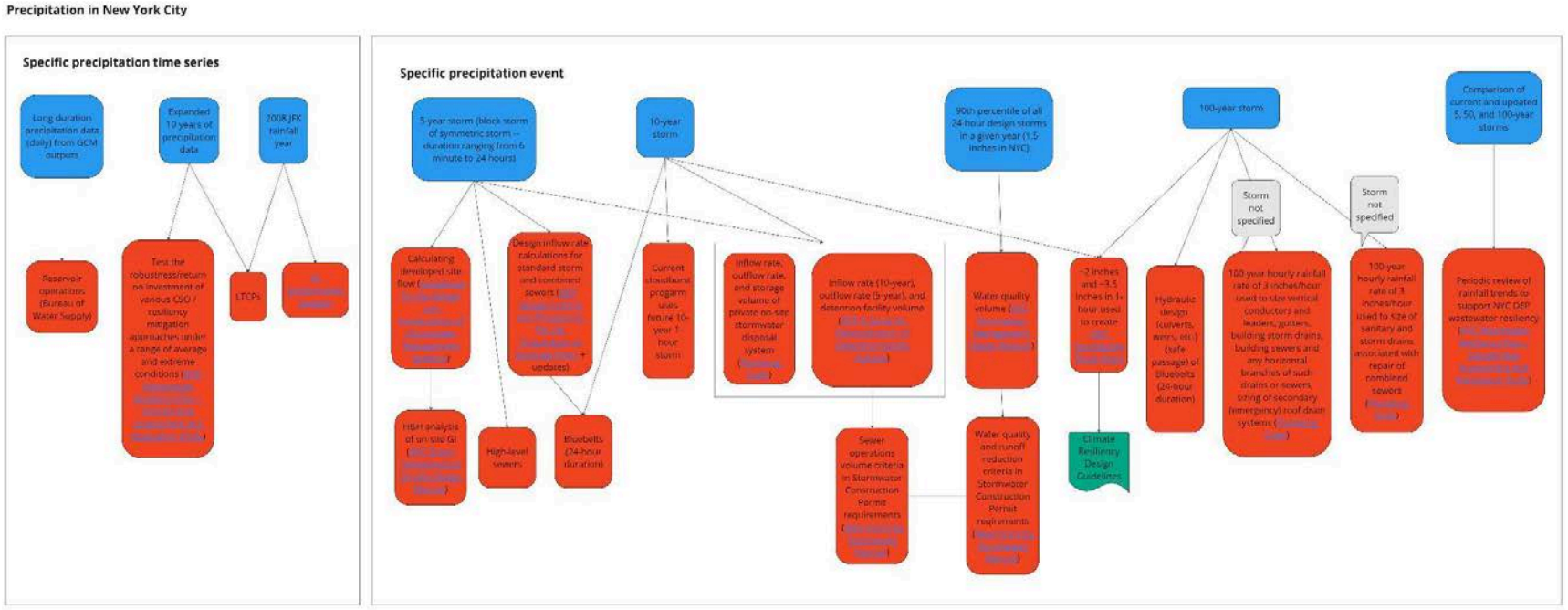

Figure 3.4: Flows of precipitation information showing precipitation information (blue), organizational processes (red), and documentation (green).

Table 3.1 shows a list of key documents and key precipitation products relevant to New York City stormwater and flooding management that incorporate the use of precipitation information.

Table 3.1: Key documentation and products that use precipitation information in New York.

Date	Document	Use of precipitation information
1973	DEP Design Criteria and Procedures for the Preparation of Drainage Plans (Department of Water Resources Drainage Section 1973)	Design flow calculations for storm and combined sewers – Steel formula using coefficients for five-year storm in New York City and six-minute time of concentration for developed areas in New York City used i=125/(t+15)
Rev. 2006	DEP Criteria for Determination of Detention Facility Volume (Bureau of Water and Sewer Operations Division of Review and Construction Compliance 2006)	Design criteria of detention facility volume – Inflow rate intensity: Steel formula using coefficients for 10-year storm in New York City Outflow rate: Steel formula using coefficients for five-year storm in New York City and six-minute time of concentration i=140/(t+15)
2013	NYC Wastewater Resiliency Plan – Climate Risk Assessment and Adaptation Study (Department of Environmental Protection 2013)	Five-year IDF curves (current for NYC sewer design + updated curves based on rainfall gauge data from hourly 1969-2010 data at four NYC rain gauges from Northeast Regional Climate Center at Cornell) for variety of durations (six minutes to 100 minutes) used in Phase 1 – Precipitation Analysis of Precipitation, Watershed, and Tide Gate Analysis 2008 JFK “typical year” used for initial assessment of annual conditions for LTCP modeling with a 10-year time series used in the final analysis (including 2005 and 2006) to account for future typical years (based on change factors from NPCC Climate Risk Information report 2009 projections and rainfall intensity findings from Forsee et al., 2010)
2021	DEP Stormwater Flood Maps (under Stormwater Resiliency Plan) (Department of Environmental Protection 2021a)	Stormwater flood scenarios modeled – ~2 inches and ~3.5 inches in one-hour using Jupiter data (different but similar to NOAA Atlas 14)
2017	Cloudburst Resiliency Planning Study – Executive Summary (Department of Environmental Protection and Ramboll 2017)	Hydraulic models to simulate cloudburst flood (100-year storm in 2015 and 2115); risk mapping for a 10-, 50-, and 100- year storm

	Long-Term Control Plans (2005 NYC CSO Consent Order) (Department of Environmental Conservation 2005)	2008 JFK Rainfall Year
2016	Green Infrastructure Performance Metrics (part of 2012 CSO Order) (Arcadis of New York, Inc. 2016)	2008 JFK Rainfall Year
2022	Climate Resiliency Design Guidelines (NYC Mayor's Office of Climate and Environmental Justice 2022)	Use DEP Stormwater Flood Maps
2023	Citywide Green Infrastructure Plan (part of 2023 CSO Consent Order Modification – Green Infrastructure) (Department of Environmental Conservation 2023)	Specific GI asset types – various design storms (1, 1.25, and 1.85 inches)
Amended 2023	Storage volume of private on-site stormwater disposal system; detention and retention tanks in flood hazard areas (Plumbing Code Chapter 11 Storm Drainage) (NYC Buildings 2022)	Runoff rate uses i=5.95 in/hr (based on six min time of concentration for the five-year storm) Storage volume uses duration of 10-year storm (duration is calculated as the time of concentration based on Equation 11-5 in Chapter 11 Storm Drainage, and i is the average rainfall intensity based on that duration)
Amended 2023	Roofs (Plumbing Code Chapter 11 Storm Drainage) (NYC Buildings 2022)	100-year one-hour rainfall rate of three inches/hour used to size vertical conductors and leaders, gutters, building storm drains, building sewers and any horizontal branches of such drains or sewers, sizing of secondary (emergency) roof drain systems
Amended 2023	Repair of CSOs installed prior to effective date of this section (1109.1 of Plumbing Code) (Plumbing Code Chapter 11 Storm Drainage) (NYC Buildings 2022)	Size of a combination sanitary and storm drain or sewer computed based on the 100-year one-hour rainfall rate of three in/hr.
2021	NYC Green Infrastructure On-site Design Manual (Department of Environmental Protection 2021b)	H&H analysis performed using the Rational Method in accordance with DEP standards (DEP's 2012 Guidelines for the Design and Construction of Stormwater Management Systems) – rainfall intensity of 5.95 in/hr. for the event with a five-year return period and a six minute time of concentration
2012	Guidelines for the Design and Construction of Stormwater Management Systems (Department of Environmental Protection and Department of Buildings (cons.) 2012)	Calculating developed site flow – rainfall intensity of 5.95 in/hr. for the event with a five-year return period and a six-minute time of concentration
2022	DEC Stormwater Management Design Manual (Department of	Water quality volume – 90th percentile of all 24-hour design storms (1.5 inches in New York City) based on

	Environmental Conservation, Environmental Facilities Corporation, and LaBella Associates 2022)	isohyetal map for NY State
2022	New York City Stormwater Manual (appendix to Chapter 19.1 of the Rules of the City of New York) (Department of Environmental Protection 2022)	Sewer operations volume criteria in Stormwater Construction Permit requirements – 10-year storm Water quality criteria in Stormwater Construction Permit requirements – 90th percentile storm (1.5 inches in New York City) Runoff reduction criteria – 1.5-inch depth

c. Discussion and Conclusions: Expert Elicitation

Based on our Expert Elicitation research, we recommend the following for New York City agencies to consider:

- In describing rainfall standards in City documentation, the duration of rainfall or the method used to establish time of concentration should be included along with precipitation frequency or return period.
- NYC should consider having a standardized interagency set of current and future IDF curves.
- NYC should consider having a methodology for incorporating climate change-based precipitation information and IDF curves into these city operations.
- NYC should consider convening annual SSC meetings to sustain discussion on how precipitation observations are used in stormwater management and periodically reevaluate how precipitation information is used in city operations.
- Following the research of Madajewicz (2020), NYC should also gather narratives of individuals who have experienced floods in New York City. Personal narratives, complemented with practitioner expertise, and enhanced precipitation and flood data will evolve understanding of the vulnerability and impacts of extreme rainfall events, leading to more holistic policy decisions.

We also identified some NYC programs that do not use precipitation information directly but may be impacted by changes in precipitation. For instance, NYCEM regularly updates its plans for flooding hazards and has categorized triggers (nuisance/low/moderate/high) associated with activating its emergency response plans for flash flooding, but is currently reviewing how to incorporate climate change into planning. Additionally, other programs are in the process of explicitly incorporating precipitation information into its plans, such as the MTA's Climate Vulnerability Assessment. We recommend that when these programs explicitly incorporate

precipitation information in their plans, they include procedures for how such information can be periodically updated as new and higher resolution (i.e., spatially and temporally) precipitation information is developed.

Many programs and agencies (DEP, MTA, MOCEJ, contractors with the city) point to a need for subhourly precipitation data products that take into account climate change, as peak flow rates occur usually at subhourly time steps and the minimum time of concentration encountered in New York City is six minutes. More studies that temporally downscale climate models for multi-model ensembles and multiple scenarios of climate change are needed.

Published documents describing programs in New York City do not highlight incorporation of precipitation information in their planning. For instance, the NYC Wastewater Resiliency Plan and updates to standards in the construction code for structures in the 1% annual chance floodplain are based on FEMA's 2022 Preliminary Flood Insurance Risk Maps, which account for fluvial and coastal flooding but not pluvial flooding. And while fluvial flooding is directly linked to precipitation, fluvial risk calculations use river discharge rates and do not incorporate precipitation information. Communication with key City staff has confirmed that internal design guidelines now consider inland flooding in the planning, pointing to an opportunity for the City to engage experts and industry professionals to be better equipped to address these types of risks.

3.5 Historic heavy rainfall observations and event identification

To date, most research on climate change and precipitation has focused on rainfall rates at daily or longer time-scales. For this assessment, we characterize subdaily rainfall in the vicinity of New York City and the upstate reservoirs that provide New York City's municipal water supply. Historic intense rainfall observed over different subdaily durations were ranked and compared with narrative observations of pluvial flooding in New York City provided through the U.S. National Weather Service *Storm Data* publication and *Storm Events Database* (NCEIa).

a. Methods: Historic heavy rainfall observations and event ranking

1. *Precipitation Data Inventory*

For all stations except Sikorsky Airport (KBDR), precipitation observations at hourly intervals through 2012 were obtained from the NOAA DSI-3240 hourly precipitation dataset (NOAA, 2003). Hourly Data post-2012 was obtained from the Local Climatological Dataset (LCD; NCEIb, 2023). The LCD was used for the full-record of hourly observations for the KBDR site.

Hourly values provided through this merged dataset represent 60-minute accumulations observed at 51 minutes after the clock-hour.

The most complete record of subhourly precipitation comes from the National Centers for Environmental Information DSI-6405 and DSI-6406 data sets (NCEI, 2022). One-minute precipitation data are available starting as early as 2000 in this data set. These data are subject to very limited, automated quality control, and our initial analyses have identified many data gaps even in the relatively short record of available data. As a result, analysis for this report will focus on hourly precipitation observations.

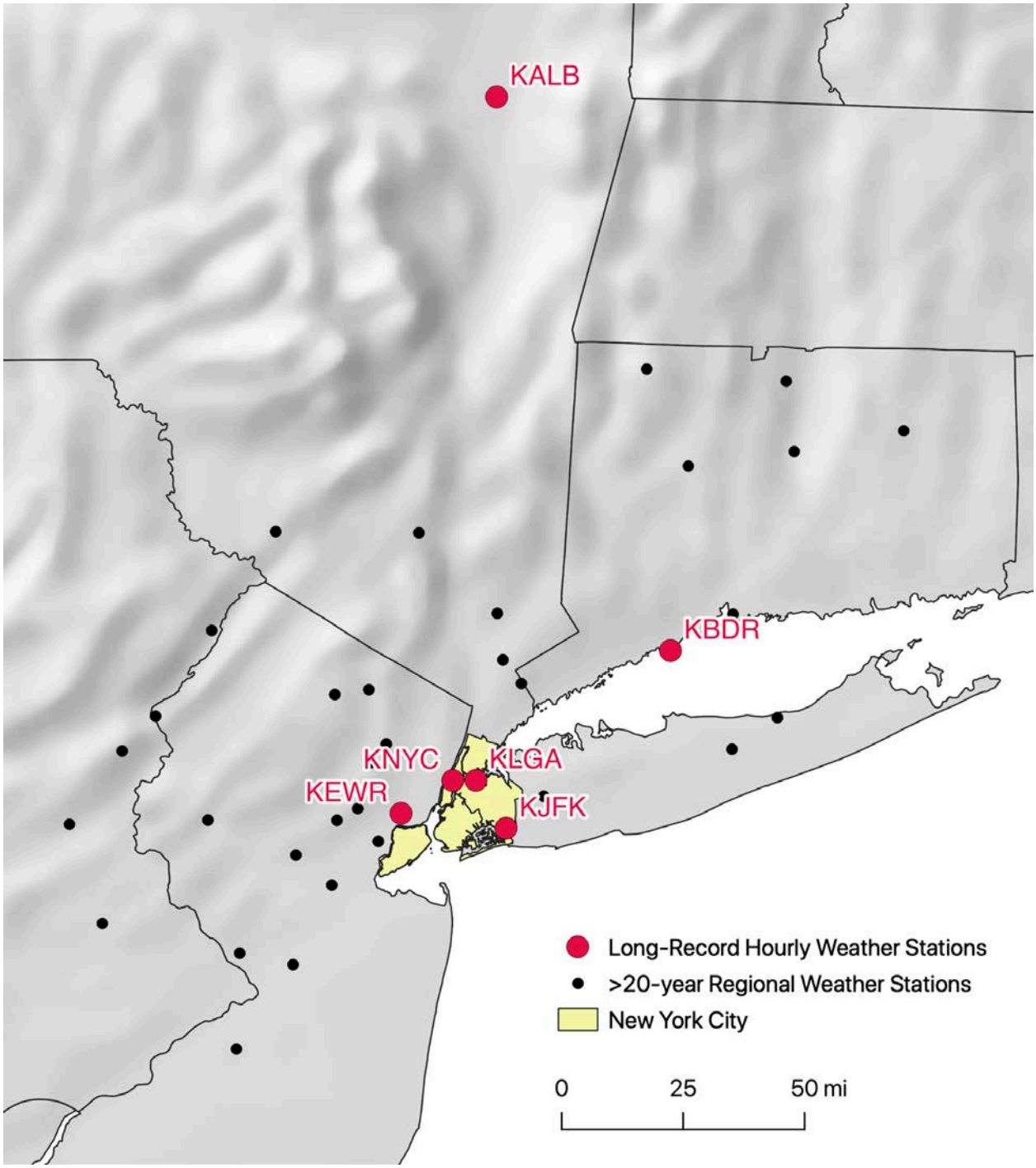

Figure 3.5: Locations of rain gauges used in study analyses.

b. Observed pluvial flood events

We compiled a list of storms causing significant pluvial flooding events in New York City from 1986 to 2022, based on the NOAA *Storm Data* publications and *Storm Events Database* (NCEIa, 2023). *Storm Data* publications are published monthly by NOAA and contain records of significant national storm occurrences and weather phenomena; they are digitized and available online. The NOAA *Storm Events Database* contains searchable records from the *Storm Data* publications and other sources. The NWS defines a significant storm event as having "met local/regional/national threshold criteria, or generated impact, or was newsworthy, even [if] it affected a small area (NWS, 2021)." Data on events are gathered from the NWS, as well as outside sources including the media, law enforcement or other government agencies, emergency managers, private companies, and trained individuals. Because the *Storm Events Database* only contains flood and flash flood events after 1996, we manually examined the monthly NWS *Storm Data* publications from 1986 to 2000 for mentions of floods, flash floods, and urban flooding. The decision to begin in 1986 follows the work of Jessup and DeGaetano (2008), where this year was identified as the start of consistent records of flash flooding in the northeastern U.S.

Meteorological conditions associated with the storm were based on the storm's episode narrative. Socioeconomic impacts of storms causing flood and flash flood events were assessed based on if the storm record's episode narrative, event narrative, or notes mentioned the following six categories: death, injury, property damage, potentially life-threatening conditions, mass transit disruptions, and roadway disruptions. This work is detailed in a Technical Supplement to this report.

To evaluate the contribution of compounding by high tide events, data from tide gauges maintained by the U.S. Geological Survey (USGS) and NOAA were utilized. The USGS provides data on daily tidal levels at Jamaica Bay at Inwood Station, and NOAA provides data on daily tidal levels at The Battery, King's Point, Bergen Point West Reach, and Willets Point. Data on maximum daily tidal levels (i.e. highest high-water relative to NAVD88 or MHHW) were downloaded for all five of these stations from Jan. 1, 1986, to Dec. 31, 2022, or where data were available within this timespan. Table 3.2 shows the data availability at these five stations, as well as the minor, moderate, and major coastal flooding thresholds from NWS NY.

Table 3.2: NYC tide gauges and NWS flood-stages used in historic flood event analyses.

Station	Data Availability	Below minor coastal threshold	Minor coastal threshold	Moderate coastal threshold	Major coastal threshold

USGS 01311850 Jamaica Bay at Inwood NY	06/11/1979 - 12/31/2022*	< 4.4’	>= 4.4’ & < 5.1’	>= 5.1’ & <5.9’	>= 5.9’
The Battery, NY - Station ID: 8518750	12/01/1978 - 06/06/1996; 11/20/1997 - 12/31/2000; 05/01/2001 - 01/31/2004. 06/01/2004 - 07/31/2023	< 4.38’	>=4.38’ & < 5.68’	>= 5.68’ & < 6.88’	>= 6.99’
Kings Point, NY - Station ID: 8516945	11/01/1998 - 12/31/2022	< 6.29’	>= 6.29’ & < 6.79	>= 6.79’ & < 8.79’	>= 8.79’
Bergen Point West Reach, NY - Station ID: 8519483**	09/18/1981 - 10/01/1992; 11/29/1993 - 12/03/2009; 03/23/2010 - 07/31/2023	< 1.7’	>= 1.7’ & < 3.0’	>= 3.0’ & <4.1’	>= 4.1’
Willets Point, NY - Station ID: 8516990***	10/01/1979 - 11/14/2000	< 6.29’	>= 6.29’ & < 6.79	>= 6.79’ & < 8.79’	>= 8.79’

** All coastal threshold values are relative to NAVD88 except Bergen Point West Reach values, which are relative to MHHW.

*** Willets Point coastal threshold values use Kings Point threshold values, as tides and water levels are fairly similar at the two stations, and they are only a few kilometers apart, which leads to very little difference and nearly interchangeable data.

For the date of each storm, we retrieved the observed daily highest high tide level at each of the five stations (if data was available for each gauge). We compared the observed daily highest high tide level to the minor, moderate, and major coastal flood thresholds at the station, and determined if a coastal flood threshold was exceeded on that day.

c. Results: Observed flood events

From 1986 to 2022, we identified 170 unique storms (Figure 3.6) that caused significant pluvial flood impacts in New York City based on the NCEI Storm Events Database (1996-2022) and monthly NCEI Storm Data Publications (1986-2000). Based on the episode narratives, six of these flooding events were associated with tropical cyclones passing through or near New York City, while 16 were tropical-associated (tropical remnants, predecessor events, or other

storms that 'tapped' moisture from tropical cyclones that did not pass through or near the city). A total of 45 floods were driven by extratropical cyclones, while 40 floods were driven by frontal systems not associated with an extratropical or tropical cyclone. The remaining 63 storms could not be associated with one of these four agents based on information provided in their Episode Narrative.

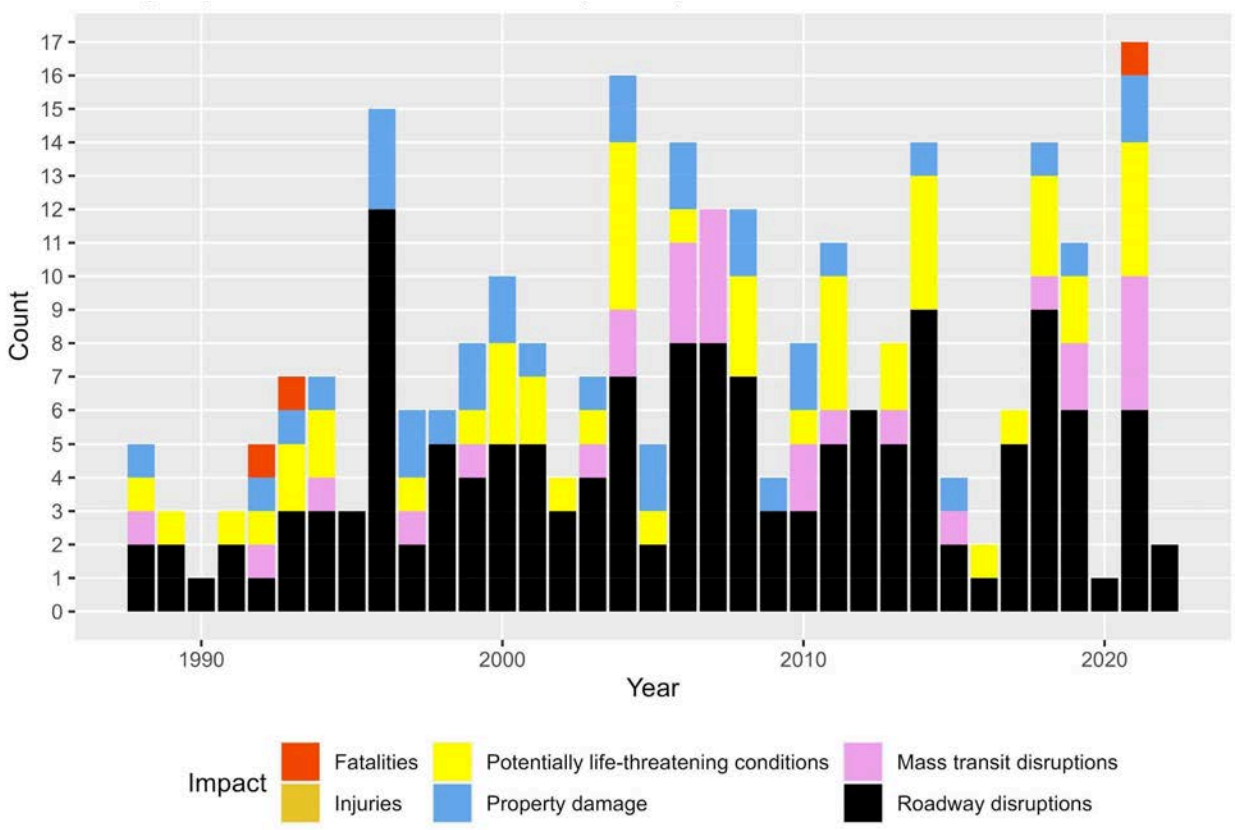

Figure 3.6: Time series of observed pluvial flooding impacts, based on narrative reports in the NWS *Storm Data* publication and *Storm Events Database*, by year from 1986-2022 (n=170).

As shown in Table 3.3, the majority of pluvial flood events (85%) occurred when the coastal flooding threshold value was below minor across all five gauges examined, indicating the flooding occurred in the absence of compounding by high tides.

Table 3.3: Number and percentage of storms that occurred when a coastal flooding threshold was reached at one of five tidal gauges in the New York City area that day.

Tidal gauge	Below minor	Minor	Moderate	Major
Jamaica Bay (n=156)	136 (87.1%)	17 (10.9%)	1 (0.64%)	2 (1.3%)

The Battery (n=166)	156 (94%)	8 (4.8%)	1 (0.6%)	1 (0.6%)
Kings Point (n=118)	118 (100%)	0 (0%)	0 (0%)	0 (0%)
Bergen Point (n=165)	151 (91.5%)	12 (7.27%)	1 (0.6%)	1 (0.6%)
Willets Point (n=53)	51 (96.2%)	0 (0%)	1 (1.9%)	1 (1.9%)
Any gauge (n=170)	**145 (85.3%)**	**21 (12.4%)**	**2 (1.18%)**	**2 (1.18%)**

Figure 3.7 shows a count of the 170 storms by month. Nearly half of the 170 storms identified occurred during the months of July or August (46%). The six months from November to April accounted for only 11% of storms; five winter storms included narratives that described rain-on-snow or -ice events. Figure 3.8 shows the diurnal period of the storms, based on the storm's recorded begin times. Most intense rainfall events associated with flooding (40.7%) began in the afternoon, defined here as the period from 12 p.m. to 6 p.m.

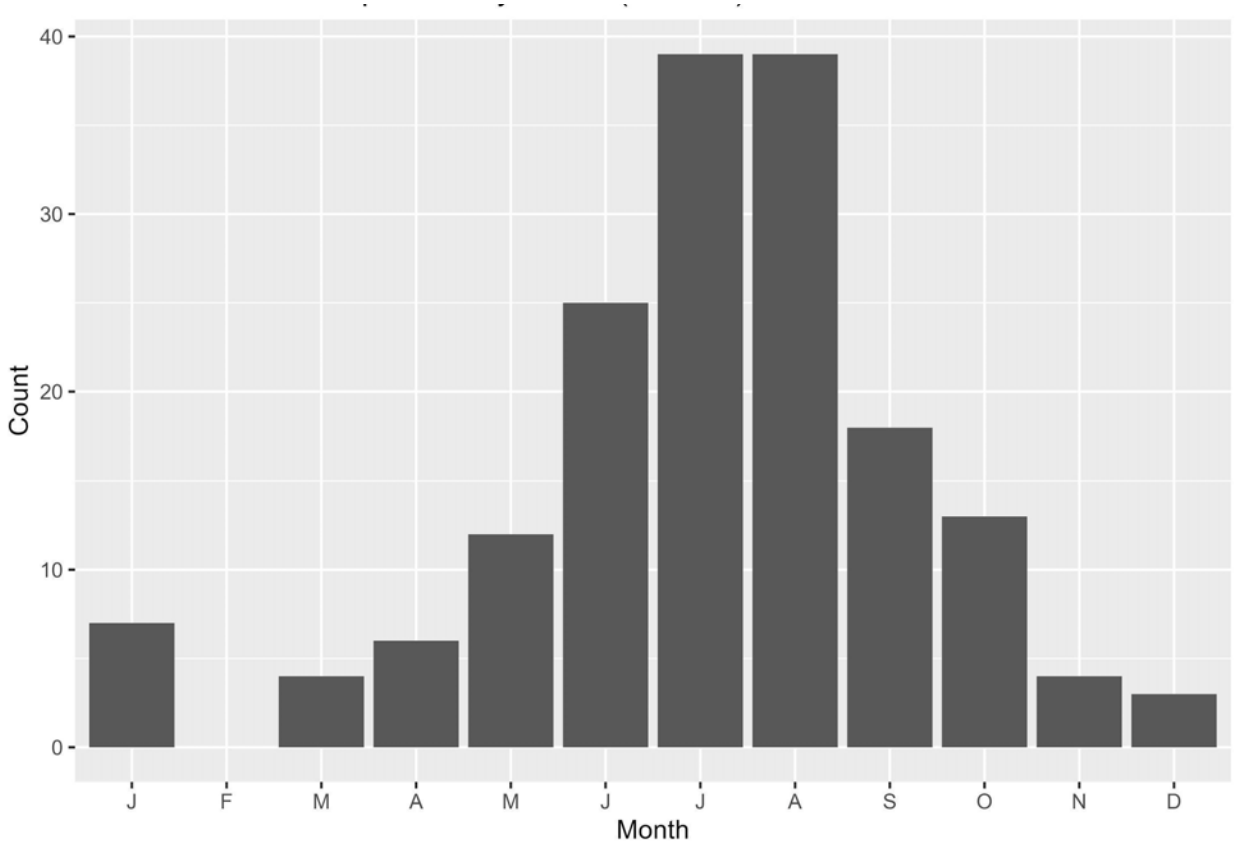

Figure 3.7: Monthly distribution of NCEI storms from 1986 to 2022 (n=170).

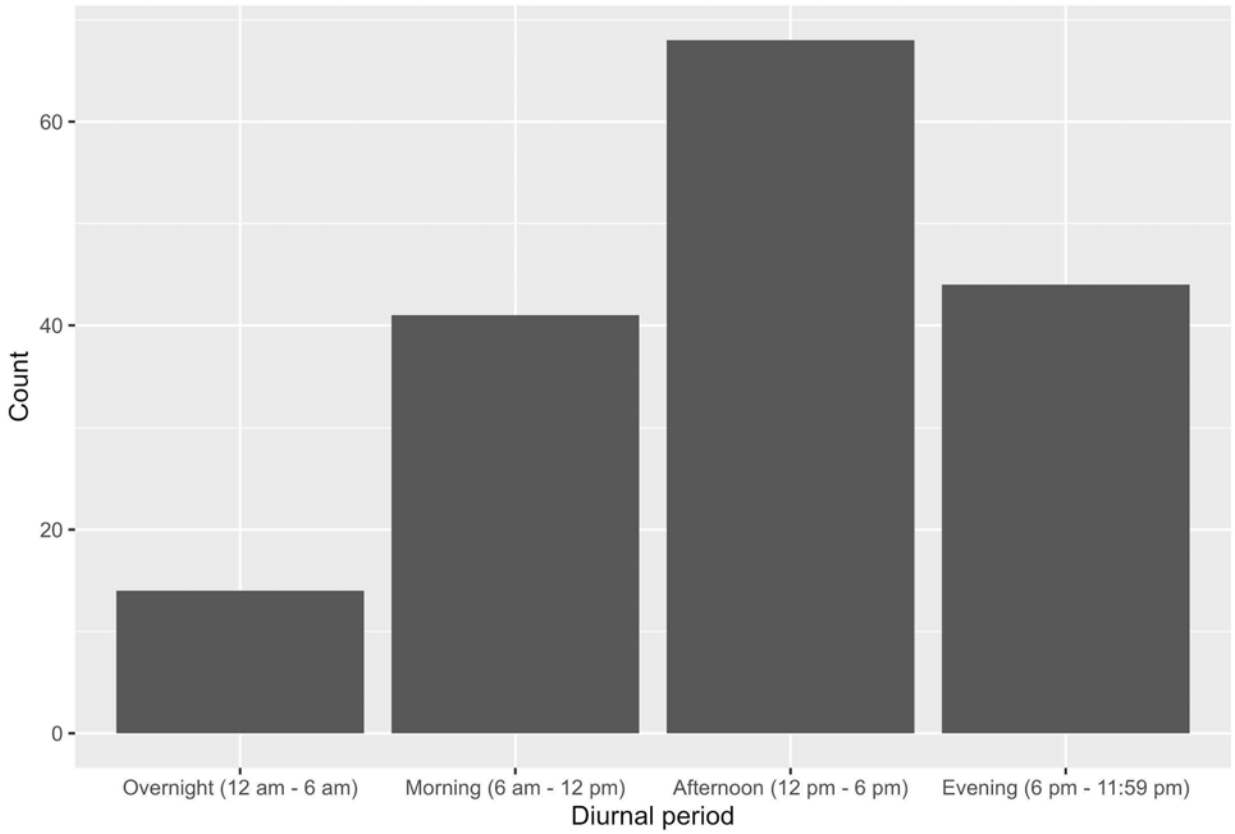

Figure 3.8: Diurnal period of NCEI storms from 1986 to 2022 (n=167), based on the storm's recorded begin times. 40.7% of rain events associated with significant flooding occurred in the afternoon (12 p.m. to 6 p.m.).

d. Results: Comparison of Observed Heavy Rainfall and Significant Pluvial Flooding

The top seven hourly observed rainfall accumulations at the three long-record rain gauges located in New York City and Newark Liberty Airport are presented in Table 3.4. Only three storms (Post-Tropical Cyclone Ida on 9/1/2021 and thunderstorms on 7/17/95 and 8/8/2007) resulted in highest-ranked hourly rainfall accumulations that were observed at more than one of the city gauges. At the three NYC sites, all observed rainfall accumulations above 1.75 inches in an hour that occurred after 1986 (when NWS flooding reports are available) were associated with significant pluvial flooding recorded in the *Storm Data* publication and *Storm Events Database*. Most significant pluvial flooding events were not associated with observations of extreme rainfall at any of the NYC-area rain gauges or at any duration (e.g. 1 hr., 2 hr., 3 hr., 24 hr.; see Technical Supplement), suggesting a denser network of sustained rain gauges is needed to represent localized intense rainfall that can still result in significant flooding in the City.

Table 3.4: Top seven hourly rainfall accumulations observed at long-record rain gauges in New York City and at nearby Newark Liberty Airport. Observed rainfall-hours shaded red are those that were associated with significant flooding recorded in the Storm Data publication or Storm Events Database. Gray-shaded rainfalls occurred before 1986.

Rank	Newark Liberty Airport (KEWR)		Central Park (KNYC)		LaGuardia Airport (KLGA)		Kennedy Airport (KJFK)	
	Time (EST)	Precip (in.)	Time (EST)	Precip (in.)	Time (EST)	Precip (in.)	Time (EST)	Precip (in.)
1	9/1/21 19:00	**3.62**	9/1/21 20:00	**3.47**	9/1/21 20:00	**2.8**	7/31/96 11:00	**2.88**
2	7/21/06 16:00	**2.63**	7/17/95 23:00	**1.95**	7/15/97 19:00	**2.44**	6/30/84 12:00*	**2.45**
3	8/17/74 17:00	**2.04**	8/10/06 19:00	**1.9**	8/17/98 14:00	**2.09**	8/14/11 4:00	**2.41**
4	7/17/95 23:00	**2.00**	8/21/21 22:00	**1.84**	11/4/50 23:00	**1.97**	6/30/84 11:00	**2.15**
5	5/27/91 23:00	**1.95**	9/8/04 7:00	**1.76**	7/17/95 23:00	**1.97**	8/8/07 6:00	**2.04**
6	8/4/03 15:00	**1.92**	6/3/91 22:00	**1.75**	8/8/07 6:00	**1.87**	8/28/83 21:00	**1.88**
7	8/8/07 5:00	**1.82**	8/14/05 19:00	**1.7**	7/6/75 17:00	**1.83**	8/20/91 16:00	**1.84**

e. Conclusions and Discussion: Historic heavy rainfall observations and event ranking

Observations of subdaily rainfall in New York City are limited. Quality controlled-hourly data are available from the mid-20th century for three sites within New York City (Central Park, LaGuardia Airport, JFK); there are extensive gaps in the record at JFK. Long-record hourly data is also available at nearby regional sites, including Newark Airport (located in close proximity to Staten Island) and Sikorsky Airport in Bridgeport, CT. Subdaily rainfall observations are limited in the vicinity of New York City's municipal reservoir watersheds, with the closest long-record site located at Albany International Airport. Subhourly data is only available for the 21st century (< 20 years) and is not quality-controlled by the U.S. National Weather Service (NWS) or NCEI.

Since 1950, there have been 13 observations of precipitation greater or equal to two inches in an hour at the four long-record rain gauges in and adjacent (Newark Liberty Airport) to NYC. Only three of these observations occurred during the same storm (Post-Tropical Cyclone Ida on 9/1/2021 at Newark Liberty Airport, Central Park, and LaGuardia Airport), suggesting intense short-duration rainfall occurs at highly-localized spatial scales in New York City. However, it is important to note that short-duration (e.g. 60-minute) rainfall events are likely to be underrepresented based on hourly observations, since accumulation can be split across the clock hour (see Technical Supplement).

Pluvial flooding can be associated with cold fronts, warm fronts, extratropical closed low-pressure systems/Nor'easters, tropical cyclones and post-tropical cyclones. Pluvial flooding is most frequent in summer, but has occurred during all seasons. Observed rainfall accumulations of 1.75 inches in an hour at stations within the city were associated with significant pluvial flooding impacts. In the absence of pluvial flood management, the frequency of impactful pluvial flooding will increase with increased frequency of short-duration intense rainfall (See Subtask 3.6).

In addition, over the past four decades, there have been many impactful pluvial floods in New York City that cannot be associated with recorded extreme precipitation at the regional gages, suggesting the current spatial distribution of rain gauges in New York City is inadequate to fully characterize pluvial flood risks. Most observed pluvial floods in New York City were not compounded by high tides, indicating that intense rainfall, alone, can cause significant flooding impacts in the city.

Based on this work, we recommend the following:

- The development of standardized quality-control procedures for subhourly rainfall
- The establishment of a network of maintained and quality-controlled subhourly (e.g. one-minute) precipitation gauges across New York City and the upstate watersheds that supply NYC's municipal water to improve characterization of intense rainfall, support continued trends analyses, and identify thresholds for impactful pluvial flooding.

3.6. Clausius-Clapeyron Scaling Analyses of Observed Heavy Rainfall

Clausius-Clapeyron (CC) scaling rates can provide important insight on the climatology of short-duration precipitation (Fowler et al., 2021). In a given location, if the relationship between precipitation and temperature follows what is predicted by the CC Relationship (CC-scaling rate; 6-7% C^{-1}), it is likely the relationship between temperature and precipitation

is dominated by thermodynamics and moisture is not limited. When scaling deviates from the CC-scaling rate, it is an indicator that dynamic meteorological processes are more significant.

Many recent studies (Lenderink et al., 2017, Martinkova and Kysely, 2020; Najibi et al., 2022; Pérez Bello et al., 2021; Pumo and Noto, 2021; Steinshchneider and Najibi, 2022) have utilized dewpoint temperature, rather than the standard dry-bulb temperature as the covariate for assessment of CC-scaling rates. Dewpoint temperature is the temperature to which air would need to be cooled (assuming constant pressure) in order to be saturated and for water to begin condensing. It can be used as a metric that describes both dry-bulb (standard) temperature and atmospheric moisture. When used as a covariate for CC-scaling, it avoids the need to assume that atmospheric moisture is not limiting - higher dewpoint temperatures represent conditions of both high temperature and high precipitable water.

a. Methods

Investigations into CC scaling were conducted for four of the regional weather stations: LaGuardia Airport (KLGA), Newark Liberty Airport (KEWR), Bridgeport Sikorsky Airport (KBDR) and Albany International Airport (KALB). Central Park, New York (KNYC) and JFK Airport (KJFK) were not included in this analysis due to gaps in the dewpoint temperature or precipitation data records, respectively. In contrast to the precipitation trends analysis, described below, which focuses on precipitation events, the CC analysis utilizes hours during which there was non-zero precipitation, for which dry-bulb and dewpoint temperature data were both available. A database of this data was created, following the methodologies of Lenderink and Van Meijgaard (2008), Utsumi et al. (2011) and Lenderink et al. (2017), as delineated below.

For hours with non-zero precipitation at each station, the corresponding dry-bulb, and dewpoint temperatures were organized into 2 °C bins over the following ranges: 0-34 C for dry-bulb temperature and 0-26 C for dewpoint temperature. Even numbers were used to label the bins (e.g. bin 14 includes temperatures that were >14 and < 16). Next, for the hourly precipitation values in each temperature bin, the 90^{th}, 95^{th} and 99^{th} percentile precipitation intensities were calculated. Relative frequency plots depicting the percentage of 99th percentile exceedances in each dry-bulb and dewpoint temperature bin were produced. Finally, plots of log-transformed hourly precipitation intensity versus temperature were created, with lines corresponding to the expected CC relation (e.g. 7% increase in hourly precipitation per degree Celsius) superimposed on the plots for reference purposes. The CC relationship is represented using an exponential equation: P=1.07^T (Utsumi, Lenderlink, personal communication).

Because it is conceivable that a given hour of precipitation was triggered by thermodynamic conditions that preempted it, the analysis described above was repeated using the highest

dewpoint temperature value recorded in a three-hour window preceding each hour of precipitation (instead of the temperature values at the time of rain). The original approach is referred to as Method #1, and the approach using the three-hour window for dewpoint is referred to as Method #2.

To investigate whether CC scaling might be changing through time as a result of climate change, Method #1 and Method #2 were each performed for two separate and non-overlapping time periods (e.g. 1955-1989, and 1990-2022).

b. Results

Figures 3.9 and 3.10 depict the percentage of 99th percentile values in each dry-bulb and dewpoint temperature bin for each gauge. The plots show that for all stations, except for Albany, more than 50 % of the extreme precipitation hours occurred between the bins 16-22 and 16-20 for dry-bulb temperature and dewpoint temperature, respectively. Albany's percentages of extreme precipitation hours are distributed more broadly over a larger range of temperature values, spanning bins 0-22.

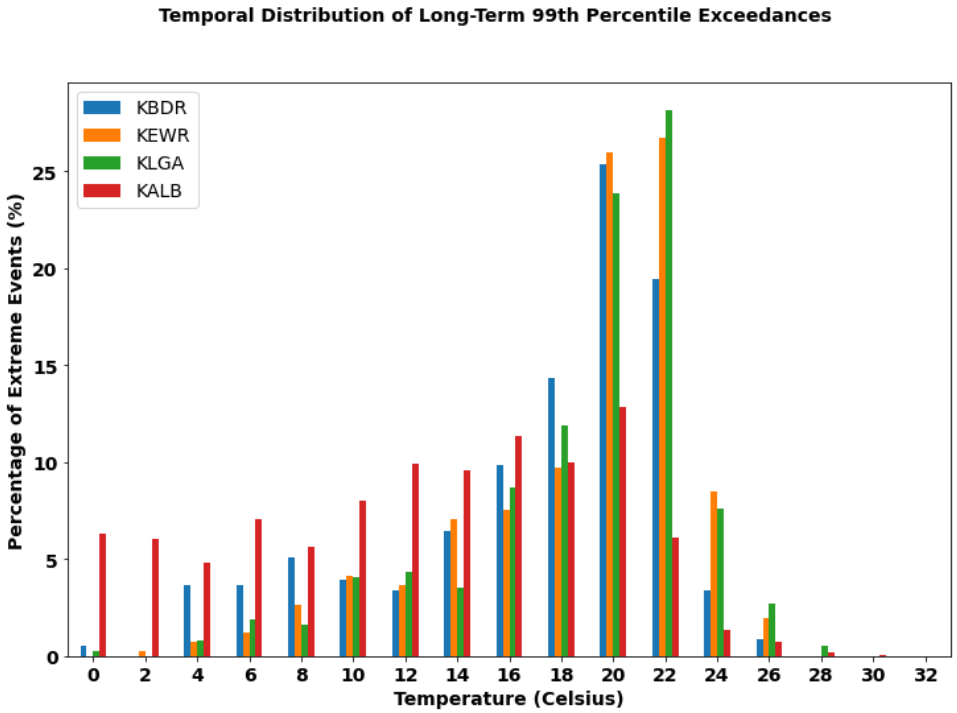

Figure 3.9: The distribution of long-term 99th percentile exceedances binned by temperature.

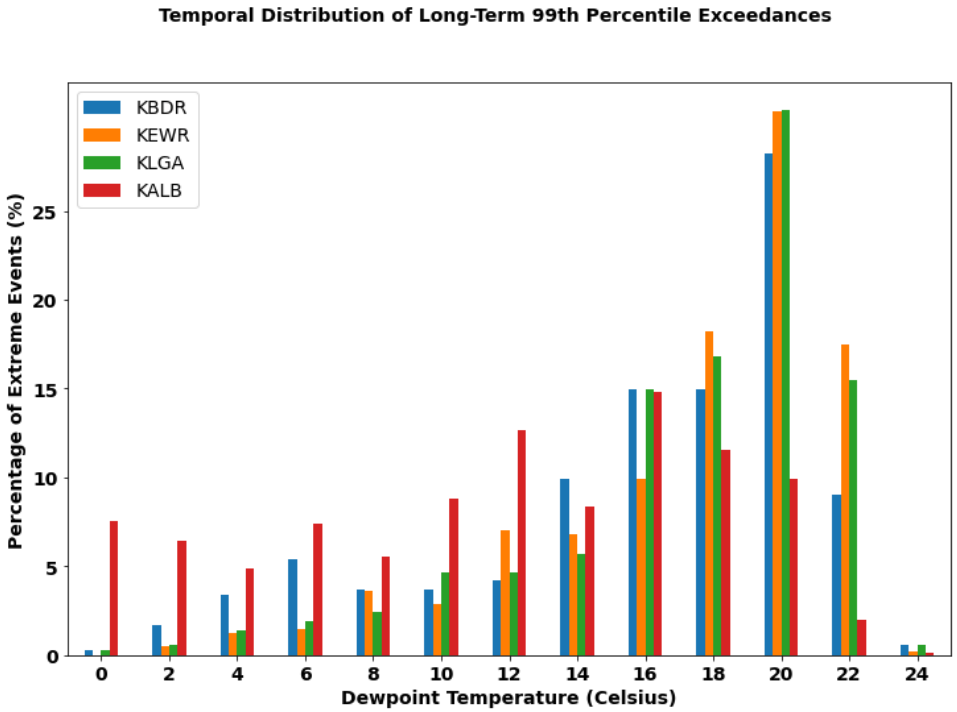

Figure 3.10: The distribution of long-term 99th percentile exceedances binned by temperature.

The observed scaling relationships are presented in Figures 3.11-3.13, along with multiple instances of the Clausius-Clapeyron scaling rate (dashed lines) for comparison. Positive slopes close to those of the CC lines were observed for most curves. As expected, all plots in both periods show an abrupt decline in slope after 20-24 C, attributed to the lesser number of low-probability extreme events at higher temperatures. The sudden decline is more striking in the more distant past (e.g. 1955-1989), than in the more recent past (e.g. 1990-2022), which could be an indication of an increase in the frequency of extreme precipitation in the higher temperature bins over time.

The most significant finding is the slopes of all three curves, for all four stations, in both time periods, using both methods for selecting the dewpoint temperature, are close to the slope of the lines representing the CC relationship. In some segments, the curves representing more extreme precipitation (e.g. 99th percentile) follow the CC relationship more closely than the curves representing the less extreme precipitation, and several of the curves have slightly steeper slopes than the CC lines in the upper ranges of temperature (just before the drop off).

Comparing results across gauges, Albany generally presents lower precipitation intensities at all percentiles (compared to the NYC metro gauges) but shows similar evidence of CC scaling.

In conclusion, hourly precipitation intensities show evidence of CC scaling over most of the temperature range, with slightly higher slopes in the upper range of temperatures (both dry-bulb and dewpoint) in which extreme precipitation intensities were observed.

Station/ Period	1955-1989	1990-2022
KBDR	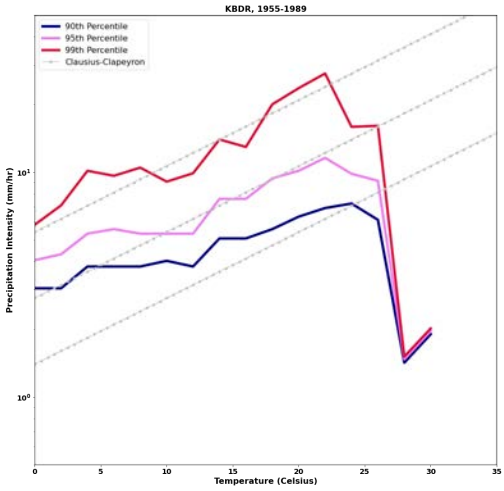	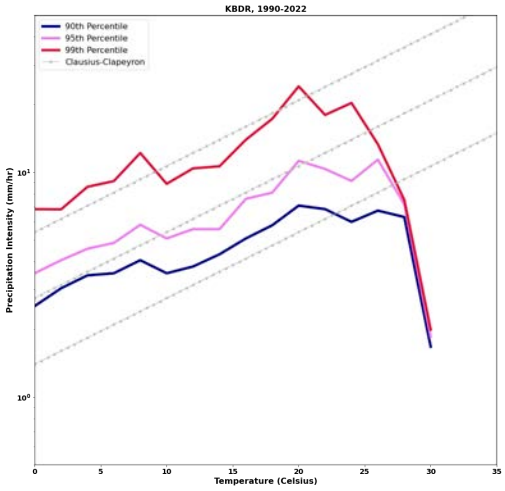
KEWR	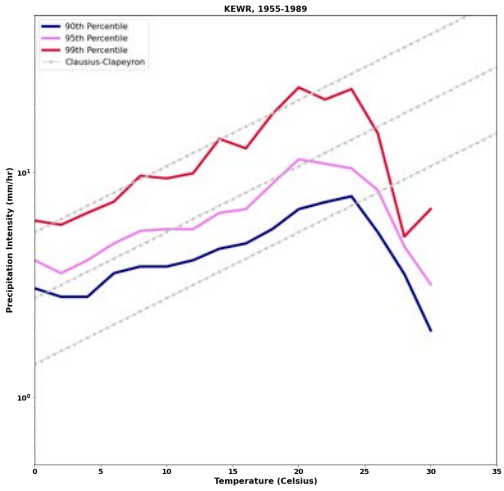	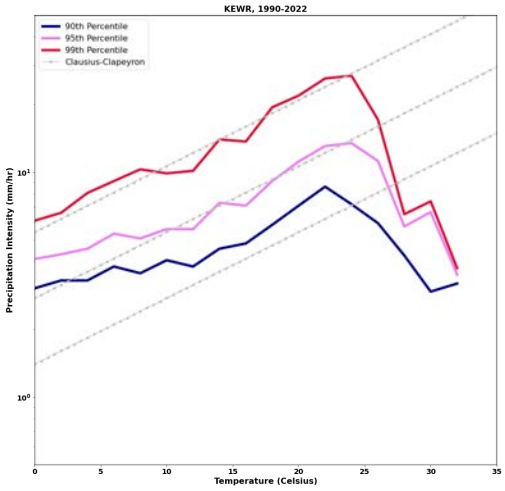

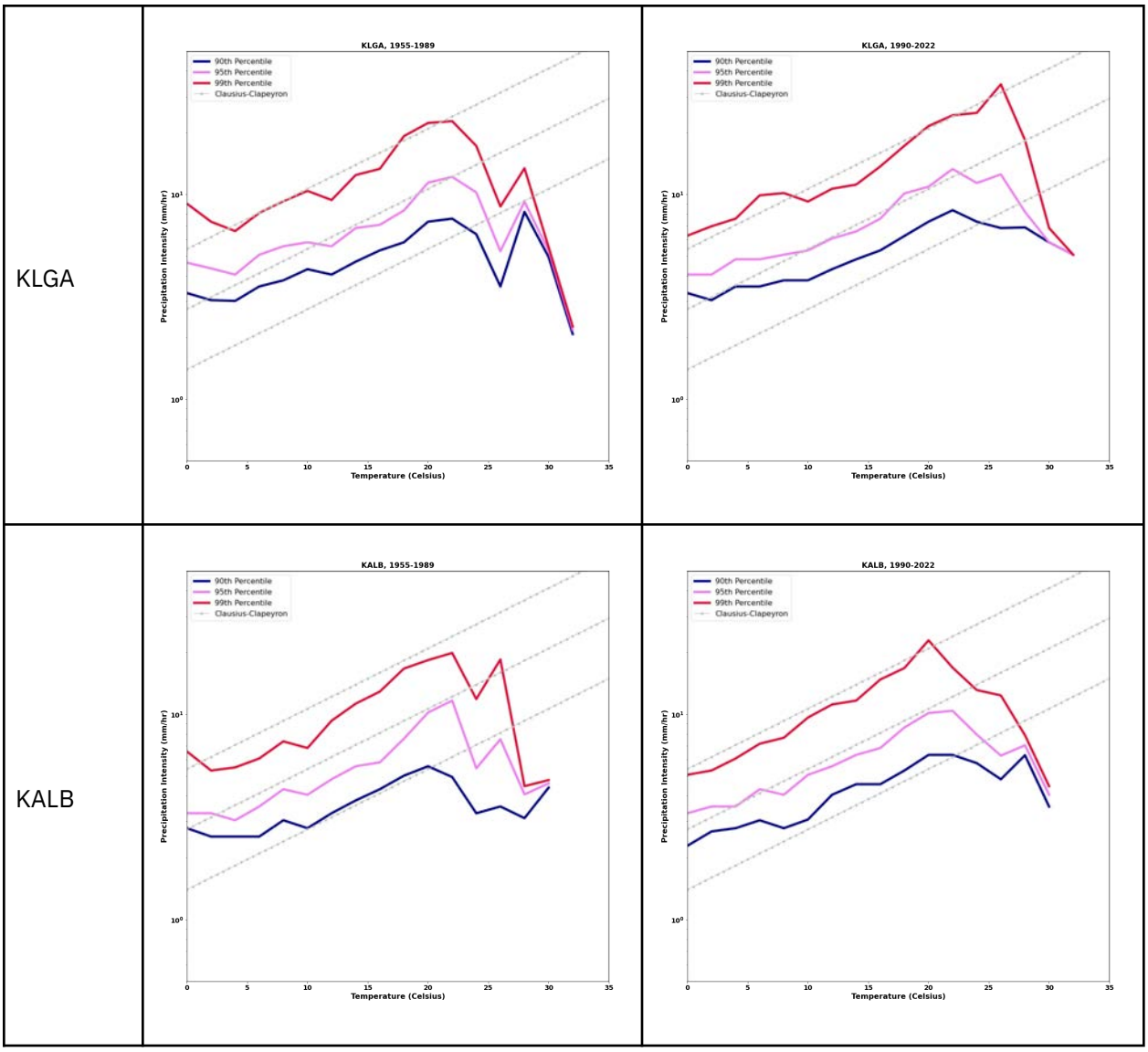

Figure 3.11: Extreme hourly precipitation intensity vs. dry-bulb temperature for distant (left) and recent (right) past.

Station/ Period	1955-1989	1990-2022
KBDR	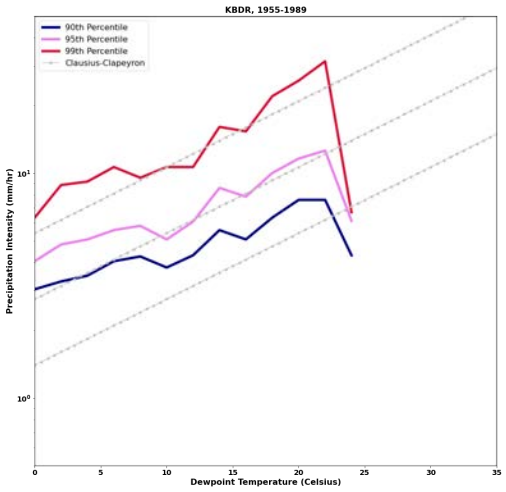	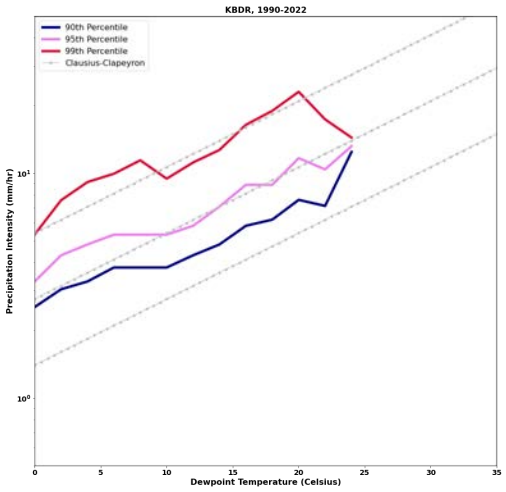
KEWR	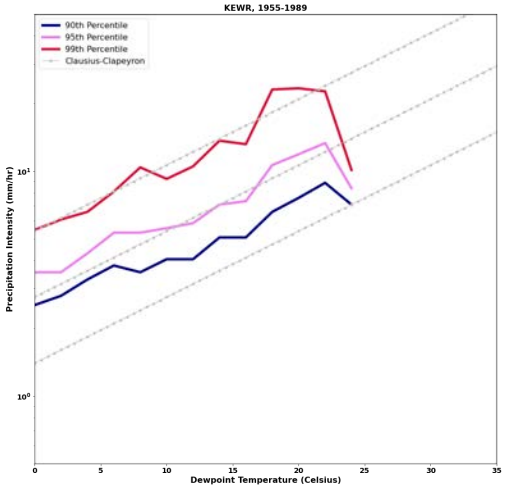	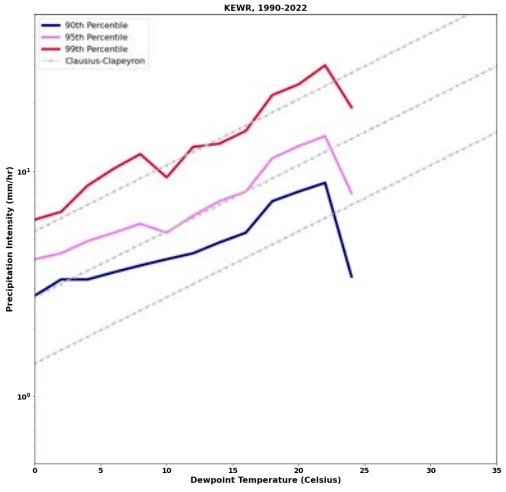

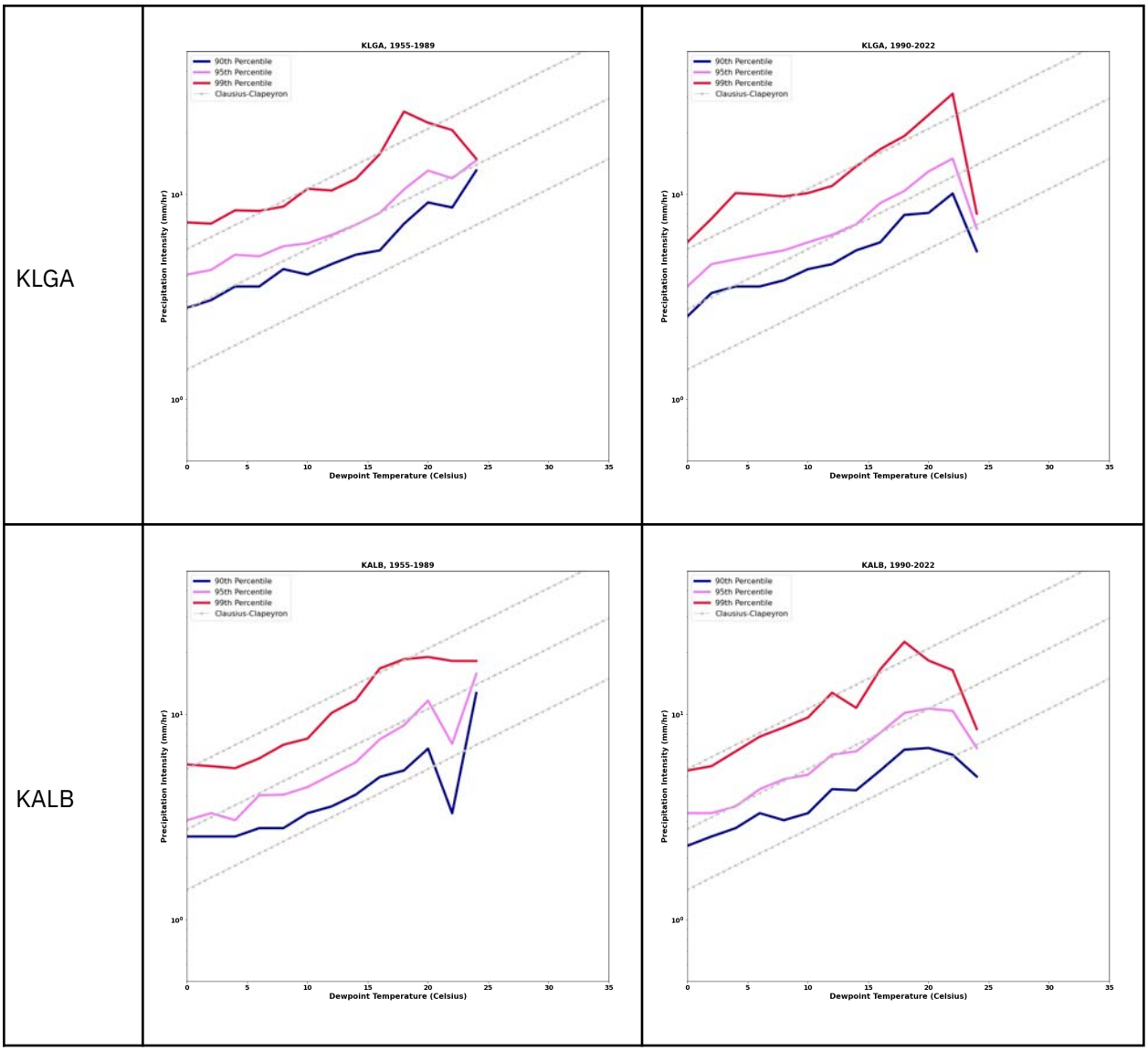

Figure 3.12: Extreme hourly precipitation intensity vs. dewpoint temperature for distant (left) and recent (right) past.

Station/ Period	1955-1989	1990-2022
KBDR	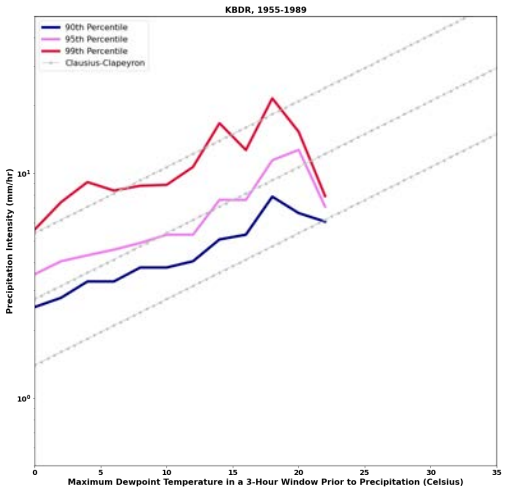	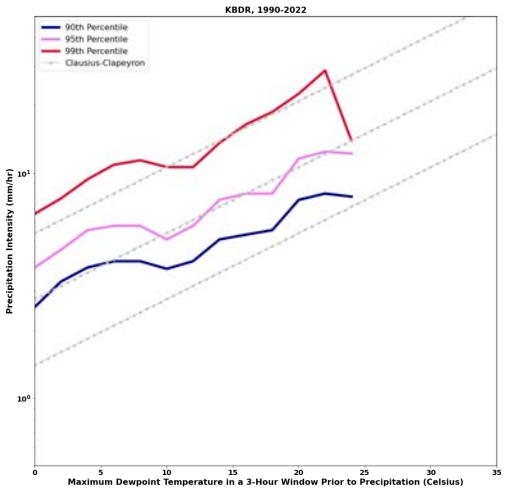
KEWR	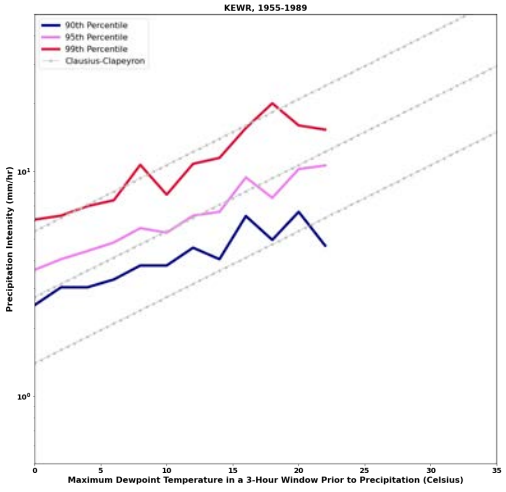	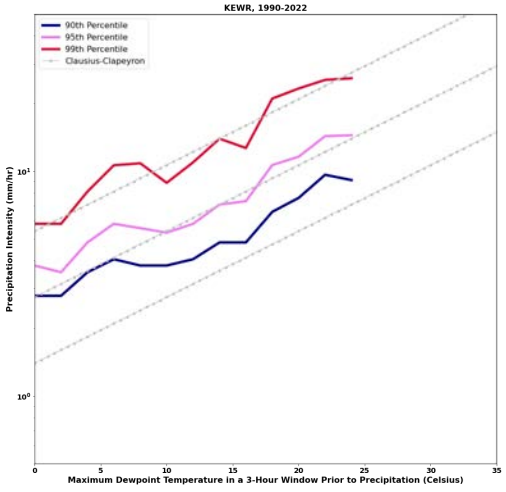

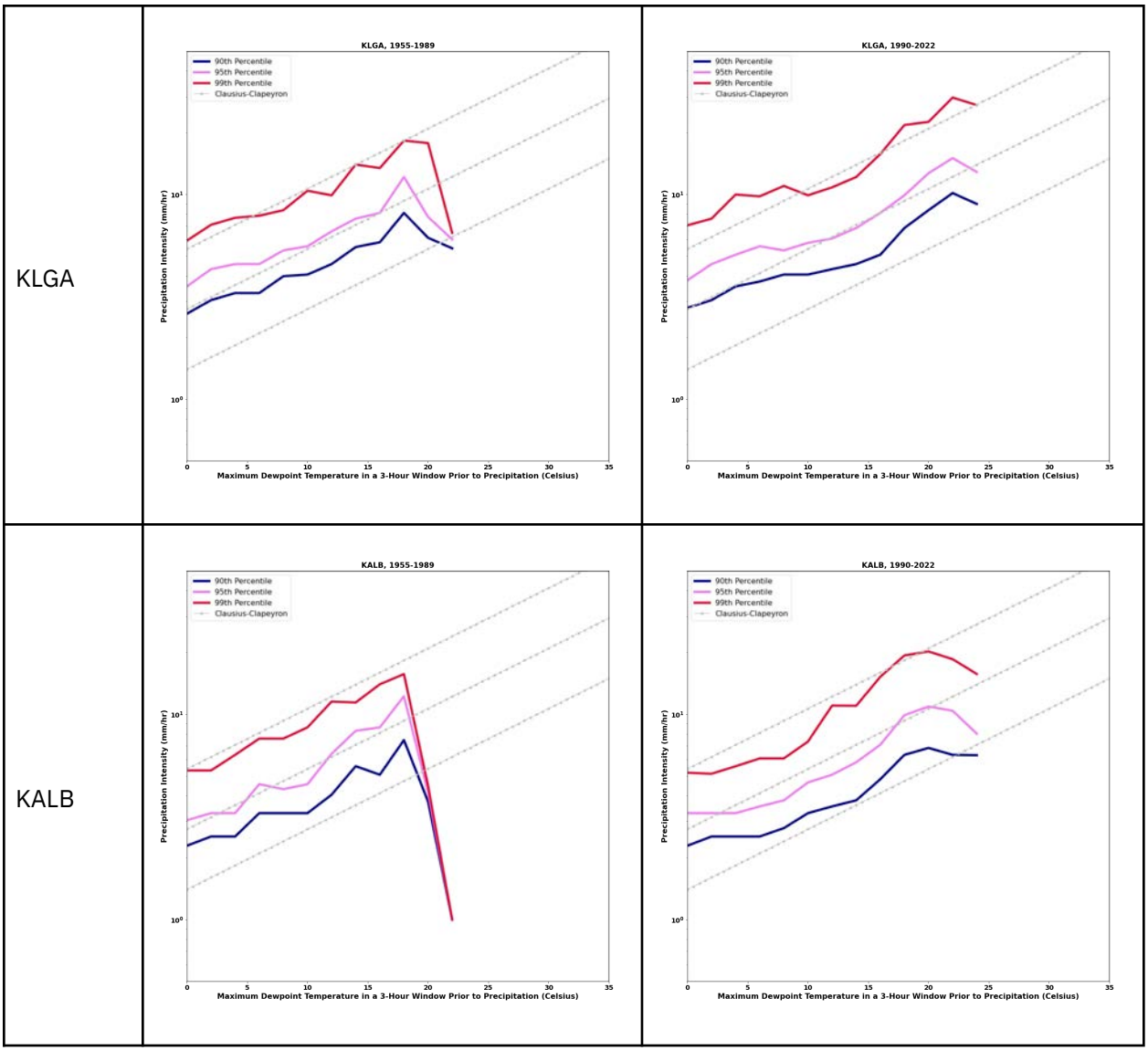

Figure 3.13: Using a three-hour window for the maximum dewpoint temperature before the precipitation occurrence.

3.7 Analysis of historical precipitation trends using non-parametric and parametric approaches

Subtask 5 quantifies historical trends in New York City extreme precipitation events. This task was challenging because, as described in Subtask 4, subdaily rainfall data is limited in availability and rainfall extremes are highly localized and not necessarily represented in the data record associated with any one particular gauge. Different approaches can be utilized to evaluate historic trends, each based on different assumptions, testing different hypotheses, and providing different levels of sensitivity. In general, parametric methods - the classical approach to development to IDF curves - are affected by tail variability, meaning that the occurrence of one or more extreme events can significantly change the extreme rainfall probabilities computed for a particular gauge. However, this approach is the most appropriate method for assessing changes in the most extreme rainfall amounts (those that on average occur less than once per year and even as infrequently as once or twice in 100 years), and is particularly necessary when inferring the probability of extreme events from relatively short data records. One or two extreme events can significantly alter the statistical distribution, especially for the most extreme rainfall values (e.g. the 100-yr. storm); thus, changes with time are best interpreted regionally rather than at any one particular station. In contrast, non-parametric methods are not based on specific assumptions about distributional form which makes them generally applicable, but less sensitive to the occurrence of specific extreme events. As such, they may not be able to detect subtle, but important temporal changes that nonetheless do occur over time. Both approaches are presented below.

a. Methods: Non-parametric analysis

The New York City Department of Environmental Protection (NYCDEP) defines precipitation events in association with discrete combined sewer overflows (CSOs). For the non-parametric trends analysis, discrete rain events were identified based on a four-hour inter-event dry period, following Restrepo-Posada and Eagleson (1982) and Yu et al. (2018). Once identified, the following attributes were assigned for each discrete event:

- Start Time
- End Time
- Peak Intensity: Maximum hourly accumulation observed between the discrete event start and end times, expressed as mm/hr. intensity
- Total Precipitation: Total event precipitation (mm)
- Duration: Duration of precipitation event (hr.)
- Average Intensity: Average intensity of precipitation event (mm/hr.) (Average Intensity = Total Precipitation/Duration)

Five different extreme precipitation events metrics were developed for this analysis. Two of the metrics were used to investigate the frequency of particular extreme event characteristics and the remainder were used to evaluate how extreme the events actually were. These metrics are listed below:

- NE95 = Number of exceedances of long-term (e.g. 1955-2022) 95th percentile value
- NE99= Number of exceedances of long-term 99th percentile value
- All Values = a precipitation event set including all the values of the event attribute from 1955 to 2022
- VE95 = a precipitation event set including the events that exceed the long-term 95th percentile values for a particular event attribute
- VE99 = a precipitation event set including the events that exceed the long-term 99th percentile values for a particular event attribute

The non-parametric Mann-Kendall test was used to test for monotonic trends in each metric over the entire period of study. Trends analysis was also performed on the number of annual events (NAA) and annual accumulated precipitation (AAP) at each gauge location.

b. Results: Non-parametric analysis

1.1 Event characteristics

Figure 3.14 includes box plots presenting the four event characteristics for each gauge, with horizontal orange lines depicting the long term 95th percentile values, and horizontal red lines depicting the long term 99th percentile values.

Albany's long-term 95th and 99th percentile values for all attributes are lower than those of the NYC metro gauges. Of the NYC gauges, Central Park has slightly higher values than the other three. The gauges with the greatest outlier values vary by event attribute.

Attribute	Events and their Long-term 95th and 99th Percentiles

Peak Intensity (mm/hr.)	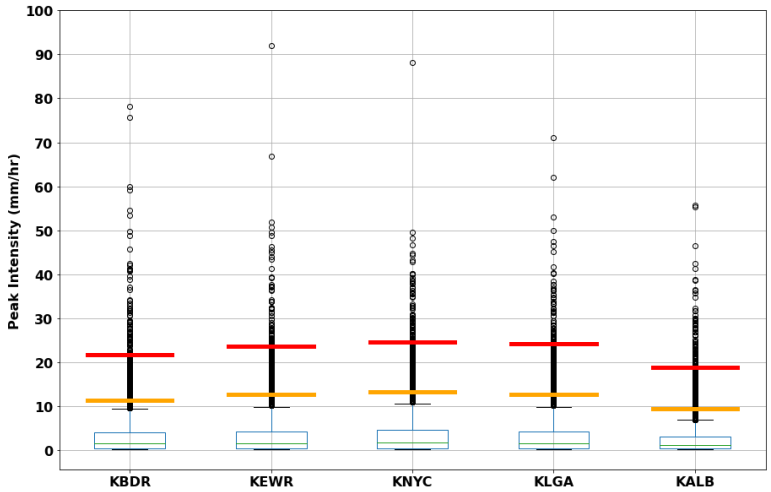
Total Precipitation (mm)	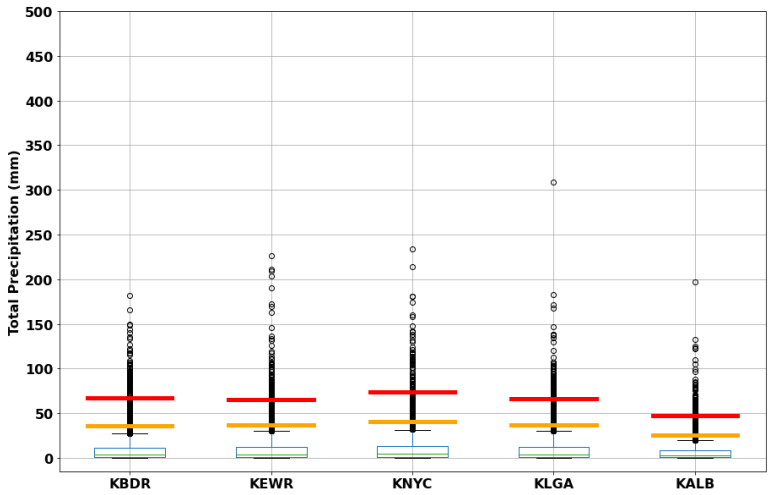

Precipitation Duration (hr.)	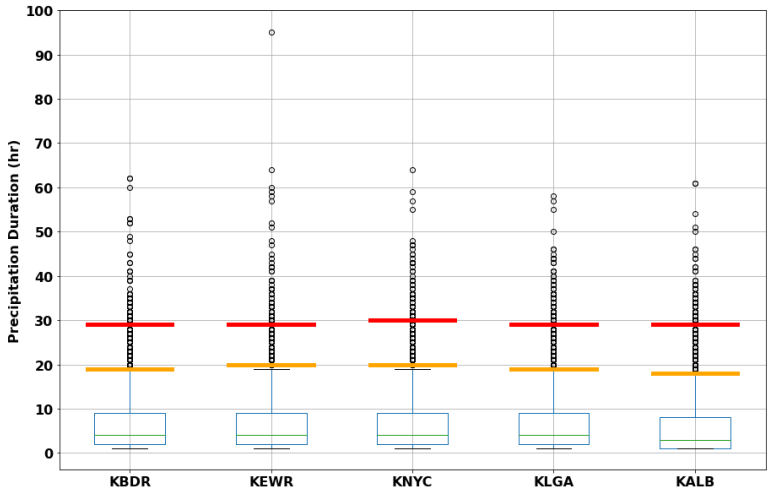
Average Intensity (mm/hr.)	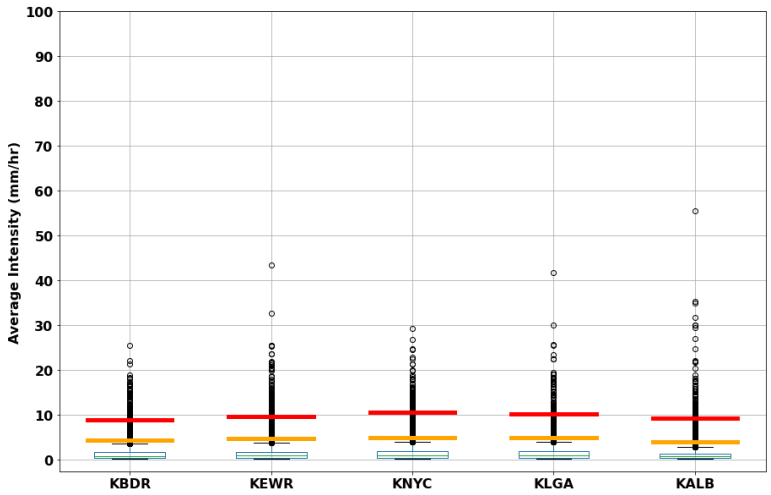

Figure 3.14: Box plots depicting events and their 95th and 99th percentiles.

1.2 Mann Kendall test results

Tables 3.5-3.9 depict the results of the Mann-Kendall test. In the tables, strongly significant results ($P<0.05$) are indicated by one asterisk and colored dark green/red for increasing/decreasing trends, respectively. Marginally significant results ($0.05<p<0.1$) are shown using two asterisks and colored light green/light red for increasing/decreasing trends, respectively.

Annual cumulative precipitation has been increasing throughout the region. The frequency of precipitation events has not been statistically changing at the NYC metro area gauges but has increased significantly in Albany and Bridgeport.

The frequency of events with >95th percentile peak and average intensities have increased significantly at all of the NYC gauges. At Newark Airport, the frequency of events with >99th percentile peak and average intensities also increased. Events with average intensities above the 99th percentile also increased at Central Park.

Statistically significant increases in the frequency of events with >95th percentile total accumulations are observed at Newark Airport and Central Park, but not at LaGuardia Airport. None of the NYC metro area gauges showed changes in the frequency of events with >99th percentile total accumulations.

Considering all events, peak and average intensities are going up throughout the NYC metro area. Event totals have increased at Newark and LaGuardia airports, but not in Central Park. Event durations have decreased in Central Park and LaGuardia, but not at Newark.

Considering only the events that exceed the 95th and 99th percentiles, the Mann Kendall test does not indicate that events are getting larger, more intense, or are changing significantly in duration.

Table 3.5: Trends in Annual Number of Precipitation Events

	NAA	AA\
KBDR	*	*
KEWR		*
KNYC		*
KLGA		**
KALB	*	*

Table 3.6: Trends in Event Peak Intensity.

	Peak Intensity (mm/hr.)				
	NE95	NE99	All Values	VE95	VE99
KBDR	*				
KEWR	*	*	*		

KNYC	*		*		
KLGA	*		*		
KALB	*	*	*		

Table 3.7: Trends in Total Precipitation Attribute.

	Total Precipitation (mm)				
	NE95	NE99	All Values	VE95	VE99
KBDR			*		
KEWR	*		*		
KNYC	**				
KLGA			*		
KALB	*	*	*		

Table 3.8: Trends in Precipitation Duration Attribute.

	Precipitation Duration (hr.)				
	NE95	NE99	All Values	VE95	VE99
KBDR			*		
KEWR					
KNYC			**		
KLGA			*		
KALB					

Table 3.9: Trends in Average Intensity Attribute.

	Average Intensity (mm/hr.)				
	NE95	NE99	All Values	VE95	VE99
KBDR			**		
KEWR	*	*	*		
KNYC	*	*	*		
KLGA	*		*		
KALB	*	*	*	**	

c. Methods: Parametric analysis

The parametric data analyses were based on partial duration series, the n largest rainfall amounts for a given duration (e.g. one-hr., 24-hours, etc.) in an n-year period. More than one partial duration series member can occur in the same year, provided they are separated by a sufficient time period (typically 14 days) to assure independence. For each station, an array of partial duration series (PDS) was generated such that the shortest PDS included data from 1950-1990 and the longest was based on data from 1950 through the most recent complete year. Additionally, we created fixed-length PDS, such that each PDS contained 50 years' worth of data, starting with 1950-1990, then 1951-1991, etc. For each PDS in the array, rainfall amounts corresponding to recurrence probabilities of 50%, 20%, 10%, 4%, 2% and 1% (i.e. 2-, 5-, 10- 25-, 50- and 100-year storms) were computed by simulating the methodology used in NOAA Atlas 14 (Bonnin et al., 2006; Perica et al., 2019). Finally, each PDS was split into an early and late period such that each year contained 46 years of data (early; 1950-1986, late; 1987-2022).

Regional L-moments were used to compute recurrence probabilities from the pds. A maximum of 20 neighboring stations was identified and formed a region around each long-term station. Neighboring stations were required to have at least 20 years of data in the 1950-present period. Sample moments were obtained for each regional station using the python lmoments[4] package (https://pypi.org/project/lmoments/) samlmu routine and a weighted average of the higher order moments computed based on the length of each station's PDS. These weighted averages along with the base station's location parameter were then used to obtain GEV

[4] In Python, lmoments refers to a statistical package used for computing L-moments, which are statistical quantities used for estimating parameters of probability distributions, particularly in hydrology, climatology, and other fields dealing with environmental data.

parameters and quantiles using the pelgev routine from the lmoments package. Other theoretical extreme value distributions exist, but the GEV has been used extensively in prior extreme rainfall analyses (e.g. Papalexiou and Koutsoyiannis, 2013). Given the L-moments estimates for the GEV parameters, the lmoments library method was used to obtain the specified quantiles of the GEV distribution.

The same analysis was performed on the CORDEX models, but note that due to the resolution, Central Park and LaGuardia are on the same grid, so there were only four stations analyzed with the CORDEX data; Central Park, JFK, Newark, and Bridgeport, CT.

d. Results: Parametric analysis

1. Observations

All stations in the study region show increasing precipitation amounts across most return periods and hourly durations (Figure 3.15; see Technical Supplement for additional figures). Figures showing results from the Central Park stations are provided as an example in this report, with additional station figures in the supplemental material. Across all stations, the 1950-2022 POR precipitation amount is higher than the 1950-1990 POR across most return periods (Figure 3.15; see Technical Supplement)). For example, the two-year return period hourly precipitation amount is roughly 5% larger for the 1950-2022 POR compared to the 1950-1990 POR (Figure 3.15).

Across the studied stations, there is a consistent pattern of increasing percent change for higher return periods. As shown in the Technical Supplement and for all hourly durations, the percent change for the 100-yr. return period is higher than the percent change for the 50-yr. return period, which is in turn higher than the percent change for the 25-yr. return period, etc. The lines for the different return periods rarely cross through time.

We also see a general decrease in percent change with precipitation duration (e.g. one-hour vs. 24 hour) across the stations and return periods. In Figure 3.15A, which shows the percent change in return periods for one-hour precipitation events for Central Park, the percent change between the 100-year return period for 1950-2022 and 1950-1990 is over 20% (pink line). Now, looking at the percent change in the 100-yr return period for the three-hour event (Figure 3.15C, pink line), the value drops to about 13%. And by the 24-hour duration (Figure 3.15F) the percent change is down to about 7%. The other stations show a similar, though less pronounced pattern, which is summarized in the Technical Supplement.

It should be noted in Figure 3.15 that the pattern of change in return period rainfall amounts computed for the increasing pds records from 1950-1990 through 1950-2022 is not smooth, but rather shows several distinct jumps. These jumps are associated with the occurrence of rainfall events that are among the highest in the pds. For example, the return periods at Central Park jump in 2021 following the occurrence of Hurricane Ida, which was associated with the highest rainfall total in the one-hour pds. The time series are also characterized by periods of slow decline in the recurrence interval rainfall amounts (e.g. between 2010 and 2020 in Figure 3.15). During these periods, the new rainfall amounts added to the pds are among the smallest, and given the increase in the number of years included in the pds, recurrence probabilities decline slightly. Despite this, from 1990-2022, predominantly larger rainfall events are included in the pds leading to a net increase in extreme rainfall intensities, at all New York City stations. A histogram comparing three PORs 1950-1990, 1950-2010, and 1950-2022 is shown in Figure 3.17 for Central Park. Across all hourly durations, the most extreme precipitation amounts tend to occur in the later 1950-2022 time series.

Hourly recurrence interval precipitation amounts have generally increased more than daily value at Central Park when comparing the 1950-1985 and 1986-2022 periods in the observational record (Figure 3.17, see Technical Supplement for additional figures), but this is not reflected across the larger region and it is not reflected in modeled data (Technical Supplement). The increase seen here, but not seen regionally, is therefore likely an artifact of Hurricane Ida in 2021. Additionally, we've found the percentage of the 24-hour total that falls during one-hour is increasing in more recent years compared to the earlier part of the record (Figure 3.18). This finding is statistically significant at Central Park and marginally significant at the other New York City stations. It is not clear what is responsible for this change. The large one-hour percentages seem to occur for both tropical and non-tropical weather systems. Additionally, we find the percentage of one-hr. pds members that correspond to storms also included in the 24-hour duration pds has not changed over time. Approximately 23% of the 24-hour pds members include one-hour pds members.

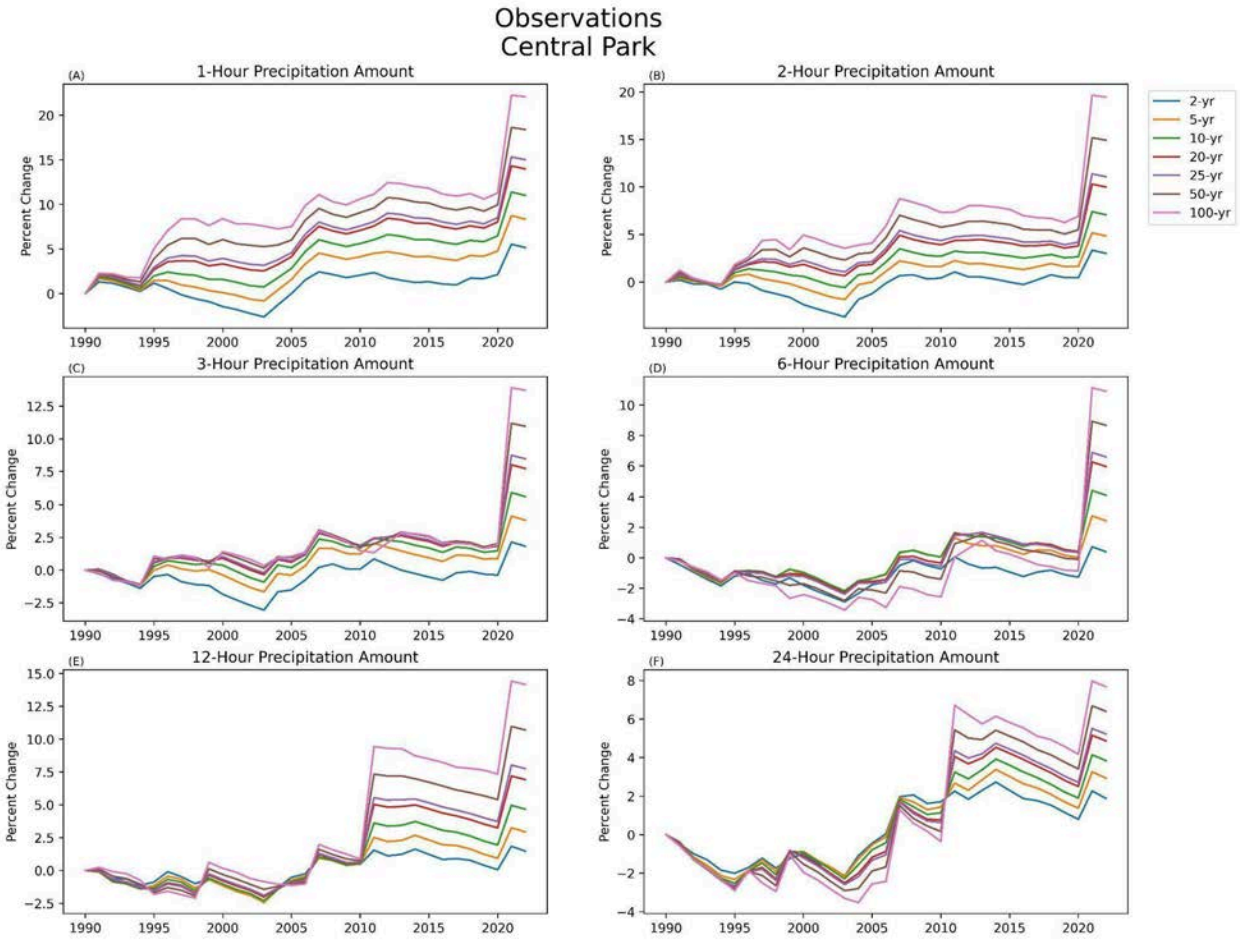

Figure 3.15: Percent change in hourly recurrence interval precipitation amounts relative to the 1990 POR (1950-1990) for PORs with sequentially more years included (1950-1990, 1950-1991, etc.) for 1-, 2-, 3-, 6-, 12-, and 24-hour precipitation (Panels A-F). The 2-, 5-, 10-, 20-, 25-, 50-, and 100-year storm values are plotted in the colored lines.

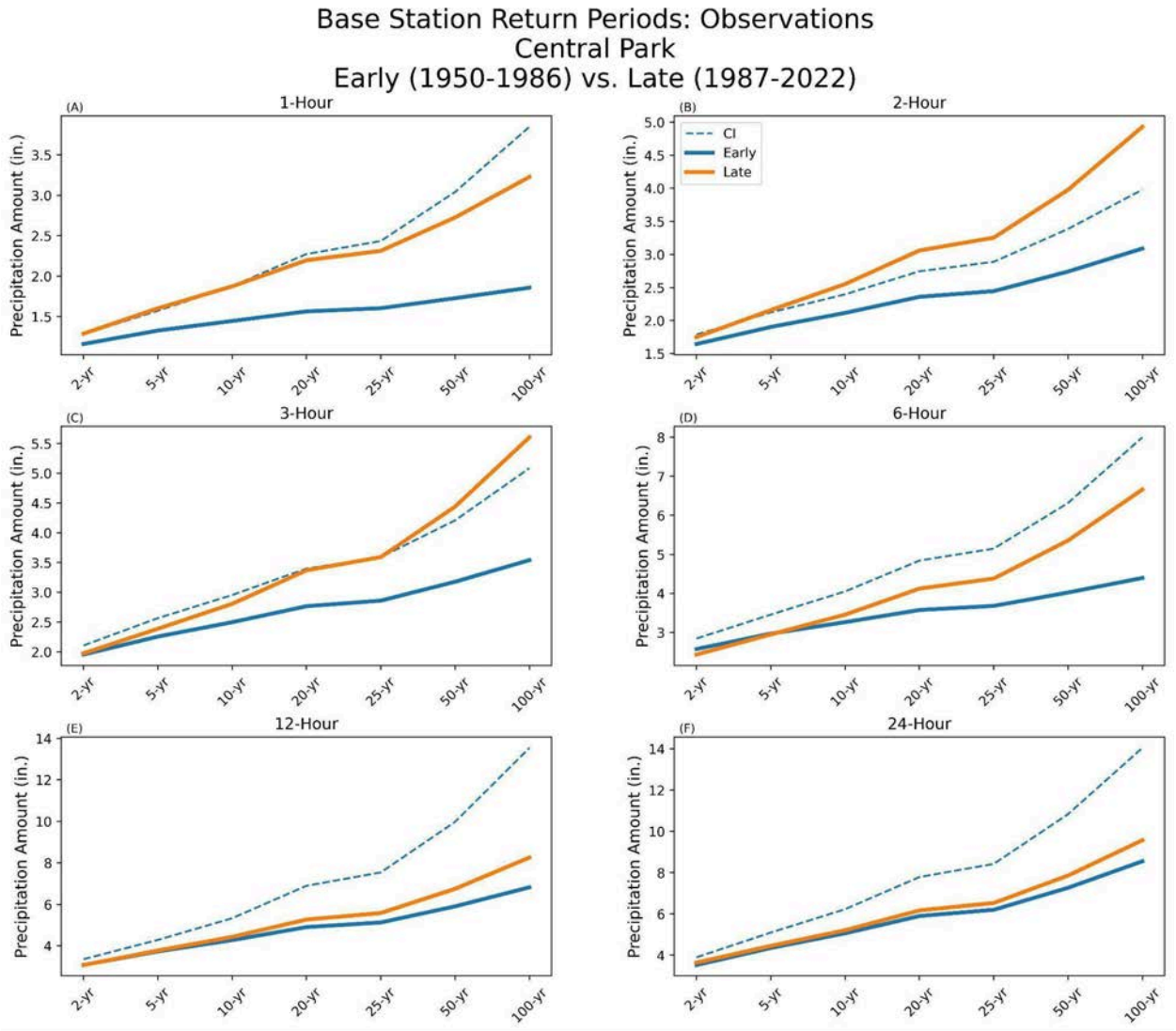

Figure 3.16: Return period (x-axis) for 1-, 2-, 3-, 6-, 12-, and 24-hour precipitation amounts (Panels A-F) based on two time periods. 1950-1986 (blue solid line) represents the early period while 1987-2022 (orange solid line) represents the late period. The blue dashed line is the 90% confidence interval for the 1987-2022 period of record.

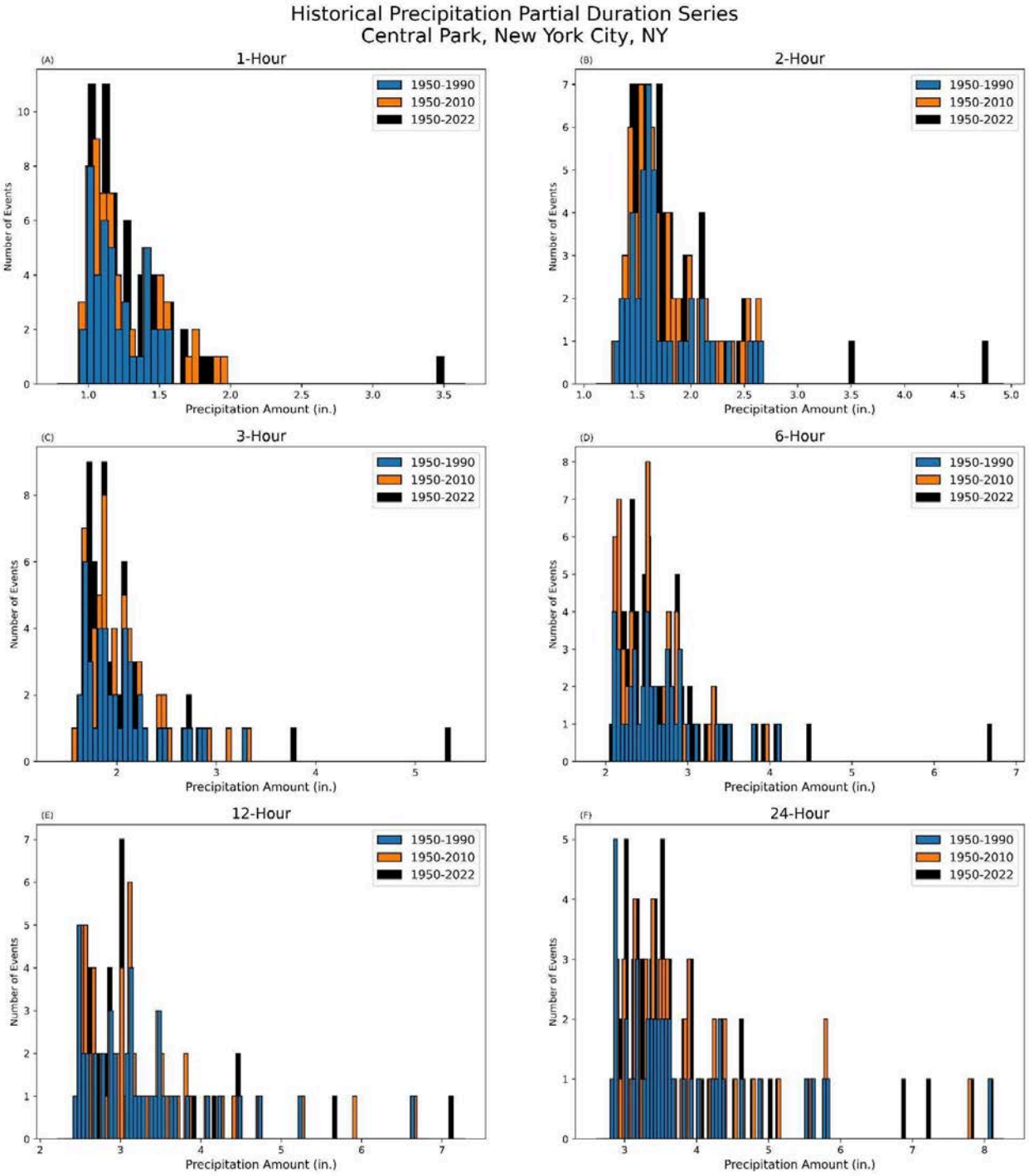

Figure 3.17: Histogram of hourly precipitation total from Central Park pds, comparing different hourly precipitation durations (panels A-F) for three subsets of years; 1950-1990 (blue), 1950-2010 (orange), and 1950-2022 (black).

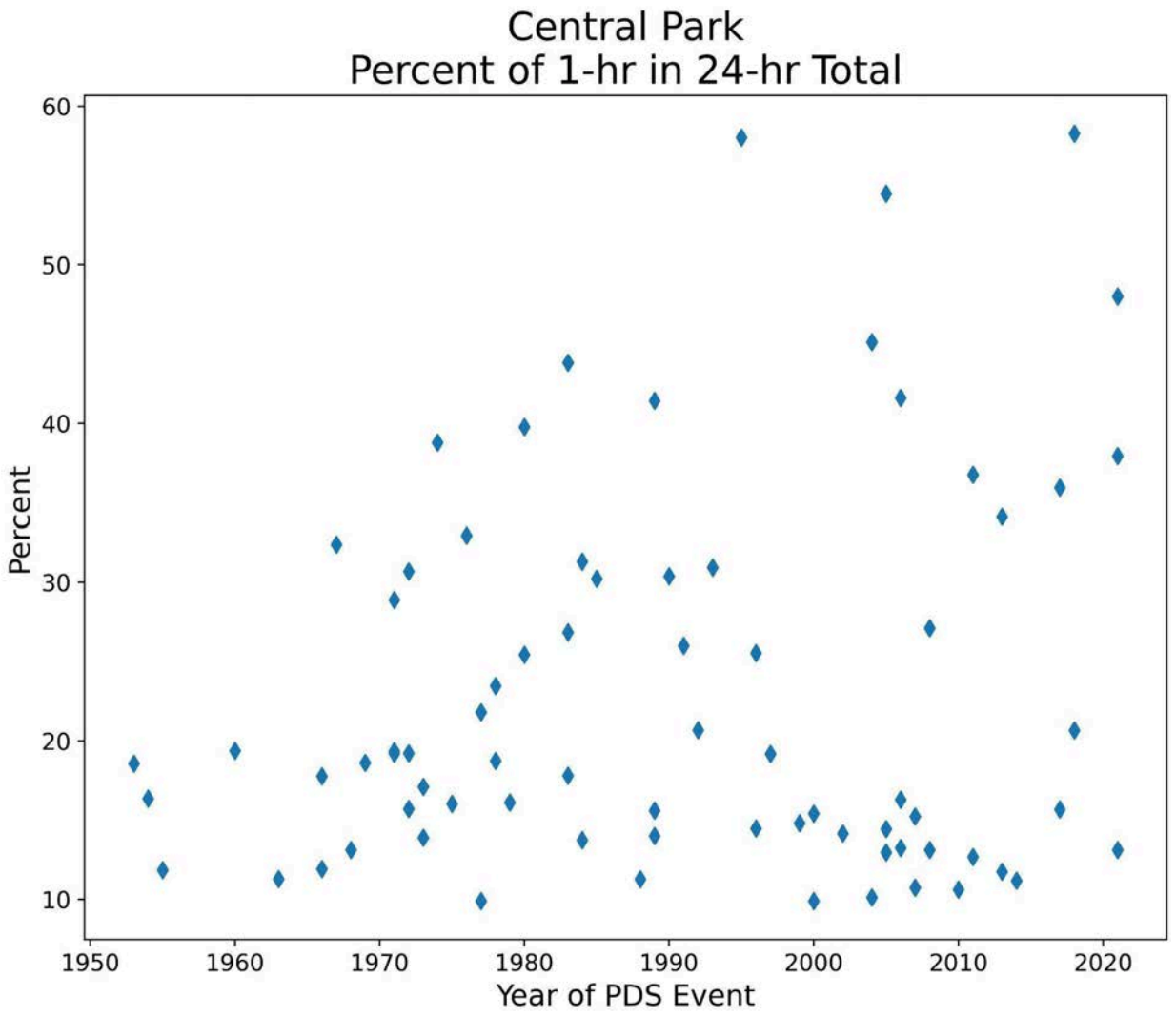

Figure 3.18: Scatterplot of the percentage of each 24-hr precipitation total that occurs during the one-hr. period with the largest precipitation occurrence for the 73 pds members in the 1950-2022 period of record.

3.8 Future IDF Curve Projections

a. Methods

Future intensity duration frequency (IDF) curves were generated using downscaled climate model data from the Localized Constructed Analogs version 1 (LOCA1) (Pierce et al., 2014) and version 2 (LOCA2) (Pierce et al., 2023) datasets. LOCA2 uses statistical downscaling techniques on coarse resolution (~250km) global climate model (GCM) output from the Coupled Model Intercomparison Project Phase 6 (CMIP6) to create high resolution (6km) future projections of temperature and precipitation. LOCA downscaling takes coarse resolution GCM data and a high-resolution observational data set from which to train on and uses a matching scheme to find corresponding analog days between the two to create the high-resolution, downscaled data (Pierce et al., 2023).

The two main differences between LOCA1 and LOCA2 are the input GCM data and the precipitation training data. LOCA1 downscaled CMIP5 whereas LOCA2 downscaled the aforementioned CMIP6. LOCA1 used an observational dataset from Livneh et al. (2015). However, additional analyses on this dataset discovered a bias in the strength of daily rain extremes which resulted in unrealistically weak values (Pierce et al., 2023). LOCA2 uses Pierce et al. (2021), which is believed to correct the bias seen in Livneh et al. (2015) and better represent daily rain extremes (Pierce et al., 2023). At the time of this research, 31 downscaled CMIP5 models and 21 downscaled CMIP6 models had available precipitation data for this study. Those models and their affiliations are broken down in Table S3.6.1 (CMIP5) and Table S3.6.2 (CMIP6) in the supplementary information.

Overall, a total of six GCM experiments were analyzed for this study. For CMIP5, the historical period covers 1950-2005. Its future climates are based on the representative concentration pathways (RCP) scenarios that represent medium-low emissions (RCP4.5) and high emissions (RCP8.5) future climates. For CMIP6, the historical period covers 1950-2014, and its two future scenarios (2015-2099) under the shared socio-economic pathways (SSP) that represent low emission (SSP245) and high emission (SSP585) future climates.

Additionally, our analysis was focused on four stations in the New York City area: Central Park, LaGuardia Airport, John F. Kennedy Airport, and Newark Airport. Future change factors were computed relative to observational data from Atlas 14 (Bonnin et al., 2006). The National Oceanic and Atmospheric Administration (NOAA) Atlas 14 dataset consists of subhourly, hourly, and daily precipitation frequency estimates over the United States (Perica et al., 2013).

The precipitation data are obtained from a network of over 8,700 precipitation gauges which are operated by state agencies and the National Weather Service. Statistical techniques are employed to estimate the frequency of precipitation events of varying intensities. The period of record (POR) for the Central Park station spans 1869 to present, while the POR for the LaGuardia and JFK stations span 1948 to present, and the Newark station spans 1931-present.

Future IDF curves were developed from change factors based on the following steps:

1. Obtain partial duration series (PDS) of the *n* largest independent daily precipitation events for each of the four stations, downscaling methods, GCMs, and emissions scenarios.
2. Compute recurrence interval precipitation amounts by fitting the generalized extreme value (GEV) distribution to each pds as was done for the parametric historical analysis.
3. Compute change factors for each station and emissions scenario based on the fit recurrence interval rainfall amounts.
4. Create future IDF curves based on the change factor and Atlas 14 data for each station and emissions scenario using the mean and 75th, 83rd, and 90th percentiles of the ensemble of models.

Step 1 – Partial Duration Series

Extreme rainfall events were extracted separately from each downscaled model and are based on the partial duration series (PDS) (Madsen et al., 1997) of the dataset. Using PDS, the *n* largest independent precipitation events are extracted, where *n* represents the number of available years of record. PDS are used as the basis of this work, given this method's widespread application (e.g. Cook et al., 2017; DeGaetano and Castellano 2017; Lopez-Cantu et al., 2020; Ragno et al., 2018; Thakali et al., 2016; Wu et al., 2019) and to ensure the inclusion of all relevant extreme rainfall events projected in the downscaled climate simulations. PDS were created for both emissions scenarios and the historical period for each model from LOCA1/LOCA2.

For each PDS, rainfall amounts corresponding to recurrence probabilities of 50%, 20%, 10%, 4%, 2% and 1% (i.e. 2-, 5-, 10- 25-, 50- and 100-year storms) were computed by simulating the methodology used in NOAA Atlas 14 (Bonnin et al., 2006; Perica et al., 2019). First, the python lmoments package (https://pypi.org/project/lmoments/) was used to fit the generalized extreme value (GEV) distribution to each grid point's PDS using the methods of Hosking (1990). Although not the only valid theoretical distribution for estimating extreme rainfall probabilities, the use of the GEV has been standard practice in prior extreme rainfall analyses (e.g. Papalexiou and Koutsoyiannis, 2013). Given the L-moments estimates for the

GEV parameters, the lmoments library quagev method was used to obtain the specified quantiles of the GEV distribution.

Step 2 – Change Factors

After the 24-hour rainfall depths were calculated for each of the return periods, the research team used these values to calculate IDF curve change factors. Change factors represent the change signal between the historic and future period in climate projections. Change factors are calculated based on the quantile delta method (QDM), in which changes between historic and future values are estimated separately by quantiles: discrete segments within a probability distribution (Cannon et al., 2015; Switzman et al., 2017). IDF curves are already calculated based on recurrence probabilities of 50 percent, 20 percent, 10 percent, 4 percent, 2 percent, and 1 percent, so the QDM or change factors are therefore a ratio of the future time-period 24-hour rainfall depth for a given recurrence interval to the historic modeled 24-hour rainfall depth for the same recurrence interval. Equation 1 shows the change factor calculation for a two-year rainfall event for the 2015-2099 high emissions future time-period.

$$Change\ factor = \frac{2yr,24hr\ rainfall\ (future)}{2yr,\ 24hr\ rainfall\ (hist)} \quad (1)$$

The change factor calculation was carried out for each recurrence interval, each station, each downscaled climate model dataset (LOCA1 and LOCA2), each GCM, and each emissions scenario. Ultimately, change factors representing the ensemble mean (mean across all models) and the 75th, 83rd, and 90th percentiles of the ensemble were retained.

For each grid-model-RCP/SSP combination, an ensemble of 1,000 simulations was also constructed via a resampling procedure. From the GEV distribution fit to the original downscaled future period PDS, 1,000 50-member PDS were randomly selected using the scipy genextremer vs function. A new GEV distribution was fit to each random PDS, retaining the original regional average of the higher order moments, and the resulting 2-, 5-, 10-, 25-, 50- and 100-year recurrence interval precipitation amounts used to compute 1000 random change factors. Ultimately, change factors representing the ensemble mean (mean across all models and resampled pds) and the 75th, 83rd, and 90th percentiles of this ensemble were retained.

Step 3 – IDF Curves

Because change factors are essentially a scalar between the historic period and the future period of interest, with the same baseline period as Atlas 14 and the underlying data derived in the same way as Atlas 14, they can be directly multiplied by the Atlas 14 values for the respective recurrence interval to obtain the climate adjusted future IDF curves for each station. This method was used to create IDF curves for each station, from each downscaled climate model dataset, for each GCM within the datasets and for both RCP4.5 and RCP8.5 from the LOCA1 dataset and SSP245 and SSP585 from the LOCA2 dataset.

b. Results

CMIP5 vs. CMIP6 Change Factors

Across the four stations (Central Park, JFK Airport, LaGuardia Airport, and Newark Airport), the change factors seen in CMIP6 tend to be larger than those in CMIP5 in both the lower and high emissions scenarios (Figure 3.19, see Technical Supplement for additional figures). Again, results for Central Park are displayed here with additional stations in the supplemental information. This is particularly evident at the longer return periods. For Central Park, the CMIP6 change factors are marginally lower than CMIP5 for the two-yr. return period, but by the five-yr. return period, the CMIP6 values exceed beyond the CMIP5 50% confidence intervals and remain high, with an exception for the 50-yr. return period (Figure 3.19A-B). For both JFK and LaGuardia Airports, CMIP6 change factors exceed CMIP5 change factors across all return periods, and sit outside the CMIP5 50% confidence interval for about half of the return periods (see figures in Technical Supplement). While Newark's CMIP6 two-yr. return period change factor is lower than CMIP5, like Central Park, CMIP6 then exceeds CMIP5 for the remaining returning periods. However, Newark is the only station where all CMIP6 change factors are within the 50% confidence interval of CMIP5 (Technical Supplement). Tables with all calculated change factors, along with the 10th, 17th, 25th, 75th, 83rd, and 90th percentiles are available in the supplemental information.

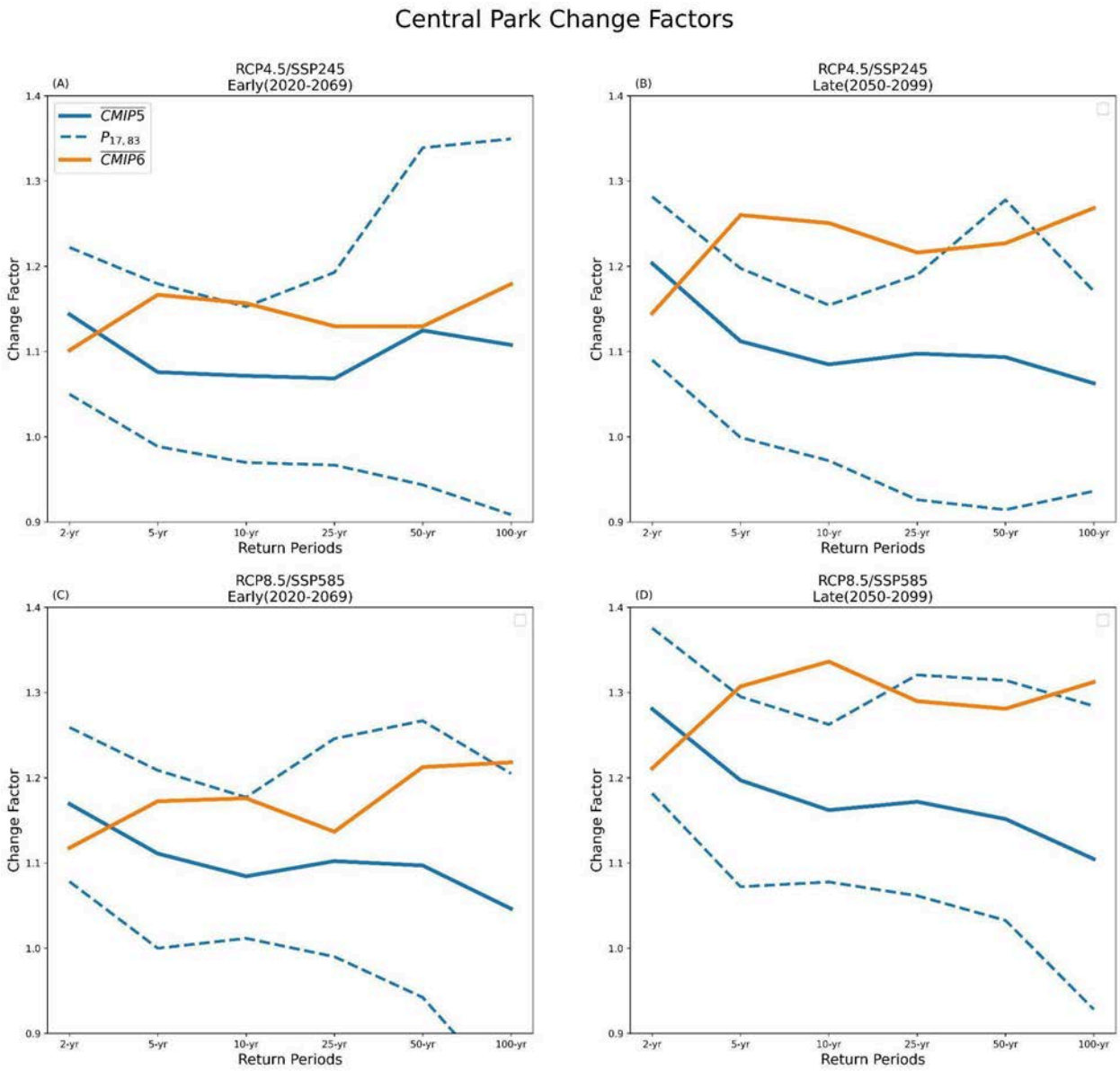

Figure 3.19: LOCA and LOCA2 change factors for Central Park. Panels A and B show the ensemble mean change factors for CMIP5 emissions scenario RCP4.5 (lower emissions) (solid blue line) and the 17th and 83rd percentiles (dashed blue lines) for an early future period (2020-2069) and a late future period (2050-2099). CMIP6 change factors for emissions scenario SSP245 are plotted in the solid orange line. Panels C and D plot the same values but for the higher emissions scenarios, RCP8.5 (CMIP5) and SSP585 (CMIP6).

IDF Curves

The projected intensity-duration-frequency curves reflect the increase in change factors from LOCA1 to LOCA2. IDF curves for the two-yr. and 100-yr. return period and emissions scenarios (RCP4.5/SSP245 and RCP8.5/SSP585) for Central Park are plotted in

Figures 3.20 and 3.21. Figures for the additional stations and return periods are in the supplemental material. The IDF curves are rain depth (in inches) versus the duration (in hours). While the IDF curves for LOCA2 are greater than LOCA across all scenarios and return periods for all stations, the LOCA1 curves do fall within the 50% confidence interval for LOCA2. For all stations, the LOCA1 and LOCA2 curves for the two-yr. return period are essentially the same (Figure 3.20). The separation between LOCA1 and LOCA2 occurs starting with the five-yr. return period.

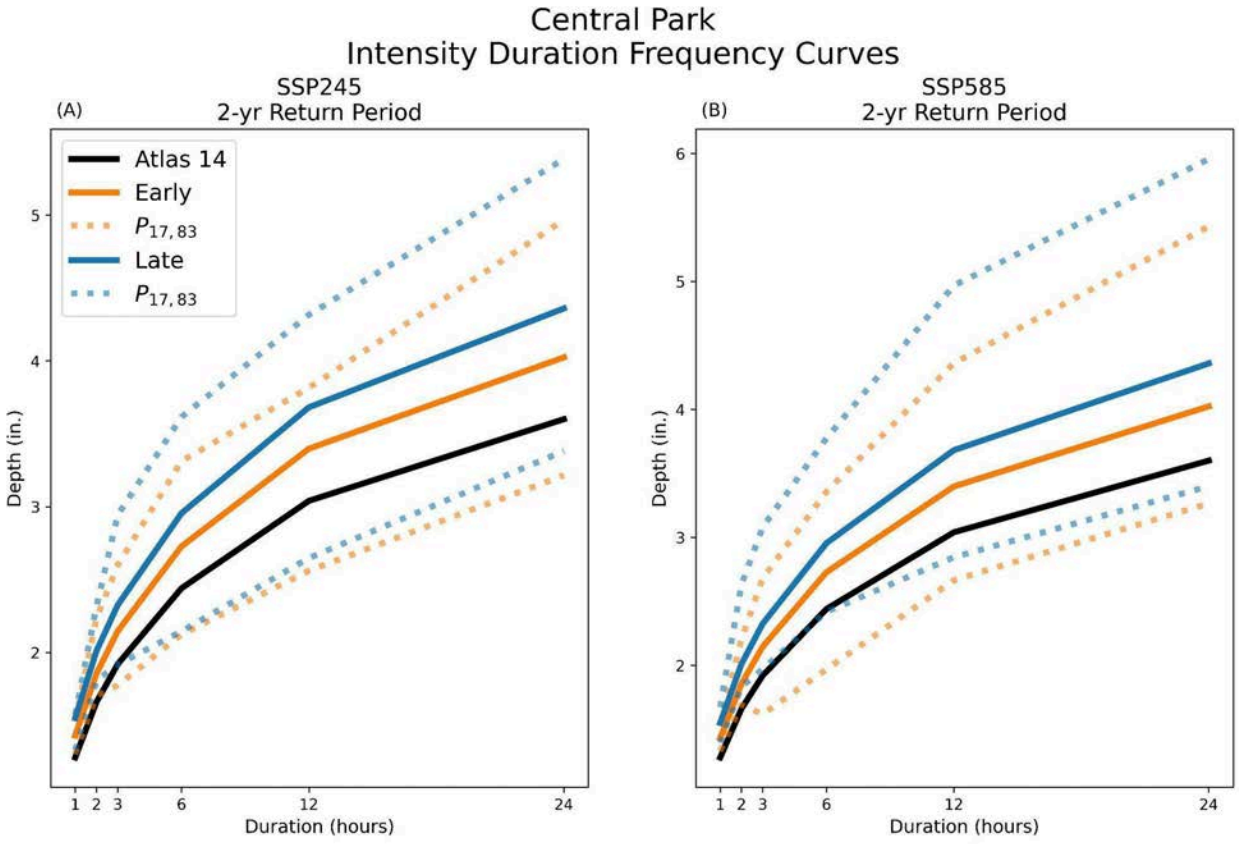

Figure 3.20: IDF curves for the Central Park station, comparing observations from Atlas 14 (black solid line), and LOCA2 early (2020-2069, orange solid lines), and LOCA2 late (2050-2099, blue solid lines). The 17th and 83rd percentiles are plotted on the dotted lines. The results for future emissions scenarios SSP245 and SSP585 are plotted in panel A and B, respectively.

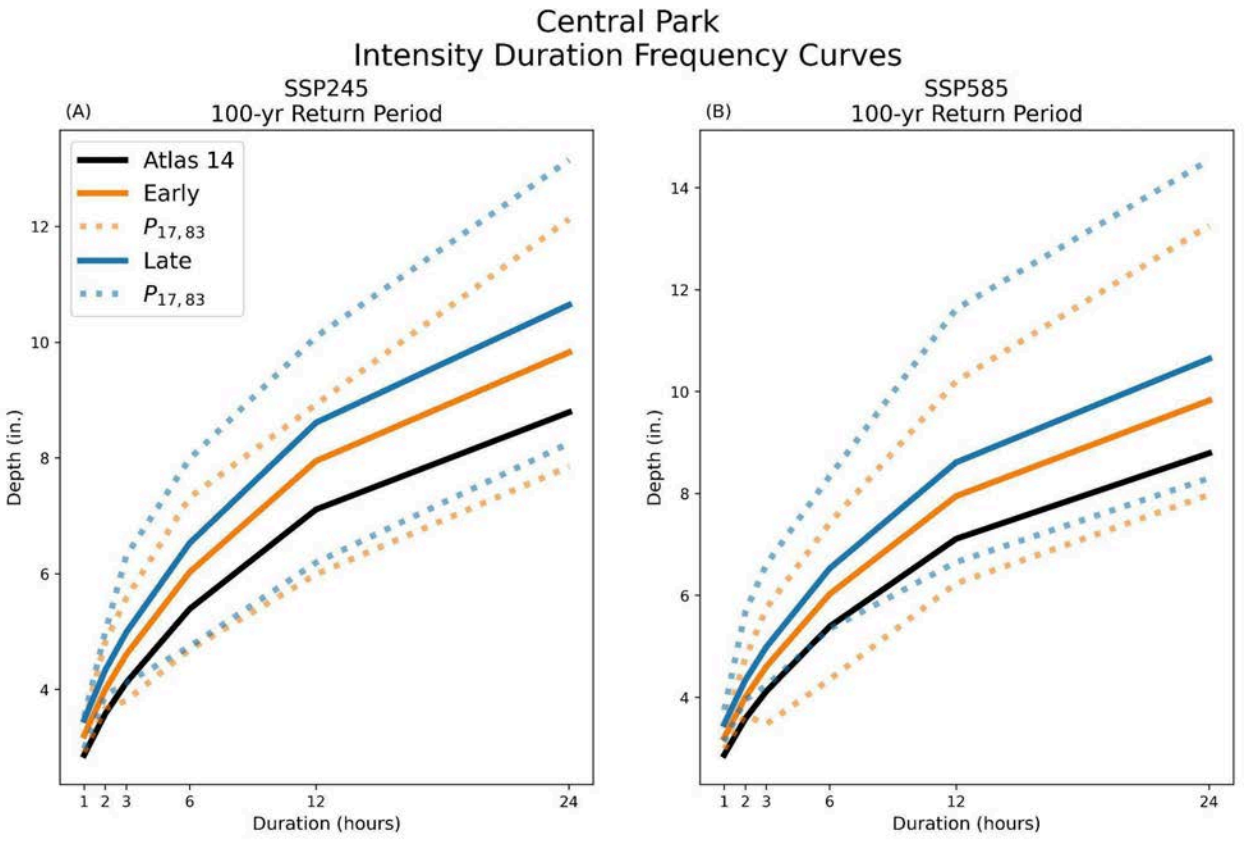

Figure 3.21: As in Figure 3.20 but for the 100-yr. return period.

Summarized Change Factors

Spatial variations in change factors between grid points associated with specific stations are likely an artifact of the downscaling process, especially in coastal areas like New York City, where grid points in the global models reflect different coastal borders and land water contrasts. Although the statistical resampling helps to smooth some of these variations, a regional average of the points representing the New York City stations is a more robust measure of the change in extreme rainfall over the City. These citywide average change factors are shown for high ssp585 and lower ssp245 emissions scenarios in Tables 3.10 and 3.11. In practical application, the values listed in these tables provide the necessary adjustment to convert values obtained from Atlas 14 to values that reflect the climate conditions of the 2020-2069 and 2050-2099 time periods. As such, they provide the basis for the hydrologic and hydraulic modeling analyses conducted under Subtask 3.7.

Table 3.10: Citywide average change factors for early (2020-2069) and late (2050-2099) time periods under high ssp585 emissions.

SSP585 EARLY:	2020-2069					
PERCENTILE	**2-yr**	**5-yr**	**10-yr**	**25-yr**	**50-yr**	**100-yr**
10th	1.04	1.00	0.93	0.82	0.79	0.84
25th	1.11	1.08	1.09	1.02	1.06	0.98
Mean	1.18	1.21	1.23	1.18	1.21	1.23
75th	1.24	1.27	1.39	1.34	1.42	1.44
83rd	1.27	1.35	1.42	1.40	1.46	1.53
90th	1.35	1.46	1.45	1.43	1.52	1.64
SSP585 LATE:	**2050-2099**					
PERCENTILE	**2-yr**	**5-yr**	**10-yr**	**25-yr**	**50-yr**	**100-yr**
10th	1.15	1.09	1.07	1.01	0.97	0.93
25th	1.18	1.17	1.16	1.09	1.07	1.05
Mean	1.28	1.32	1.35	1.32	1.30	1.30
75th	1.39	1.46	1.59	1.53	1.47	1.56
83rd	1.41	1.55	1.61	1.58	1.59	1.63
90th	1.45	1.59	1.64	1.67	1.68	1.75

Table 3.11: City-wide average change factors for early (2020-2069) and late (2050-2099) time periods under a lower ssp245 emissions scenario.

SSP245 EARLY:	2020-2069					
PERCENTILE	**2-yr**	**5-yr**	**10-yr**	**25-yr**	**50-yr**	**100-yr**

10th	1.04	1.02	0.97	0.85	0.84	0.84
25th	1.09	1.07	1.08	1.02	0.94	0.95
Mean	1.16	1.20	1.19	1.16	1.14	1.17
75th	1.20	1.27	1.25	1.27	1.29	1.29
83rd	1.26	1.35	1.34	1.37	1.35	1.39
90th	1.32	1.44	1.44	1.46	1.44	1.58
SSP245 LATE:	**2050-2099**					
PERCENTILE	**2-yr**	**5-yr**	**10-yr**	**25-yr**	**50-yr**	**100-yr**
10th	1.08	1.08	1.04	0.91	0.88	0.87
25th	1.14	1.14	1.14	1.06	1.03	1.05
Mean	1.22	1.28	1.28	1.23	1.24	1.26
75th	1.28	1.40	1.37	1.35	1.36	1.40
83rd	1.31	1.44	1.51	1.45	1.43	1.52
90th	1.34	1.47	1.61	1.58	1.56	1.64

3.9 Hydrologic and Hydraulic Modeling to Evaluate Implications of Design Hyetograph Assumptions and Future IDF Curves on Pluvial Flooding in New York City

Hydrologic and Hydraulic (H&H) modeling was conducted in support of two objectives:

1. **Evaluate the impact that hyetograph assumptions have on flooding for present-day rainfall:** To simulate a rainfall event in a dynamic H&H model, a rainfall hyetograph is required that distributes the total rainfall depth specified from the IDF curve over the specified duration. There are many hyetograph shapes that can be used and appropriate choice of a hyetograph (or multiple) is an important consideration for any H&H modeling application (research, planning, design, funding, etc.).
2. **Evaluate changes in flooding as a result of increasing rainfall with climate change:** The primary objective of the H&H modeling was to assess how increased precipitation from climate change (see Subtask 6) may impact flooding. Selection of a hyetograph was an input to this assessment.

a. Methods

Evaluate the impact that hyetograph assumptions have on flooding for present-day rainfall

To assess pluvial-driven sewer-system flooding in New York City, models developed by the NYC Department of Environmental Protection (NYC DEP) as part of the Citywide Stormwater Engineering Analysis and Planning Region 2 (CSEAP-2) project were utilized. These models are 1-D models developed using Innovyze InfoWorks Integrated Catchment Model (ICM) software. They represent all sewers above 30 inches in diameter, and include higher-resolution (i.e. sewers less than 30") in lower-lying areas.

The CSEAP-2 models were calibrated to in-sewer flow monitoring data following the Chartered Institution of Water and Environmental Management (CIWEM) calibration standards for in-sewer peak flows, total volume, and peak depths. The flow monitoring period ranged from two-four months depending on flow meter location. The rainfall events captured range from less than one-year return periods to 46-year return periods, including significant rainfall events such as the predecessor rain event associated with Tropical Storm and Henri and Post Tropical Cyclone Ida.

Figure 3.22: Study areas for H&H modeling.

CSEAP-2 model simulations were conducted for two study drainage areas: the Jamaica Water Resources Recovery Facility (WRRF) Drainage Area and the Rockaway WRRF Drainage Area (Figure 3.22). The DEP Bureau of Water and Sewer Operations (BWSO) 24-hr. Symmetric Hyetograph, which was developed by the BWSO to design new city sewers, was selected as the baseline hyetograph for the precipitation analyses per discussion with Interagency Collaborators members (BWSO, 2023). This hyetograph is composed of six-minutes of uniform intensity rainfall centered at the halfway point and of two gradually changing tails of lower-intensity precipitation that the area under the curve (rainfall depth) for any duration event matches the TP-25 IDF Curve (U.S. Weather Bureau, 1955) (U.S. Department of

Commerce, 1955). Figure 3.23, below depicts the hyetograph for the 10-yr. and 100-yr. present-day events.

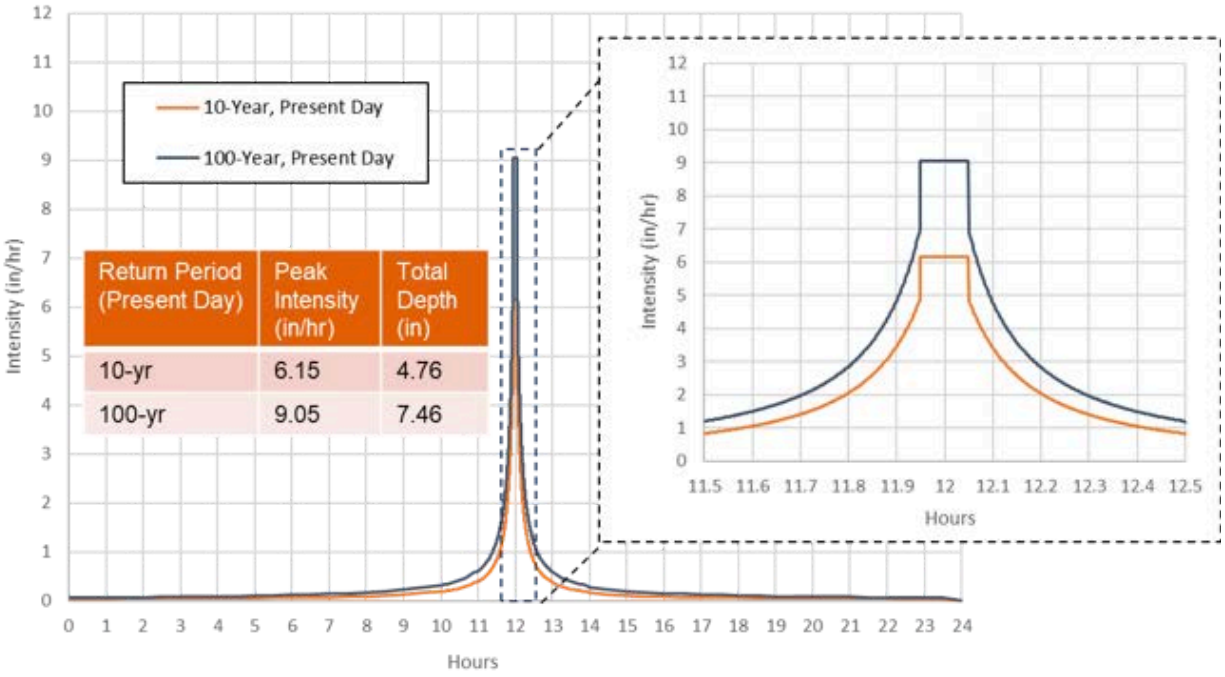

Figure 3.23: Hyetograph for the 10-yr and 100-yr present-day events.

Based on discussions with Interagency Collaborators members and the SSC (see Subtask 3.2), two additional design hyetographs commonly-used in the NYC-area were chosen for comparison with the DEP BWSO Symmetric Hyetograph:

- The NOAA Atlas 14 hyetograph: Atlas 14 hyetograph shapes are commonly used in engineering practice to distribute a total rainfall depth over a target storm duration. Atlas 14 Volume 10, Northeastern Region 2 (Coastal) covers the NYC area and was used for the hyetographs in this analysis. Four quartile distributions are available to choose from, and within each quartile, the 10% to 90% occurrence probabilities are provided, in 10% increments. Atlas 14 suggests that the choice of quartile and percent-occurrence should be based on model application and/or comparison to historic storms. The team found no recommended standards specific to NYC for choosing a specific shape (see Subtask 3.1). For the purposes of this study, all four quartiles were assessed, using both the 50% and 90% occurrence probabilities.
- The Soil Conservation Service (SCS) Dimensionless Unit Hydrograph, Type III distribution: Type III aligns with the NYC region per TR-55).

All hyetographs were assumed to be 24 hours in duration to allow for comparison with the BWSO 24-hour Symmetric Hyetograph. The total rainfall depth represented by the Atlas 14 and SCS hyetographs is that associated with a 10-yr., 24-hr. storm for Central Park.

Table 3.22: NOAA Atlas 14 quartiles for 50% and 90% temporal distributions for the 10-year, 24-hour storm.

10-yr, Atlas 14, 24-hr*		Rainfall Metrics	
Temporal Distribution	Quartile	Peak Intensity (in/hr)	Total Rainfall Depth (in)
50%	Q1	0.59	5.6
	Q2	0.54	5.6
	Q3	0.47	5.6
	Q4	0.57	5.6
90%	Q1	0.42	5.6
	Q2	0.52	5.6
	Q3	0.56	5.6
	Q4	0.90	5.6

*ICM-Generated Atlas 14 design storms. Peak intensities vary slightly relative to manually calculated Atlas 14 hyetograph.

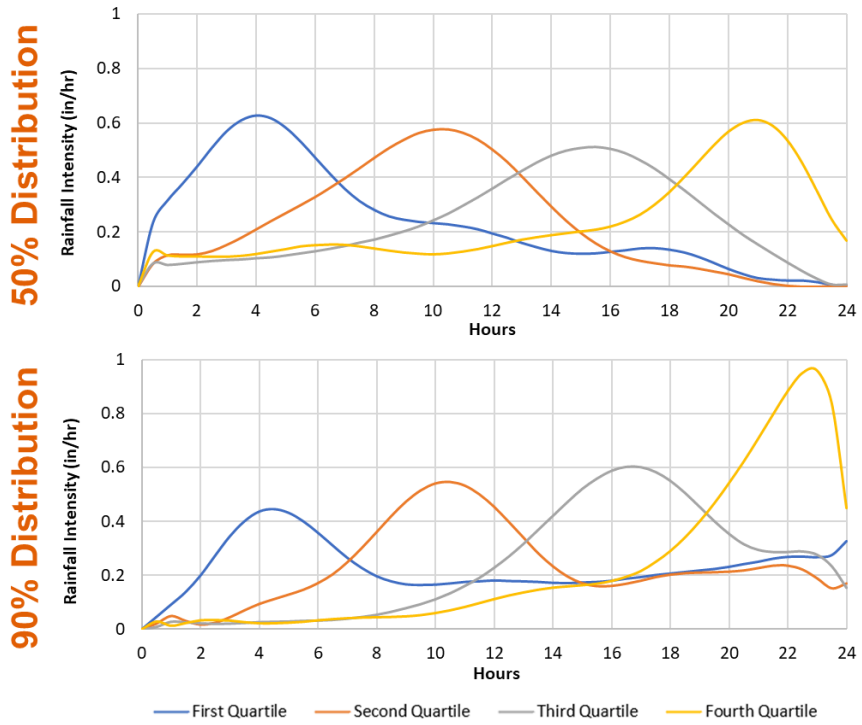

Figure 3.24: NOAA Atlas 14 quartiles for 50% and 90% temporal distributions for the 10-year, 24-hour storm.

Table 3.13: Parameters of commonly used hyetographs and simulated in the H&H models.

Rainfall (10-year, 24-hr, Present Day) [Hyetograph source | Temporal Distribution | Quartile]			Peak Intensity (in/hr)	Total Rainfall Depth (in)
BWSO Symmetric Hyetograph			6.15	4.76
ATLAS	50%	Q2	0.58	5.6
	90%	Q4	0.96	5.6
SCS (Type-III per TR-55)			4.72	5.6

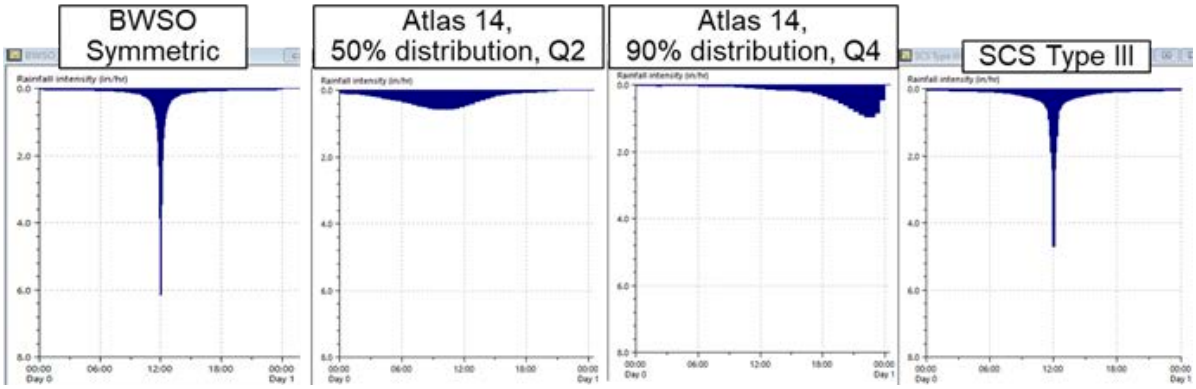

Figure 3.25: Shape of hyetographs simulated in the H&H models.

Evaluate changes in flooding as a result of increasing rainfall with climate change

The BWSO Symmetric Hyetograph present-day 10-yr. and 100-yr. return periods were chosen as the baseline hyetographs for this assessment per discussion with Interagency Collaborators members. Increased precipitation with climate change was represented using the change factors developed through Subtask 3.6.

Table 3.14: Climate scenarios and change factors used to represent increased precipitation in H&H modeling analyses.

Climate Change Factors and Percent Change for Station-Averaged Climate Models Using Late Period (2050-2099)			
Climate Scenario	**Return Period**	**Change Factor**	**Percent Change**
SSP245	10-yr	1.2800	28.00%
	100-yr	1.2575	25.75%
SSP585	10-yr	1.3525	35.25%
	100-yr	1.2975	29.75%

Table 3.15: Projected 24-hour rainfall totals after applying each change factor. Change factors were applied consistently to each timestep.

24-Hour Total Rainfall Depth for BWSO Symmetric Hyetograph Under Present-Day Conditions and Projected Conditions Using Station-Averaged Climate Models			
Return Period	**Present Day Total Depth (in)**	**SSP245 Late Period (2050-2099) Total Depth (in)**	**SSP585 Late Period (2050-2099) Total Depth (in)**
10-yr	4.76	6.09	6.44
100-yr	7.46	9.38	9.68

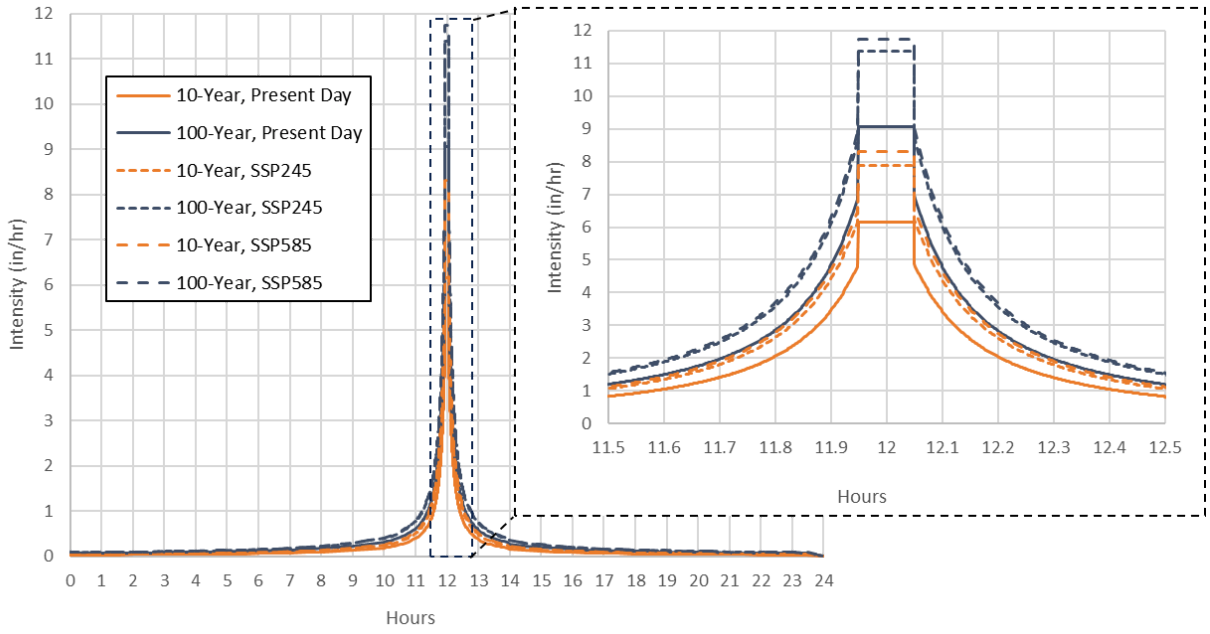

Figure 3.26: The six hyetographs used in H&H modeling climate change analysis. These hyetographs are all based on the BWSO 24-hour Symmetric Hyetograph.

b. Results

Evaluate the impact that hyetograph assumptions have on flooding for present-day rainfall

H&H modeling (detailed in the Methods section) comparing NOAA Atlas 14 hyetographs using different probabilities and quartile distributions show that, if using the 50% occurrence probabilities, the relative impact of choosing different quartile distributions on flooding is minimal. However, if using the 90% occurrence probability, the impact of quartile distribution is more significant. Under this 90% occurrence probability, Quartile 4 results in significantly more flooding. These observations are relatively consistent across the two drainage areas studied.

Table 3.16: Modeled flooding results comparing quartile distributions and occurrence probabilities of NOAA Atlas 14 hyetographs.

10-yr, Atlas 14, 24-hr		Jamaica-WRRF		Rockaway-WRRF	
Temporal Distribution	Quartile	% Change in Number of Flooded Nodes Relative to 50% Q1	% Change in Flood Volume Relative to 50% Q1	% Change in Number of Flooded Nodes Relative to 50% Q1	% Change in Flood Volume Relative to 50% Q1
50%	Q1	-	-	-	-
	Q2	1%	18%	1%	23%
	Q3	-27%	-14%	-26%	-6%
	Q4	-2%	-9%	-3%	-3%
90%	Q1	-65%	-44%	-66%	-46%
	Q2	-28%	-30%	-34%	-21%
	Q3	3%	18%	4%	21%
	Q4	174%	195%	126%	145%

Modeling comparing three different types of hyetographs indicates that the SCS type hyetograph produces similar results to the BWSO Symmetric Hyetograph and that the two chosen Atlas 14 shapes produce significantly less flooding. Similar to the prior analysis, trends are relatively consistent across both neighborhoods.

Table 3.17: Comparison of modeled flooding results for three types of hyetographs.

Rainfall (10-year, 24-hr, Present Day) [Hyetograph source | Temporal Distribution | Quartile]			Jamaica-WRRF		Rockaway-WRRF	
			% Change in Flooded Nodes Relative to BWSO	% Change in Flood Volume Relative to BWSO	% Change in flooded Nodes Relative to BWSO	% Change in Flood Volume Relative to BWSO
BWSO			-	-	-	-
ATLAS	50%	Q2	-87%	-80%	-82%	-71%
	90%	Q4	-66%	-50%	-60%	-42%
SCS (Type-III per TR-55)			-6%	1%	-7%	0%

Evaluate changes in flooding as a result of increasing rainfall with climate change

H&H modeling results indicate increases in flooded locations due to climate change (represented by SSP2545 and SSP585) are smaller than increases in flooded volume. Trends are generally consistent across both study areas, although the Jamaica drainage area had a greater impact in the number of flooded nodes due to climate change than the Rockaway drainage area. Compared to the present-day conditions, this impact in the number of flooded nodes is greater for the 10-yr. storm than the 100-yr. storm, likely due to the 10-yr. storm being closer to the target design level-of-service of sewers (typically three-five-yr. return period in New York City).

Table 3.18: Modeled flooding results for 6 precipitation scenarios

BWSO Symmetric Hyetograph	Climate Scenario	Jamaica WRRF		Rockaway WRRF	
		% Change in Number of Flooded Nodes	% Change in Flood Volume Relative	% Change in Number of Flooded Nodes	% Change in Flood Volume
10-year	Present Day		-		-
	SSP245 (28%)	**24%**	**79%**	**7%**	**79%**
	SSP585 (35.25%)	**29%**	**100%**	**8%**	**102%**
100-year	Present Day		-		-
	SSP245 (25.75%)	**13%**	**53%**	**7%**	**59%**
	SSP585 (29.75%)	**14%**	**62%**	**9%**	**69%**

Note: All percentages shown were calculated relative to present-day flood results for the same return period

When comparing these results with those of the prior two analyses, results indicate the choice of an Atlas 14 design hyetograph shape vs. a BWSO or SCS-type shape can have impacts on flooding in the same order-of-magnitude as those due to anticipated increases in rainfall from to climate change.

The results also show increases in flood volume exceed increases in precipitation (Figure 3.27). This is likely due to the fact that a large portion of the baseline precipitation is handled

by existing drainage infrastructure (closer to design level-of-service), but all additional rainfall is above the capacity of the existing system.

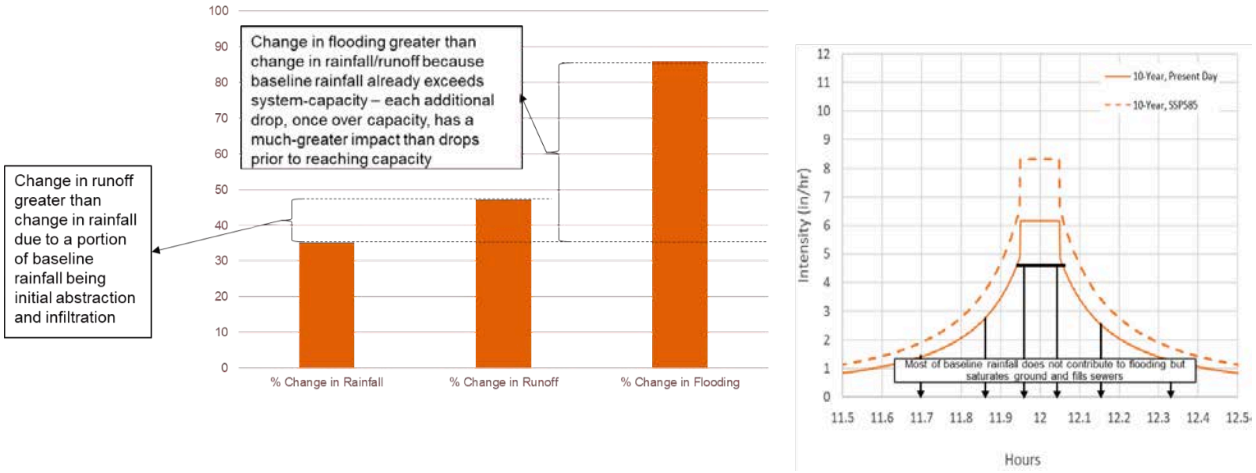

Figure 3.27: Modeled percent change in runoff, rainfall and flooding.

c. Recommendations

Results indicated the shape of rainfall distribution (the hyetograph) has a significant impact on flooding, but the research team was unable to identify any overarching policy or standard in New York City that specifies use of specific hyetographs for the broad range of ongoing and future research, planning, and engineering initiatives. Although several design hyetograph shapes were assessed in this study, future research is recommended to develop a broad policy or standard that will guide practitioners in New York City on which type of design event hyetograph (or combination of multiple events and/or use of historic storms) to use for each application. This guidance should consider the project goals (risk assessment, master planning, funding application, infrastructure design, etc.), project budget (assessing more events increases project engineering costs), and level-of-service goals, if applicable. In addition to hyetograph shape, the guidance should also identify the event duration and return period, or combinations, that should be assessed. Future research can incorporate assessment of the rainfall distribution during historic events in New York City to help inform this policy.

We were unable to identify any standardized practices for downscaling typical 24-hour design events to durations less than or equal to one hour in duration. The team considered using Atlas 14's shortest-provided rainfall distribution (the six-hour event) and downscaling it proportionally to a one-hour and/or 30-minute event but was unable to identify a scientific recommendation that supported this approach. To advance future assessment in New York City of short-duration cloudburst type rainfall events, as opposed to more traditional and standard

24-hour events, additional research is recommended to develop the sub one-hour hyetographs that can be used in policy making and engineering planning and design.

3.10 Recommendations for Future Research

1. Analysis of recently developed radar-rainfall products could help the City determine the necessary spatial density of high temporal frequency (e.g. 1 minute) precipitation gauging stations across the city.
2. The City should invest resources to centralize, quality control, warehouse, develop procedures to maintain and facilitate access to precipitation data so it is available to governmental and non-governmental stakeholders, and so policy and codes reference the same information and can be easily updated.
3. The database should be dynamic, with key trends and figures updated as new observations are produced, and climate projections are published.
4. The City should develop guidance for H&H modeling regarding event duration and return period, as well as the characteristics (e.g. type, interval, temporal distribution, duration) of design event hyetographs that are used for different types of analyses (e.g. risk assessment, master planning, funding application, infrastructure design, etc.), project budgets (assessing more events increases project engineering costs), and level-of-service goals (e.g. flooding, MS4, CSO, etc.).
5. Climate model projections consistently show increases in future design storms of 15-30% through the 21st century. Such changes should be factored into storm water design guidance.
6. Procedures should be put in place to routinely evaluate future IDF projections as new downscaling techniques are developed and newer generations of climate models become available.
7. Research is needed to quantify the types of weather systems responsible for different rainfall intensities, how these weather types (e.g. hurricanes) are projected to change in the future and how these events impact the parametric extreme value distributions used to derive design storms.
8. The meteorological mechanisms most responsible for subdaily rainfall extremes should also be quantified to refine the assumptions regarding similar changes in daily and sub daily rainfall intensities.

References

Agilan, V., & Umamahesh, N. V. (2017). What are the best covariates for developing non-stationary rainfall intensity-duration-frequency relationship? Advances in Water Resources, 101, 11–22.

Allan, R. P., & Soden, B. J. (2008). Atmospheric warming and the amplification of precipitation extremes. Science, 321(5895), 1481–1484.

Armstrong, W. H., Collins, M. J., & Snyder, N. P. (2014). Hydroclimatic flood trends in the northeastern United States and linkages with large-scale atmospheric circulation patterns. Hydrological Sciences Journal, 59(9), 1636–1655. https://doi.org/10.1080/02626667.2013.862339

Bacmeister, J. T., Reed, K. A., Hannay, C., Lawrence, P., Bates, S., Truesdale, J. E., Rosenbloom, N., & Levy, M. (2018). Projected changes in tropical cyclone activity under future warming scenarios using a high-resolution climate model. Climatic Change, 146(3), 547–560.

Bao, J., & Sherwood, S. C. (2019). The role of convective self-aggregation in extreme instantaneous versus daily precipitation. Journal of Advances in Modeling Earth Systems, 11(1), 19–33.

Barbero, R., Abatzoglou, J. T., & Fowler, H. J. (2019). Contribution of large-scale midlatitude disturbances to hourly precipitation extremes in the United States. Climate Dynamics, 52(1), 197–208.

Barlow, M. (2011). Influence of hurricane-related activity on North American extreme precipitation: HURRICANES AND NORTH AMERICAN EXTREMES. Geophysical Research Letters, 38(4), n/a-n/a. https://doi.org/10.1029/2010GL046258

Bonnin, G.M., Martin, D., Lin, B., et al. (2006) NOAA Atlas 14: Precipitation-frequency atlas of the United States, volume 2, Version 3.0.

BWSO. (2023). Sewer System Design, Drainage Plan Preparation, and Analysis (DRAFT). Bureau of Water and Sewer Operations, NYC Department of Environmental Protection.

Cannon, A.J., Sobie, S.R., and Murdock, T.Q. (2015) Bias correction of GCM precipitation by quantile mapping: How well do methods preserve changes in quantiles and extremes, Journal of Climate, 28(17), 6938-6959.

Chand, S. S., Walsh, K. J., Camargo, S. J., Kossin, J. P., Tory, K. J., Wehner, M. F., Chan, J. C., Klotzbach, P. J., Dowdy, A. J., & Bell, S. S. (2022). Declining tropical cyclone frequency under global warming. Nature Climate Change, 12(7), 655–661.

Collins, M. J. (2009). Evidence for Changing Flood Risk in New England Since the Late 20th Century. JAWRA Journal of the American Water Resources Association, 45(2), 279–290. https://doi.org/10.1111/j.1752-1688.2008.00277.x

Cook, L.M., Anderson, C.J., and Samaras, C. (2017) Framework for incorporating downscaled climate output into existing engineering methods: Application to precipitation frequency curves, Journal of Infrastructure Systems, 23(4), doi: 10.1061/(ASCE)IS.1943-555X.0000382.

DeGaetano, A. T. (2009). Time-Dependent Changes in Extreme-Precipitation Return-Period Amounts in the Continental United States. Journal of Applied Meteorology and Climatology, 48(10), 2086–2099. https://doi.org/10.1175/2009JAMC2179.1

DeGaetano, A. and Castellano, C.M. (2018) Selecting time series length to moderate the impact of nonstationarity in extreme rainfall analyses, Journal of Applied Meteorology and Climatology, 57(10).

Easterling, D. R., Arnold, J. R., Knutson, T., Kunkel, K. E., LeGrande, A. N., Leung, L. R., Vose, R. S., Waliser, D. E., & Wehner, M. F. (2017). Ch. 7: Precipitation Change in the United States. Climate Science Special Report: Fourth National Climate Assessment, Volume I. U.S. Global Change Research Program. https://doi.org/10.7930/J0H993CC

Eggers, S., Thorne, S., Butte, G., & Sousa, K. (2011). A Strategic Risk Communications Process for Outreach and Dialogue on Biosolids Land Application. WERF.

Fowler, H. J., Lenderink, G., Prein, A. F., Westra, S., Allan, R. P., Ban, N., Barbero, R., Berg, P., Blenkinsop, S., & Do, H. X. (2021). Anthropogenic intensification of short-duration rainfall extremes. Nature Reviews Earth & Environment, 2(2), 107–122.

Frei, A., Kunkel, K. E., & Matonse, A. (2015). The Seasonal Nature of Extreme Hydrological Events in the Northeastern United States. Journal of Hydrometeorology, 16(5), 2065–2085. https://doi.org/10.1175/JHM-D-14-0237.1

Georgakakos, A. (2014). Climate Change Impacts in the United States CHAPTER 3 WATER RESOURCES. In Climate Change Impacts in the United States.

Gutmann, E. D., Rasmussen, R. M., Liu, C., Ikeda, K., Bruyere, C. L., Done, J. M., Garrè, L., Friis-Hansen, P., & Veldore, V. (2018). Changes in hurricanes from a 13-yr convection-permitting pseudo–global warming simulation. Journal of Climate, 31(9), 3643–3657.

Horton, R., Bader, D., Kushnir, Y., Little, C., Blake, R., & Rosenzweig, C. (2015). New York City Panel on Climate Change 2015 ReportChapter 1: Climate Observations and Projections: NPCC 2015 Report Chapter 1. Annals of the New York Academy of Sciences, 1336(1), 18–35. https://doi.org/10.1111/nyas.12586

Huang, H., Winter, J. M., Osterberg, E. C., Horton, R. M., & Beckage, B. (2017). Total and Extreme Precipitation Changes over the Northeastern United States. Journal of Hydrometeorology, 18(6), 1783–1798. https://doi.org/10.1175/JHM-D-16-0195.1

Jackson, E., E. Richter, P.L. Gurian, A. Pradhan, E. Aktan, and F. Moon. (2012). “Knowledge Management for Aging Infrastructures,” The 6th International Conference on Bridge Maintenance, Safety and Management (IABMAS 2012), Lake Como, Italy, on July 8-12, 2012.

Jessup, S. M., & Colucci, S. J. (2012). Organization of Flash-Flood-Producing Precipitation in the Northeast United States. Weather and Forecasting, 27(2), 345–361. https://doi.org/10.1175/WAF-D-11-00026.1

Kendon, E. J., Blenkinsop, S., & Fowler, H. J. (2018). When will we detect changes in short-duration precipitation extremes? Journal of Climate, 31(7), 2945–2964.

Knutson, T., Camargo, S. J., Chan, J. C., Emanuel, K., Ho, C.-H., Kossin, J., Mohapatra, M., Satoh, M., Sugi, M., & Walsh, K. (2020). Tropical cyclones and climate change assessment. Bulletin of the American Meteorological Society, 101(3), E303–E322.

Kunkel, K. E., Easterling, T.R., Biard, J.C., Champion, S.M., Gleason, B.E., Johnson, K.M., Li, A., Stegall, S., Stevens, L.E., Stevens, S.E., Squires, M., Sun, L., & Yin, X. (2020). Incorporation of the Effects of Future Anthropogenically Forced Climate Change in Intensity-Duration-Frequency Design Values. Version 2 (RC-2517). North Carolina Institute for Climate Studies (NCICS), North Carolina State University. https://precipitationfrequency.ncics.org/pdfs/RC_2517_Final_Report_version2_Sep_04_2020_clean.pdf

Laprise, R., De Elia, R., Caya, D., Biner, S., Lucas-Picher, P. H., Diaconescu, E., Leduc, M., Alexandru, A., & Separovic, L. (2008). Challenging some tenets of regional climate modelling. Meteorology and Atmospheric Physics, 100(1), 3–22.

Lenderink, G., Barbero, R., Loriaux, J. M., & Fowler, H. J. (2017). Super-Clausius–Clapeyron Scaling of Extreme Hourly Convective Precipitation and Its Relation to Large-Scale Atmospheric Conditions. Journal of Climate, 30(15), 6037–6052. https://doi.org/10.1175/JCLI-D-16-0808.1

Lenderink, G., de Vries, H., Fowler, H. J., Barbero, R., van Ulft, B., & van Meijgaard, E. (2021). Scaling and responses of extreme hourly precipitation in three climate experiments with a convection-permitting model. Philosophical Transactions of the Royal Society A, 379(2195), 20190544.

Lenderink, G., & Van Meijgaard, E. (2008). Increase in hourly precipitation extremes beyond expectations from temperature changes. Nature Geoscience, 1(8), 511–514.

Lengfeld, K., Kirstetter, P.-E., Fowler, H. J., Yu, J., Becker, A., Flamig, Z., & Gourley, J. (2020). Use of radar data for characterizing extreme precipitation at fine scales and short durations. Environmental Research Letters, 15(8), 085003.

Livneh, B., Bohn, T.J., Pierce, D.W., Munoz-Arriola, F., Nijssen, B., Vose, R., Cayan, D.R., and Brekke, L. (2015), A spatially comprehensive, hydrometeorological data set for Mexico, the U.S., and Southern Canada 1950-2013, Scientific Data, 2(150042), doi: 10.1038/sdata.2015.42.

Lochbihler, K., Lenderink, G., & Siebesma, A. P. (2019). Response of extreme precipitating cell structures to atmospheric warming. Journal of Geophysical Research: Atmospheres, 124(13), 6904–6918.

Lopez-Cantu, T., Prein, A. F., & Samaras, C. (2020). Uncertainties in future US extreme precipitation from downscaled climate projections. Geophysical Research Letters, 47(9), e2019GL086797.

Madajewicz, M. (2020) Who is vulnerable and who is resilient to coastal flooding? Lessons from Hurricane Sandy in New York City, Climate Change, 163.

Madsen, H., Rasmussen, P.F., and Rosbjerg, D. (1997) Comparison of annual maximum series and partial duration series methods for modeling extreme hydrologic events: 1. At-site modeling, Water Resources Research, 33(4), doi: 10.1029/96WR03848.

Maimone, M., Malter, S., Rockwell, J., & Raj, V. (2019). Transforming global climate model precipitation output for use in urban stormwater applications. Journal of Water Resources Planning and Management, 145(6), 04019021.

Milly, P. C. D., Betancourt, J., Falkenmark, M., Hirsch, R. M., Kundzewicz, Z. W., Lettenmaier, D. P., & Stouffer, R. J. (2008). Stationarity Is Dead: Whither Water Management? Earth, 4, 20.

Moseley, C., Hohenegger, C., Berg, P., & Haerter, J. O. (2016). Intensification of convective extremes driven by cloud–cloud interaction. Nature Geoscience, 9(10), 748–752.

Najibi, N., Mukhopadhyay, S., & Steinschneider, S. (2022). Precipitation Scaling With Temperature in the Northeast US: Variations by Weather Regime, Season, and Precipitation Intensity. Geophysical Research Letters, 49(8), e2021GL097100.

NCEI (2023a). Storm Events Database. National Centers for Environmental Information, https://www.ncdc.noaa.gov/stormevents/, Accessed June 2023.

NCEI (2023b). Local Climatological Dataset. National Centers for Environmental Information (NCEI), NESDIS, NOAA, U.S. Department of Commerce. 2023.

NCEI (2022). Data Documentation for Data Set 6405 (DSI-6405). ASOS Surface 1-MINUTE, Page 1 Data. National Centers for Environmental Information (NCEI). https://www.ncei.noaa.gov/data/automated-surface-observing-system-one-minute-pg1/doc/asos-1min-pg1_documentation.pdf

NOAA (2003), Data Documentation for Data Set 3240 (DSI-3240), Hourly Precipitation Data. National Climatic Data Center, Ashville, NC 28801-5001, USA. https://www.ncei.noaa.gov/pub/data/hourly_precip-3240/dsi3240.pdf

NWS (2016). Storm Data Preparation, 10–1605 National Weather Service Instruction (2016). U.S. National Weather Service, http://www.nws.noaa.gov/directives/sym/pd01016005curr.pdf

NYC DEP. (2013). Wastewater Resiliency Plan Climate Risk Assessment and Adaptation Study [J]. New York City Department of Environmental Protection.

Papalexiou, S. M., and Koutsoyiannis, D. (2013) Battle of extreme value distributions: A global survey on extreme daily rainfall, Water Resources Research, 49(1), https://doi.org/10.1029/2012WR012557.

Parodi, A., & Emanuel, K. (2009). A Theory for Buoyancy and Velocity Scales in Deep Moist Convection. Journal of the Atmospheric Sciences, 66(11), 3449–3463. https://doi.org/10.1175/2009JAS3103.1

Pendergrass, A. G. (2020). Changing degree of convective organization as a mechanism for dynamic changes in extreme precipitation. Current Climate Change Reports, 6(2), 47–54.

Pérez Bello, A., Mailhot, A., & Paquin, D. (2021). The Response of Daily and Sub-Daily Extreme Precipitations to Changes in Surface and Dew-Point Temperatures. Journal of Geophysical Research: Atmospheres, 126(16), e2021JD034972.

Perica, S., Martin, D., Pavlovic, S., Roy, I., St. Laurent, M., Trypaluk, C., Unruh, D., Yekta, M., and Bonnin, G.M. (2013) Precipitation-frequency atlas of the United States, southeastern states, Atlas 14, volume 9.

Perica, S., Pavlovic, S., Laurent, M. S., Trypaluk, C., Unruh, D., Martin, D., & Wilhite, O. (2019). NOAA Atlas 14: Precipitation Frequency Atlas of the United States Volume 10 Version 3.0: Northeastern States. National Weather Service. https://www.weather.gov/media/owp/oh/hdsc/docs/Atlas14_Volume10.pdf

Peterson, T. C., Heim, R. R., Hirsch, R., Kaiser, D. P., Brooks, H., Diffenbaugh, N. S., Dole, R. M., Giovannettone, J. P., Guirguis, K., Karl, T. R., Katz, R. W., Kunkel, K., Lettenmaier, D., McCabe, G. J., Paciorek, C. J., Ryberg, K. R., Schubert, S., Silva, V. B. S., Stewart, B. C., … Wuebbles, D. (2013). Monitoring and Understanding Changes in Heat Waves, Cold Waves, Floods, and Droughts in the United States: State of Knowledge. Bulletin of the American Meteorological Society, 94(6), 821–834. https://doi.org/10.1175/BAMS-D-12-00066.1

Pierce, D. W., Cayan, D. R., Feldman, D. R., & Risser, M. D. (2023). Future Increases in North American Extreme Precipitation in CMIP6 downscaled with LOCA. Journal of Hydrometeorology, 1(aop). https://doi.org/10.1175/JHM-D-22-0194.1

Pierce, D. W., Cayan, D. R., & Thrasher, B. L. (2014). Statistical downscaling using localized constructed analogs (LOCA). Journal of Hydrometeorology, 15(6), 2558–2585.

Pierce, D. W., Su, L., Cayan, D. R., Risser, M. D., Livneh, B., & Lettenmaier, D. P. (2021). An extreme-preserving long-term gridded daily precipitation dataset for the conterminous United States. Journal of Hydrometeorology, 22(7), 1883–1895.

Prein, A. F., Liu, C., Ikeda, K., Trier, S. B., Rasmussen, R. M., Holland, G. J., & Clark, M. P. (2017). Increased rainfall volume from future convective storms in the US. Nature Climate Change, 7(12), 880–884.

Pumo, D., & Noto, L. V. (2021). Exploring the linkage between dew point temperature and precipitation extremes: A multi-time-scale analysis on a semi-arid Mediterranean region. Atmospheric Research, 254, 105508.

Ragno, E., A. AghaKouchak, C.A. Love, L. Cheng, F. Vahedifard, and C. HR Lima. (2018) Quantifying changes in future intensity-duration-frequency curves using multimodel ensemble simulations, Water Resources Research, 54(3).

Retrepo-Posada, P.J. and Eagleson, P.S. (1982), Identification of independent rainstorms. Journal of Hydrology, 55(1-4), pp.303-319.

Rosenzweig, B. R., McPhillips, L., Chang, H., Cheng, C., Welty, C., Matsler, M., Iwaniec, D., & Davidson, C. I. (2018). Pluvial flood risk and opportunities for resilience. WIREs Water, 5(6). https://doi.org/10.1002/wat2.1302

Santer, B. D., Wehner, M. F., Wigley, T. M. L., Sausen, R., Meehl, G. A., Taylor, K. E., Ammann, C., Arblaster, J., Washington, W. M., & Boyle, J. S. (2003). Contributions of anthropogenic and natural forcing to recent tropopause height changes. Science, 301(5632), 479–483.

Seneviratne, S.I, Zhang, X., Adnan, M., Badi, W., Dereczynski, C., A. Di Luca, S. Ghosh, I. Iskandar, J. Kossin, S. Lewis, F. Otto, I. Pinto, M. Satoh, S.M. Vicente-Serrano, M. Wehner, & B. Zhou, 2021. (2021). Weather and Climate Extreme Events in a Changing Climate. In Climate Change 2021: The Physical Science Basis. Contribution of Working Group I to the Sixth Assessment Report of the Intergovernmental Panel on Climate Change (pp. 1513–1766). Cambridge University Press. https://www.ipcc.ch/report/ar6/wg1/chapter/chapter-11/#11.4

Shepherd, J. M., & Burian, S. J. (2003). Detection of urban-induced rainfall anomalies in a major coastal city. Earth Interactions, 7(4), 1–17.

Singh, M. S., & O'Gorman, P. A. (2015). Increases in moist-convective updraught velocities with warming in radiative-convective equilibrium: Increases in Updraught Velocities with Warming. Quarterly Journal of the Royal Meteorological Society, 141(692), 2828–2838. https://doi.org/10.1002/qj.2567

Smith, B., & Rodriguez, S. (2017). Spatial Analysis of High-Resolution Radar Rainfall and Citizen-Reported Flash Flood Data in Ultra-Urban New York City. Water, 9(10), 736. https://doi.org/10.3390/w9100736

Stansfield, A. M., Reed, K. A., & Zarzycki, C. M. (2020). Changes in Precipitation From North Atlantic Tropical Cyclones Under RCP Scenarios in the Variable-Resolution Community Atmosphere Model. Geophysical Research Letters, 47(12). https://doi.org/10.1029/2019GL086930

Steinschneider, S., & Najibi, N. (2022). Observed and Projected Scaling of Daily Extreme Precipitation with Dew Point Temperature at Annual and Seasonal Scales across the Northeastern United States. Journal of Hydrometeorology, 23(3), 403–419.

Switzman, H., Razavi, T., Traore, S., Caulibaly, P., Burn, D.H., Henderson, J., Fausto, E., and Ness, R. (2017) Variability of future extreme rainfall statistics: Comparison of multiple IDF projections, Journal of Hydrologic Engineering, 22(10).

Teale, N., & Robinson, D. A. (2020). Patterns of water vapor transport in the eastern United States. Journal of Hydrometeorology, 21(9), 2123–2138.

Thakali, R., Kalra, A., and Ahmad, S. (2016) Understanding the effects of climate change on urban stormwater infrastructures in the Las Vegas Valley, Hydrology 3(4), doi: 10.3390/hydrology3040034.

Trenberth, K. E. (2011). Changes in precipitation with climate change. Climate Research, 47(1–2), 123–138.

U.S. Weather Bureau. (1955). Technical Paper No. 25 (TP25) Rainfall Intensity-Duration-Frequency Curves for Selected Stations in the United States, Alaska, Hawaiian Islands and Puerto Rico. U.S. Department of Commerce.

Utsumi, N., Seto, S., Kanae, S., Maeda, E. E., & Oki, T. (2011). Does higher surface temperature intensify extreme precipitation? Geophysical research letters, 38(16).

Utsumi, N. (2024) Personal Communication.

Wright, D. B., Smith, J. A., Villarini, G., & Baeck, M. L. (2013). Estimating the frequency of extreme rainfall using weather radar and stochastic storm transposition. Journal of Hydrology, 488, 150–165.

Wu, S., Markus, M., Lorenz, D., Angel, J.R. and Grady, K. (2019) A comparative analysis of the historical accuracy of the point precipitation frequency estimates of four data sets and their projections for the Northeastern United States, Water 11(6), doi: 10.3390/w11061279.

Yu, Z., Miller, S., Montalto, F., & Lall, U. (2018). The bridge between precipitation and temperature – Pressure Change Events: Modeling future non-stationary precipitation. Journal of Hydrology, 562, 346–357. https://doi.org/10.1016/j.jhydrol.2018.05.014

Yu, Z., Montalto, F., Jacobson, S., Lall, U., Bader, D., & Horton, R. (2022). Stochastic Downscaling of Hourly Precipitation Series From Climate Change Projections. Water Resources Research, 58(10). https://doi.org/10.1029/2022WR033140

Task 4: Systematic Assessment of Health-Related Economic Costs from Climate-Sensitive Events in New York City

Task 4: Systematic Assessment of Health-Related Economic Costs from Climate-Sensitive Events in New York City 2000-2019

Core Team Members:

- Matthew Neidell (Columbia University)
- Deborah Balk (CUNY)
- Christian Braneon (NASA)
- Kim Knowlton (NRDC and Columbia University)
- Leiwen Jiang (Population Council)
- Marianthi-Anna Kioumourtzoglou (Columbia University)
- Vijay Limaye (NRDC)
- Santiago Munoz Perez (Columbia University and NRDC)
- Thomas Matte (Columbia University)
- Jenna Tipaldo (CUNY)
- Hamid Zoraghein (Population Council)

NYC Interagency Collaborators:

- Katie Lane (Department of Health)
- Kaz Ito (Department of Health)
- Mallory Rutigliano (Office of Management and Budget)
- NYC DCP (Peter Lobo, Eric Ketcham, Erica Mauer)
- Julia Eiferman (MOCEJ)
- Hayley Elszasz (MOCEJ)

4.1 Key Messages

- Climate-sensitive events over the past 20 years have led to an additional 361 deaths and at least an additional 1,833 hospital visits and 1,404 emergency department visits per year in New York City
- These mortality and morbidity cases lead to annual health-related economic costs of $4.17 billion per year, amounting to a total of $83.45 billion over the 20-year time period
- Approximately 98.5% of these costs are due to mortality, though the full morbidity costs are likely underestimated for various reasons
- Using alternative measures to monetize the mortality impacts, we find a range of annual costs from $1.97 billion to $6.34 billion

- When applying SSP narratives to the future population, New York City's population in 2100 will range from 6.2 to nearly 9 million persons. The middle-of-road of road (SSP2) future projects a population of about 7.5 million whereas the sustainability (SSP1) future projects a population of 6.7 million in 2100.
- When applying SSP narratives to the future population, New York City's population in 2100 will be older and in some scenarios much older, with the exception of the regional rivalry (SSP3) scenario. These changes are unprecedented.
- The future population of New York City is in large part dependent on migration, as fertility falls and deaths (due to an increasingly older population) rise.

4.2 Objective

Task 4 aims to perform a systematic assessment of the health-related economic costs attributable to climate-sensitive events in New York City (NYC). In order to do so, Task 4 is split into understanding the health impacts from exposures to past climate-sensitive events and their associated costs, as well as understanding future changes in New York City's population in order to understand how many, as well as which New Yorkers, and where, these costs are more likely to occur. This task was thus divided into three distinct parts: (1) A systematic assessment of the health-related economic costs attributable to climate-sensitive events; (2) understanding the size and spatial distribution of the population of NYC in the future; and (3) understanding the implications of future populations on health economic damages. We conclude with a section on (4) next steps.

a. Health-related economic costs due to past climate-sensitive events

This section aims to perform a systematic assessment of the health-related economic costs attributable to climate-sensitive events in New York City (NYC). Over the past decade, NYC has experienced numerous climate-sensitive events, including heat waves, coastal storms, Nor'easters, and associated power outages. These hazards are considered "climate-sensitive" because they can reasonably be expected to increase in frequency, intensity, and/or areal extent as climate change progresses (USGCRP, 2023). A substantial body of evidence has accumulated on the impacts of these climate-sensitive events on adverse health outcomes.

As part of Task 4, we calculated the impacts from climate-sensitive events during 2000-19 in New York City according to the following steps:

- Compile available literature that documents the impact of climate-sensitive events on health outcomes, with a focus on studies relevant to NYC and outcomes amenable to valuation

- Calculate mortality and morbidity in New York City attributable to climate-sensitive events using the dose-response estimates from existing literature
- Monetize the mortality and morbidity cases to calculate the health-related economic costs from these events

From this analysis, we computed the additional deaths, hospital visits and emergency department visits per year in New York City due to climate-sensitive events, and monetized these health impacts to provide estimates of the health-related economic costs.

1. Compile available literature

The aim of this review was to synthesize existing literature that explores the health impacts of climate-sensitive events relevant to NYC from the year 2000 to 2019. We conducted this review by performing a systematic search using keywords for studies related to health impacts of climate-sensitive events, focusing on the following keywords: floods, temperature, rainfall, precipitation, storm, cyclone, hurricane, Sandy, New York, New York City. Our inclusion criteria adhered to the following:

- observational studies, reviews (narrative/systematic), and white papers;
- studies conducted in New York City or NYS or that provide NYC-specific estimates;
- studies using outcomes amenable to valuation, which included either mortality or morbidity resulting in health services assigned an International Classification of Disease (ICD) -9 or -10 code;
- studies using appropriate epidemiological methodologies, which largely consisted of distributed-lag linear or non-linear statistical models;
- studies exploring climate-sensitive events that included at least part of the 2000-2019 period.

We used Microsoft Excel 365 (Microsoft Corporation; Redmond, WA), and Zotero 6.0.16 (Corporation for Digital Scholarship; Vienna, VA) to import all the studies obtained from different databases. We reviewed all studies based on the above inclusion criteria.

After an extensive review, our analysis was refined to three main climate-sensitive events strongly linked with health impacts in New York City: heat-related events, tropical cyclones, and power outages. We describe each in turn, noting the specific studies.

Heat-related events. Strong evidence shows New York City's climate is experiencing higher temperatures, which is expected to cause hotter warm season weather and increase the

frequency of extreme heat events, both of which cause morbidity and mortality. DOHMH (2022) provides estimates of the relationship between mortality and maximum temperature specific to NYC from 2011-2019.

Several studies provide estimates of the relationship between morbidity and higher temperatures. Some provide estimates for the entire state, whereas others provide estimates specifically for the City. Statewide estimates are heavily influenced by the City since it captures roughly half of the total population, though we use City-specific estimates when available. Lin et al. (2009) estimated the relationship between average temperature and respiratory hospitalizations in New York City. Adeyeye et al. (2019) produced estimates of a non-linear relationship between maximum temperature and hospital and ED visits in NYS for cardiovascular conditions, dehydration, heat stress, and kidney disease. Estimates were linearly interpolated between the 5C breakpoints that were directly provided by the authors. Lin et al. (2016) estimated the relationship between maximum temperature and gastrointestinal (GI) hospitalizations in NYS. Yoo et al. (2021) produced a non-linear relationship between average temperature and ED visits for mental health disorders in New York City. Table 4.1 provides a complete listing of these studies.

Tropical cyclones (TCs). As noted in Task 2 Key Point, TCs generally cause more extreme hazards compared with other storm types and are responsible for a majority of the most extreme events, even though they occur far less frequently. Anthropogenic climate change may lead to increased frequency or severity of hurricanes, posing a greater threat to coastal communities. In the aftermath of a hurricane, morbidity and mortality can result from injuries, infectious and parasitic diseases, cardiovascular diseases, neuropsychiatric conditions, and respiratory diseases. For mortality, we rely on two studies: 1) Parks et al. (2023) provide estimates of excess mortality counts, along with confidence intervals, at the county level for all tropical cyclones from 1988-2019; and 2) Seil et al. (2016) provide deaths directly attributable to Hurricane Sandy in 2012. For morbidity, we rely on Limaye et al. (2019), who provide monetized health impacts aggregated across numerous hospital and emergency department visits for the greater NYC area, which includes Westchester, Nassau and Suffolk County, due to Hurricane Sandy. Appendix 4.1
Table 4.2 provides a complete listing of these studies.

Power outages. With changes in climate, power outages represent a relevant public health concern as increased electricity demands to offset higher temperatures strain the electric grid. These power outages could increase the risk of health consequences by limiting the regulation of indoor temperatures and through disruption in electrically-powered medical devices. Anderson and Bell (2012) investigated the effect on mortality in New York City due to the Northeast blackout on August 14-15, 2003. Dominianni et al. (2018) examined the morbidity

impacts of the same blackout as well as more localized outages in New York City, exploring hospitalizations due to cardiovascular, respiratory and renal diseases. Appendix 4.1 Table 4.3 provides a complete listing of these studies.

2. Calculate climate-sensitive mortality and morbidity

After identifying the above studies, the next step of our analysis involved calculating the climate-sensitive mortality and morbidity cases over the 2000-2019 period for the climate sensitive events. This process involved different strategies depending on the strategies used in the above studies. In some instances, climate-sensitive cases were directly provided in the study or obtained from the authors. In other instances, we calculated climate-sensitive cases by combining the existing dose-response estimate provided in the study with data on climate-sensitive events and baseline counts of mortality or morbidity.

Heat. Existing studies produced either linear or non-linear estimates of the relationship between temperature (t) and health, measured by either mortality (m^d) or morbidity (m^b). Since all studies focused on the relationship between daily temperature and health, we focus on daily mortality or morbidity measures. When a linear estimate was provided, we proceeded with the following formula:

$$\Delta m^j = \sum m_o^j * \left(1 - e^{-\beta * \Delta t}\right) \quad (4.1)$$

(4.1)

where m_0^j is the daily baseline counts for j = mortality or morbidity and β = ln(RR), where RR is the estimated relative-risk produced in the study. When a non-linear estimate was provided, we proceeded with the following formula:

$$\Delta m^j = \sum m_o^j * ln(DR_t) \quad (4.2)$$

(4.2)

where $ln(DR_t)$ is the non-linear dose-response curve (for each temperature t) produced in the study. Since these curves were provided in figures, we contacted the authors of each study to obtain the data underlying such figures.

For choosing the appropriate change in outcomes for each study, we define estimates relative to a reference point. For mortality impacts, in DOHMH (2022), the authors choose 71°F as the

reference point (the minimum mortality value) and interpret all estimates as relative to the impact at 71°F. Therefore, the impact at, say, 90°F is defined as $\beta = \beta_{90} - \beta_{71}$. For the morbidity impacts, we use the reference point as the minimum morbidity value reported in the study or the value of 71°F when not reported. Lin et al. (2016) and Yoo et al. (2021) did not provide reference points; since Yoo et al. (2021) used average temperature, we applied the average temperature that corresponded with maximum temperature for the reference point (64°F). Lin et al. (2009) provided a reference point for average temperature of 84°F. Adeyeye et al. (2016) provided a reference point for maximum temperature of 74.8°F for cardiovascular conditions, 76.5°F for kidney disease, 80.6°F for heat stress, 78.1°F for dehydration.

In order to calculate climate-sensitive cases, we defined a threshold above which heat impacts arise. We apply the methodology from DOHMH (2022), which used a threshold for daily maximum temperatures above 82°F. For the morbidity estimates, we use this same threshold of 82°F for maximum temperature (which corresponds to 74.5°F for average temperature) except when the reference point exceeded the threshold; this only occurred for Lin et al. (2009), who produced a reference point of 84°F for respiratory conditions.

Temperature data was obtained from the National Weather Service station at LaGuardia Airport for the years 2000 to 2019. We obtained the daily maximum, mean, and minimum temperature by date in each year. In instances where mean temperature was unavailable, we averaged the maximum and minimum temperature. Figure 4.1 shows the number of days above 82°F in each year from 2000-19, and Figure 4.2 shows the variation in maximum temperature for days above 82°F. As these figures demonstrate, there is considerable year-to-year variation, with an upward trend over time.

For an estimate of the baseline daily mortality counts (m^d_o), we proceeded in several steps. First, annual mortality counts for the years 2007-2019 were obtained from the annual Summary of Vital Statistics Reports (NYC Office of Vital Statistics). From this, we created an annual average of mortality counts. Second, since DOHMH (2022) focuses on deaths from May through September, we adjusted annual mortality counts to a monthly level. This was accomplished by incorporating restricted-access data on the monthly count of total deaths for the years 2007-19. From the restricted access data, we calculated the percent of deaths occurring in each month from May through September, and multiplied this percent by the annual mortality counts to obtain the monthly mortality counts for each month. Last, we divided the monthly counts by 30 to obtain daily mortality counts.

For an estimate of baseline counts for morbidity (m^b_o), we followed a similar procedure but with minor modifications given the different data sources. Counts of hospital and ED visits (census of counts) were obtained from the Healthcare Cost and Utilization Project (HCUP),

using the State Inpatient Database (SID) for hospital visits and the State Emergency Department Database (SEDD) for ED visits, for the years 2008-19. A restricted-use version of the data that provides the patient ZIP code was accessed, enabling identification of NYC residents.[5] Using ICD-9 codes prior to 2016 and ICD-10 codes from 2016 forward, we calculated the annual average morbidity counts for the entire city for each health condition being considered for the corresponding months given in each study. For example, Lin et al. (2016) measures GI hospital visits in the months June through August, so we measure morbidity counts for GI illness for those three months. We then divide the average seasonal morbidity counts by the number of days in that season to obtain daily morbidity counts.[6]

Tropical cyclones. Through direct communication with the author (Parks et al., 2023), we obtained mortality estimates specific to the five counties of NYC. Estimates were provided for multiple storms across all counties in New York City, but we only used estimates that were statistically significant, which amounted to an extra 104 deaths in Staten Island from Hurricane Sandy in 2012. Seil et al. (2016) provided a count of 52 deaths directly attributable to Hurricane Sandy, of which we excluded 23 that occurred in Staten Island to avoid double-counting those included in Parks et al. (2023). This led to a total of 133 deaths due to tropical cyclones, noting all were due to Hurricane Sandy, since 2019.

For morbidity, we relied on estimates from Limaye et al. (2019). As a review study, the authors provided monetized outcomes across numerous health outcomes for the NYC metro area. Since this included three additional counties beyond NYC, we weighted the estimates by 2010 population to produce NYC specific estimates. These estimates are also specific only to Hurricane Sandy.

Power outages. Anderson and Bell (2012) provide direct mortality counts of 90 for the 2003 blackout. For morbidity, we use estimates from Dominianni et al. (2018) to calculate additional respiratory hospitalizations. Although the study examined several types of hospitalizations, we focus solely on those with statistically significant estimates, which limited our analysis to the 2003 blackout for respiratory hospitalizations. Since the study provides a linear relative risk estimate, we apply the method described in equation (1) above, noting we use a variable to indicate presence of the blackout in place of temperature, obviating the need to specify a reference point or threshold. This resulted in 410 respiratory hospitalizations due to power outages.

[5] The ZIP codes within New York City were based on the 2010 Census (Baruch College, 2020).
[6] As a measure of quality control, we compared the number of admissions reported in the published studies with our own calculations using the ICD-9 or 10 codes provided in the studies, and found comparable counts.

3. Health-related economic costs

To calculate economic costs of these mortality and morbidity changes, we monetize them using a willingness-to-pay approach for mortality monetization and a cost-of-illness (COI) approach for morbidity monetization. Specifically, we value changes in mortality using estimates of the value of a statistical life (VSL) and changes in morbidity (hospital or emergency department visits) using direct health care costs and the lost wages associated with the hospital length of stay.

For mortality costs, we use the following equation to produce calculations for each year:

$$(4.3) \quad \text{Mortality costs}_y = \Delta m_y^d * \text{VSL}_{2020}$$

where Δm_y^d is annual mortality (m^d) cases in year y. For estimates of the VSL, we used recent recommendations from the Department of Health and Human Services (U.S. DHHS, 2021). A range of VSL estimates were employed to provide low-midrange-high estimates ($5.3 million, $11.4 million, and $17.4 million, respectively) of mortality-associated costs, in 2020 $USD.[7]

Cost of illness estimates consisted of health care costs and lost wages, calculated according to the following equation:

$$(4.4) \quad \text{Morbidity costs}_y = \Delta m_y^b * \text{charge per case}_y * \text{CCR}_y * (\text{PCEI}_{2020} / \text{PCEI}_y) + \text{LOS}_y * \text{daily wage}_{2020}$$

where Δm_y^b is annual morbidity (m^b) cases in year y. The first component of the right-hand side of the equation is health care costs and the second is lost wages. For the charge per case, we use data from HCUP. These data include the primary diagnosis at admission and monetary charges at discharge, which we use to calculate the charges specific to each outcome, separately by year. We apply the charges from 2008 to the years 2001-2007, where no HCUP data was available. Using the patient ZIP code of residence, we calculate charges specific to NYC residents. Since charges do not reflect actual costs, we produce estimates of health care costs by scaling the charge estimates by the national cost-to-charge ratio (CCR) per year, separately for ED and hospital visits, provided by HCUP.[8] All cost estimates are inflation

[7] Since we use the VSL measured in $2020, we do not need to apply an inflation adjustment.
[8] CCR was only available beginning in 2001 for hospital visits and 2012 for ED visits. As with the procedure for charges and LOS, we applied values from the earliest reported year to the prior years.

adjusted to $2020 using the seasonally adjusted medical module of the Personal Consumption Expenditures Index (PCEI) (FRED, 2023).

For lost wages, we followed standard practice by assuming the lost value from a day in the hospital is valued at the daily wage rate. We calculated the mean LOS in the hospital related to each ICD code using the HCUP data, again applying the value from 2008 to all earlier years. We multiplied the total number of cases for each code by its corresponding average LOS value to obtain the total change in LOS, and multiplied by the average daily wage within the city to provide a monetary value. We obtained 2020 wage and employment data from the Quarterly Census of Employment and Wages available from the Bureau of Labor Statistics (BLS, 2024), which provides data for 95% of US jobs at the county level. We computed the average weekly wage for NYC by weighting the county wages by employment counts, and divided by five to obtain a daily wage of $409.05.[9]

The mortality and morbidity costs were summed across the study area and study period to provide estimates of the total and annual health-economic related costs due to climate-sensitive events.

4. Results

Table 4.4 provides an overview of the results. Across all climate-sensitive events, we compute an annual average of 361 mortality cases, with 97% due to heat. Over the 20-year time period, there was an average of 1833 hospital visits and 1404 ED visits per year, with 97% and 94%, respectively, due to heat. Monetizing these impacts, we estimate an annual average mortality cost of $4.11 billion using the middle VSL. We estimate annual average morbidity costs of $60.6 million. The morbidity costs are 1.46% of the total costs, suggesting the bulk of health costs come from mortality, which is not surprising given the high value of the VSL compared to a hospital or ED admission. The annual average of the total health-related economic costs is $4.15 billion using the middle VSL, which amounts to $81.91 billion over the time period 2000-19. Using the low VSL lowers the annual and 20-year costs to $1.97 billion and $39.45 billion, respectively, and the high VSL raises the annual and 20-year costs to $6.34 billion and $126.73 billion, respectively.

The next three figures display the variation in counts and costs per year. Figure 4.3 provides climate-sensitive mortality counts per year, separately indicating cases due to all climate-sensitive events and those due solely to higher temperature. Consistent with the variation in maximum temperature over time, mortality varies over time, ranging from a low of 184 in 2009 to a high of 538 in 2010. The power outage in 2003 and Hurricane Sandy in 2012

[9] Since we use wages measured in $2020, we do not need to apply an inflation adjustment

increased mortality cases in those specific years, with their separate contribution highlighted in the figure. Figure 4.4 displays climate-sensitive morbidity counts per year, showing results for hospital visits and ED visits for all conditions. As with mortality cases, this figure displays considerable variation over time, with a high of 2647 hospital visits in 2010 and a low of 885 in 2009 and a high of 1837 ED visits in 2016 and a low of 713 in 2009. Figure 4.5 plots the annual costs per year, aggregating the mortality and morbidity costs. We continue to see considerable variation over time, with a low of $2.1 billion in 2009 and a high of $6.2 billion in 2010.

Population Futures of NYC: Long-term Projections and Spatial Distributions of Population

To understand and prepare and adapt to the impacts of future climates, it is necessary to know the population of a future population of New York. State and local projections have a long tradition using a method called “cohort-component” or closely related methodologies, that produce population futures in the fairly near-term time horizons, in order to reduce uncertainty in the estimation that can arise in local-area projections. This stands in contrast to global population forecasting which includes long-term time horizons and often use a variety of demographic, statistical and exploratory scenario methods (see review in Balk et al., 2022). As part of the New York Metropolitan Transportation Council, New York City’s Department of City Planning (DCP) projects the total population of NYC to be nearly 9.5M in 2055 (Morozovskaya and Lund, 2020), gaining small amounts of population from the present population of about 8.8M. Using a downscaling method, the city allocates the total population to the census-tract level. These projections result in population projections by age and sex, but they do not account for race/ethnic compositions, or under different internal and international migration circumstances. Nevertheless, in a recent neighborhood analysis, DCP (2023) finds: “Roughly half of neighborhoods experienced net outflows [from 2010-2020]. The vast majority of these still experienced population growth through natural increase, reflecting the citywide pattern of population growth despite net migration losses.” Understanding such neighborhood change and associated vulnerabilities is important for understanding the future health impacts and flood vulnerabilities.

Thus, to improve thematically, temporally and spatially, we apply a population projection methodology that is used within the climate community, by adopting the shared socio-economic pathways (SSP) framework for developing future population scenarios. This method, developed initially for global application, has been adopted for all states and counties of the U.S. (Jiang et al., 2020, Zoraghein & O’Neill, 2020a, 2020b). The steps to produce those population futures, and resulting output, are described below, along with a basic demographic description of New York in the present period, and recent past.

Input data used for SSP-consistent population projections

Population projections are built on data on population age-sex structure, as well as information on births, deaths, and migration. If population projections are desirable to produce by other characteristics (such as educational groups or race and ethnic subpopulations), such information must be available on the data input side. That is, to produce population projections by age-sex-race/ethnicity groups for New York City, it is necessary to know historical information on fertility, mortality and migration by age-sex and race/ethnicity groups. Further, if such information is desirable by borough (or finer-scale geographic units), then those variables would be necessary further stratified by those geographic divisions. In short, the data requirements for this type of analysis are large, in some part because migration information is sparse. During the data collection phase, we also determined it would not be possible to produce robust projections below the county-level (as there were too many input units with missing values), and thus defer the spatial distribution component to downscaling.
As Figure 4.1, an analysis of the DCP, shows citywide race/ethnic composition, New York City is increasingly diverse, from the 1950s to the present. Thus, the data we collected were specified by major race/ethnicity groups (Asian and other races, (non-Hispanic) Black, Hispanic, (non-Hispanic White) as these strata were available in all data collections we used in the analysis.

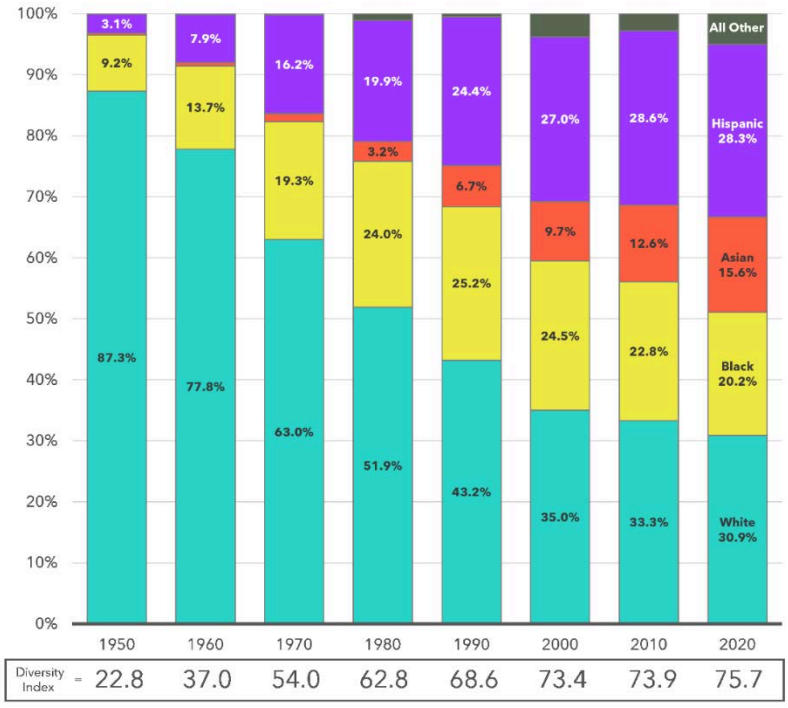

Figure 4.1: Share of Population by Race/Hispanic Origin, New York City, 1950-2020. Source: (City of New York Department of City Planning, 2023).

Figure 4.2, showing population pyramids, is compiled from our analysis using data from 2010 Census (10% sample, IPUMS), and demonstrates that population compositions by age, sex, and race differ substantially across the boroughs of New York City. (Age is shown in 5-year age groups on the y-axis; males on the left half and females on the right half; race/ethnicity groups indicated by color: blue=White, orange=Hispanic, black=Black; yellow=Asian.) While the population in Manhattan is dominated by young adults aged between 25 and 40 and has an extremely low share of school-age children, the Bronx and Staten Island display relatively high proportions of school-age children and, with Staten Island having more middle-aged persons relative to the Bronx. The racial distribution of the population in Brooklyn is rather even, while all other boroughs exhibit larger shares of some populations than others: the population in the Bronx is mostly Hispanic and Black and Queens has a very large share of Asians, whereas Staten Island has a majority White population.

DCP also undertakes periodic short-term analysis of the dynamics of racial and ethnic composition of NYC neighborhoods (City of New York Department of City Planning, 2021) (DCP., 2021). New York City's remarkable diverse population is not evenly dispersed (nor has it ever been) across boroughs or neighborhoods. To understand neighborhood change, DCP also examines decadal change in new construction at the neighborhood level and places these in the context of the change in the racial and ethnic composition of neighborhoods (DCPs "Net New Housing Construction, 2010-2020"), information essential for understanding climate impacts with a racial justice lens despite the short-term nature of the change analysis."

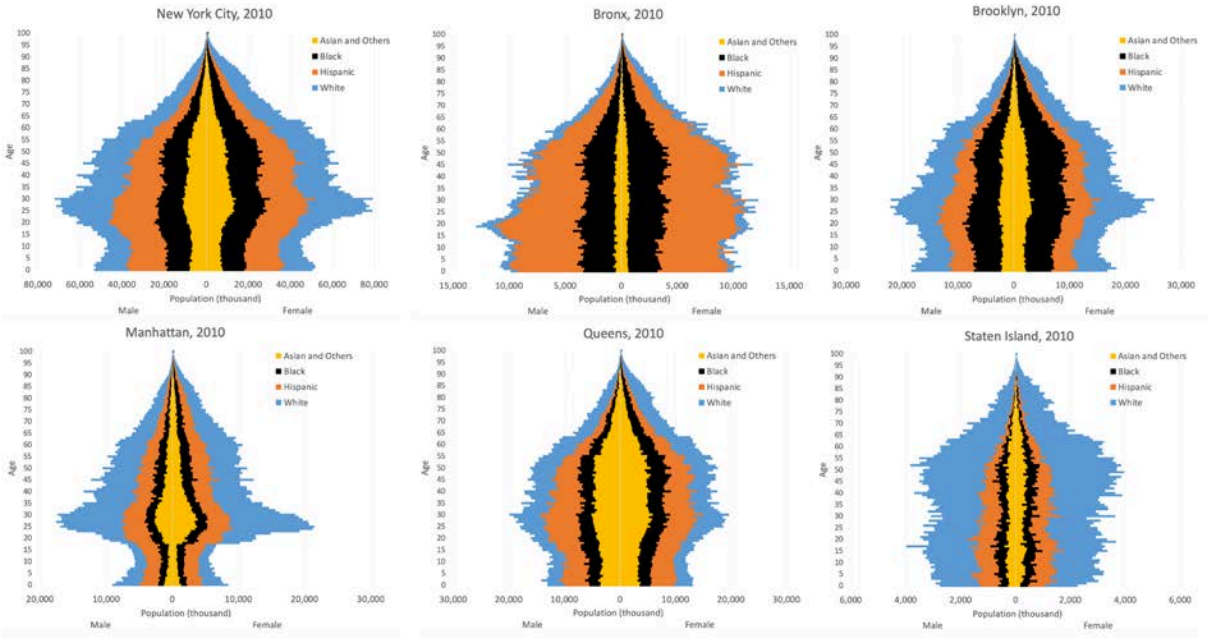

Figure 4.2: Population by age, sex and race for New York City, 2010 (source: authors calculations based on data from 10% sample of U.S. Census microdata, IPUMS). (For higher resolution images see document.)

Methodology

The methodology is divided into three parts: (1) develop demographic assumptions of population futures associated with the SSPs; (2) project the population futures to 2100 with a "multiregional" demographic model; (3) downscale those future populations.

Demographic Assumptions of the Shared Socioeconomic Pathway (SSP) Narratives

In order to project to 2100 in a manner consistent with plausible emissions pathways, the SSP narratives (Riahi et al., 2017) must make assumptions about population processes -- fertility, mortality and life expectancy, migration -- and this has been undertaken as part of a deliberative process at the global scale (KC and Lutz, 2017). Extensions of the SSPs for cities and smaller than national regions are new (Rohat et al., 2019, 2021), and must expand the input narratives to address migration to and within cities. Thus, as a first step in this exercise, and with feedback from demographic analysts at DCP, we identified assumptions about the demographic rates that correspond to the SSP narratives. The projection was undertaken for population by age and sex by borough and broad race/ethnicity groups, but the narratives and their associated assumptions about future population change (such as fertility, mortality and migration futures) were not crafted to be borough-specific or race-specific groups. As a first-attempt to adapt global narratives to New York City and to imagine long-term population

futures, future work could expand these further with narratives about different future demographic rates by borough and race/ethnicity groups. SSP2 -- also called middle of the road -- assumes constant medium fertility, mortality, international and domestic migration; and assumes that the internal migration rates remain unchanged. SSP2 is the first scenario that was explored as its assumptions are most similar to currently observed rates. An SSP1 world is considered a sustainable world, and as such has low fertility, low mortality, and medium low international migration and domestic migration with the rest of the county, but a medium high internal migration between NYC counties. SSPS -- characterized by a conventional development and fossil fuel dependent world -- assumes medium low fertility, low mortality, high international and domestic migration, as well as high internal migration. We highlight these three divergent pathways below. (The two other SSPS are: SSP3 -- which carries the name regional rivalry from the global framework -- is characterized by high fertility and high mortality, low international and domestic migration and medium low internal migration rates. SSP4 -- known as the highly unequal future -- with with very low fertility, medium mortality, medium high international and domestic migration, but low internal migration.) [See Supplemental Materials for the specific application of the changes in demographic rates associated with these underlying assumptions.]

Projection of Population to 2100

We develop a multidimensional and multiregional demographic model for making the county-level population projections. The model is based on the widely-used multistate demographic method and extended from the multiregional model developed by Rogers (1991, 1995, and 2015). For each county, the population is distinguished by age, sex, and race (Figure 4.3a). Age-, sex- and race-specific mortality and fertility are applied to corresponding states of the population leading to reduction and addition of its population. Population also changes due to migration. More importantly, the bilateral migration flows between each of two counties connect all counties into an integrated demographic system (Figure 4.3b). Any changes in a single county due to each component of demographic events (fertility, mortality, internal and external migration of two varieties -- international and domestic) will have impacts on other counties and consequently change the population of the whole city. Moreover, external migrations, either the in- and out-migration from and to other parts of the country or the immigration and emigration from and to foreign countries, also contribute to the population changes of all the counties and the whole city.

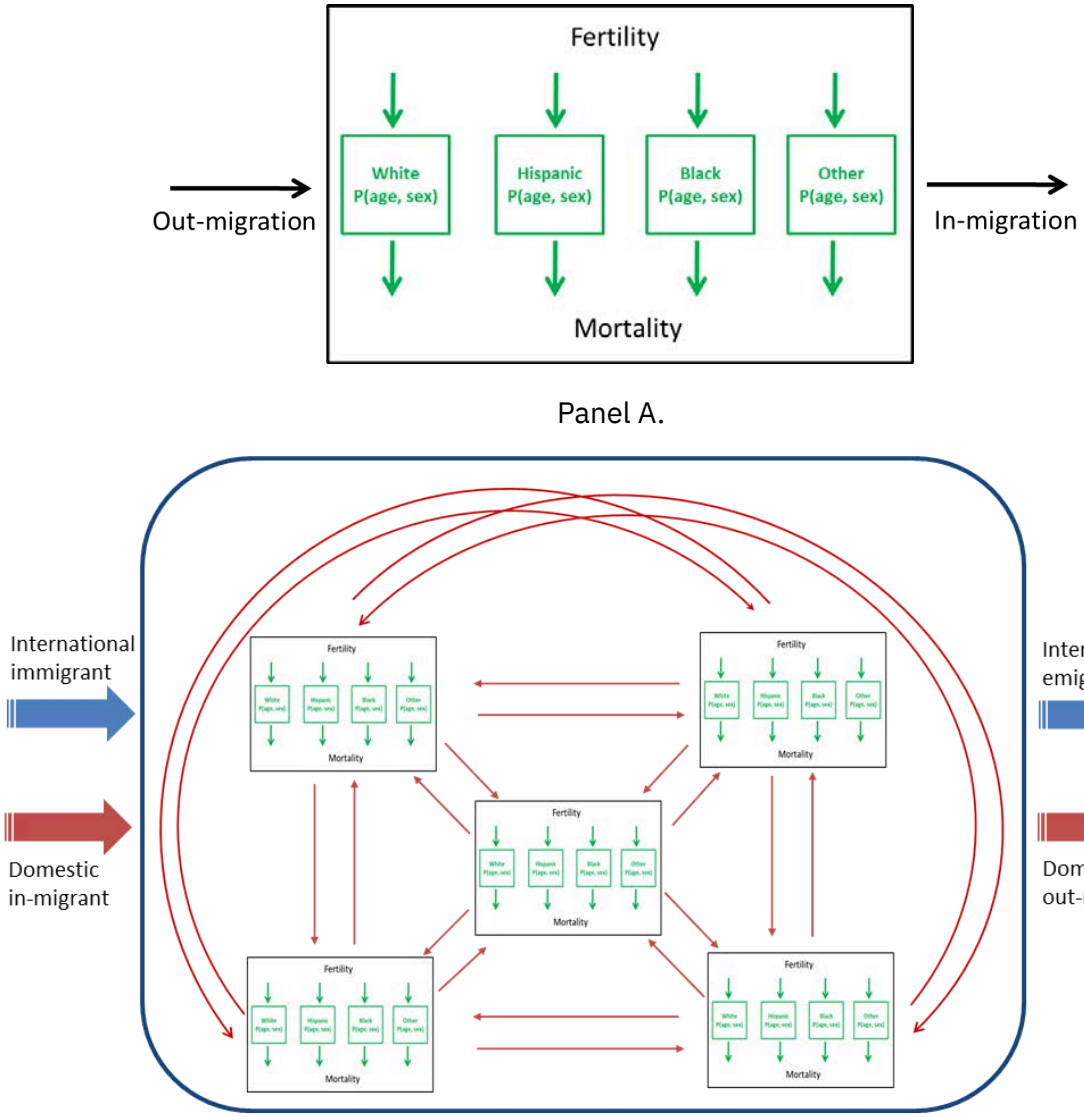

Figure 4.3: Schematic of inputs required for multiregional and multidimensional population projection model by age, sex, and race/ethnicity groups.

The accounting strategy of the model is expressed in the equation below (4.5).

$$\begin{bmatrix} \begin{pmatrix} P_{r1,f}^{0,t+1} \\ P_{r2,f}^{0,t+1} \\ P_{r3,f}^{0,t+1} \\ P_{r4,f}^{0,t+1} \\ P_{r1,f}^{1,t+1} \\ P_{r2,f}^{1,t+1} \\ P_{r3,f}^{1,t+1} \\ P_{r4,f}^{1,t+1} \\ \vdots \end{pmatrix} \\ \begin{pmatrix} P_{r1,m}^{0,t+1} \\ P_{r2,m}^{0,t+1} \\ P_{r3,m}^{0,t+1} \\ P_{r4,m}^{0,t+1} \\ P_{r1,m}^{1,t+1} \\ P_{r2,m}^{1,t+1} \\ P_{r3,m}^{1,t+1} \\ P_{r4,m}^{1,t+1} \\ \vdots \end{pmatrix} \end{bmatrix} = \begin{bmatrix} S_f + B_f & 0 \\ B_m & S_m \end{bmatrix} \begin{bmatrix} \begin{pmatrix} P_{r1,f}^{0,t} \\ P_{r2,f}^{0,t} \\ P_{r3,f}^{0,t} \\ P_{r4,f}^{0,t} \\ P_{r1,f}^{1,t} \\ P_{r2,f}^{1,t} \\ P_{r3,f}^{1,t} \\ P_{r4,f}^{1,t} \\ \vdots \end{pmatrix} \\ \begin{pmatrix} P_{r1,m}^{0,t} \\ P_{r2,m}^{0,t} \\ P_{r3,m}^{0,t} \\ P_{r4,m}^{0,t} \\ P_{r1,m}^{1,t} \\ P_{r2,m}^{1,t} \\ P_{r3,m}^{1,t} \\ P_{r4,m}^{1,t} \\ \vdots \end{pmatrix} \end{bmatrix}$$

Equation 4.5

The population by single year of age (0, 1, ...), sex (f, m), and race (r1, r2, ...) of each county are projected forward in single-year step by a multidimensional transition matrix $\begin{bmatrix} S_f + S_m & 0 \\ B_m & S_m \end{bmatrix}$ where *Bf* and *Bm* are the matrix of birth rates of female population for girls and boys, *Sf* and *Sm* are the survival ratio for female and male population. The survival matrix of *Sg* is derived from the matrix which is constructed based on the combined mortality rate and migration rate.

Using this multiregional and multidimensional model, three goals can be achieved. First, it assists in addressing New York City's demographic heterogeneity, especially racial differences. The model not only accounts for current differences in racial, age, and gender compositions between counties, but also for considerable differences in mortality, fertility, and migration rates by races that will affect future population dynamics in the counties. Furthermore, the multiregional model structure is capable of projecting the population changes of all counties

simultaneously and achieving consistent results for each county and for the City as a whole. Lastly, it provides a model system that meets the requirements for developing scenarios under a variety of socioeconomic and demographic conditions. The model integrates not only all counties into one system through bilateral migration flows, but also connects them to other parts of the country and the world through domestic and international migration. Using this model system, it is possible to make assumptions about future socio-demographic changes that are consistent with the global and national scenarios under the SSP framework.

To make multidimensional population projections for local places like the New York counties, we adopt various indirect estimate techniques, model schedules, and other demographic methods to address data limitations. For instance, the *Whipple Index* and *Myers Index* are applied to correct for age heaping (that is, when population counts "heap" on round numbers, such as those ending in 5 and 10, in part due to recall error when individuals report their age) and other problems related to inaccurately reported ages of the populations. We further use the *Brass Relation Model* to fill gaps of missing data on child mortality (suppressed due to small numbers of observation) for "Asian and other races" in all counties.

Downscaling borough-level future population

We further downscale aggregate (borough-level) population projections of the five counties to 100m resolution grid cells using gravitational population downscaling models (Grubler et al., 2007, Jones & O'Neill, 2013, 2016). These models operate at the grid cell level and assume that people tend to settle closer to already populated places. They parameterize the effects of distance decay and local attractiveness using optimization approaches based on historical grid-based population distributions. They assign a suitability weight to each cell informing its population share from the larger geography. We use Equation 4.6 to derive suitability values.

$$v_i(t) = l_i \left(\sum_{j \in N_i} P_j^{\alpha}(t) e^{-\beta d_{ij}} \right) \qquad \text{Equation 4.6}$$

Where v_i is the suitability weight representing the share of population to be assigned to the focal grid cell i, l_i is the proportion of cell i available for allocation, which is derived by employing physical layers that determine the land availability for population allocation, P_j is the population of neighboring cell j at time t, and d_{ij} is the distance between cells i and j. The number of neighboring cell indices N_i is determined by the gravity window within which the distance-decay effect applies, which we set to 40 km for New York City. Finally, the α and β parameters govern the importance of existing surrounding population concentrations within the 40km neighborhood and their accessibility (as a function of distance) in determining the suitability value, respectively.

The downscaling model is composed of two components, namely calibration and projection. The calibration component uses historical population grids and an optimization approach to estimate the best values for α and β that minimize differences between observed and modeled population grids. The projection component then either uses the estimated values or adjusts them following the scenario guidelines to downscale projected population values at the county level to their constituent 100m resolution grid cells.

We used census blocks and parcel records to create historical population grids for New York City in 2000, 2010 and 2020. We first used the built-year attribute of parcel records to generate the three snapshots, and then allocated population values of blocks to residential parcels weighted by the number of their units. This approach only assigns population values to grid cells within the city boundary. However, we also need population values for the 40 km buffer area around the city. Therefore, we also used GHS-Pop (Schiavina et al., 2023a) products in 2000, 2010 and 2020 from the Global Human Settlement Layer (GHSL) for the buffer area (Schiavina et al., 2023b). This led to historical population grids in the three years for New York City and its surrounding areas (Figure 4.4).

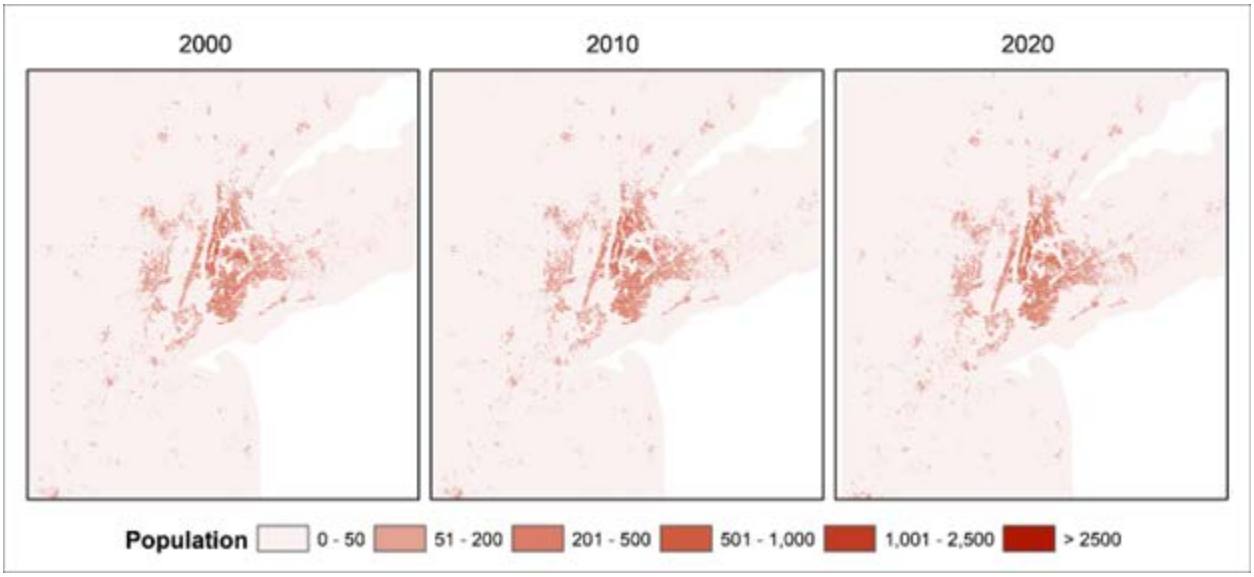

Figure 4.4: Historical population grids in 2000, 2010 and 2020 for New York City and its surrounding areas.

To create a mask layer and quantify l_i values for each grid cell within New York City, we apply different layers, such as protected lands (e.g., national parks), highways and buffers around them, water bodies, cemeteries, and airports to exclude areas within each grid cell. Figure 4.5 shows the current mask layer with values ranging from 0 to 1 demonstrating how much of each pixel is available for population allocation, noting that most area fall into either the first quartile (areas that we do not expect future habitation) or the highest quartiles (areas currently

inhabitant and available for future inhabitation); the middle quartiles represent areas that are comprised of mixed pixels (areas made up of partially protected area and partly inhabited areas).

According to future scenarios rooted in technological developments and policy decisions, we also consider adjusting the estimation of l_i. For example, we may exclude areas that fall in locations prone to sea level rise to conform to SSP1, the scenario where sustainability is prioritized.

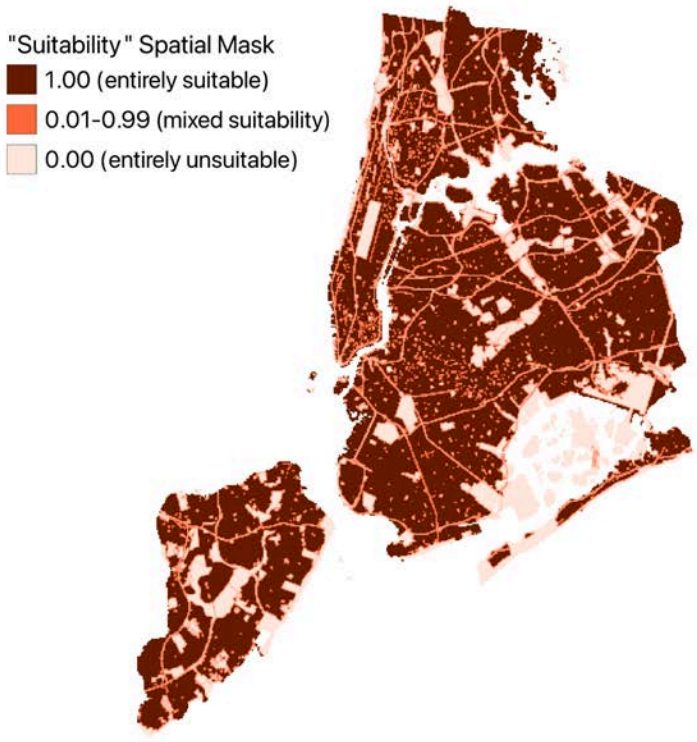

Figure 4.5: Mask layer for New York City regarding suitability for population allocation. Suitability is determined by calculating the proportion of land area in a pixel that is suitable for population allocation, such that it is an area that may have residential housing (not considering the amount of housing currently has) and is not an area that is unlikely to be developed in the future (such as parks, cemeteries, airports, or roads). Higher (darker) values indicate a higher proportion of that pixel has suitability for population allocation to grid cells.

NYC is well known for its ethnic neighborhoods, some of which have emerged, grown, or been displaced over time. We investigated geographic clustering by race/ethnicity and age over time to assess historic trends and the stability of clusters of demographic groups who may vary in their vulnerability to climate change impacts, at a sub-borough level, in order to help frame the downscaling component of this research.

Spatial analyses at the Census tract level revealed clustering with regard to the proportion of people living in each tract who identify with four racial/ethnic groups non-Hispanic Black, non-Hispanic White, Asian, and Hispanic) as well as who are aged 65 and above. The composition of Census tracts in decennial years was analyzed using a Local Indicators of Spatial Autocorrelation (LISA) analysis based on available data from the National Historical Geographic Information System online database (NHGIS). Race/ethnicity data was available at the Census tract level from 1970 through 2020 (Hispanic) or 1980 through 2020 (non-Hispanic White, non-Hispanic Black, Asian) and age data was available from 1970 to 2020. LISA analyses generate local statistics (for each tract) that indicate geographic clusters and outliers (Anselin, 1995). To determine stability over time, since Census tract boundaries have changed within the time period, a spatial join using 2020 tracts was performed to determine if the centroid of a 2020 tract was contained within a high-high cluster for other years, which were calculated based on tracts and corresponding data for each decennial year. Figure 4.6 shows trends over time in high-high clusters of the proportion per tract of each of four race/ethnicity categories and Figure 4.7 shows high-high (HH) clusters for proportion over 65 years of age. There is considerable clustering and stability over time for each racial/ethnic group as well as for population over 65 years of age.

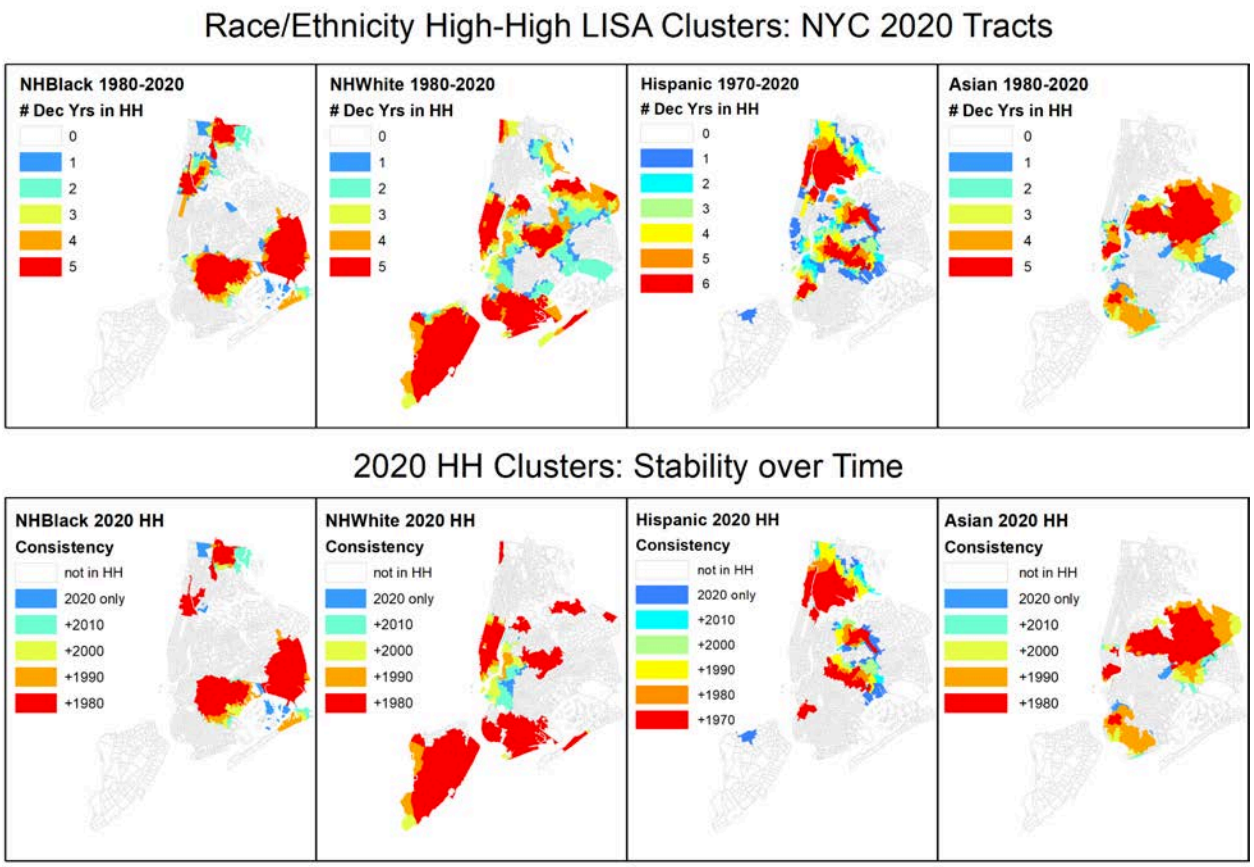

Figure 4.6: Local Indicator of Spatial Autocorrelation (LISA) Maps by race and ethnicity,

tract-level. Note: Census tract boundaries may include some areas where people do not actually live, as indicated in the spatial mask in Figure 4.5. (source: authors calculations based on data from US Decennial Census data, NHGIS)

These maps show census tracts identified as being part of high-high (HH) clusters in a Local Indicators of Spatial Autocorrelation analyses of proportion of tract of each race/ethnicity category. The top row shows census tracts that were identified as high-high in any decennial year (1980-2020 for non-Hispanic Black, non-Hispanic White, and Asian and 1970-2020 for Hispanic) with colors indicating how many decennial years that tract was in the high-high cluster. The bottom row shows the tracts that were identified as part of the high-high cluster for 2020 with colors indicating how many continuous previous decennial years that tract was identified as part of a high-high cluster.

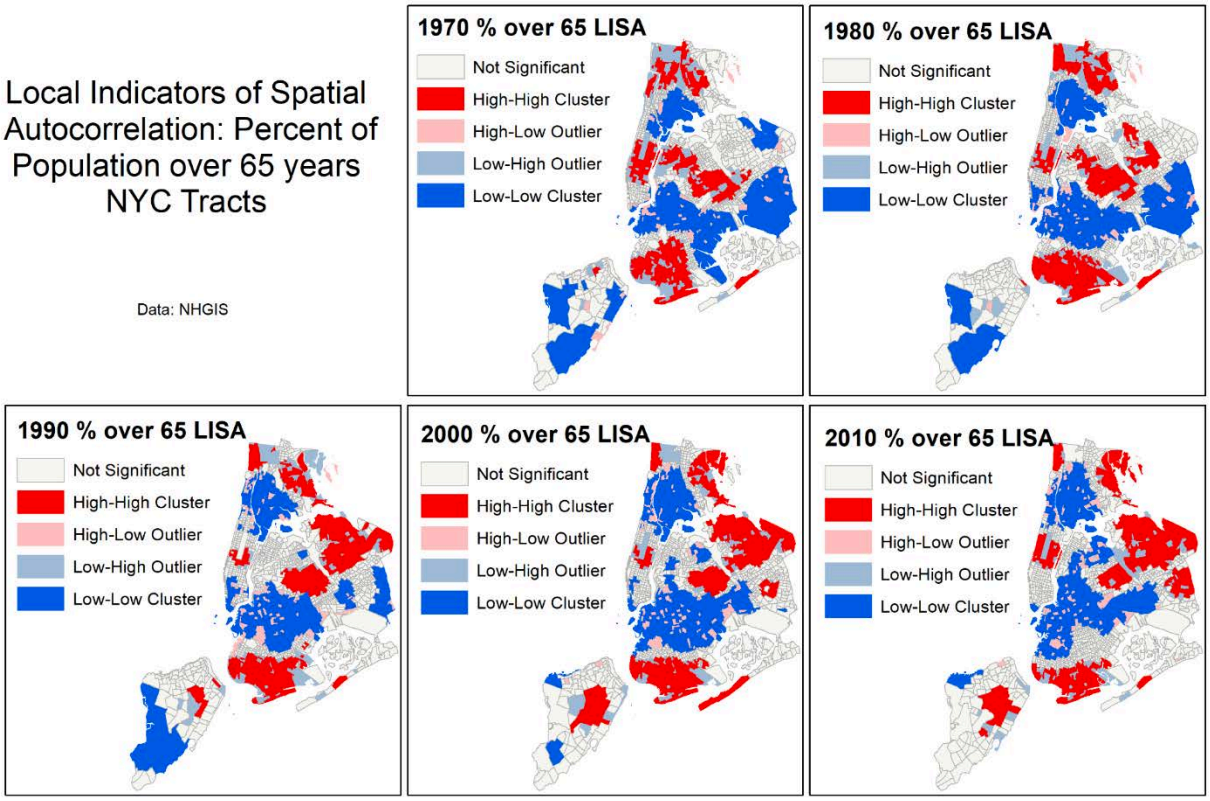

Figure 4.7: These maps show census tracts identified as being part of high-high clusters in a Local Indicators of Spatial Autocorrelation analyses of proportion of people over the age of 65 years in decennial census years 1970 through 2010. Note: Census tract boundaries may include some areas where people do not actually live, as indicated in the spatial mask in Figure 4.5. (Source: authors calculations based on data from U.S. Decennial Census data, NHGIS)

By identifying key change patterns in neighborhoods, the downscaling can maintain such patterns in the future, or loosen them, in accordance with the various SSP scenarios.

Results

The following results are preliminary as of this writing. Using an SSP2 narrative, we begin by estimating the current population -- as a check on our methodology -- and find a total population of NYC at around 8.8 million in 2020, which is reasonably similar to the recorded population of the City of 8.77 million persons. Figure 4.8 shows the total population for NYC each SSP throughout the century. As for the projected population in the future, under an SSP2 future, the total population is expected to reach a maximum of nearly 9 million in 2040, and is estimated to be around 7.5 million in 2100. In an SSP1 world, population also declines to a much lower level of 6.7 million by the end of the century, but remains close to 8.5 million mid-century. SSP4, the unequal future, also sees population loss to 6.2 million at the end of the century. Growth is seen in both SSP3 and SSP5, with population reaching near 9.2 million mid-century in SSP5. It is notable that in none of these narratives that the future population of NYC grows by more than an additional million persons from its current population size. (This may be as much a constraint in our imagining of future demographic narratives as it is in the observed historical patterns and trends from which the futures rates are applied.)

New York City Population Projected, according to Shared Socioeconomic Pathways, to 2100

Total Population, by year and Shared Socioeconomic Pathway		
SSP	2050	2100
1	8,490,829	6,724,512
2	8,868,458	7,467,009
3	8,815,229	8,969,614
4	8,521,897	6,156,485
5	9,174,676	8,337,778
Constant	6,900,331	5,803,989

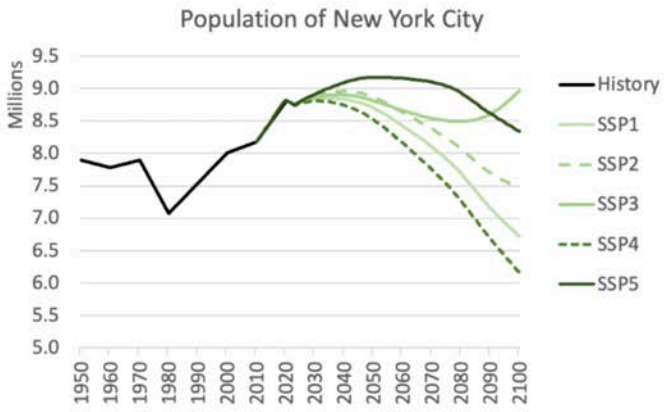

Figure 4.8: Population Projection for New York City according to five adapted Shared Socioeconomic Pathways, through 2100.

As for comparison, if we assume the constant demographic rates from 2010 continue into the future, and remain unchanged throughout the century (a pattern heretofore unobserved but frequently used by models that simply interpolate future trends based on the past decade), we project the population was at its maximum in 2010 and continues to decrease until it reaches

5.8M in 2100. (The annual series for this constant rate series and the five SSPs are shown in Supplemental Table 4.5.)

Population for each borough, projected and for the historical period, according to SSP1, SSP2 and SSP5 is shown in Figure 4.9.

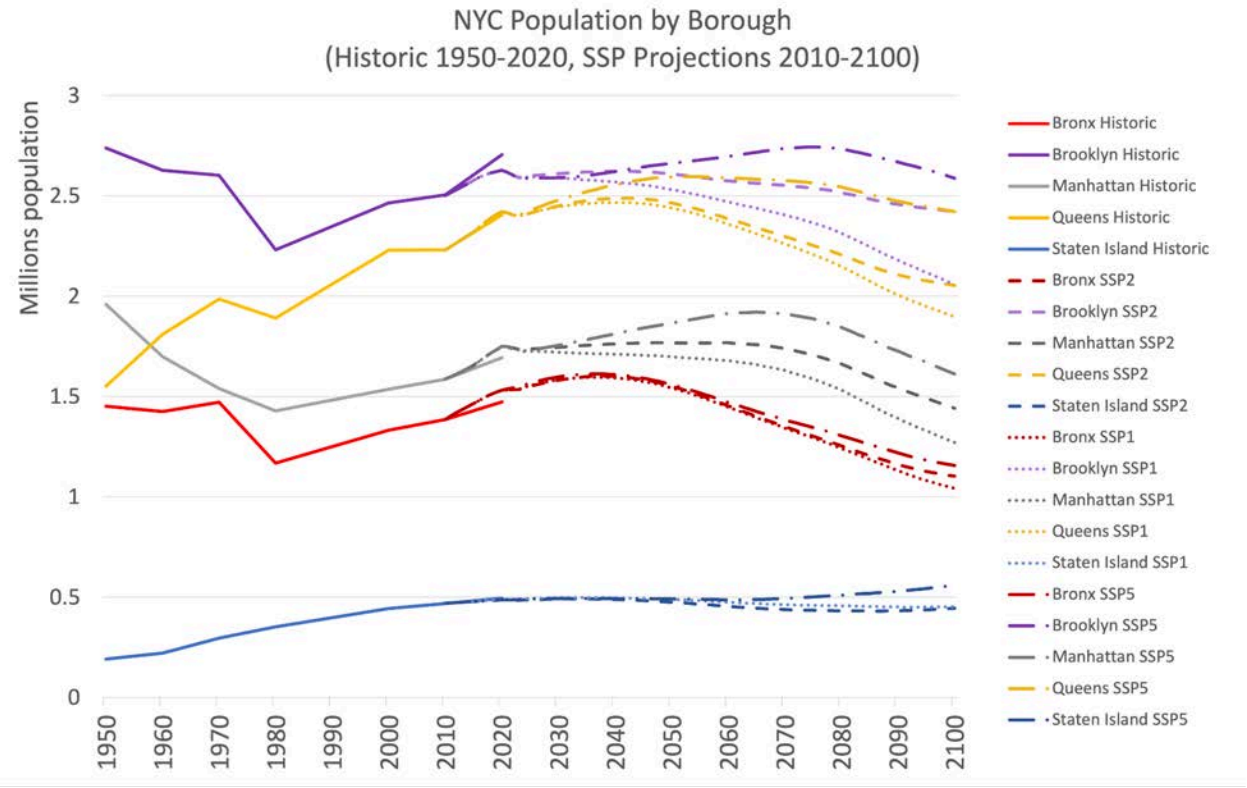

Figure 4.9: Population by borough, for the historic period (1950-2022) and future (2010-2100) corresponding to the SSP1, 2 and 5 narratives. *Historic indicates historic record (solid line) and projection has dashed line.*

The city-wide fluctuations (Figure 4.8) are in part due to differences in borough-specific growth, seen in Figure 4.9, where in an SSP5 world growth is predicted for Manhattan, Brooklyn and Queens but declines for the Bronx. (Staten Island's population remains largely stable.) These changes result from assumptions about natural increase -- fertility and mortality -- as well as migration (international, in-and-out domestic [i.e., between NYC and the rest of the U.S.], and internal [between boroughs of NYC]). Figure 4.10 shows the decomposition of future population change. For example, under SSP2 the population of Queens (bottom middle panel), which is a destination for many international migrants, is projected to decline as its fertility declines and as residents (including new international migrants)

out-migrate to the rest of the U.S.

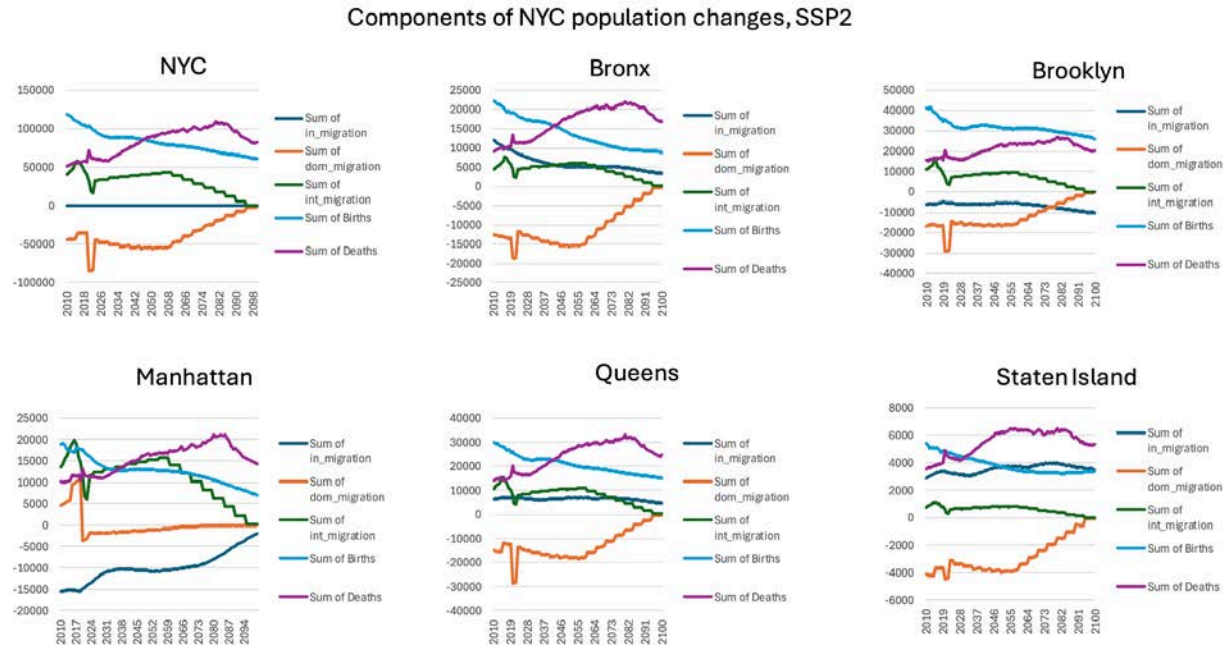

Figure 4.10: Demographic components of change (internal migration, domestic migration, international migration, births and deaths) according to an SSP2 future, all NYC and by borough.

As seen in Figure 4.10, all else equal, migration (domestic and international) is an important contributor to the future population of NYC, especially in futures where natural increase (births minus deaths) continue the current pattern of decline. Predicting migration rates, particularly at a sub-city level, is much more variable than predictions of changes based on fertility and mortality which have fairly stable long-term trends. Associated with these trends are important implications for population aging. In sum, the total population size as well as the age and race/ethnicity composition of NYC will be largely impacted by migration trends, such as the magnitude of international immigration and the rate of migration from NYC to and from other parts of the U.S.

Figure 4.11 shows the implications of an SSP2 future on the race and ethnic composition in the city, by borough. The Black population as a share of the total population declines, largely because in the observed historical period, the share as well as the absolute number of New York City's Black population has been declining (DCP 2023). This is most notable in Brooklyn but occurs in all boroughs. Other notable shifts include increasing shares of the White population of Brooklyn and the Asian population in Queens. Staten Island also sees an increasing share of the Asian population from mid-century onward. (Similar broad-strokes patterns are observed across all SSPs.)

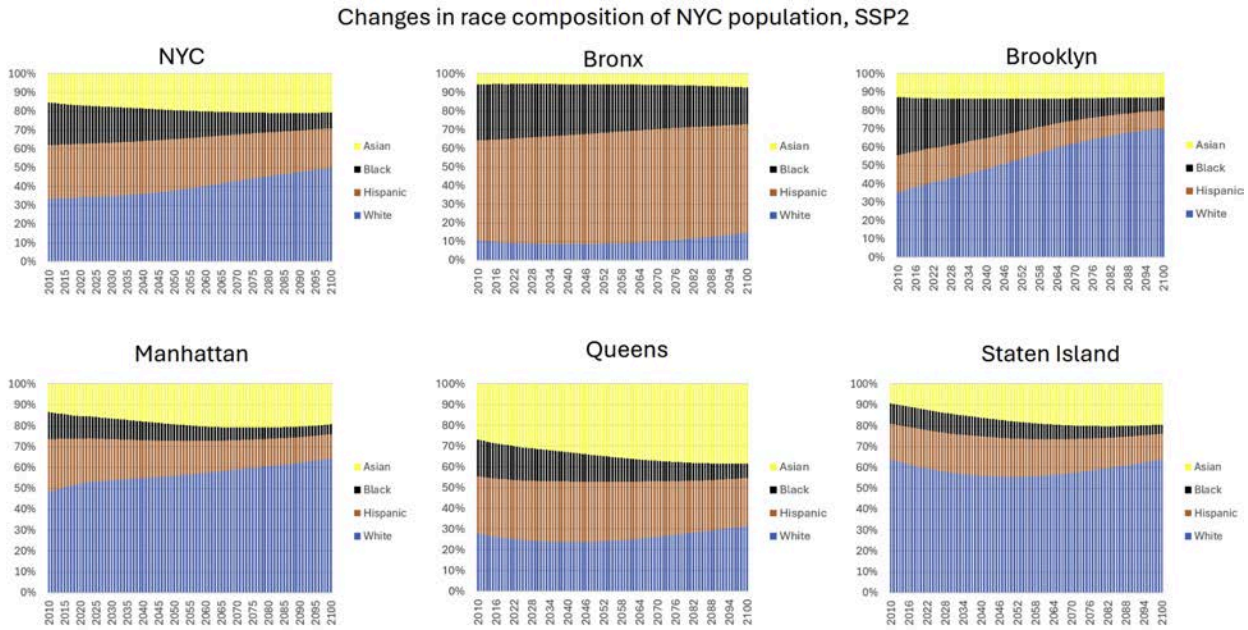

Figure 4.11: Changes in race and ethnic composition of New York City, to 2100 according to an SSP2 future.

Finally, this exercise allows us to project future population by age (and borough) and race, shown in Figure 4.12 for all NYC by SSP. In all future scenarios, NYC population is much older, except for SSP3. In SSP1 (the sustainable future), SSP3 (inequality), and SSP5 (the fossil-fuel development) the population pyramid is inverted showing that there are more older adults than young persons. This has implications for future growth, but also for vulnerability to climate change. (The gender-unevenness, driven by more young women relative to men, seen clearly in 2010 makes its way through the pyramid as population ages.)

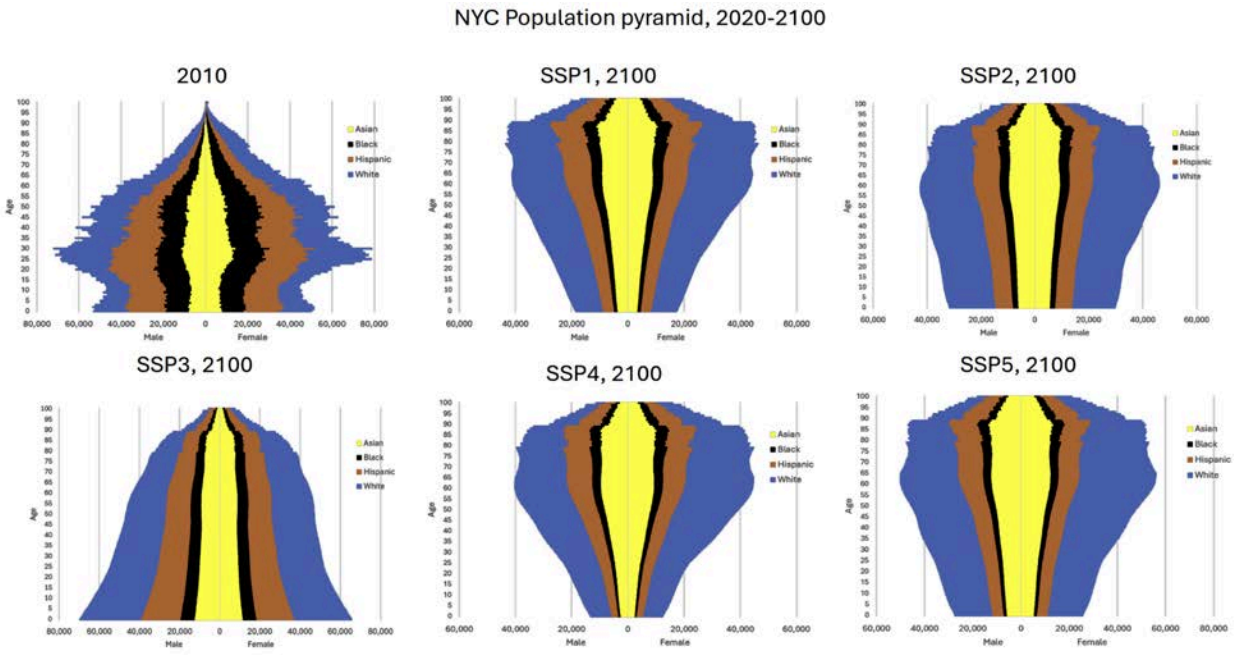

Figure 4.12: Population pyramid projected for New York City, 2100 by 5 SSPs compared to 2010.

4.3 Next steps

The Task 4 team conducted a valuation of human health-related costs associated with the harmful impacts of several types of climate-sensitive events in New York City, between the years 2000 to 2019. The hazards considered include mortality (premature deaths) and morbidity (illnesses) from heat, tropical cyclones, and power outages during the study period. Valuation studies can contribute to our understanding of climate change's impacts on New York City for several reasons: health impacts of observed climate hazards are very seldom incorporated into economic assessments of climate change's effects; these analyses demonstrate the possible future costs of continued greenhouse gas emissions without more robust adaptation investments; and the cost estimates can help target health interventions to avoid even more dramatic impacts costs and evaluate the effectiveness of adaptation measures (Limaye et al., 2020).

Our overall estimates of morbidity cases should generally be considered conservative tallies of total morbidity for at least two reasons. First, since our analysis was not a climate attribution study but instead relied on estimates from existing studies, we limited our investigation to a subset of epidemiological studies that examined climate hazards in New York State or City. For example, we did not investigate the health-related impacts of ambient ozone air pollution or airborne allergenic pollen, even though those types of health hazards have been characterized

in other geographies during our overall analysis period (Cromar et al., 2016; Anenberg et al., 2017). Likewise, we did not capture the impacts of heat on non-health care related impacts, such as academic performance (Park et al., 2020) and labor market outcomes (Graff Zivin and Neidell, 2014) because geographically-appropriate estimates were not available. As such, there are likely to be other climate-sensitive events or outcomes relevant to NYC that our analysis did not capture. Second, even for the climate-sensitive hazards that we did analyze, we could not quantify the full range of health effects known to be associated with each climate-sensitive event. Our health cost estimates include ED and hospital visits, but do not include other types of health care impacts, such as outpatient care, use of prescription medications, and home health care services. While other healthcare cost and utilization databases can enable estimation of these additional health-related costs (Declet-Barreto et al., 2021), we lacked epidemiological evidence relevant to NYC for these additional endpoints. Additional epidemiological evidence relevant to NYC is an important step for understanding the full range of morbidity impacts.

The process for monetizing the mortality and morbidity counts required assumptions that introduced two important limitations. First, we valued changes in mortality as lives lost rather than life-years lost, a necessary step given that the existing studies provided estimates of changes in mortality counts and not changes in life expectancy. Without knowing the changes in life expectancy that accompany the loss in mortality, it is difficult to assess the impact of this assumption on the total monetary value we estimate. Second, our morbidity costs were calculated using a cost of illness approach, which only includes health care costs and lost wages. This approach generally understates the true costs from environmental impacts (Harrington and Portney, 1987), excluding factors such as pain and suffering people experience from climate-sensitive events and avoidance behaviors people engage in to reduce the impacts from climate-sensitive events. Epidemiological evidence of the impacts of climate-sensitive events on these other outcomes relevant to NYC was unavailable. Both of these limitations represent important areas for improving the monetized values.

Another important limitation in our analysis regards the role of adaptation. Throughout the analysis, we assume a constant dose-response relationship between the climate-sensitive event and health outcomes. Various adaptations, such as residential air conditioning (AC), can moderate the impact of climate-sensitive events. Since access to such technologies varies throughout the city, their benefits are unlikely to be evenly felt across the city. Accounting for such technologies not only affects the estimated dose-response relationship between the climate-sensitive event and health outcome, but also represents a defensive health cost expenditure that is part of the cost of exposure to climate-sensitive events. Future efforts to incorporate this adaptation is important for understanding the full economic costs from a warmer climate.

The health effect estimates and corresponding economic damages we estimated represent aggregate numbers for the entire city. Marginalized populations, including low-income populations, populations of color, and Medicare and Medicaid recipients, shoulder a disproportionate burden of the health harms of climate change (U.S. Global Change Research Program, 2016; Limaye et al., 2019). This burden is linked to disproportionate exposures to climate hazards, higher rates of pre-existing health conditions that make people more vulnerable to climate hazards, and economic insecurity related to lack of healthcare access and affordability (Limaye, 2022). For example, for our heat vulnerability analysis, we estimated morbidity and mortality linked to a uniform estimate of temperature applied across the entire city population, which did not represent the spatial variability in vulnerability to hot weather that has been demonstrated by other studies of NYC (Declet-Barreto et al., 2021, Rosenthal et al., 2014, Madrigano et al., 2015). Further efforts to understand the distribution of these impacts across the City will highlight important gaps in our understanding and help to better direct city resources.

Additional next steps for population futures include downscaling constraints (including one for an “equity” based future, and one that prevents future population from living in expected floodable areas). Results of downscaling maps (not included in results above) will also be shared, including adding layers of future flood zones, consistent with a ‘sustainability’ SSP narrative.

In addition to exploring the implications of all five SSP narratives for NYC, another next step is to look at the implications of these narratives for the population composition as broken down by age, gender, and race/ethnicity for each borough - different narratives may produce highly varying racial compositions, in part because of the differential rates of fertility and mortality, as well as migration, assumed by more and less equal or affluent socioeconomic futures. The different SSP narratives also reveal the possibility of aging pathways -- that is, the degree and pace of population aging -- which has important implications for climate adaptation planning but these were not showcased herein. Another next step would be to facilitate further development of these SSP narratives with a wide range of engagement, including stakeholders such as city planners and community members. These narratives could make borough- or race/ethnicity-specific adjustments or assumptions about demographic futures, for example, exploring the potential demographic conditions that might foster or respond to future higher density development in areas that have more single-family housing such as Staten Island or Eastern Queens (such as through migration and fertility).

Finally, additional next steps for integrating health impacts with future populations here will be to link the population future with the possible future health exposures, in order to estimate

future health cost by race/ethnicity and age, as well as neighborhood. This will allow us to associate health costs with futures that take different expected pathways.

References

Adeyeye, T., T. Insaf, M. Al-Hamdan 4, S. Nayak, N. Stuart, S. DiRienzo, W. Crosson (2019). "Estimating policy-relevant health effects of ambient heat exposures using spatially contiguous reanalysis data." Environmental Health, 18:35.

Anderson, G., M. Bell (2012). "Lights out. Impact of the August 2003 Power Outage on Mortality in New York, NY." Epidemiology, 23(2): 189-193.

Anenberg, S., K. Weinberger, H. Roman, J. Neumann, A. Crimmins, N. Fann, J. Martinich, P. Kinney. 2017. "Impacts of Oak Pollen on Allergic Asthma in the United States and Potential Influence of Future Climate Change: Climate Impacts on Oak Pollen and Health." GeoHealth 1 (3): 80–92. https://doi.org/10.1002/2017GH000055.

Balk, D., Tagtachian, D., Jiang, L., Marcotullio, P., Cook, E.M., Jones, B., Mustafa, A. and McPhearson, T., 2022. Frameworks to envision equitable urban futures in a changing climate: A multi-level, multidisciplinary case study of New York City. *Frontiers in Built Environment*, *8*, p.949433.

Baruch College. (2020). NYC Geodatabase. Baruch Geoportal - Baruch College Confluence Service. https://www.baruch.cuny.edu/confluence/display/geoportal/NYC+Geodatabase

BLS (2004). Quarterly Census of Employment and Wages. Available at https://www.bls.gov/cew/.

City of New York Department of City Planning. (2023, March 30). Stability & Change in New York City Neighborhoods, 2010 to 2020. Stability & Change in New York City Neighborhoods, 2010 to 2020. https://storymaps.arcgis.com/stories/c7bf9175168f4a2aa25980cf31992342

Cromar, K., L. Gladson, L. Perlmutt, M. Ghazipura, G. Ewart. 2016. "American Thoracic Society and Marron Institute Report. Estimated Excess Morbidity and Mortality Caused by Air Pollution above American Thoracic Society–Recommended Standards, 2011–2013." Annals of the American Thoracic Society 13 (8): 1195–1201. https://doi.org/10.1513/AnnalsATS.201602-103AR.

Declet-Barreto J, C Herrera, A Huang, C Corbin-Mark (2021). Summer in the City: Improving Community Resilience to Extreme Summertime Heat in Northern Manhattan. WEACT and NRDC report. Available at: https://www.nrdc.org/sites/default/files/community-resilience-summertime-heat-nomanhattan-report.pdf.

Dominianni, C., K. Lane, S. Johnson, K. Ito, T. Matte (2018). "Health Impacts of Citywide and Localized Power Outages in New York City." Environmental Health Perspectives, 126(6).

Gamble, J, J. Balbus, M. Berger, K. Bouye, V. Campbell, K. Chief, K. Conlon, A. Crimmins, B. Flanagan, C. Gonzalez-Maddux, E. Hallisey, S. Hutchins, L. Jantarasami, S. Khoury, M. Kiefer, J. Kolling, K. Lynn, A. Manangan, M. McDonald, R. Morello-Frosch, M.H. Redsteer, P. Sheffield, K. Thigpen Tart, J. Watson, K.P. Whyte, A.F. Wolkin (2016). Ch. 9: Populations of Concern. The Impacts of Climate Change on Human Health in the United States: A Scientific Assessment. U.S. Global Change Research Program, Washington, DC, 247–286. http://dx.doi.org/10.7930/J0Q81B0T

Graff Zivin, J., M. Neidell (2014). "Temperature and the allocation of time: Implications for climate change," *Journal of Labor Economics* 32 (1), 1-26.

Harrington, W., P. Portney (1987). "Valuing the benefits of health and safety regulation." Journal of Urban Economics, 22(1): 101-112.

Jiang, L., O'Neill, B. C., Zoraghein, H., & Dahlke, S. (2020). Population scenarios for U.S. states consistent with shared socioeconomic pathways. Environmental Research Letters, 15(9), 094097. https://doi.org/10.1088/1748-9326/aba5b1

KC, S., and Lutz, W. (2017). The human core of the shared socioeconomic pathways: Population scenarios by age, sex and level of education for all countries to 2100. Glob. Environ. Change 42, 181–192. doi:10.1016/j.gloenvcha.2014.06.004

Lamie, C., D. Bader, K. Graziano, R. Horton, K. John, N. O'Hern, S. Spungin, S. (2024). Chapter 2: New York State's changing climate. In New York State Climate Impacts Assessment [Interim version for public release].

Limaye, V, W. Max, J. Constible, K. Knowlton (2019). "Estimating the Health-Related Costs of 10 Climate-Sensitive U.S. Events During 2012." GeoHealth, 3(9): 245-265.

Limaye, V. (2022). "Reducing the Inequitable Health and Financial Burdens of Climate Change." One Earth 5 (4): 320–23.

Limaye, V., W. Max, J. Constible, K. Knowlton (2020). "Estimating the Costs of Inaction and the Economic Benefits of Addressing the Health Harms of Climate Change." Health Affairs 39 (12): 2098–2104.

Lin, S., M. Luo, R. Walker, X. Liu, S. Hwang, R. Chinery (2009). "Extreme High Temperatures and Hospital Admissions for Respiratory and Cardiovascular Diseases." Epidemiology, 20 (5): 738-746.

Lin, S., M. Sun, E. Fitzgerald, S. Hwang (2016). "Did summer weather factors affect gastrointestinal infection hospitalizations in New York State?" Science of the Total Environment, 550:38-44.

Madrigano, J., K. Ito, S. Johnson, P. Kinney, T. Matte (2015). "A Case-Only Study of Vulnerability to Heat Wave–Related Mortality in New York City (2000–2011)." Environmental Health Perspectives, 123(7): 672-678.

Morozovskaya, L. and Lund, T. (2020). 2055 Socioeconomic & Demographic Forecasts Overview. New York Metropolitan Transportation Council.

New York City Department of Health and Mental Health (DOHMH) (2022). “2022 New York City Heat-Related Mortality Report.” Accessed at https://nyccas.cityofnewyork.us/nyccas2022/report/1.

NOAA. (n.d.). Daily summaries station details (LAGUARDIA AIRPORT, NY US). National Centers for Environmental Information. Available at https://www.ncdc.noaa.gov/cdo-web/datasets/GHCND/stations/GHCND:USW00014732/detail

Park, R., J. Goodman, M. Hurwitz, J. Smith (2020). "Heat and Learning." American Economic Journal: Economic Policy, 12 (2): 306-39.

Parks, R., V. Kontis, G. Anderson, J. Baldwin, G. Danaei, R. Toumi, F. Dominici, M. Ezzati, M. Kioumourtzoglou, (2023). “Short-term excess mortality following tropical cyclones in the United States.” Science Advances, 9(33).

Riahi, K., Van Vuuren, D. P., Kriegler, E., Edmonds, J., O’Neill, B. C., Fujimori, S., et al. (2017). The shared socioeconomic pathways and their energy, land use, and greenhouse gas emissions implications: An overview. Glob. Environ. change 42, 153–168. doi:10.1016/j.gloenvcha.2016.05.009

Rohat, G., Wilhelmi, O., Flacke, J., Monaghan, A., Gao, J., Dao, H., et al. (2019). Characterizing the role of socioeconomic pathways in shaping future urban heat-related challenges. Sci. total Environ. 695, 133941. doi:10.1016/j.scitotenv.2019.133941

Rohat, G., Wilhelmi, O., Flacke, J., Monaghan, A., Gao, J., van Maarseveen, M., et al. (2021). Assessing urban heat-related adaptation strategies under multiple futures for a major US city. Clim. Change 164 (3), 61–20. doi:10.1007/s10584-021-02990-9

Rosenthal, J., P. Kinney, K. Metzger (2014). “Intra-urban vulnerability to heat-related mortality in New York city,” 1997–2006. Health Place 30, 45–60

Qu, Y., W. Zhang, A. Boutelle, I. Ryan, X. Deng, X. Liu, S. Lin (2023). “Associations Between Ambient Extreme Heat Exposure and Emergency Department Visits Related to Kidney Disease.” American Journal of Kidney Disease, 81(5):507-516.

Seil, K, A. Spira-Cohen, J. Marcum (2016). “Injury Deaths Related to Hurricane Sandy, New York City, 2012.” Disaster Medicine and Public Health Preparedness, 10(3):378-85.

Shi, Liuhua, Pengfei Liu, Yan Wang, Antonella Zanobetti, Anna Kosheleva, Petros Koutrakis, and Joel Schwartz. 2016. “Chronic Effects of Temperature on Mortality in the Southeastern USA Using Satellite-Based Exposure Metrics.” Scientific Reports 6 (1): 30161.

US DHHS (2021). “Updating Value per Statistical Life (VSL) Estimates for Inflation and Changes in Real Income.” Office of the Assistant Secretary for Planning and Evaluation, available at https://aspe.hhs.gov/reports/updating-vsl-estimates.

U.S. Global Change Research Program (2016). “The Impacts of Climate Change on Human Health in the United States: A Scientific Assessment.” https://health2016.globalchange.gov/downloads.

Yoo, E., Y. Eum, J. Roberts, Q. Gao, K. Chen (2021). “Association between extreme temperatures and emergency room visits related to mental disorders: A multi-region time-series study in New York, USA.” Science of the Total Environment, 792:148246.

Zoraghein, H., & O’Neill, B. C. (2020a). A spatial population downscaling model for integrated human-environment analysis in the United States. Demographic Research, 43, 1563–1606.

Zoraghein, H., & O’Neill, B. C. (2020b). U.S. State-level Projections of the Spatial Distribution of Population Consistent with Shared Socioeconomic Pathways. Sustainability, 12(8), Article 8. https://doi.org/10.3390/su12083374

Appendix 4.1

Table 4.1: Summary of heat-health studies relevant for NYC

Study	Location & time period	Months analyzed	Outcome	Visit	ICD9 or 10 codes	Temp. measure	RP (°F)	TT (°F)
DOHMH (2022)	NYC, 2011-20	May-Sep	Natural cause mortality	-	<800; A00-R99	Daily Max. Temp.	71	82
Yoo et al. (2021)	NYS, 2009-16	all year	Mental health	ED	290-319; F00-F99	Daily Ave. Temp.	64	74.5
Lin et al. (2016)	NYS, 1991-2004	Jun-Aug	GI	H	1-5, 8, 8.6, 6, 7, 9	Daily Max. Temp.	71	82
Adeyeye et al. (2019)	NYS, 2008-12	May-Sep	Heat stress	ED & H	992.0–992.9; E900.0, E900.9	Daily Max. Temp.	80.6	82
			Dehydration		276.51		78.08	82
			AKF		584.5–584.9		76.46	82
			CVD		390–398, 401–405, 410–417, 420–438, 440–448, 451–459		74.84	82
Lin et al. (2009)	NYC, 1991-2004	Jun-Aug	CVD	H	393–396, 401–405, 410 – 414, 427, 428, 430–434, 436–438	Daily Max. Temp.	84.92	84.92

			Respiratory		491, 492, 493, 496 (plus 466 and 490 for age 0-4)		84.02	84.02

Notes: H = hospital visits, ED = emergency department visit, GI = gastrointestinal, AKF = acute kidney failure, CVD = cardiovascular, RP = reference point, TT = temperature threshold. Reference point is the reference category for the relative risk. Temperature threshold is the threshold above which we calculate climate-sensitive events.

Table 4.2: Summary of tropical cyclone studies relevant for NYC

Study	Location	Time Period	Event(s)	Outcome	Visit	ICD9 or 10 codes
Parks et al. (2023)	United States	1988–2019	Tropical Cyclones	All-Cause Mortality		A00-Y89
Seil et al. (2016)	NYC	2012	Hurricane Sandy	External cause of death		X37
Limaye et al. (2019)	New York State	2012	Hurricane Sandy	Various morbidity outcomes	ED & H	

Notes: H = hospital visits, ED = emergency department visit. Although Parks et al. estimated mortality impacts for all tropical cyclones, only estimates for Hurricane Sandy were statistically significant.

Table 4.3: Summary of power outage studies relevant for NYC

Study	Location	Time Period	Event(s)	Outcome	Visit	ICD9 or 10 codes
Anderson et al. (2012)	New York City	2003	2003 Northeast Blackout	All-Cause Mortality		A00-Y89

Dominianni et al. (2018)	New York City	2003	2003 Northeast Blackout	Respiratory	H	490-497, J40-J47

Notes: H = hospital visits

Table 4.4: Total health-related cases and economic costs from climate-sensitive events in New York City, 2000-19

Climate Sensitive event	Mortality counts	Hospital visits	ED visits	Mortality costs (mid-VSL, $bn)	Morbidity costs ($bn)	Total costs (mid-VSL, $bn)	Total costs (low-VSL, $bn)	Total costs (high-VSL, $bn)
Heat	6,991	35,698	26,429	79.69	1.13	80.83	38.18	122.77
Power Outage	90	410	-	1.03	0.01	1.03	0.48	1.57
Tropical cyclones	133	552	1,659	1.52	0.08	1.59	0.78	2.39
Total	7,214	36,660	28,088	82.24	1.21	83.45	39.45	126.73
Annual Average	361	1,833	1,404	4.11	0.06	4.17	1.97	6.34

Figure 4.9: Number of days with daily maximum temperature above 82°F in New York City, 2000-2019

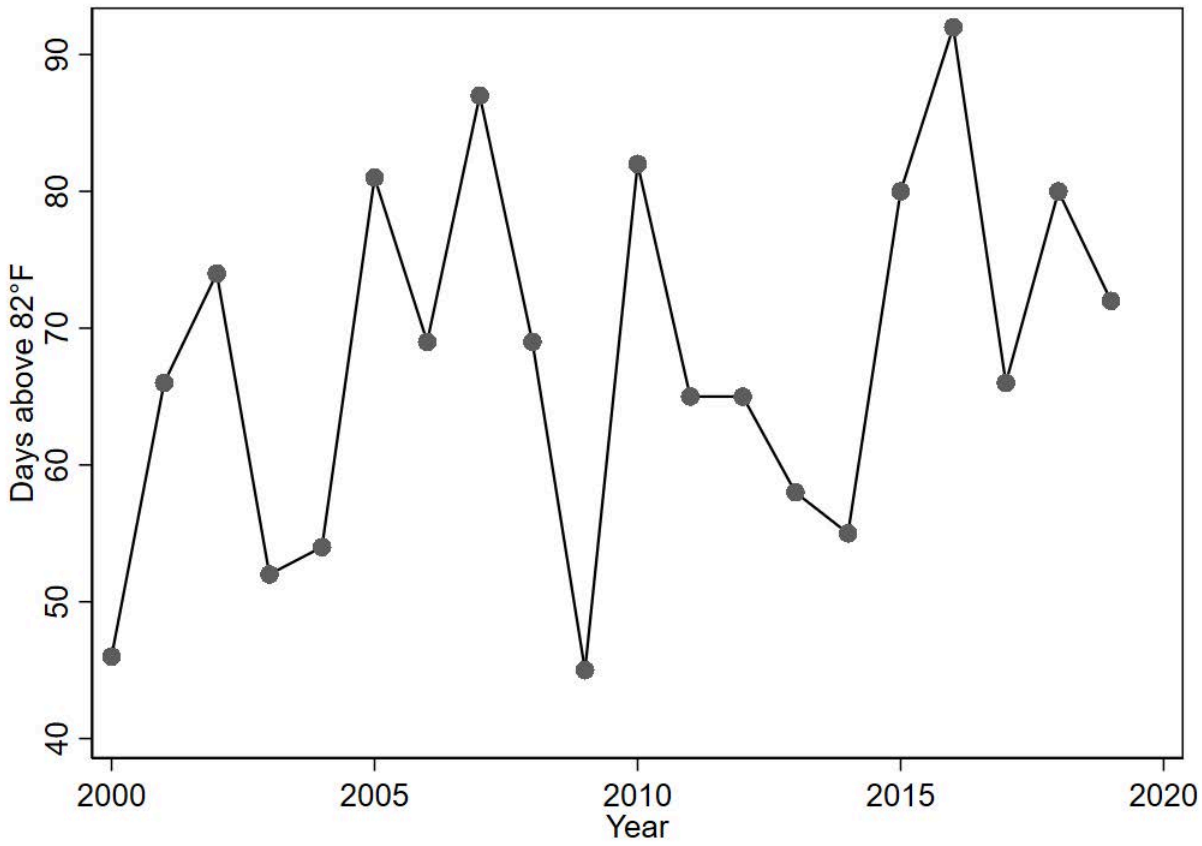

Notes: Maximum Daily Temperature from 2000 to 2019 was obtained from the NOAA station at LaGuardia Airport. This data encompasses all days of the year.

Figure 4.10: Variation in maximum daily temperature for days above 82°F in New York City, 2000-2019

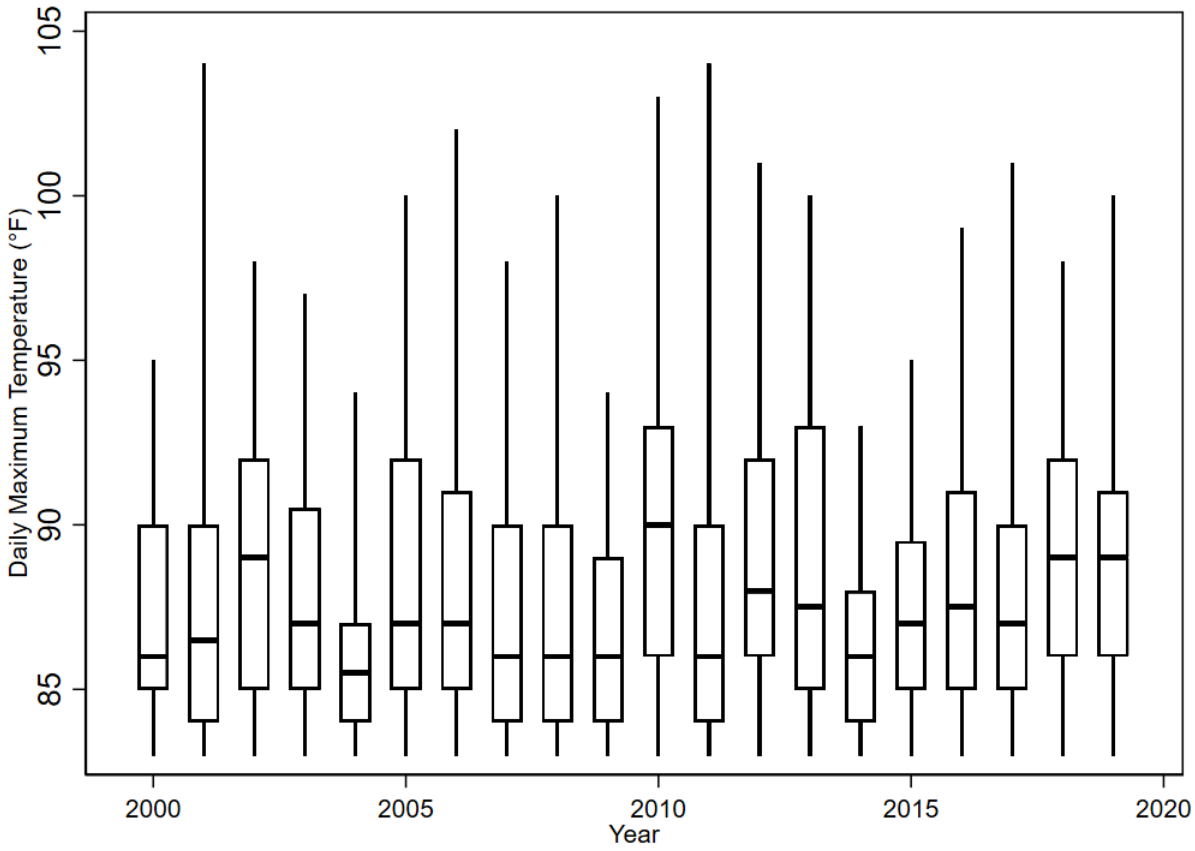

Notes: Daily Maximum Temperature from 2000 to 2019 was obtained from the NOAA station at LaGuardia Airport. This data encompasses all days of the year. The top and bottom of each line represents the maximum and minimum temperature, respectively, for each year. The top and bottom of each box represents the 75th and 25th percentile, respectively, for each year. The middle line represents the median for each year.

Figure 4.11: Mortality from climate-sensitive events in New York City, 2000-2019

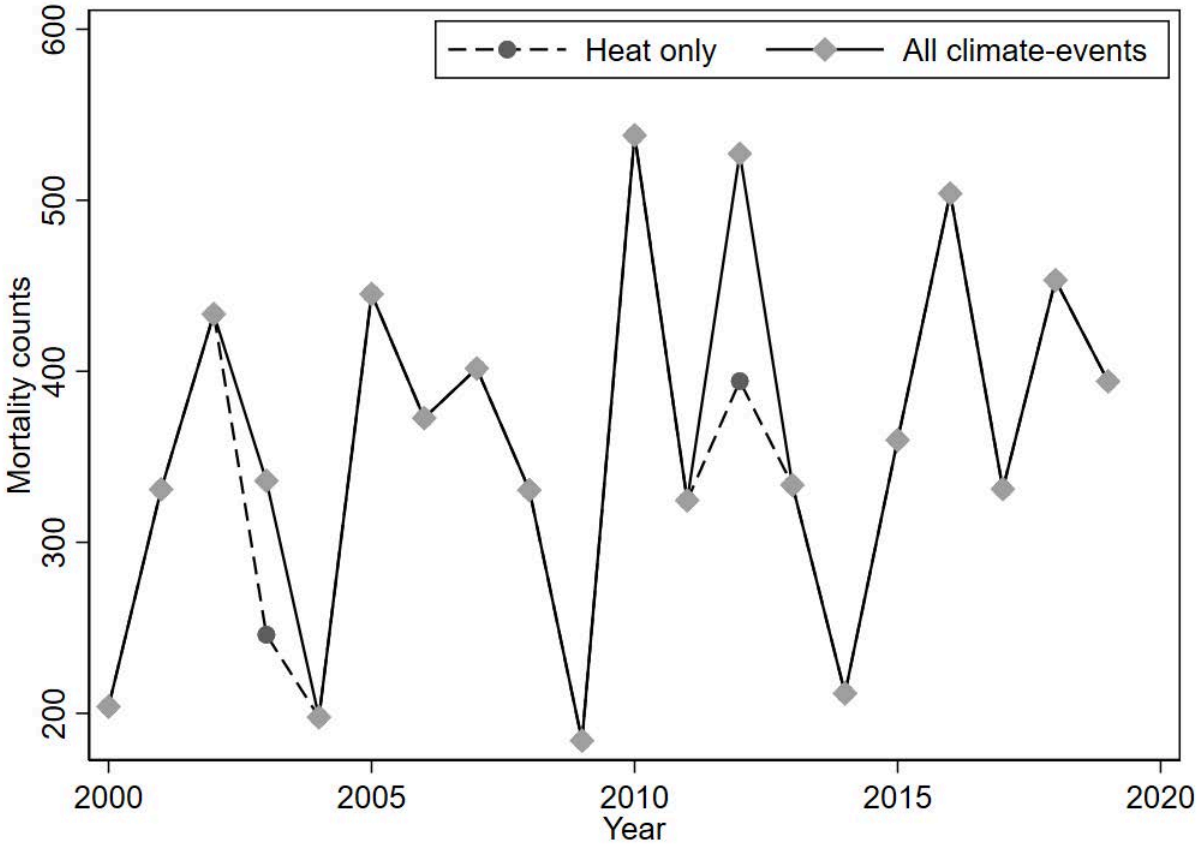

Notes: This figure shows the total mortality counts due to climate-sensitive events per year. The solid line shows total mortality counts due to all climate-sensitive events (heat, power outages and tropical cyclones) and the dotted line shows total mortality due solely to heat.

Figure 4.12: Cardiovascular and total morbidity cases from climate-sensitive events in New York City, 2000-2019

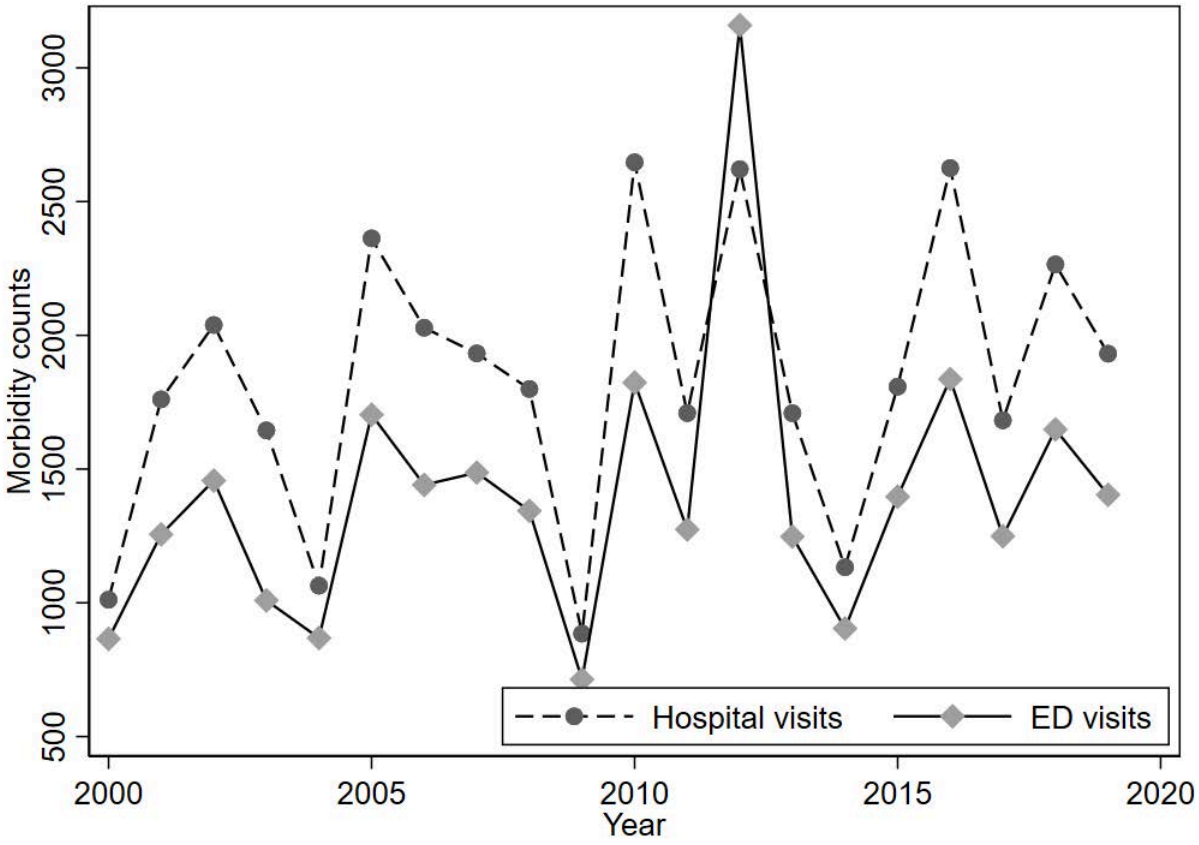

Notes: This figure shows the total morbidity counts due to climate-sensitive events per year, separately for hospital visits (dashed line) and ED visits (solid line).

Figure 4.13: Annual estimated health-related costs (in billions of 2020 $USD) from climate-sensitive events in New York City, 2000-2019.

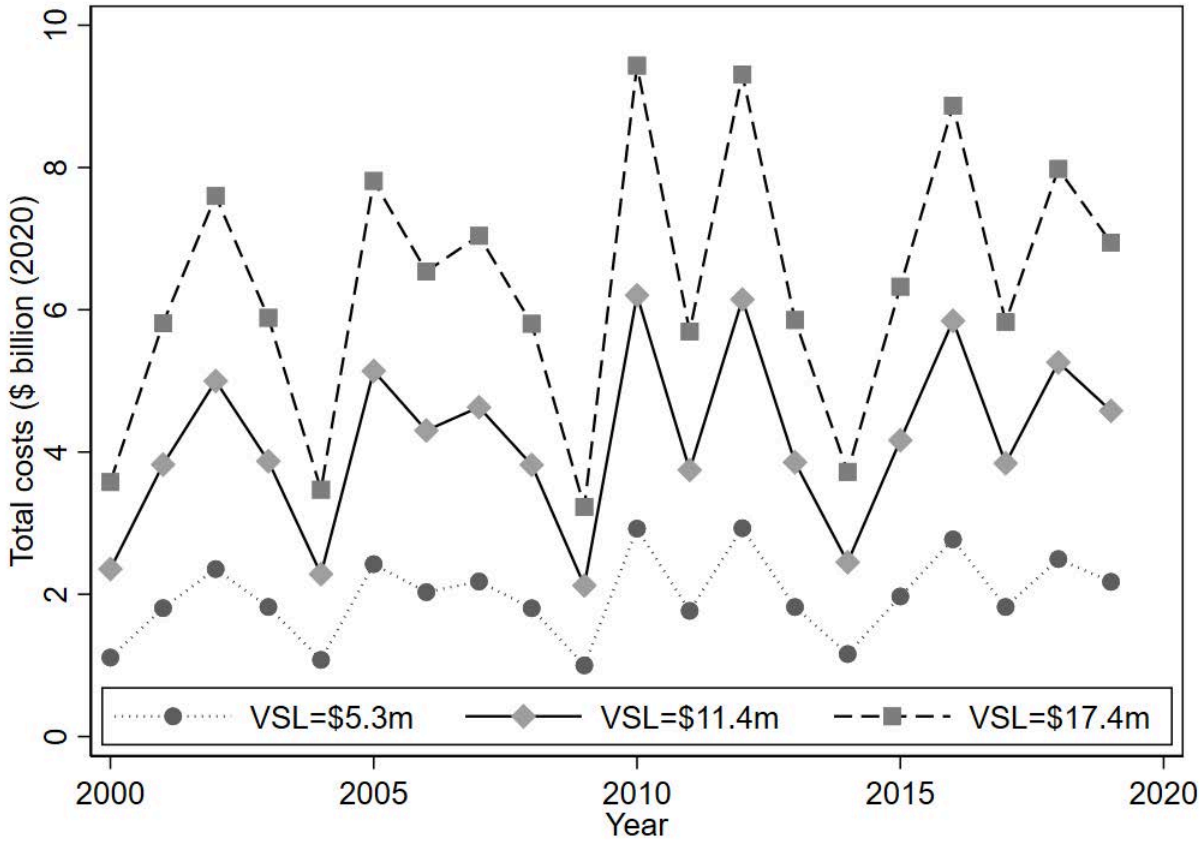

Notes: This figure shows the total health-related economic costs due to climate-sensitive events, under different values for the VSL.

Task 5: Flooding Vulnerability Index for New York City

Task 5: Flood Vulnerability Index for New York City

Core Team:

- Timon McPhearson (Co-lead, The New School)
- Malgosia Madajewicz (Co-lead, Columbia University)
- Pablo Herreros-Cantis (The New School)

Advisory Team

- Jerry Kleyman and Mary Kimball (Arcadis)
- Franco Montalto (Drexel University)
- Bernice Rosenzweig (Sarah Lawrence)
- Brett Branco (CUNY/SRIJB)
- Katie Graziano (Sea Grant/Cornell)
- Lindsay Campbell (US Forest Service)
- Erika Svendsen (US Forest Service)
- Michelle Johnson (US Forest Service)

NYC Interagency Collaborators:

- Jessica Colon (Mayor's Office of Climate & Environmental Justice)
- Carrie Grassi (Mayor's Office of Climate & Environmental Justice)
- Hayley Elszasz (Mayor's Office of Climate & Environmental Justice)
- Erika Jozwiak (Mayor's Office of Climate & Environmental Justice)
- Katie Lane (Department of Health and Mental Hygiene)
- Kaz Ito (Department of Health and Mental Hygiene)
- Gregory Mayes (Department of Environmental Protection)
- Alan Cohn (Department of Environmental Protection)
- Novem Auyeung (Department of Parks and Recreation)
- Georgina Cullman (Department of Parks and Recreation)
- Melissa Umberger (Department of Emergency Management)
- William Pappas (Department of Emergency Management)

5.1 Objective and overview: New York City's Flood Vulnerability Index

NYC experiences multiple types of flooding, including pluvial flooding, storm surge, tidal flooding, groundwater flooding, riverine, and compound flooding. The occurrence and magnitude of each flooding type is moderated by a different combination of biophysical and meteorological factors. Researchers are at disparate stages of understanding the different flooding types in New York City. While substantial knowledge and advanced hazard mapping

exist for flooding due to storm surges, pluvial flooding is less well understood and research on groundwater flooding is in even earlier stages.

The objective of Task 5 was to develop a Flood Vulnerability Index (FVI) for NYC that assesses the distribution of vulnerability to flooding across the population of NYC in order to guide flood resilience policies and programs. Based on a literature review, the team used a definition of vulnerability that consists of three components: exposure to a hazard, susceptibility to harm from the exposure, and capacity to recover (Cutter et al., 2009).

In collaboration with MOCEJ, Interagency Collaborators, and the advisors, the Task 5 team produced six hazard-specific FVIs, one for each of six different flood hazard scenarios, which include current and two future storm surge scenarios and current and two future tidal flooding scenarios. Exposures vary widely for different types of flooding and different scenarios within each flood type. The resulting separate FVIs for different flood hazard scenarios are easier to interpret and can provide clearer guidance for decisions than would an index that combines exposure to all types of flooding.

Each FVI consists of two component sub-indices: an exposure index and an index that reflects susceptibility to harm and capacity to recover. The exposure index is different in each FVI in order to capture the different exposures to each of the flood hazard scenarios. The sub-index that reflects susceptibility to harm and capacity to recover, which we call the Flood Susceptibility to Harm and Recovery Index (FSHRI), is the same in each FVI. It aggregates twelve socio-economic indicators correlated with various types of hardships that people may suffer due to flooding and different dimensions of ability to recover. Figure 1 demonstrates the process of producing the six FVIs.

5.2 Key Messages

- The FVIs are based on one of the most comprehensive and widely accepted definitions of vulnerability, consisting of three components: exposure to hazard, susceptibility to harm from the hazard, and capacity to recover. The definition covers dimensions of vulnerability that policies and programs need to consider in order to reduce vulnerability.
- The FVI is constructed from two component sub-indices that correspond to this definition. First, the exposure sub-index is a function of proximity to flooding caused by a specific event. Second, the sub-index that reflects susceptibility to harm due to flooding and capacity to recover is a function of sociodemographic characteristics known to be associated with the outcomes experienced during and after flooding by populations in New York City.

- Mapping vulnerability for different flood hazard types highlights how vulnerability differs across types of hazards and allows vulnerability maps to be easily updated over time as the understanding of hazard exposure improves.
- The FVIs provide guidance regarding vulnerability to storm surge and tidal flooding in the present and the future. Sources of extensive exposure to flooding that remain for future research are pluvial and groundwater flooding.
- FVI indicators were selected through literature review and discussions with Interagency Collaborators and the advisory team. Analyses compared two common aggregation approaches (geometric and linear averaging) during the spatial analysis and selected the geometric averaging method for the final index.
- The different FVIs show consistently high values in some NYC neighborhoods such as west Coney Island, southeast Staten Island (e.g. Oakwood, New Dorp Beach, Midland Beach, Dongan Hills, Arrochar), east Rockaway (e.g. Far Rockaway, Edgemere, Arverne), and areas around the perimeter of Jamaica Bay such as Hamilton Beach, Broad Channel, and Rosedale (Figure 8). The majority of neighborhoods in Jamaica Bay show high vulnerability to both storm surge and coastal flooding. Other locations with generally high FVIs appear in the southern coast of Manhattan (e.g. Lower East Side), in northern Manhattan by the Harlem River, and east Bronx (e.g. City Island, Pelham Bay).

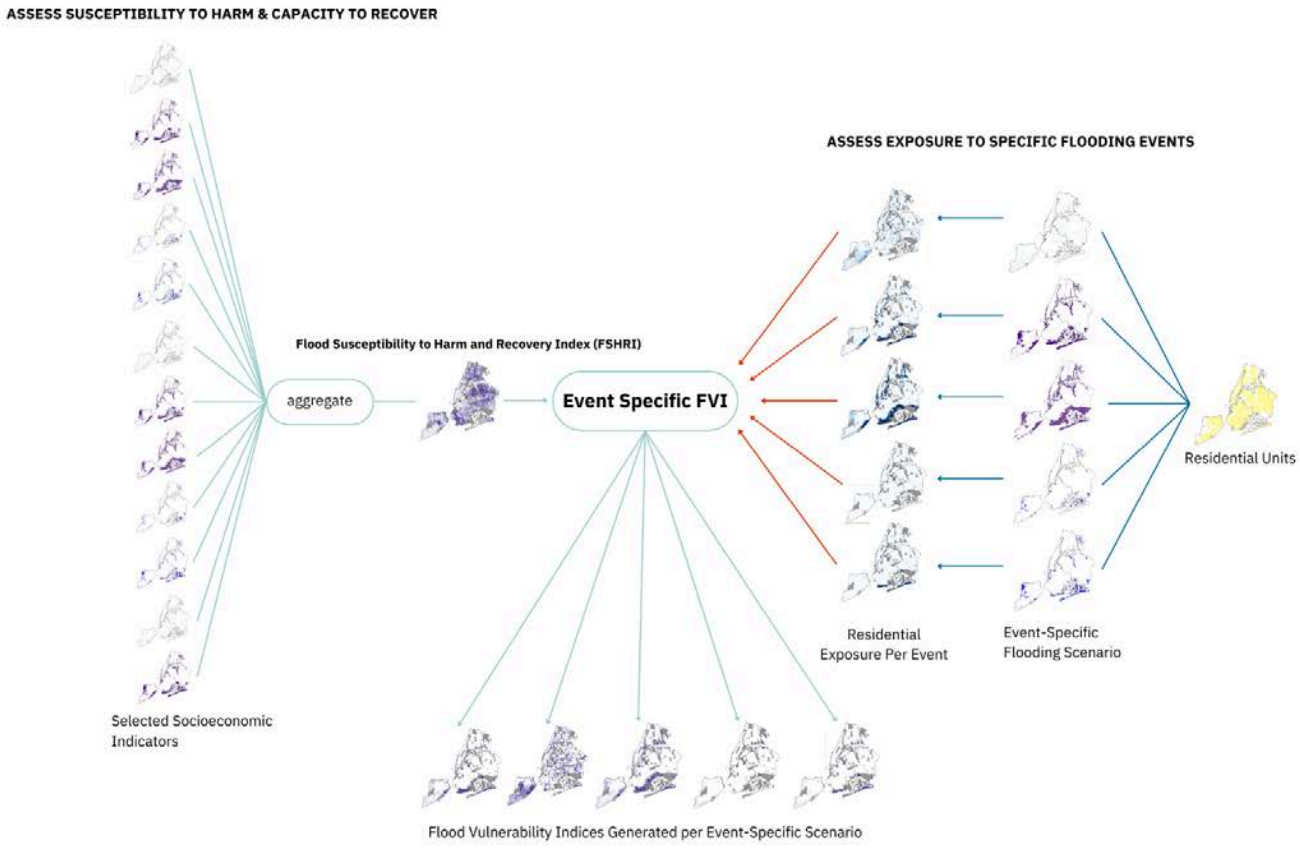

Figure 5.1: Development of the Flood Vulnerability Index. Graphic design by Pablo Herreros-Cantis and Sofya Krasnaya

5.3 The definition of vulnerability

A literature review provided flood vulnerability frameworks and definitions to guide FVI development. This review explored different approaches to defining and assessing vulnerability proposed in the literature, and identified methods for selecting vulnerability indicators and for aggregating indicators into vulnerability indices. Further, we assessed the state of the knowledge regarding different flood hazards known to impact NYC in order to evaluate which flood hazards should be included in the final set of hazard specific FVIs for NYC.

The literature proposes several different frameworks and definitions of vulnerability without a consensus regarding the preferred one. A key distinction between different approaches to vulnerability lies in the inclusion of hazards and exposure as part of vulnerability. For instance, CDC's social vulnerability index presents vulnerability as a pre-existing condition based on socio-economic indicators regardless of exposure to any type of hazard (Flanagan et al., 2011). On the other hand, vulnerability has also been conceptualized as including exposure. For instance, Cutter (2009) defines vulnerability as a combination of exposure and susceptibility to

harm from a hazard shortly after a flood event as well as capacity to recover. Examples of vulnerability assessment efforts using this definition include NYC's Heat Vulnerability Index (Madrigano et al., 2015), Balica et al. (2012), Scheuer et al. (2011), Fekete (2009), Kleinosky et al. (2007), Yarnal (2007), Chakraborty et al. (2005), Wu et al. (2002), Cutter et al. (2000), and Clark et al. (1998).

For the purpose of constructing the FVI, we adopt the latter definition, which conceptualizes vulnerability as exposure to the hazard, susceptibility to harm from exposure, and capacity to recover for several reasons. First, the definition is the broadest one, encompassing all dimensions that policies and programs would need to address in order to reduce vulnerability. Second, the definition supports investigating how the factors that compose vulnerability differ across different hazards as well as different built environment and socio-economic conditions, It allows the indicators of vulnerability to differ across conditions, which is more consistent with evidence than the view that they are constant (e.g. Eriksen and Kelly 2007; Madajewicz 2020).

In the FVIs, we consider exposure of the population to different types of flood hazard. Susceptibility to damage from flooding captures the extent to which populations are prepared to weather the hazard, including the ability of populations to avoid threat to life and health, and to maintain their access to basic needs, services, and sources of livelihoods. Capacity to recover reflects multiple dimensions of the population's capacity to return at least to the pre-hazard level of livelihood, including financial state and access to housing, employment, supportive social networks, food, health care, and education.

5.4 Quantifying Vulnerability: Selecting Indicators for NYC's FVI

We selected indicators for the exposure sub-index and for the FSHRI following the processes described below.

a. Exposure

The exposure component of the FVI assesses the percentage of the population that may experience flooding in order to remain consistent with the sociodemographic indicators included in the FSHRI. Two spatial analysis methods were considered to assess exposure to specific flooding scenarios:

- Census Block level population exposure assessment: In this approach, we calculated the percentage of each Census Tract's population deemed exposed to flooding. We retrieved population data from the U.S. Decennial Census, which provides population

counts at the Census Block level, and we flagged each census block as exposed to flooding if it overlapped with the extent of the flooding in each scenario considered.

- Parcel level residential units exposure assessment: We calculated the percentage of each Census Tract's residential units deemed exposed to flooding. We retrieved residential parcels from NYC's MapPLUTO 2023 V1. A distance analysis assigned to each parcel the minimum distance from that parcel to flooding in each scenario. The exposed parcels were those whose minimum distance to flooding was less than 32.8ft (10m) to consider flooding exposure of nearby residential areas, consistent with approaches taken in other related exposure studies. This distance threshold was considered over a direct overlap in order to consider the impacts of flooding that may occur in the immediate surroundings of homes. Further iterations of this exposure assessment may adapt to specific use-cases and updates by considering different distance thresholds. Finally, we computed the percentage of the residential units in each Census Tract that were flagged as exposed.

The Census Block approach assessed the entire population of a block that would be exposed if the block overlaps with flooding. The approach may overestimate the percentage of the population that is actually exposed as shown in the first panel of Figure 2. A potential solution to the problem is to consider the percentage of the exposed population to be the same as the percentage of the flooded area in the block but the population is not likely to be uniformly distributed in each block. In addition, using coarser resolutions to assess exposure may conceal disproportionate risks faced by disadvantaged communities (Maantay & Maroko, 2009).

The exposure sub-index of the FVI is based on the parcel level approach to assessing exposure. The parcel level spatial analysis enabled assessing exposure at a higher resolution than the Census Block approach, which also prevented overestimating the total number of residents exposed to flooding implied in assuming full exposure at the Census Block level (see second panel of Figure 5.2).

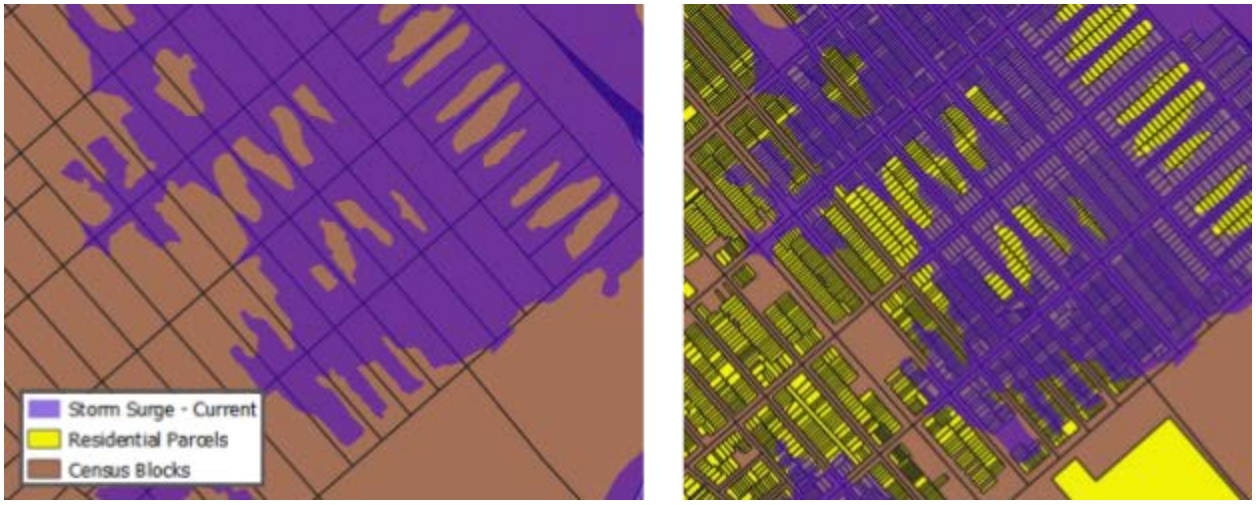

Figure 5.2: Parcel level spatial analysis

The Team selected the final six flooding scenarios (Table 5.1) from a larger initial set based on input from MOCEJ and Interagency Collaborators. The scenarios consider the two coastal flood hazard types identified in the literature review (storm surge and tidal flooding). Exposure to each flood hazard includes a “current'' scenario that depicts the distribution of a flooding event under current conditions. For storm surge and tidal flooding, two additional “future” scenarios assess exposure in the 2050s and 2080s based on data developed by the New York City Panel on Climate Change (NPCC). Figure 3 shows the exposure assessments, or exposure indices, calculated for each scenario.

Table 5.1: Summary of flooding scenarios considered to assess exposure across NYC.

Scenario Name	Flooding Type	Hazard Layer and Source
Vulnerability to Storm Surge Flooding - current	Coastal-Storm Surge	FEMA’s Special Flood hazard Area - 2015 Preliminary release (FEMA, n.d.)
Vulnerability to Storm Surge Flooding - 2050s	Coastal-Storm Surge	FEMA’s Special Flood Hazard Area with sea level estimates for the 2050s, high estimate scenario (Patrick et al., 2015)
Vulnerability to Storm Surge Flooding - 2080s	Coastal-Storm Surge	FEMA’s Special Flood Hazard Area with sea level estimates for the 2080s, high estimate scenario (Patrick et al., 2015)
Vulnerability to Tidal Flooding - 2020S	Coastal-Tidal	Mean Higher High Water (mhhw) estimates for 2020s, high estimate scenario (Horton et al., 2015)

Vulnerability to Tidal Flooding - 2050s	Coastal-Tidal	Mean Higher High Water (mhhw) estimates for the 2050s, high estimate scenario (Horton et al., 2015)
Vulnerability to Tidal Flooding - 2080s	Coastal-Tidal	Mean Higher High Water (mhhw) estimates for the 2080s, high estimate scenario (Horton et al., 2015)

EXPOSURE - STORM SURGE
CURRENT

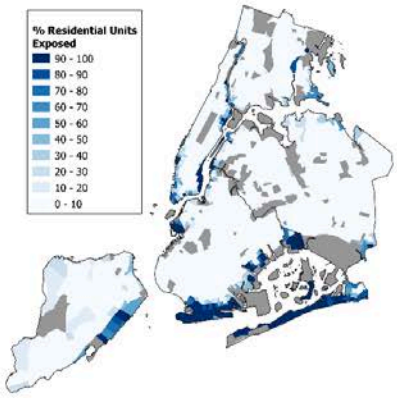

EXPOSURE - TIDAL
2020S

EXPOSURE - STORM SURGE
2050S

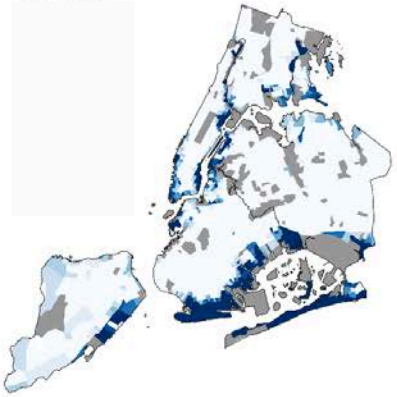

EXPOSURE - TIDAL
2050S

EXPOSURE - STORM SURGE
2080S

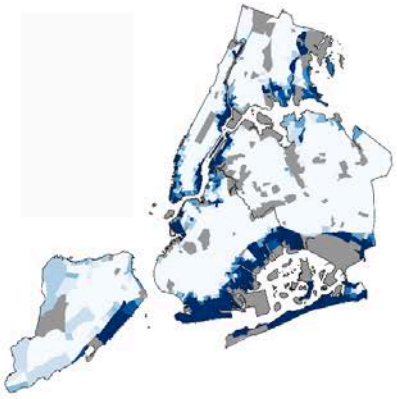

EXPOSURE - TIDAL
2080S

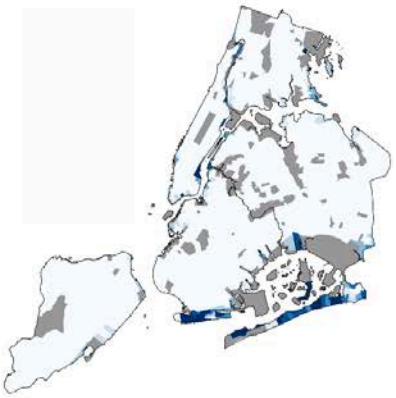

Figure 5.3: Exposure per flooding scenario considered, measured as the % of residential units within the Census Tract located within a 32.8ft buffer of the closest flooding. Full page individual maps are provided in Appendix 5.2.

b. Susceptibility and Capacity to Recover

The FVIs reflect susceptibility to harm from flooding and capacity to recover to the extent that the indicators that are included in the index accurately capture each of these dimensions of vulnerability in the population. The team developed a preliminary list of indicators of susceptibility to harm from flooding and capacity to recover based on the indicators identified in the literature review. We focused on indicators that were validated in prior research through empirical studies like Rufat et al. (2019), Madajewicz (2020), and Tellman et al. (2020), conducted primarily for the case of storm surge flooding. We finalized the list in consultation with Interagency Collaborators and the advisory team (Table 2).

We eliminated some indicators from the final list due to statistical multicollinearity or lack of data. Multicollinearity was tested in this set of indicators through the Variance Inflation Factor (VIF), a metric that depicts collinearity. According to the approach, VIF values higher than five indicate excessively high multicollinearity, and may require removing or replacing them with others (McPhearson et al., 2021). We removed median income and poverty rate based on their high VIF values and their redundancy with other economic variables. We selected per capita income rather than median income because of the evidence in Madajewicz (2020) that per capita income is strongly correlated with a number of dimensions of vulnerability to flooding. The same paper suggests that poverty rate would not reflect the particularly high vulnerability to flooding among low to middle-income homeowners, which is much higher on some measures than vulnerability among poorer renters. The higher annual household income threshold of $75,000 is more effective at identifying vulnerability among low to middle income homeowners, and is not much higher than the originally considered threshold that was two times the poverty level. The highest VIF value in the final set of variables is 5.01 for the annual household income lower than $75,000 threshold.

The team used the final set of 12 indicators to map susceptibility to harm and capacity to recover flooding across NYC. All data are from the US Decennial Census for 2020 or the US American Community Survey 5-year estimates for the years 2016-2020, as shown in Table 5.2, aggregated at the Census Tract level.

Data availability limited the consideration of indicators to those that could be sourced from the US Census Bureau. We discarded other indicators initially flagged as desirable, such as the proportion of homes and businesses insured against flooding, due to lack of consistent data. We consulted FEMA's openly available data that reports the NFIP's redacted policies. The dataset did not provide full coverage of the city's residential insurance coverage.

During the data gathering processes, we removed the Census Tracts (CTs) that overlap with large city parks, cemeteries, and airports due to gaps and inconsistencies in the raw sociodemographic data. A list with the 35 CTs that were removed based on this criteria is in Appendix 5.3.

Table 5.2: Susceptibility to harm and capacity to recover indicators selected based on the literature review and the inputs provided by Interagency Collaborators and the advisory team. Indicators highlighted in red were omitted due to high multicollinearity values based on their Variance Inflation Factor (VIF) and/or high correlations with other indicators. See Appendix 5.1. for a full list of pre-selected indicators during the project's literature review.

Indicator	Data Source	VIF before removal of discarded variables	VIF after removal of discarded variables
% Population self-reported as Black, Indigenous, Person Of Color (BIPOC)	2020 US Decennial Census	2.20	2.16
% Population in vulnerable age - elderly (+60 years old)		2.53	2.44
% Population in vulnerable age - infant (0-5 years old)		1.72	1.59
% Population with a disability	2016-2020 US American Community Survey (ACS)	1.70	1.63
% People above 5 years old living in Language Isolation (speaks English "not well" or "not at all")		1.88	1.80
% Elder adults living alone		2.01	1.98
% People without health insurance		1.81	1.81
% HH with HH income below 75K		6.72	5.01
% owner occupied homes		2.96	2.63
Per capita income		6.85	2.73
Median Income		9.43	-

% Population living below 2x the federal poverty line		5.54	-
% owned HH with expenses higher than 30% HH income		1.19	1.19
% rented HH with rent costs higher than 30% HH income		1.54	1.52

5.5 Creating NYC's FVI: Aggregating Indicators Into an Index

The team aggregated the indicators that represent susceptibility to harm and capacity to recover into a base Flooding Susceptibility to Harm and Recovery Index (FSHRI). Then, we aggregated the single FHSRI with each of the six scenario-specific exposure indicators to develop the final six versions of the hazard specific Flood Vulnerability Indices.

The team proposed to average indicators to construct the index rather than using the principal component analysis (PCA) approach due to limitations of the PCA approach explained in the literature review. We tested and compared two averaging methods:

- A linear aggregation approach, which sums the normalized indicators[10] and divides the sum by the number of indicators considered (arithmetic mean).
- A geometric aggregation approach, which yields the nth root of the product of n normalized indicators (geometric mean).

In consultation with Interagency Collaborators and the advisory team, the Task 5 team calculated the final FVIs using the geometric approach, based on an analysis of the trade-offs between the two approaches to aggregation. First, how index components are normalized affects their ranking with respect to an arithmetic average but not the geometric. Therefore, as maximum and minimum values of indicators change over time, the change will alter the ranking of areas whose indicator values do not change if we use an arithmetic average, but not if we use a geometric one. Second, the geometric average treats the indicators as having more distinct effects on vulnerability that are not necessarily substitutable. A given increase in one indicator can be completely offset by an equal decline in another indicator in an arithmetic average, but not in a geometric average. Third, the geometric average takes into account the dependence of values of different indicators, which may be due to correlation between them, whereas an arithmetic average does not. Fourth, the geometric average reduces the effect of extreme values on the average relative to the arithmetic. For example, a Census tract with a

[10] Indicators were normalized using a min-max normalization approach by which the values are re-scaled to a 1-100 scale. $I(indicator_i) = 1 + 100*(indicator_i - indicator_{min})/(indicator_{max} - indicator_{min})$.

very high value for one index component but relatively low values for other components may look more vulnerable than a Census tract with moderately high values for all components if we use the arithmetic average. Taking a geometric average instead will reduce the average of the tract with the one high value relative to the value of the tract all of whose components are moderately high.

Figure 4 compares the two aggregation approaches applied to the FSHRI. Of the 2227 CTs considered in the final analysis, 394 CTs (18%) obtained an index value in the 4th quartile under the two aggregation methods considered. 326 (15%) obtained an index value in the 4th quartile for one of the methods considered, and 1507 (67%) did not obtain an index value in the 4th quartile for any of the methods. A look at a map showing the areas with high FSHRI based on both aggregation methods provides important insights (Figure 5). First, the CTs with consistently high FVIs are clustered spatially in the Central Bronx, North Queens, Southwest Brooklyn, and a SW-NE corridor across Brooklyn and Queens. Other isolated hotspots appear in North Staten Island and Rockaways. Second, the vast majority of CTs that scored high (4th quartile) under only one of the two aggregation methods are heavily correlated spatially with those that scored high for both. An additional scatterplot shows how the two indices are correlated with the mentioned tendency of the geometric average to generate lower values than the linear average.

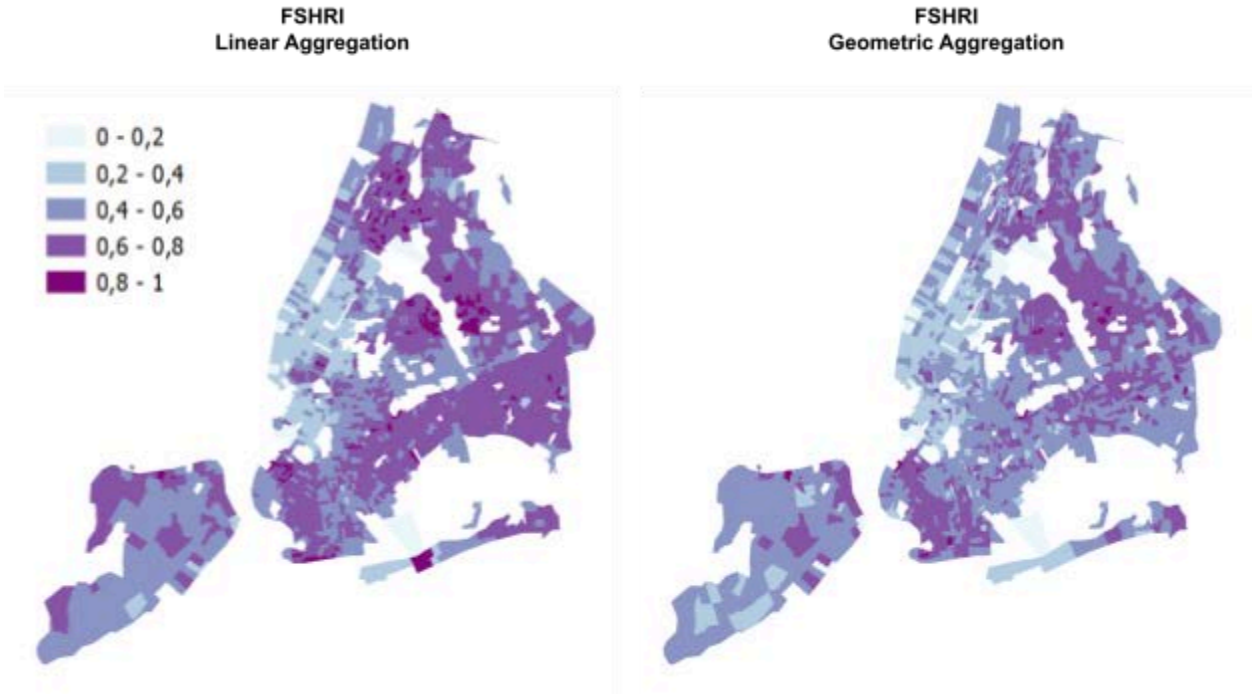

Figure 5.4: Preliminary results of the Flood Susceptibility to Harm and Recovery Index (FSHRI), comparing the two data aggregation approaches considered. The FSHRI corresponds to the aggregate of the indicators depicting susceptibility to harm and capacity to recover,

without considering event-specific exposures. As shown in the maps, the geometric aggregation method shows a lower density of tracts earning a high index value as it limits the influence of individual indicators in the final result.

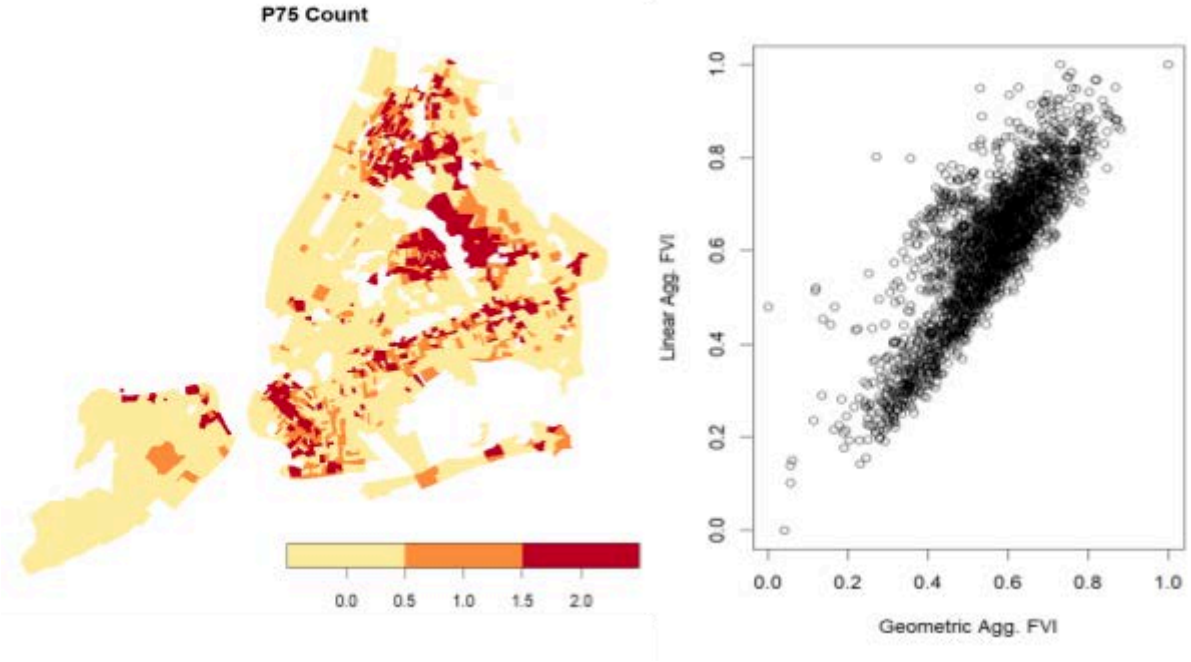

Figure 5.5: Map showing the number of aggregation methods in which Census Tracts scored a FSHRI within the highest quartile. A value of two indicates a CT scored a high FSHRI under both aggregation scenarios, while a value of one indicates only one aggregation method produced a high index value. On the right, a scatterplot comparing both aggregation methods.

Finally, we developed six scenario-specific Flood Vulnerability Indices by combining the final FSHRI (Figure 6) with each of the exposure indices, which are the normalized percentages of residential units exposed to flooding in each flood hazard scenario (Figure 7). Each FVI is the geometric average of the FSHRI and one of the six exposure indices. We aggregated Census tracts into vulnerability quintiles and assigned a score ranking from one to five accordingly, with one being the lowest vulnerability quintile and five being the highest.

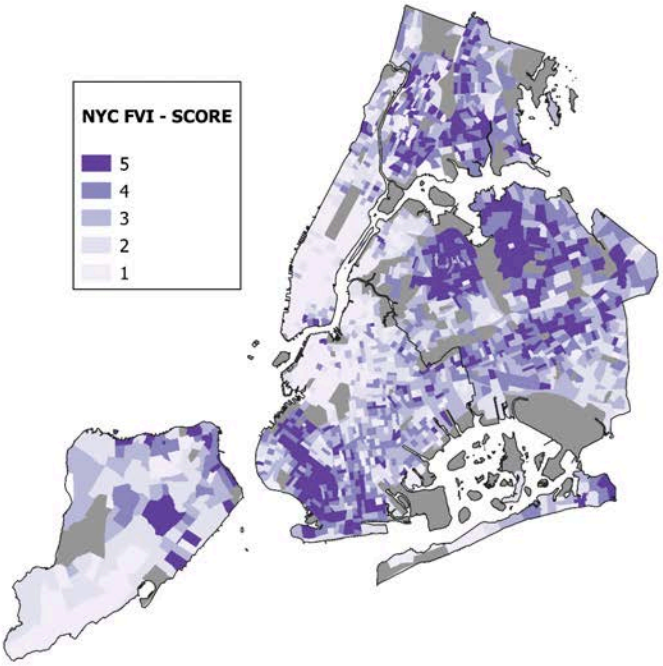

Figure 5.6: Final Flood Susceptibility to Harm and Recovery Index (FSHRI) with values aggregated using a geometric averaging approach. Values represent the tract's ranking in quintiles, where one means lowest vulnerability and five means the highest. Greyed Census Tracts were omitted from the FVI due to a lack of sociodemographic data available that avoided the FSHRI from being computed.

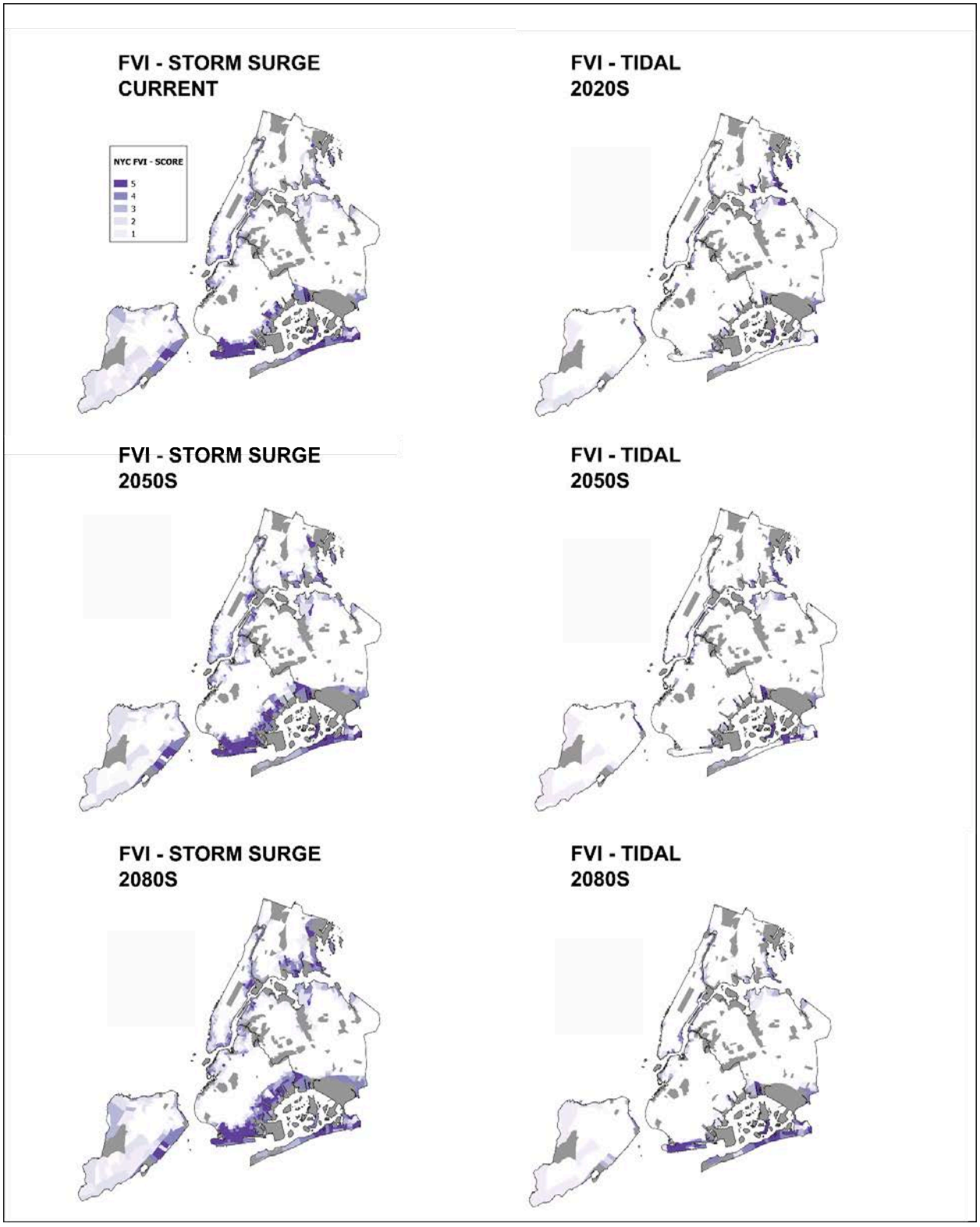

Figure 5.7: Final Flood Vulnerability Indices for each flood hazard scenario. Each FVI is the result of aggregating the FSHRI with one of the six scenario-specific exposure indices.

Exposure and FSHRI were aggregated using their normalized values before being ranked in quintiles. Grey Census Tracts were omitted from the FVI due to a lack of sociodemographic data, without which we could not compute the FSHRI. Full page individual maps are provided in Appendix 5.4.

5.6 Discussion/Conclusions

Interpreting the FVIs

The value of each FVI indicates relative vulnerability or differences in vulnerability between different Census tracts. The value is not an absolute measure of vulnerability. Census tracts with higher FVI values are more vulnerable and bigger differences between FVI values indicate bigger differences in vulnerability. However, equal values of the FVI do not mean the areas that share the same values are vulnerable to flooding in the same ways. The nature of vulnerability in areas that share the same values of any of the FVIs can be very different. Understanding differences between the components of each FVI across Census tracts can provide information about the nature of vulnerability in different tracts.

Each FVI combines exposure to flooding in a given scenario and the FSHRI with equal weights. The FVI has a value of zero (no vulnerability) for any area that is not exposed to flooding under the given flood hazard scenario. The greater is the number of residential units in proximity to the given flood hazard, the higher is the value of the FVI, reflecting greater vulnerability because of greater exposure.

The value of the FVI also rises as the value of the FSHRI increases, indicating greater vulnerability because of greater susceptibility to harm and/or lower capacity to recover. Higher values of the FSHRI likely reflect high values of multiple indicators. The FSHRI is a geometric rather than an arithmetic average of the normalized indicator values, making it less responsive to high values of a single indicator than an arithmetic average would be. However, a high value of the FSHRI does not mean all component indicators have high values, and a low value does not mean that all indicators have low values. Furthermore, two areas with the same value of the FSHRI may have very different values of all component indicators. Indicators with high values in one area may have low values in another area with the same value of the FSHRI.

Understanding differences between the values of component indicators between areas provides some information about the differences in drivers of vulnerability across those areas. Studies show that different indicators are correlated with different dimensions of vulnerability. (e.g. Madajewicz 2020) Dimensions of susceptibility to harm include harm to life or health, severity of damage to property, displacement from home, and disruption in access to critical services, such as food, health care, education, transportation, and utilities. Each of these dimensions is correlated with different socio-economic indicators, which comprise the FHSRI.

For example, risk to life or health tends to be greater in areas that have a higher proportion of the elderly and the very young. Damage to property tends to be greater for owner-occupied homes, the lower income homeowners, and households with disabled or chronically ill members. Disruptions of access to food tend to be greater where the percentage of BIPOC residents is higher, and disruptions to health care where the proportion of the disabled or chronically ill is higher. Dimensions of capacity to recover include length and completeness of recovery and financial vulnerability, which includes cost of recovery, change in assets, and change in employment. Cost of recovery is orders of magnitude higher for homeowners and increases as a proportion of income as income declines, and recovery tends to be longer and loss of job more likely for the disabled and the chronically ill.

Understanding which indicator values are high in a given area can provide guidance regarding programs that may reduce vulnerability in that area in a way that knowing the FVI or FSHRI value cannot. For example, high proportions of owner-occupied homes strongly indicate that financial vulnerability is high and the residents need programs that help them to make well-informed decisions about and to finance mitigation of flood damages in the short- and medium- term to reduce repetitive recovery costs. If these owner-occupied homes are low-rise, the financial vulnerability is also likely to be exacerbated by relatively high damages in case of flooding. Areas with high proportions of BIPOC populations need special attention to securing access to food during and after flood events. Households with chronically ill and/or disabled residents especially need assistance with access to health care, with repairing flood damage both because they tend to suffer greater damages and they require more time to repair damages without assistance, and with ability to go to work in order to maintain job security.

Distribution of FVI across NYC

The different FVIs show consistently high values in some NYC neighborhoods, such as west Coney Island, southeast Staten Island (e.g. Oakwood, New Dorp Beach, Midland Beach, Dongan Hills, Arrochar), east Rockaway (e.g. Far Rockaway, Edgemere, Arverne), and areas around the perimeter of Jamaica Bay such as Hamilton Beach, Broad Channel, and Rosedale (Figure 8). The majority of neighborhoods in Jamaica Bay show high vulnerability to both storm surge and coastal flooding. Other locations with generally high FVIs appear in the southern coast of Manhattan (e.g. Lower East Side), in northern Manhattan by the Harlem River, and east Bronx (e.g. City Island, Pelham Bay).

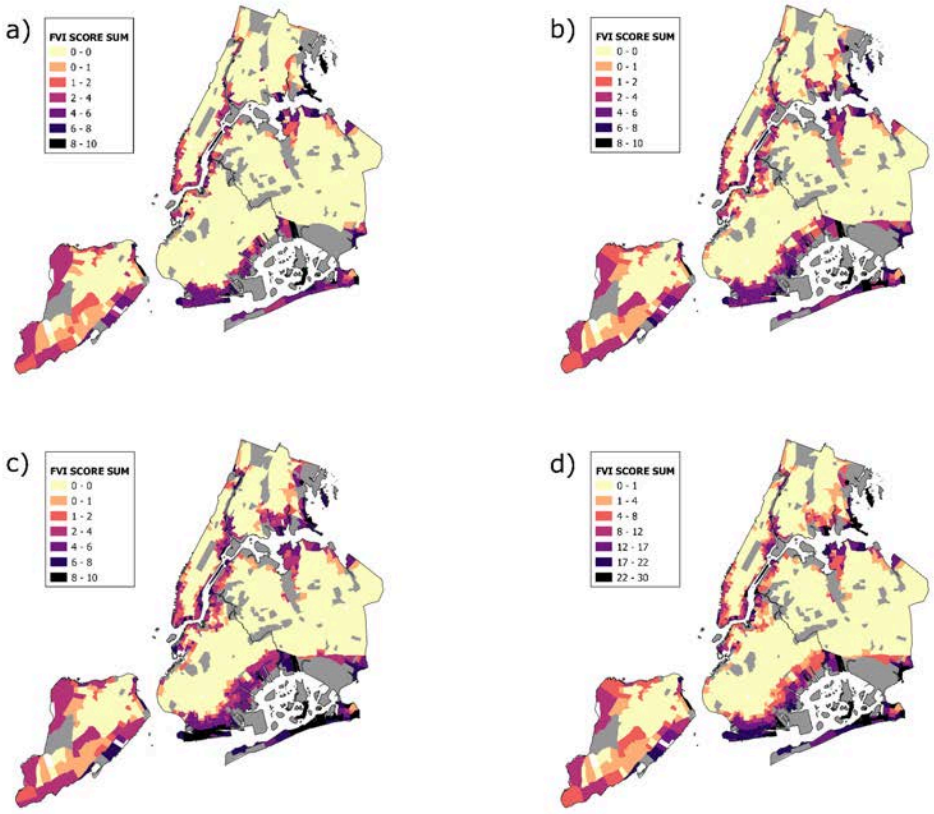

Figure 5.8: Flood vulnerability hotspots based on calculating the sum of the FVI scores. Four different aggregations are presented: Figure a) aggregates the FVIs including current flood hazard estimates (2020s tidal, storm surge - current). Figure b) shows the aggregate of FVIs considering future flood hazard projections for the 2050s (2050s tidal, storm surge - 2050s). Figure c) shows the aggregate of FVIs considering future flood hazard projections for the 2080s (2080s tidal, storm surge - 2080s). Figure d) shows the aggregate of all six FVIs developed.

Future directions

The development of NYC's FVI encountered some limitations, which may guide future updates and improvements. For instance, we did not consider a future or extreme stormwater flood hazard scenario because the current available hazard layer conflates stormwater and future tidal flooding, masking areas that suffer from extreme stormwater flooding today. Using this hazard layer would have implied either a) considering pluvial and tidal flooding as a single hazard, biasing exposure metrics to low-lying coastal areas, or b) omitting tidal flooding and assuming no exposure in the same coastal areas.

The exposure assessment in each FVI relies on residential units as a proxy for population density at a granular level that was not possible using Census data. However, this approach assumes all households in New York City are equally important regardless of their size, and all households are equally exposed to flooding regardless of their elevation above the ground. Data may support an approach that is more representative of the differences in household size across NYC. Another aspect that may be revisited in future iterations of the exposure component of the FVI is the distance threshold used to flag residential parcels as exposed to flooding (32.8 ft. /10m). We selected this threshold under the premise that having floodwaters 10m away from home or less will impact residents, as well as accounting for varying resolutions and assumptions made in mapping flood hazards (i.e. pluvial flooding is published for Right of Way areas such as roads, potentially masking or ignoring flooding that may occur closer to homes). Future iterations may consider how using wider or narrower thresholds to deem a property as exposed may influence the analysis of vulnerability to flooding.

The exposure component of the FVI considers only residential units. Growing evidence suggests certain structural elements, which could be included in the exposure sub-index, contribute to greater flood damages. Many deaths by drowning as well as the bulk of repetitive damages due to flooding and recovery expenses occur in basements (Madajewicz et al., 2022). In general, low-rise housing experiences much greater damages from flooding than do high-rise buildings (City of New York 2013). Future iterations of the FVIs could capture these structural elements in the exposure component to highlight where exposure is likely to cause the most harm.

Future research should investigate further which indicators are correlated with which dimensions of vulnerability. The nature of vulnerability to flooding differs across the City's neighborhoods. As the evidence improves, future versions of the FVIs could include the option to map individual indicators or subsets of indicators that comprise the FHSRI in order to provide more information about the types of vulnerability present in each neighborhood and better guidance for the reduction of vulnerability. Further research can also shed light on the tradeoffs between the geometric and the arithmetic average as approaches to aggregating the indicators. In particular, research should examine how outcomes experienced as a result of flooding differ in areas with very high values of a small number of indicators and areas in which a larger number of indicators have moderately high values. The arithmetic approach may consider the former case more vulnerable, while the geometric may assign a higher vulnerability value to the latter.

The NYC FVIs may be updated in the future in order to reflect evolving knowledge and resources. In addition to points discussed above, further empirical work may shed light on indicators whose correlation with vulnerability to flooding require their addition or removal from the FVI. Research may suggest new indicators, for which improved data may become

available, such as data on relevant measures of social capital, and/or studies may show that different indicators are correlated with vulnerability to different types of flooding. New estimates from the American Community Survey (ACS) and a new Decennial Census release for the year 2030 will provide updated sociodemographic data in the coming years. Ongoing research efforts across VIA, the NPCC, and other organizations are expected to generate novel flood hazard layers that would enable exposure assessments under a wider variety of scenarios, and future projections will improve for the future scenarios considered in the current FVIs.

References

Balica, S. F., Wright, N. G., & van der Meulen, F. (2012). A flood vulnerability index for coastal cities and its use in assessing climate change impacts. Natural Hazards, 64(1), 73–105. https://doi.org/10.1007/s11069-012-0234-1

Chang, H., Pallathadka, A., Sauer, J., Grimm, N. B., Zimmerman, R., Cheng, C., Iwaniec, D. M., Kim, Y., Lloyd, R., McPhearson, T., Rosenzweig, B., Troxler, T., Welty, C., Brenner, R., & Herreros-Cantis, P. (2021). Assessment of urban flood vulnerability using the social-ecological-technological systems framework in six US cities. *Sustainable Cities and Society*, *68*, 102786. https://doi.org/10.1016/j.scs.2021.102786

City of new York. (2013). *PlaNYC: A Stronger, More Resilient New York* (p. 445). The City of New York. http://s-media.nyc.gov/agencies/sirr/SIRR_singles_Lo_res.pdf

Chakraborty, J., Tobin, G. A., & Montz, B. E. (2005). Population Evacuation: Assessing Spatial Variability in Geophysical Risk and Social Vulnerability to Natural Hazards. Natural Hazards Review, 6(1), 23–33. https://doi.org/10.1061/(ASCE)1527-6988(2005)6:1(23)

Clark, G. E., Moser, S. C., Ratick, S. J., Dow, K., Meyer, W. B., Emani, S., Jin, W., Kasperson, J. X., Kasperson, R. E., & Schwarz, H. E. (1998). Assessing the Vulnerability of Coastal Communities to Extreme Storms: The Case of Revere, MA., USA. Mitigation and Adaptation Strategies for Global Change, 3(1), 59–82. https://doi.org/10.1023/A:1009609710795

Cutter, S. L., Emrich, C. T., Webb, J., & Morath, D. (2009). *Social vulnerability to climate variability hazards: A review of the literature. Final Report to Oxfam America* (pp. 1–44). Hazards and Vulnerability Research Institute.

Cutter, S. L., Mitchell, J. T., & Scott, M. S. (2000). Revealing the Vulnerability of People and Places: A Case Study of Georgetown County, South Carolina. Annals of the Association of American Geographers, 90(4), 713–737. https://doi.org/10.1111/0004-5608.00219

de Sherbinin, A., & Bardy, G. (2015). Social vulnerability to floods in two coastal megacities: New York City and Mumbai. *Vienna Yearbook of Population Research*, *13*, 131–165.

Eriksen SH, Kelly PM (2007) Developing credible vulnerability indicators for climate adaptation policy assessment. Mitig Adapt Strateg Glob Chang 12(4):495–524.
Fekete, A. (2009). Validation of a social vulnerability index in context to river-floods in Germany. Natural Hazards and Earth System Sciences, 9(2), 393–403. https://doi.org/10.5194/nhess-9-393-2009

FEMA. (n.d.). *FEMA Flood Map Service Center*. https://msc.fema.gov/portal/home

Herreros-Cantis, P., Olivotto, V., Grabowski, Z. J., & McPhearson, T. (2020). Shifting landscapes of coastal flood risk: Environmental (in)justice of urban change, sea level rise, and differential vulnerability in New York City. *Urban Transformations*, *2*(1), 9. https://doi.org/10.1186/s42854-020-00014-w

Horton, R., Little, C., Gornitz, V., Bader, D., & Oppenheimer, M. (2015). New York City Panel on Climate Change 2015 Report Chapter 2: Sea Level Rise and Coastal Storms. *Annals of the New York Academy of Sciences*, *1336*(1), 36–44. https://doi.org/10.1111/nyas.12593

Kleinosky, L. R., Yarnal, B., & Fisher, A. (2007). Vulnerability of Hampton Roads, Virginia to Storm-Surge Flooding and Sea-Level Rise. Natural Hazards, 40(1), 43–70. https://doi.org/10.1007/s11069-006-0004-z

Kontokosta, C. E., & Malik, A. (2018). The Resilience to Emergencies and Disasters Index: Applying big data to benchmark and validate neighborhood resilience capacity. *Sustainable Cities and Society*, *36*, 272–285. https://doi.org/10.1016/j.scs.2017.10.025

Maantay, J., & Maroko, A. (2009). Mapping urban risk: Flood hazards, race, & environmental justice in New York. *Applied Geography*, *29*(1), 111–124. https://doi.org/10.1016/j.apgeog.2008.08.002

Madajewicz, M. (2020). Who is vulnerable and who is resilient to coastal flooding? Lessons from Hurricane Sandy in New York City. *Climatic Change*, *163*(4), 2029–2053. https://doi.org/10.1007/s10584-020-02896-y

Madajewicz, M., Kane, J. P., Romero, C. F., Orton, P., Dupont, J., Fisyak, A., Asimov, J., Labriole, M., Hutton, J., Connolly-Dougherty, I., Falik, E., Ferguson, F., King, P., Tuccio, F., Yarde, L., & Rogers, J. (2022). *Rockaway Homeowner's Guide to Preparing for Flooding*. ArcGIS StoryMaps. https://storymaps.arcgis.com/stories/9f30a17af33049e69bbf9b0bb92c6d87

Madrigano, J., Ito, K., Johnson, S., Kinney, P. L., & Matte, T. (2015). A Case-Only Study of Vulnerability to Heat Wave–RelatedMortality in New York City (2000–2011). Environmental Health Perspectives, 123(7), 672–678. https://doi.org/10.1289/ehp.1408178

McPhearson, T., Grabowski, Z., Herreros-Cantis, P., Mustafa, A., Ortiz, L., Kennedy, C., Tomateo, C., Lopez, B., Olivotto, V., & Vantu, A. (2021). Pandemic Injustice: Spatial and Social Distributions of COVID-19 in the US Epicenter. *Journal of Extreme Events*, 2150007.

https://doi.org/10.1142/S234573762150007X

NYC Department of Environmental Protection. (2022). *NYC Stormwater Flood Map—Moderate Flood with Current Sea Levels | NYC Open Data*. https://data.cityofnewyork.us/Environment/NYC-Stormwater-Flood-Map-Moderate-Flood-with-Curre/7r5q-vr7p

Patrick, L., Solecki, W., Jacob, K. H., Kunreuther, H., & Nordenson, G. (2015). New York City Panel on Climate Change 2015 Report Chapter 3: Static Coastal Flood Mapping. *Annals of the New York Academy of Sciences*, *1336*(1), 45–55. https://doi.org/10.1111/nyas.12590

Reckien, D. (2018). What is in an index? Construction method, data metric, and weighting scheme determine the outcome of composite social vulnerability indices in New York City. *Regional Environmental Change*. https://doi.org/10.1007/s10113-017-1273-7

Rufat, S., Tate, E., Emrich, C. T., & Antolini, F. (2019). How Valid Are Social Vulnerability Models? *Annals of the American Association of Geographers*, *109*(4), 1131–1153. https://doi.org/10.1080/24694452.2018.1535887

Scheuer, S., Haase, D., & Meyer, V. (2011). Exploring multicriteria flood vulnerability by integrating economic, social and ecological dimensions of flood risk and coping capacity: From a starting point view towards an end point view of vulnerability. Natural Hazards, 58(2), 731–751. https://doi.org/10.1007/s11069-010-9666-7

Tellman, B., Schank, C., Schwarz, B., Howe, P. D., & de Sherbinin, A. (2020). Using Disaster Outcomes to Validate Components of Social Vulnerability to Floods: Flood Deaths and Property Damage across the USA. *Sustainability*, *12*(15), Article 15. https://doi.org/10.3390/su12156006

Yarnal, B. (2007). Vulnerability and all that jazz: Addressing vulnerability in New Orleans after Hurricane Katrina. Technology in Society, 29(2), 249–255. https://doi.org/10.1016/j.techsoc.2007.01.011

Winderl T (2014) Disaster resilience measurements: stocktaking of ongoing efforts in developing systems for measuring resilience. UNDP http://www.preventionweb.net/files/37916_disasterresiliencemeasurementsundpt.

Wu, S.-Y., Yarnal, B., & Fisher, A. (2002). Vulnerability of coastal communities to sea-level rise: A case study of Cape May County, New Jersey, USA. Climate Research, 22(3), 255–270. https://doi.org/10.3354/cr022255

Zahmatkesh, Z., & Karamouz, M. (2017). An uncertainty-based framework to quantifying climate change impacts on coastal flood vulnerability: Case study of New York City. *Environmental Monitoring and Assessment*, *189*(11), 567. https://doi.org/10.1007/s10661-017-6282-y

Appendix 5.1

Indicators submitted in the literature review based on identified coastal vulnerability assessments and correlation studies. Bolded indicators were pre-selected based on Interagency input for further consideration by exploring available data. Indicators reflecting outcomes from previous flooding events were not considered due to potential data gaps across the entire city. Indicators are highlighted with superscripts if an empirical study has obtained statistically significant results to determine the correlation between the indicator and flooding outcomes based on Madajewicz (2020) "MM", Tellman et al. (2020) "T" and Rufat et al. (2019) "R". Each initial is added "ns" or "ss" if the indicator tested produced statistically significant results. A relationship indicated as both positive and negative (+/-) means that the tests produced mixed results on the relationship between the indicators and vulnerability.

Table 5.5: FVI Indicators

Vulnerability Category	**Indicator (relationship)**	**Source(s)**
Capacity to Recover	Educational attainment e.g. Population lacking a High School Diploma (+) (validated for population lacking college degree)(-) ^{MMns}	(de Sherbinin & Bardy, 2015; Herreros-Cantis et al., 2020; Kontokosta & Malik, 2018; Zahmatkesh & Karamouz, 2017)
Capacity to Recover	**Households/people living below poverty level (+)** $^{Tss\ MMns}$	(de Sherbinin & Bardy, 2015; Herreros-Cantis et al., 2020; Reckien, 2018; Zahmatkesh & Karamouz, 2017) Phase 1 stormwater resiliency plan
Capacity to Recover	Single parent families (+)^{MMns}	(de Sherbinin & Bardy, 2015; Herreros-Cantis et al., 2020)
Capacity to Recover	Single occupant homes (+) ^{MMns}	(Kontokosta & Malik, 2018; Reckien, 2018)
Capacity to Recover	Non-family households with under 18 occupants (+) (validated for families with children under 18) ^{MMns}	(Kontokosta & Malik, 2018)
Capacity to Recover	Vacant housing (+) $^{Rss\ Tss}$	(Kontokosta & Malik, 2018; Zahmatkesh & Karamouz, 2017)
Capacity to Recover	Population over 3 not enrolled in school (+)	(Kontokosta & Malik, 2018)
Capacity to Recover	**Population lacking health insurance coverage** (+)	(Kontokosta & Malik, 2018)
Capacity to Recover	Unemployment rate (+)	(Kontokosta & Malik, 2018)
Capacity to Recover	Gini Index (income inequality) (+)	(Kontokosta & Malik, 2018)
Capacity to Recover	Economic diversity (% employed population working in the single largest economic sector)	(Kontokosta & Malik, 2018)

	(-)	
Capacity to Recover	Households receiving social security support (+) MMns	(de Sherbinin & Bardy, 2015)
Capacity to Recover	Households making more than 200000 annually (-)	(de Sherbinin & Bardy, 2015)
Capacity to Recover	**People / Businesses with Flood Insurances** (-)	(Zahmatkesh & Karamouz, 2017)
Capacity to Recover	Population employed in vulnerable jobs (+)	(Zahmatkesh & Karamouz, 2017)
Capacity to Recover/ Susceptibility	**Language isolation** (+) Tns	(Chang et al., 2021; de Sherbinin & Bardy, 2015; Herreros-Cantis et al., 2020; Zahmatkesh & Karamouz, 2017)
Capacity to Recover/ Susceptibility	**Income (-)** MMss Rns Tns	(Chang et al., 2021; Herreros-Cantis et al., 2020)
Capacity to Recover/ Susceptibility	Presence of Emergency Centers (-)	(Chang et al., 2021)
Capacity to Recover/ Susceptibility	Female headed households MMns	(de Sherbinin & Bardy, 2015)
Capacity to Recover/ Susceptibility	Density of critical services (hospitals, schools, food sources, evacuation shelters, homeless shelters, public safety, WWTP, Airports, Bridges, Tunnels, streets, subway lines and stop) (-) MMss	(Kontokosta & Malik, 2018; Zahmatkesh & Karamouz, 2017) Phase 1 stormwater resiliency plan
Capacity to Recover/Susceptibility	**Owner occupied households** (+/-) Rss Tss MMss	(Chang et al., 2021; de Sherbinin & Bardy, 2015; Herreros-Cantis et al., 2020) Phase 1 stormwater resiliency plan
Exposure	Number of buildings exposed (+)	(Herreros-Cantis et al., 2020; Zahmatkesh & Karamouz, 2017) Phase 1 stormwater resiliency plan
Exposure	Building Density (+)	(Kontokosta & Malik, 2018)
Exposure	Number of residential units exposed (+)	(Herreros-Cantis et al., 2020; Zahmatkesh & Karamouz, 2017)
Exposure	Total residential area exposed (+)	(Herreros-Cantis et al., 2020)
Exposure	Total industrial area exposed (+)	(Herreros-Cantis et al., 2020)
Exposure	Total commercial area exposed (+)	(Herreros-Cantis et al., 2020; Zahmatkesh & Karamouz, 2017)
Exposure	Total office area exposed (+)	(Herreros-Cantis et al., 2020)
Exposure	Total value of exposed properties (-) Tss	(Herreros-Cantis et al., 2020; Zahmatkesh & Karamouz, 2017)
Exposure	Total exposed population (+)	(Chang et al., 2021; Herreros-Cantis et al., 2020; Zahmatkesh & Karamouz, 2017)

Exposure	Population density (+)	(Chang et al., 2021; de Sherbinin & Bardy, 2015; Kontokosta & Malik, 2018; Reckien, 2018; Zahmatkesh & Karamouz, 2017)
Exposure	Proximity to locations listed in the Toxic Release Inventory (+)	(Chang et al., 2021)
Exposure	Population per housing unit (+/-) MMns Tss	(de Sherbinin & Bardy, 2015)
Exposure	Area in the floodplain (+)	Phase 1 stormwater resiliency plan
Exposure	311 call counts reporting flooding (+)	Phase 1 stormwater resiliency plan
Exposure	Average elevation (-)	Phase 1 stormwater resiliency plan
Exposure	Length of coastline (+)	(Zahmatkesh & Karamouz, 2017)
Susceptibility	**Population identified as BIPOC** (+/-) Rss Tss MMss	(de Sherbinin & Bardy, 2015; Herreros-Cantis et al., 2020; Reckien, 2018) Phase 1 stormwater resiliency plan
Susceptibility	Impervious surfaces (-) Tss	(Chang et al., 2021; Zahmatkesh & Karamouz, 2017) Phase 1 stormwater resiliency plan
Susceptibility	Wetlands (-)	(Chang et al., 2021)
Susceptibility	Road density (+)	(Chang et al., 2021)
Susceptibility	Presence of Green Infrastructure (-)	(Chang et al., 2021) Phase 1 stormwater resiliency plan
Susceptibility	Density of subway stations (redundancy for evacuation) (-)	(Kontokosta & Malik, 2018)
Susceptibility	Tree density (-)	(Kontokosta & Malik, 2018)
Susceptibility	Open Space (-)	(Kontokosta & Malik, 2018)
Susceptibility	Median Age (+)	(de Sherbinin & Bardy, 2015)
Susceptibility	Female population (+)	(de Sherbinin & Bardy, 2015; Reckien, 2018)
Susceptibility	People living in a nursing home or skilled-nursing facility (+)	(de Sherbinin & Bardy, 2015)
Susceptibility	Average building age (+)	Phase 1 stormwater resiliency plan
Susceptibility	**Presence of basements** (+)	Phase 1 stormwater resiliency plan
Susceptibility	Presence of coastal structural measures to control floods and flood/storm control capacities (-)	(Zahmatkesh & Karamouz, 2017)
Susceptibility	**Building height / residential building type**	

Susceptibility/ Capacity to recover	Households without a car (+/-) Rss	(de Sherbinin & Bardy, 2015; Herreros-Cantis et al., 2020; Reckien, 2018) Phase 1 stormwater resiliency plan
Susceptibility/ Capacity to recover	**Vulnerable age (e.g. less than 5, over 65)** (+/-) Tss Rss MMns	(Chang et al., 2021; de Sherbinin & Bardy, 2015; Herreros-Cantis et al., 2020; Kontokosta & Malik, 2018; Reckien, 2018; Zahmatkesh & Karamouz, 2017) Phase 1 stormwater resiliency plan
Susceptibility/ capacity to recover	**Residents' awareness and preparedness** (-)	(Zahmatkesh & Karamouz, 2017)
Susceptibility/ Capacity to recover	**People with a disability or chronic illness** (+) Tss MMss	(Zahmatkesh & Karamouz, 2017)

Appendix 5.2

Full-size individual exposure maps for each scenario.

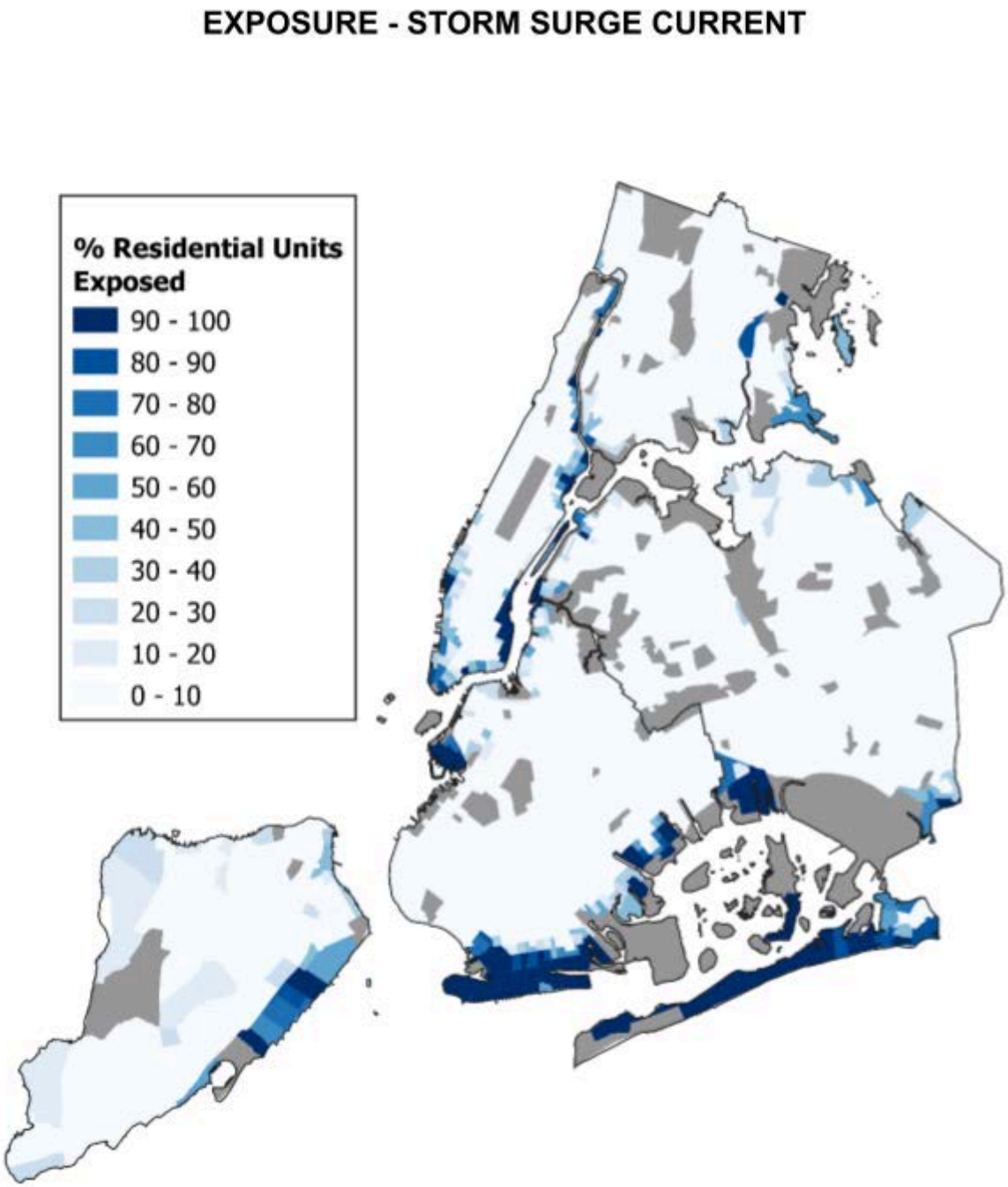

Figure 5.9: Exposure - Storm Surge Current

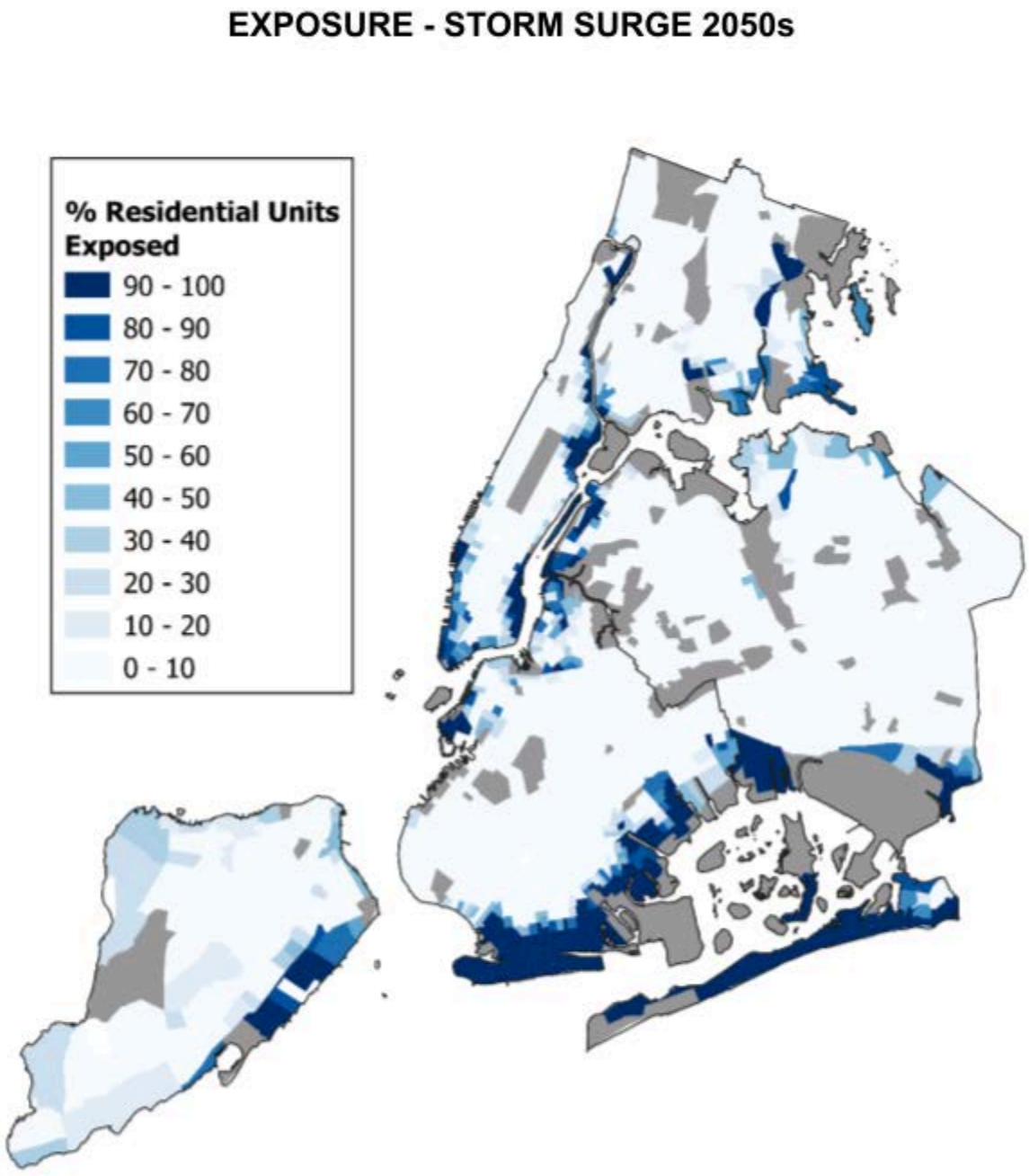

Figure 5.10: Exposure - Storm Surge 2050s

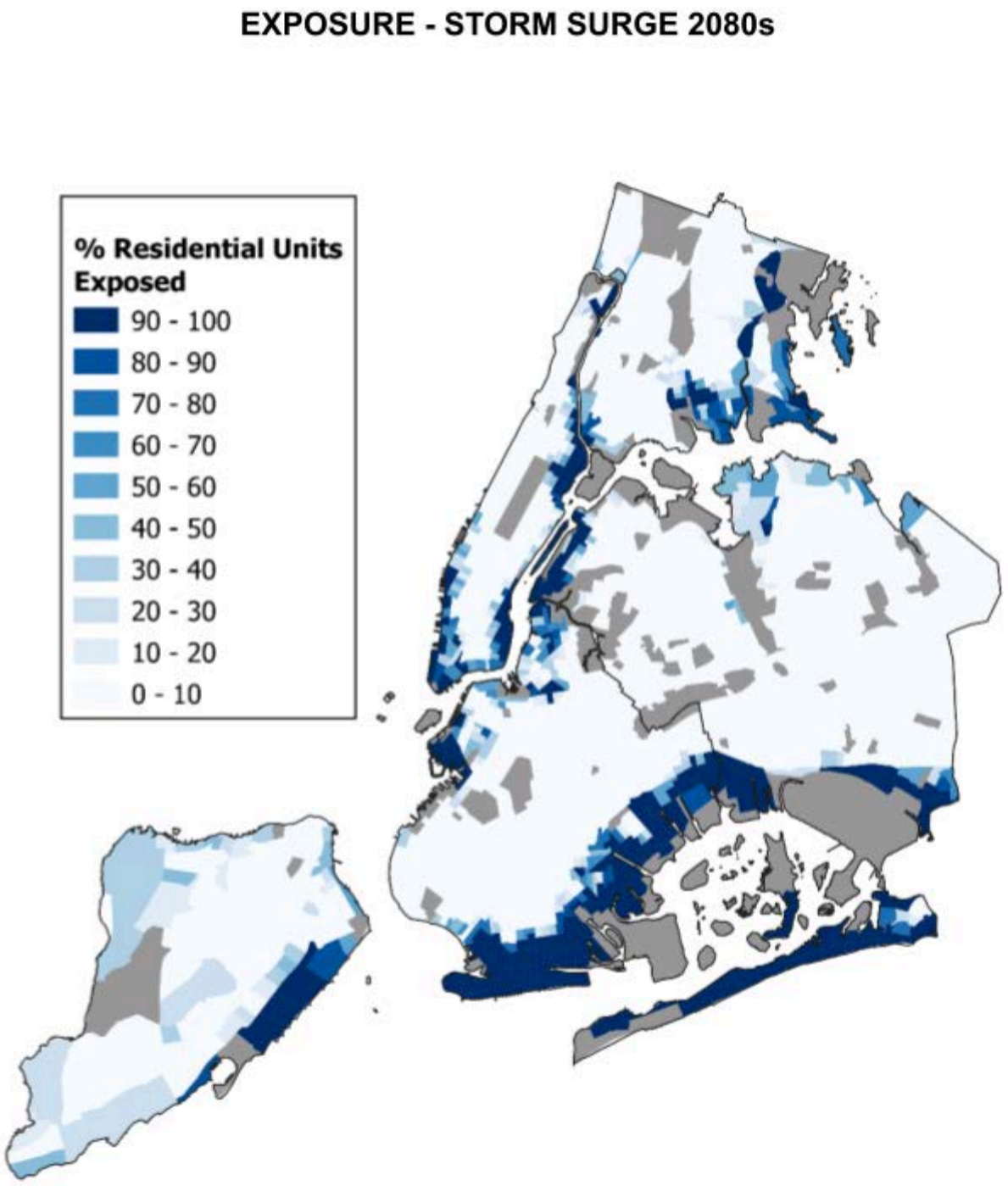

Figure 5.11: Exposure - Storm Surge 2080s

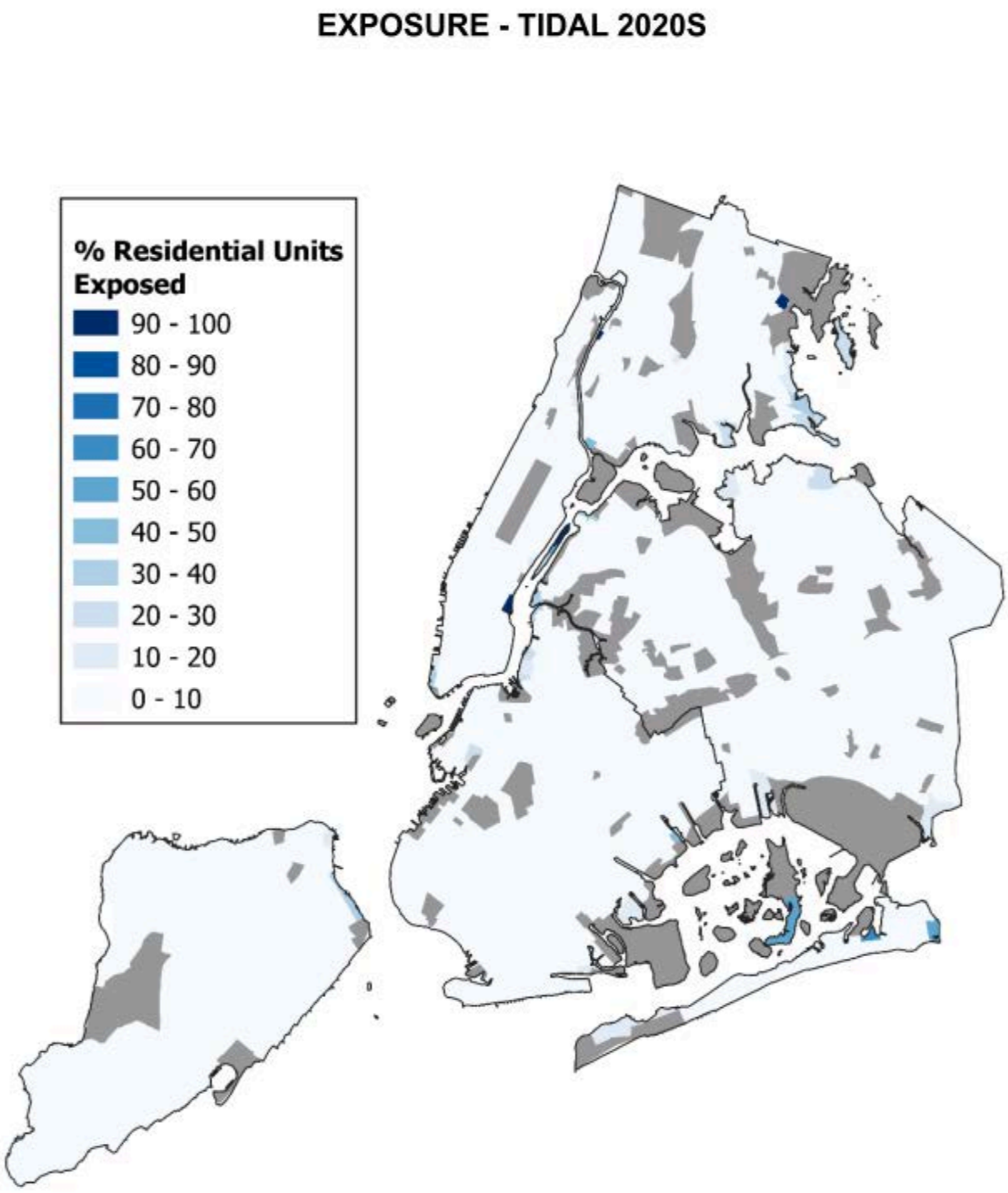

Figure 5.12: Exposure - Tidal 2020s

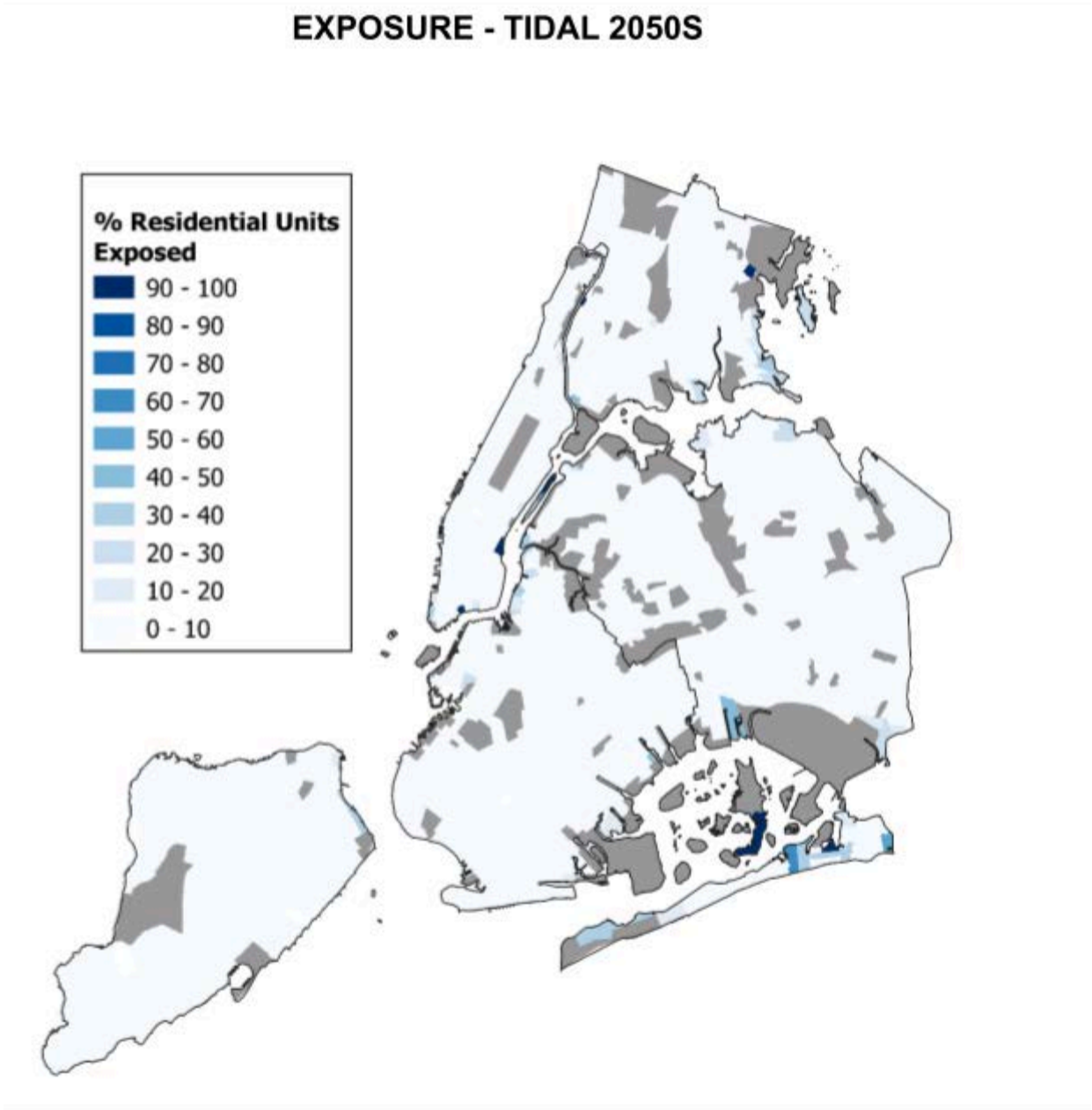

Figure 5.13: Exposure - Tidal 2050s

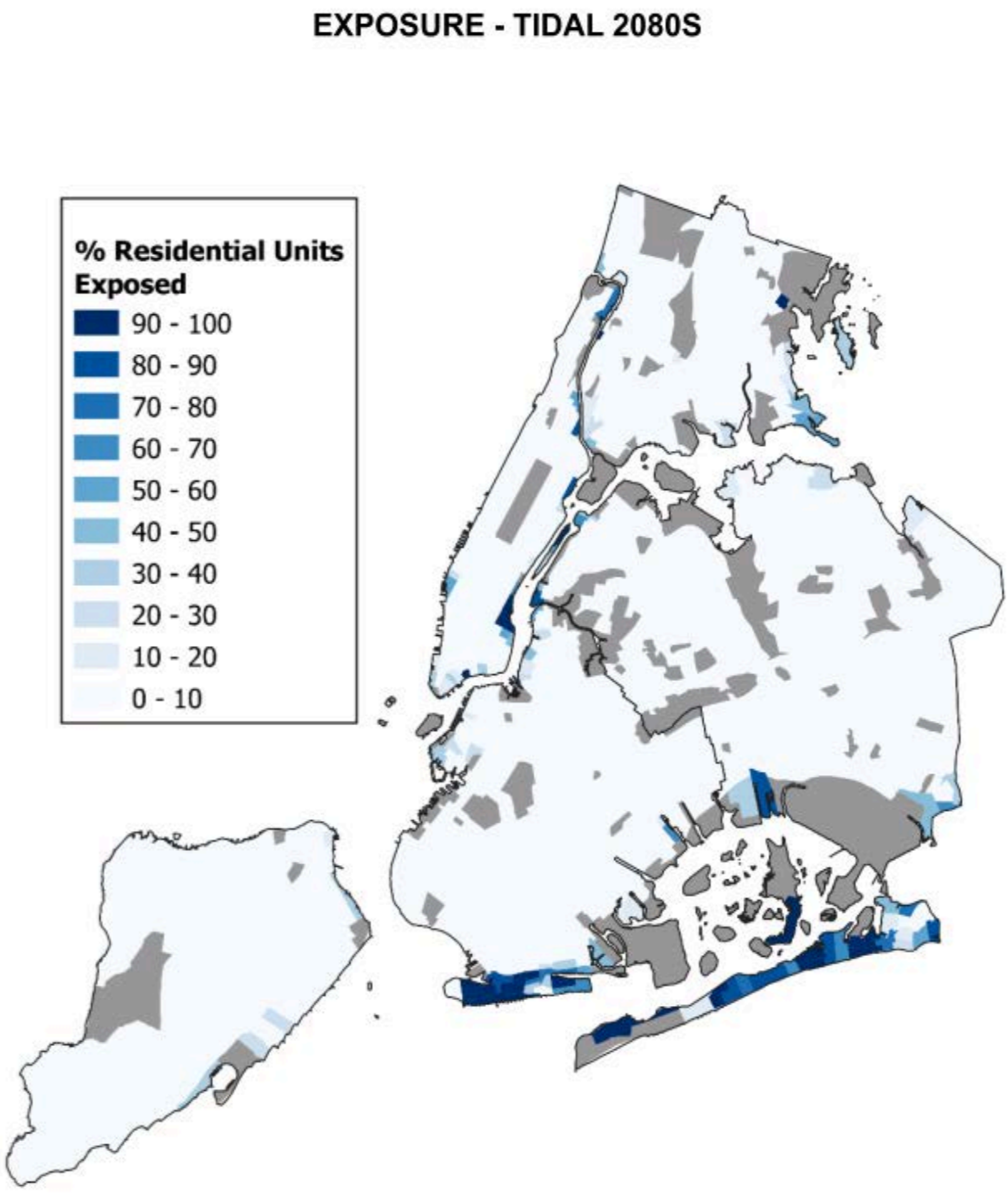

Figure 5.14: Exposure - Tidal 2080s

Appendix 5.3

Table 5.5: Census Tracts removed from the FVI development due to a lack of consistent sociodemographic data. Population 2020 shows the amount of people counted in the U.S. Census.

Tract GEOID 2020	Park / Site Name	Population 2020
36061014300	Central Park	129
36005043503	Van Cortlandt Park	122
36005050400	Pelham Bay Park NORTH	5
36005027600	Pelham Bay Park SOUTH	23
36005033400	Bronx Zoo + Botanical Park	69
36061029700	Inwood Hill Park	16
36005016300	Crotona Park	34
36005002400	Soundview Park	6
36047017700	Prospect Park	15
36047017500	Greenwood Cemetery	5
36047035702	Lincoln Terrace	15
36047015400	Dyker Beach Park	9
36047066600	Marine Park	1
36047102802	Canarsie Park	5
36081071600	JFK	2
36081064102	Forest Park	4
36047118000, 36081056100, 36047040700	Highland Park	33

36081066302	Juniper Valley Park	4
36081065501	St. John Cemetery	3
36081060701	Mt. Olivet Cemetery	3
36081053902	Linden Hill cemetery	88
3608103z8302	Flushing Meadows Corona Park	44
36081121100	Kissena Park	2
36081079300	Mt. Hebron Cemetery	1
36081128300	Cunningham Park	5
36081138502	Alley Pond Park	85
36081028803	Baisley Pond Park	8
36081065402	Brookville Park	5
36081010701	LaGuardia Airport	7
36085022802	Freshkills Park	15
36085022801	Freshkills Park WEST	95
36085015400	Great Kills Park	5
36085005902	Silver Lake Park	5

Appendix 5.4

Full-size individual FVI maps for each scenario.

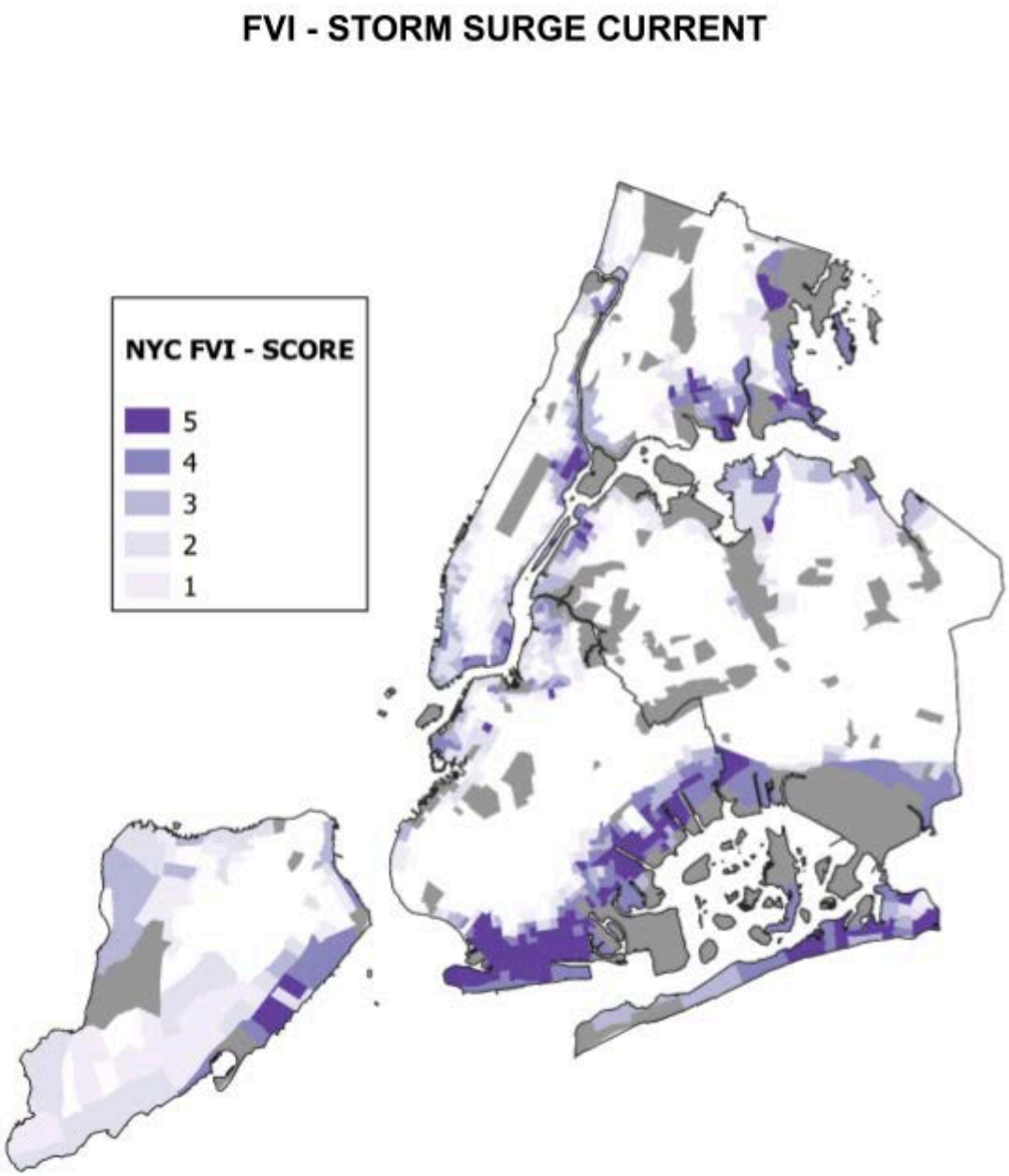

Figure 5.15: FVI- Storm Surge Current

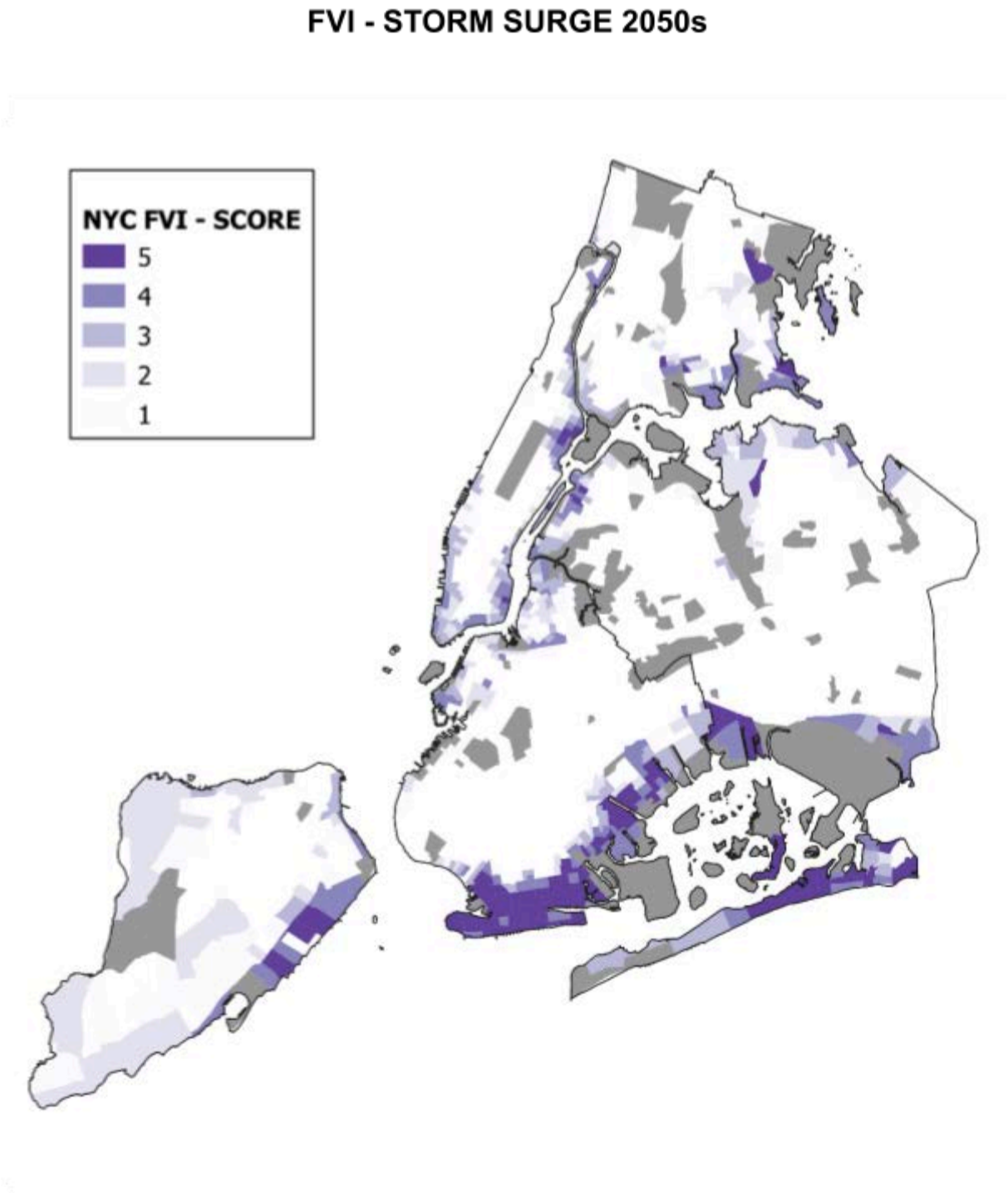

Figure 5.16: FVI- Storm Surge 2050s

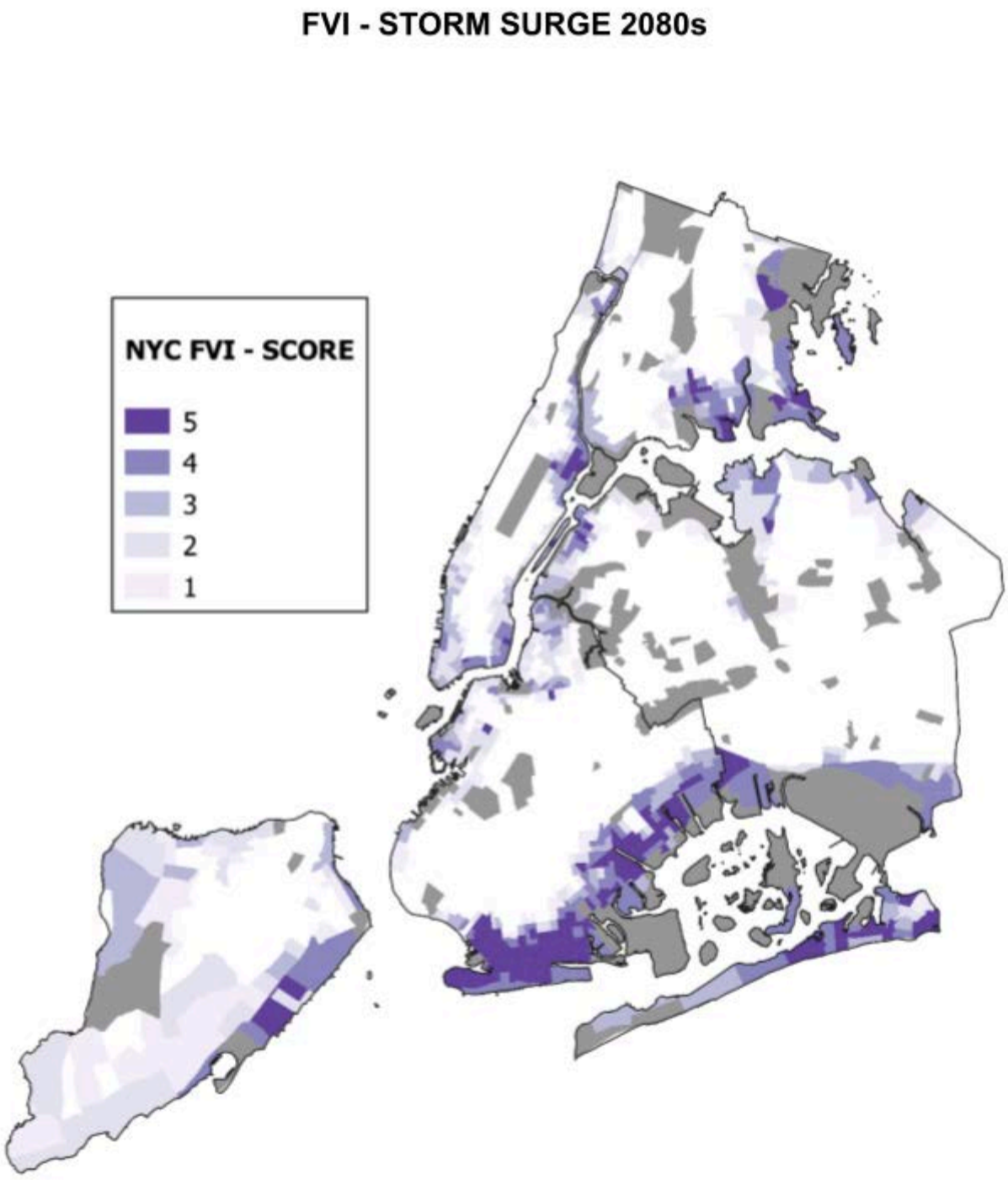

Figure 5.17: FVI - Storm Surge 2080s

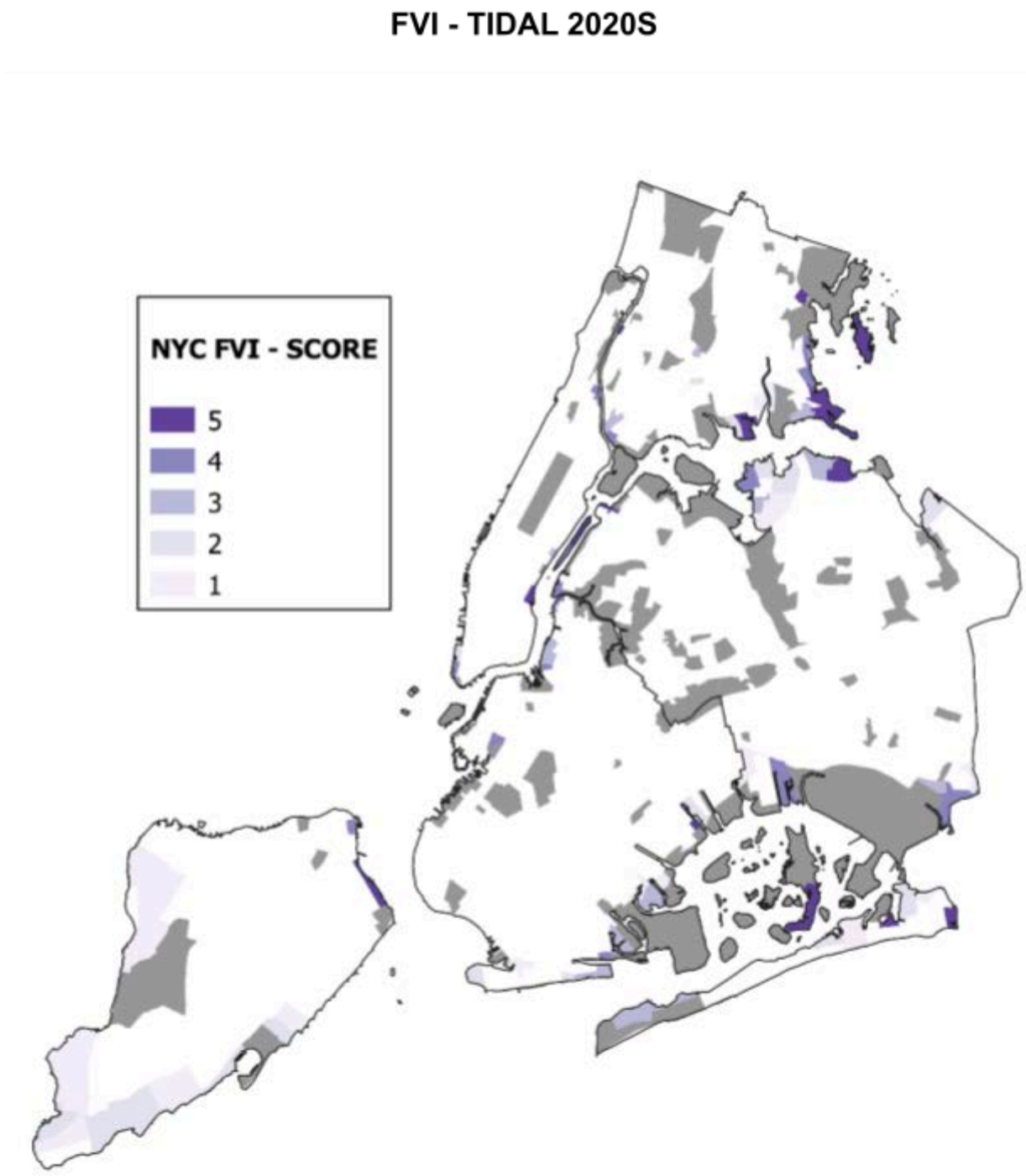

Figure 5.18: FVI - Tidal 2020s

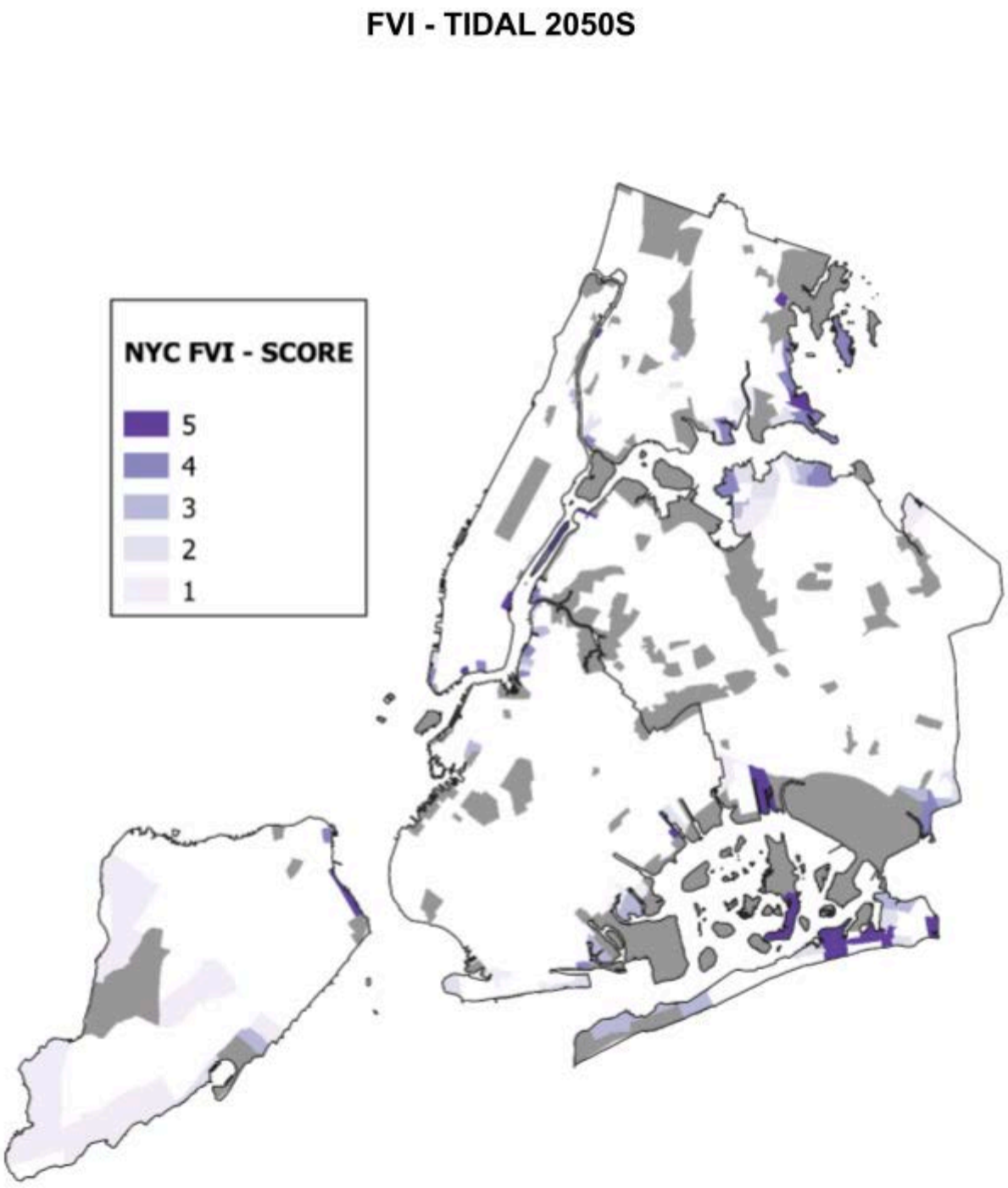

Figure 5.19: FVI - Tidal 2050s

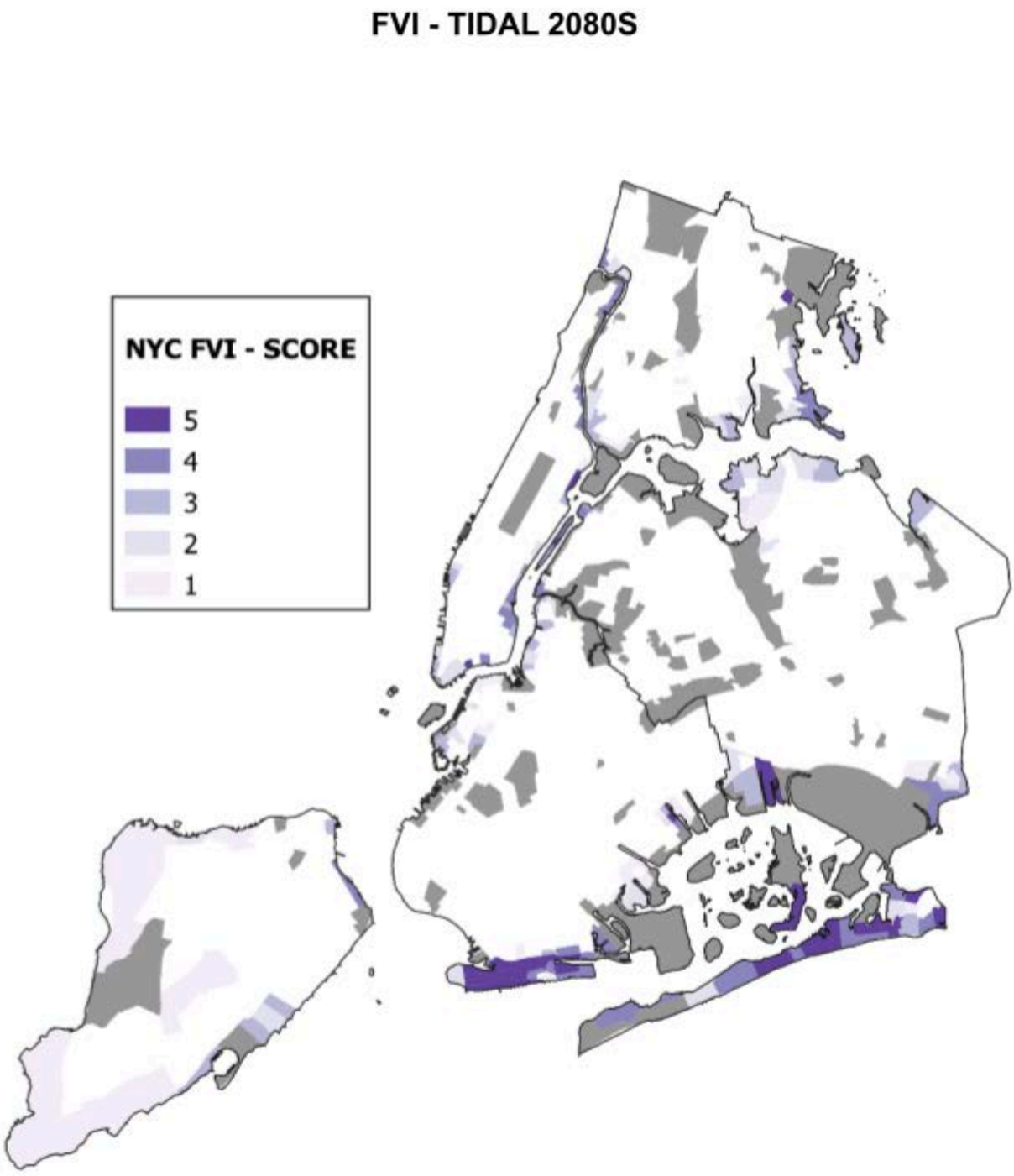

Figure 5.20: FVI - Tidal 2080s

Cross-Cutting Themes and Task Synthesis

Interactions and Synergies

Throughout the VIA process, there is a collaborative effort among the task teams to integrate data and methodological expertise across the diverse climate, impacts, and vulnerability research areas. These collaborative approaches are crucial in the multi-faceted and co-produced research process. The Task teams, aside from the deep research in each Task, have also met regularly to share interim and final results, discuss cross-cutting themes, and to synthesize findings across the VIA project to provide conclusions and recommendations that are robust and comprehensive.

Task 2 (Climate Projections and Climate-Sensitive Hazards) & Task 3 (Extreme Heavy Rainfall Analysis):

- *Shared Climate Modeling Data*: Task 2's climate projections, including sea level rise and temperature changes, and Task 3 analyses of extreme heavy rainfall are important to consider together. These tasks shared climate modeling data to ensure consistency in their projections and to understand the interplay between different climate variables.
- *Joint Impact Analysis*: The insights from Task 2 regarding climate-sensitive hazards helped guide Task 3 in understanding the potential impacts of heavy rainfall events, particularly in the context of urban flooding and storm surges.

Task 2 (Climate Projections) and Task 4 (Health-Related Economic Costs of Climate Events):

- *Utilizing Climate Data for Health Impact Assessment:* The climate projections from Task 2 were pivotal for Task 4's assessment of health-related economic costs. Understanding the frequency and severity of climate-sensitive events, such as heat waves or extreme weather, was important for evaluating the impact on public health.
- *Collaborative Risk Assessment*: The risk assessments conducted in Task 2 provided a foundational basis for Task 4's evaluation of economic impacts, ensuring that the health impact assessments are aligned with the latest climate projections.

Task 3 (Heavy Rainfall) and Task 4 (Health-Related Economic Impacts):

- *Data on Rainfall Intensity and Health Outcomes*: The findings of Task 3, particularly regarding the increase in frequency and intensity of heavy rainfall, helped assess the

potential increase in health-related incidents, such as injuries or illnesses due to flooding or mold exposure.

- *Infrastructure Development and Health Risk:* The insights from Task 3 on urban flooding informed Task 4's analysis of economic costs, particularly in urban planning and infrastructure development, to mitigate health risks.

Task 5 (Flood Vulnerability):

- *Flood Vulnerability Index development*: The final FVIs were not only included in the NPCC4 Flooding chapter, but the hazard data were also provided to Task 4 to inform population projections and shared with other key partners in the city during development, for example to inform the FloodNet team's strategy for placing new flood sensors in flood vulnerable locations.

Further Research

The VIA study has illuminated several critical areas for future research, essential for deepening our understanding of climate change impacts in New York City. These areas include, but are not limited to, acquiring more detailed data on precipitation and storm surge patterns, examining the potential effects of climate change on urban heat islands and related health costs, analyzing the impacts of drought and air quality, understanding the combined effects of multiple climate hazards, validating vulnerability indicators for different types of flooding, documenting the relationship between indicators and different components of vulnerability to guide the development of programs that reduce vulnerability, and advancing the vulnerability assessment methodology to better track the change in vulnerability over time. Despite the comprehensive insights provided by the VIA process, the importance of ongoing research cannot be overstated.

Continued investigation is crucial. Even with the detailed reporting presented in VIA, these identified research gaps are stepping stones for further collaborations and investments involving academic institutions, city government, and local community members. Proactively identifying these avenues for future research is a crucial step toward making New York City more forward-thinking in its approach to climate adaptation.